PETROLOGY AND PETROGENESIS OF THE RONDA HIGH-TEMPERATURE PERIDOTITE INTRUSION, SOUTHERN SPAIN

By

MASAAKI OBATA

B.S., Kyoto University (Japan)(1970)

M.S., Kanazawa University (Japan)(1972)

SUBMITTED IN PARTIAL FULFILLMENT
OF THE REQUIREMENTS FOR THE
DEGREE OF
DOCTOR OF PHILOSOPHY
at the
MASSACHUSETTS INSTITUTE OF TECHNOLOGY

(May, 1977)

Signature of Author.....
Department of Earth and Planetary Sciences, May, 1977

Certified by.....
s/ Supervisor

Accepted by.....
Chairman, Department Committee on Graduate Students

TABLE OF CONTENTS

LIST OF FIGURES

LIST OF TABLES

LIST OF ABBREVIATIONS

Ab	albite	K	kyanite
Amph	amphibole	Ol	olivine
An	anorthite	Opx	orthopyroxene
C	corundum	Plag	plagioclase
Cpx	clinopyroxene	Py	pyrope
Di	diopside	Qz	quartz
En	enstatite	Serp	serpentine
Fo	forsterite	Sp	spinel
Gar	garnet		

PETROLOGY AND PETROGENESIS OF THE RONDA HIGH-TEMPERATURE PERIDOTITE INTRUSION, SOUTHERN SPAIN

By

MASAAKI OBATA

Submitted to the Department of Earth and Planetary Sciences on May 5, 1977 in partial fulfillment of the requirements for the Degree of Doctor of Philosophy.

ABSTRACT

The Ronda peridotite is a high-temperature peridotite intrusion of the upper mantle emplaced in the internal zone of the Betic Cordillera, S. Spain. The massif was mapped in 4 zones of mineral facies: garnet lherzolite facies, ariegite subfacies and seiland subfacies of spinel lherzolite facies, and plagioclase lherzolite facies. Coexisting minerals of 12 peridotites and 9 mafic layers were analyzed by electron microprobe analyzer. The mineral analyses were correlated to the 4 mineral facies. Equilibrium conditions of the massif were determined by element partitioning: The peridotite once equilibrated at 1100-1200^{o}C and 20-25 kb in the upper mantle. It was then recrystallized and reequilibrated at 800-1000^{o}C and 5 to 13 kb in the 4 mineral facies zones during intrusion into the earth's crust. Different parts of the massif followed different P-T trajectories because of different local cooling rates during decompression. This dynamic cooling model explains the apparent large pressure manifested in a relatively small body.

Phase relations of a mafic layers of the Ronda massif at high T and P were determined by solid media piston cylinder apparatus. The mafic layer is not in equilibrium with peridotite in upper mantle conditions. It was concluded that the mafic layers do not represent melts but high pressure cumulates from the partial melts of peridotite. The sequence of cumulate precipitation was Opx+Cpx+Sp $\rightarrow$ Opx+Cpx+Gar $\rightarrow$ Cpx+Gar. The depth of precipitation was proberbly near 70 km.

A 3 step process is proposed for the peridotite intrusion: 1. Mantle diapir rose to 70 km depth, causing igneous differentiation and volcanism followed by subsolidus (metamorphic) recry-

stallizationin probable Late Triassic age; 2. tectonic vertical emplacement of the metamorphosed peridotite into crust caused the second recrystallization of peridotite in the 4 mineral facies and contact metamorphism of the crustal rocks; 3. tectonic lateral re-emplacement in the Late Cretaceous to Miocene age broughtthe massif to its present position in the Betic zone. The second and the third step of peridotite emplacements were probably related to relative motions of the Iberian and African plates in the Mesozoic to Early Tertiary.

Thesis Supervisor: Dr. J. S. Dickey, Jr.

Title: Associate Professor of Earth and Planetary Sciences

Chapter 1

INTRODUCTION

Problems

The Ronda peridotite is a large high-temperature peridotite intrusion emplaced in the internal zone of the Betic Cordillera (alpine fold belt, Spain). The Ronda massif is differentiated into 80-95% peridotite and ~5% mafic layers. This differentiation of the massif was thought to be by partial fusion processes in the upper mantle (Dickey, 1970). Certain geochemical features, however, had been left unexplained.

This restudy of the Ronda peridotite started with electron microprobe analyses of minerals in peridotites and mafic layers in an attempt of determining physical conditions of the igneous differentiation. In the early stages of the investigation, however, it was recognized that the effect of metamorphism during the intrusion was more intense than previously realized. As with many alpine-type peridotites, much petrographic and mineralogic information about the petrogenesis of the Ronda massif was obscured by the metamorphism. In order to discuss the igneous history of the massif, therefore, the effects of metamorphism had to be correctly defined.

The study of such metamorphism would also provide petrologic constraints to the tectonics of the peridotite intrusion. The tectonic models of peridotite intrusion must be closely linked to regional tectonics, and the concepts of regional tectonics, in turn, may be, to some extent, affected by the concepts of the intrusion tectonics. This study involved mapping, petro-

graphic work, mineral analyses by electron microprobe, high P-T experiments and theoretical work on Al_2O_3 in orthopyroxenes. The principal problems focussed on in the discussions are;

1) metamorphism and equilibration history, 2) igneous differentiation, and 3) tectonics of the peridotite intrusion.

Previous Works

A major petrographic study of the Ronda massif was first published by Orueta in 1917. The massif was not subjected to modern petrologic techniques until 1966 (Dickey 1970). Metamorphism and structure of the contact aureole were studied in detail by Loomis (1972a,b). Structural and petrofabric analyses of the peridotite were performed by Darot (1973, 1974) and by Lundeen (1976). Several attempts have been made to interpret the peridotite intrusion in the framework of Alpine tectonics (Loomis, 1975; Lundeen, 1977).

Construction of Thesis

The thesis consists of 8 chapters and 4 appendices. Chapter 2 summarizes the tectonic and geologic setting of the peridotite and describes the field occurrence of the peridotite and mafic layers. Chapter 3 describes the peridotites and mafic layers. Based on analyses of mineral parageneses the massif was mapped in 4 mineral facies zones. Chapter 4 presents microprobe analyses of minerals in the peridotites and mafic layers. Chapter 5, by reviewing several geothermometers and geobarometers, estimates equilibrium conditions of the massif. P-T trajectories of the intrusion were deduced.

Chapter 6 presents the results of high P-T experiments of a Ronda mafic layer. Interpreting the experimental results, field, petrologic and chemical evidences, igneous differentiation of peridotite is discussed. Chapter 7 discusses the tectonics of the periditite intrusion based on the results of Chapters 5 and 6. Chapter 8 is a summary of main conclusions.

There are 4 appendices: Appendix 1 is a method of electron microprobe analyses. Appendix 2 is a list of modal analyses and normalized modes of the 21 peridotites as discussed in Chapter 6. Appendix 3 is a complete list of microprobe analyses of minerals which were used in the discussions but not listed in the text. Appendix 4 is a publication of the author's which was produced as a part of his thesis work.

Chapter 2

FIELD RELATIONS

2.1 Tectonic Setting and Regional Geology

The Betic Cordillera, a south-west flank of the Alpine fold belt, lies between the exposed Hercynian and older rocks of the continental Iberian block and the basin of the Alboran Sea. To the south-west the Alpine orogen curves sharply across the Straits of Gibraltar and forms the Rif Mountains. The Betic Cordillera is, on the basis of rock facies and structures, subdivided into three tectonic zones (Fallot, 1948) (Fig. 2-1): 1) Prebetic Zone, relatively undeformed autochthonous continental and shallow marine sediments of Mesozoic and Tertiary ages; 2) Subbetic Zone, internally displaced and folded continental and shallow marine sediments of Mesozoic and younger age; 3) Betic or Internal Zone, a structurally complex association of metamorphic, volcanic, and plutonic rocks and pelitic sediment of Paleozoic and younger age. The Ronda peridotite massif crops out ($\sim$300 km^2) in the west end of the Internal Zone near the Mediterranean coast between Estepona and Marbella.

The internal zone is a pile of at least four major nappes overthrust toward the north or northwest. The peridotite was involved in the overthrusting of the major phase of the alpine orogeny.

The country rock around the peridotite comprise four major tectonic units (Fig. 2-2). They are, structurally in

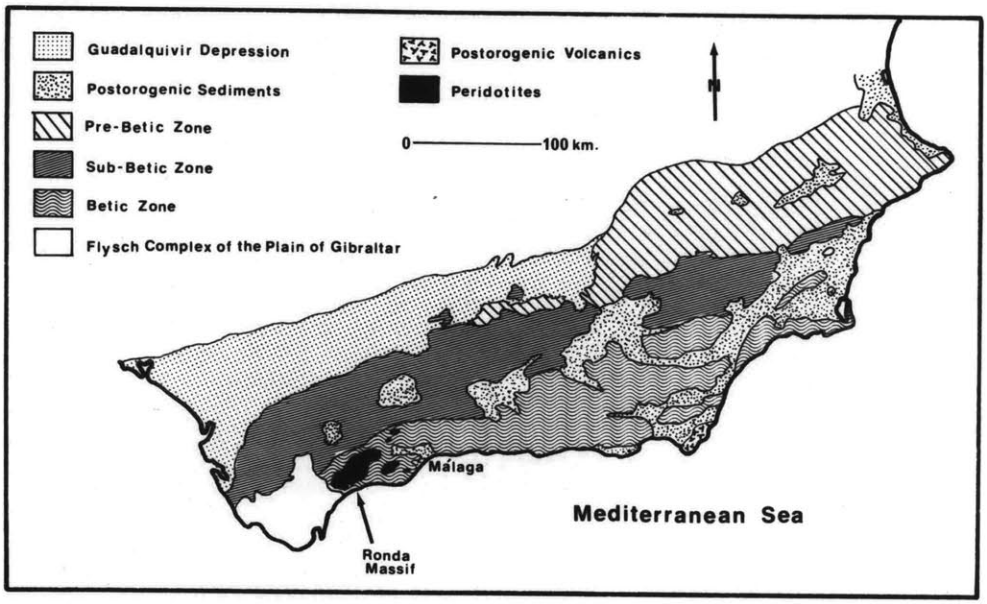

Figure 2-1. Tectonic map of the Betic Cordillera (after Dickey, 1970, modified from Fontobte, 1966).

in descending order:

1) Malaguide nappe: Paleozoic pelitic sediments and their metamorphosed equivalents and Permo-Triassic conglomerate, limestone and dolomite and Jurassic limestone.

2) Casares unit: probable Paleozoic pelitic sediments and their metamorphosed equivalents and marble and dolomitic marble of Triassic age.

3) Blanca unit: marble and gneiss with minor quartzite and amphibole layers of Triassic and Paleozoic age.

4) Nieves unit: dolomite and limestone of Triassic and Jurassic Age.

The Casares unit has been interpreted as the western continuation of the Alpujarride nappe complex identified within the Internal Zone farther east (Dürr, 1967). The Blanca unit may correspond to the tectonically deepest member of the Internal Zone, the Nevado-Filabride complex as suggested by Egeler and Simon (1969) and Lundeen (1977). The position of the Nieves unit is not well defined, though it has been suggested to be between the Casares and the Blanca units (Egeler and Simon, 1969).

The Ronda peridotite lies structurally between the top of the Blanca unit and the base of the Casares unit as a slab approximately 2 km thick. The peridotite is not deeply-rooted in its present position, as suggested by Loomis (1972b), and together with its surroundings, it should be regarded as allochthonous.

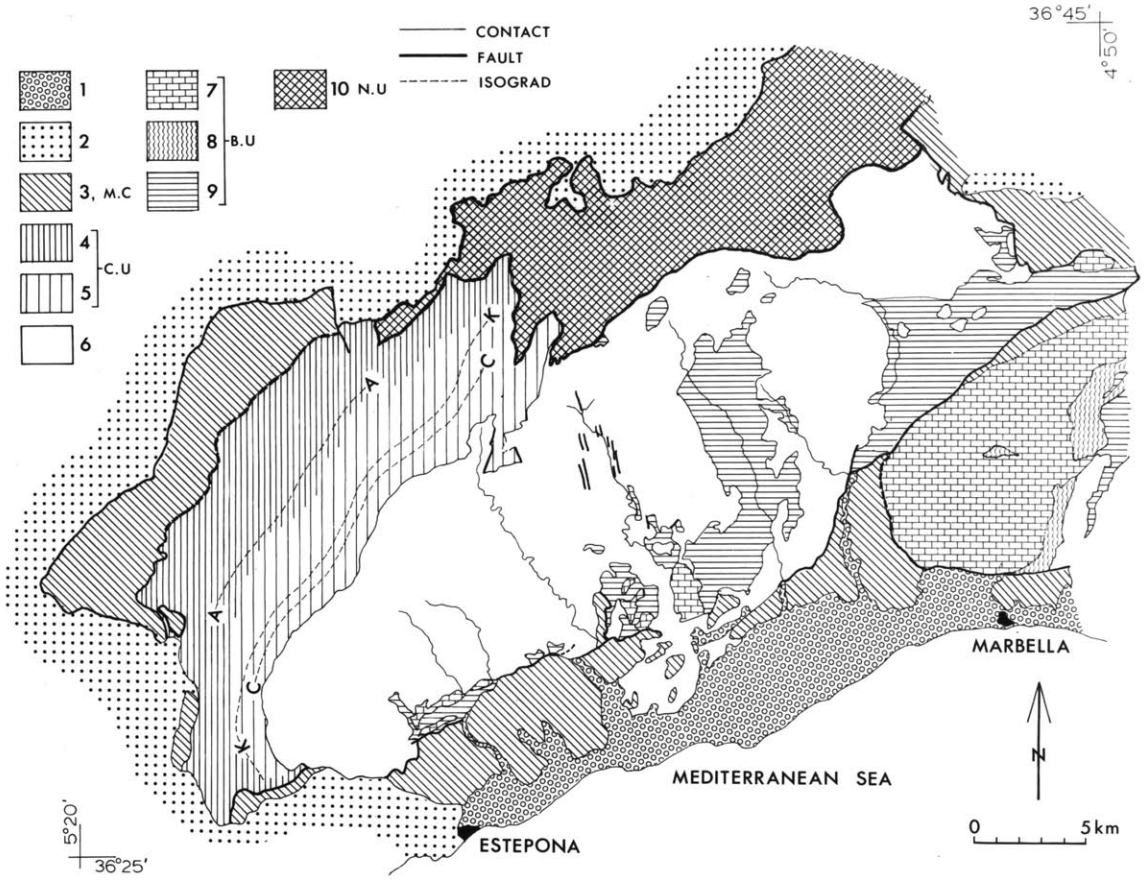

Figure 2-2. Geologic setting of the Ronda peridotite massif, simplified from Lundeen's (1976) compilation of earlier workers'. 1, Coastal deposits and alluvium (Pliocene - Holocene); 2, Marl (Cretaceous), sandy flysch (Oligocene), and coarse clastic rocks (Miocene); 3, Malaguide complex (see text); 4, 5, Casares unit, (4, unmetamorphosed pelitic sediments; 5, metamorphosed pelitic sediments, see text); 6, peridotite and related rocks; 7,8,9, Blanca unit (7, dolomite and marble; 8, amphibolite; 9, gneiss); 10, Nieves unit (see text). Isograds: A, andalusite; K, K-feldspar; C, cordierite.

There is a pronounced positive Bouguer anomaly (>100 mgal) south-west of Málaga (Robertson, 1970) which has been attributed by Bonini et al. (1973) to a vertical column of peridotite extending to the mantle through 35 km of continental crust. The actual outcrop of the peridotite, however, is offset 50 km northwest of the position of the proposed column of peridotite (Darot, 1974). This offset is compatible with the sense of the alpine thrusting (Mollat, 1968; Didon et al., 1973).

2.2 Contact metamorphism

The peridotite has distinct metamorphic aureoles approximately 5 km thick in the Casares unit and a few hundred meters thick in the Blanca unit. The nature of metamorphism in the Casares unit and the Blanca unit differs in grade, structure, thickness, and perhaps age.

The Paleozoic pelitic sediments of the Casares unit, approaching the contact, grade from low grade phyllite, through mica shist, and to garnet cordierite gneiss at the contact. The stable mineral assemblage sequence is summarized by Loomis (1972a), in order of increasing grade, as follows:

1) quartz + sericite + chlorite + (plagioclase);
2) quartz + muscovite + biotite + andalusite $\pm$ garnet $\pm$ plagioclase;
3) quartz + muscovite + biotite + andalusite $\pm$ staurolite + plagioclase; quartz + K + feldspar +

biotite + chlorite + diopside + plagioclase + sphene;

quartz + biotite + chlorite ± staurolite + garnet + plagioclase;

4) quartz + muscovite + biotite + sillimanite + staurolite + plagioclase;
5) quartz + K - feldspar + biotite + sillimanite + staurolite + plagioclase.
6) quartz + K - feldspar + biotite + sillimanite + garnet + plagioclase + (hercynite); quartz + K - feldspar + biotite + clinopyroxene + orthopyroxene + plagioclase.

Kyanite also appears in the high-grade gneiss near the contact. Loomis (1972a) interpreted the kyanite to be a relict of early contact metamorphism caused by the hot peridotite intrusion deep in the crust. The fact that the isograds are parallel to the peridotite contact (Fig. 2-2) and the coherency of structural elements within the aureole and the peridotite near the contact provide strong evidence of the contact metamorphic origin (Loomis, 1972b). A contact temperature of 800 ± 100°C has been estimated by extrapolation of a thermal gradient 80°C/km, and a final overburden pressure of 4.3 ± 1 kbar has been deduced from the coincidence of the andalusite - sillimanite and muscovite + quartz = K - feldspar + sillimanite reactions in the assemblage sequence (Loomis, 1972a).

The contact aureole in the Blanca unit contains a different assemblage sequence from the Casares contact: Adjacent to the peridotite is a well-crystallized, massive, cordierite-bearing hornfels (cordierite + biotite + sillimanite + K -

feldspar + plagioclase + quartz), a few hundred meters thick, grading through a thin zone of blastomylonite of essentially the same mineralogy, into a foliated andalusite schist (andalusite + biotite + cordierite + muscovite + quartz) (Lundeen, 1977). Similar cordierite-bearing rocks also occur as dikes and inclusions in the peridotite near its base (Dickey and Obata, 1974). In these dikes and inclusions, garnets are common instead of sillimanite. The metamorphic condition of the Blanca aureole has been estimated to be 700 to 800°C and 3 to 4 kbar (Loomis, 1972a; Dickey and Obata, 1974; Lundeen, 1976). There is no mineralogical indication of earlier higher pressure metamorphism such as kyanite.

Loomis (1972a) interpreted the Blanca unit as a roof pendant overlying the peridotite and metamorphosed only at shallow level by the heat from the peridotite. Lundeen (1976), however, based on the field evidence, placed the Blanca unit beneath the peridotite "sheet." She concluded that although the metamorphism was due to heat from the peridotite, it occurred during the lateral re-emplacement of the peridotite over the Blanca unit along a major thrust fault, as a part of Alpine nappe tectonics. Loomis' model for the Casares contact metamorphism is probably correct, but, considering the present tectonic position of the peridotite, the vertical movement of the peridotite intrusion into the crust (Casares unit) must have taken place somewhere in the south prior to the Alpine nappe emplacement.

2.3 Age of peridotite emplacement

Two stages should be distinguished in the discussion of the age of the peridotite emplacement: a vertical intrusion of an upper mantle fragment into the crust and its lateral re-emplacement to the present position in the Betic zone. Dating the initial peridotite intrusion is difficult because of the scarcity of fossils in the surrounding units and ambiguities of lithologic correlation. A lateral transition of metamorphic rocks into fossiferous rocks of Triassic to Liassic age was observed in the Casares and Nieves units, and serpentine detritus has been found in a Miocene molasse (Dürr, 1967). The age of the initial peridotite intrusion is, therefore, post Triassic to pre-Miocene.

The contact metamorphic rocks of the Casares and the Blanca units have been dated by the K-Ar method (Table 2-1). There is considerable scatter in the whole rock and the biotite ages. Loomis (1975) suggested that the older ages of the Blanca contact were due to radiogenic Ar inherited from the Paleozoic sediments, and, by taking the youngest concordant age, 22 my, he concluded that the peridotite intrusion occurred at the end of the Oligocene or early in the Miocene. The K-Ar age, however, may have been reset by regional metamorphism caused by the Malaguide nappe emplacement over the peridotite and the Casares unit in the Miocene as argued by Lundeen (1977). In fact, Alpine regional metamorphism up to almandine-amphibole facies are documented farther east of the Alpujarride

Table 2-1. Potassium-Argon ages of metasedimentary gneisses in contact with the Ronda peridotite massif (Loomis, 1975)

Sample no.		Age (m.y.)	
		Whole rock	Biotite
168	(Blanca Unit*)	81.2 ± 1.4	34.6 ± 1.4
8	(")	53.4 ± 1.5	30.2 ± 1.0
245	(Casares Unit†)	22.1 ± 0.2	———
131	(")	———	23.4 ± 0.9

* "hornfels series" of Loomis.

† "gneiss series" of Loomis.

nappe and the Nevado-Filabride complex (DeRoever and Nijhuis, 1963).

The meaning of the measured K-Ar "ages" are still ambiguous, and the peridotite intrusion from the upper mantle may have been even older.

2.4 Peridotite

The massif is 80 to 95% peridotite with minor amounts of serpentinite, pyroxene-rich layers or bands and some leucocratic dikes or veins. The peridotite contact is typically a sheared surface between country rocks and serpentinite. The serpentinite varies in thickness from a few meters to several hundred meters. Massive serpentinites also occur sporadically at sheared zones inside the massif. On the south the peridotite and the Blanca unit beneath it are overlain by the Malaguide nappe, resulting in a geometrically complex contact.

Attached to the massif near Benahavis (Fig. 2-2) is a Miocene breccia of subangular peridotite boulders cemented in serpentine matrix. This breccia forms a low, gentle hill, making a topographic contrast to the adjacent steeper, rocky massif of peridotite. Less voluminous, similar serpentinite breccias appear along other parts of the contact.

Compositional layering of peridotite, due to modal variation of pyroxene, is ubiquitous throughout the massif. Pyroxene-rich bands vary from a few millimeters to a few tens of centimeters in thickness and maintain strict parallelism over tens or hundreds of meters. No evidence of sedimentation

like graded bedding or cross bedding is observed.

In some outcrops younger foliation, defined by preferred orientation of pyroxene or elongation of spinel and plagioclase is overprinted on the older compositional layering.

2.5 Mafic layers

Perhaps the most striking feature of the Ronda peridotite is the presence of the mafic layers. Dickey (1970) recognized two types of mafic layers which, he believed, developed by two different processes.

They were called tectonic- and magmatic-type, according to the interpretation that the former developed by a crystal segregation of pyroxenes during a tectonic flow of a hot and solid peridotite and the later by a segregation of magma droplets during flow of partially molten peridotite.

Distinguishing these two types in the field is not always clear-cut. There are layers where one type grades to the other. Nevertheless, there are at least two major varieties of mafic layers, and it would be convenient to treat them separately until the origin of the layered structure is clarified. The author, therefore, prefers to rename them in a purely descriptive way: chromian pyroxenite layers for the former and magmatic-type layers for the later, simply in a sense that they have magmatic affinities by having higher Na_2O, Al_2O_3, CaO contents and higher Fe/Mg ratios and lower MgO contents relative to the peridotite. The chromian pyroxenite layers are predominantly websterite followed by

orthopyroxenite and clinopyroxenite. They appear as massive layers of up to 1 meter thick. The color is light green due to chromian diopside. They are parallel to the compositional layering of the peridotite, but in a few cases, thin pyroxenite veins crosscut the structure of the peridotite. Apparently, there are several generations of this type. A definitive characteristic of the chromian pyroxenites is that the colors and compositions of the constituent pyroxenes match those in the peridotite.

Magmatic-type mafic layers are more abundant than chromian-pyroxenite layers in the Ronda massif. The mineralogy of the magmatic-type mafic layers varies systematically with their geographic locations and the massif had been subdivided into three zones, from west to east: garnet pyroxenite zone, spinel pyroxenite zone, and olivine gabbro zone (Dickey, 1970). In the present study, the map has been revised (Fig. 3-9, discussed in detail in the next chapter) by expanding the garnet pyroxenite zone significantly, but the overall pattern is unchanged.

The magmatic-type mafic layers form massive layers from a few cm to 2 m thick. The colors are variable: dark green, dark brown, purplish brown, gray, or grayish green, depending on the mineralogy and the chemistry of the minerals. The layers parallel the compositional layering of the peridotite with more or less constant thickness for tens of meters before they terminate by pinching out. They also appear as

schlieren, boudinage, and irregular lenses. This appearance is especially common near the northwest contact of the massif. Small scale s-shaped folding and isoclinal folds are present, but rather rare (Fig. 2-3). Most layers appear to be homogeneous in the field, but there are many exceptions to this generalization: internal layered structures due to modal variation of plagioclase on a scale of cm is clearly seen in some layers, and the color of constituent pyroxenes changes from dark colored to lighter greenish within a few mm or a few cm from the layer boundaries. Contacts between the layers and the peridotite are typically sharp on a macroscopic scale. Boundaries of some layers, however, are fuzzy, especially where younger foliations crosscut the layer penetrating inside, resulting in saw-toothed boundaries.

The distribution of mafic layers is not uniform in the massif (Fig. 2-4). They tend to concentrate in a northwestern zone of approximately one-third of the area of the massif. The proportion of mafic layers to peridotite in the massif is difficult to estimate because of their uneven distribution. In some part it is as much as 30%. Some parts completely lack mafic layers. An overall average of the massif would not exceed five percent mafic layers.

The compositional layering of the peridotite and mafic layers define simple structures over some area of the massif (Fig. 2-5). The strike changes gradually forming a continuous wavy pattern. In the western half of the massif a general

Figure 2-3. Deformed spinel pyroxenite layers (top) and olivine gabbro layers (bottom).

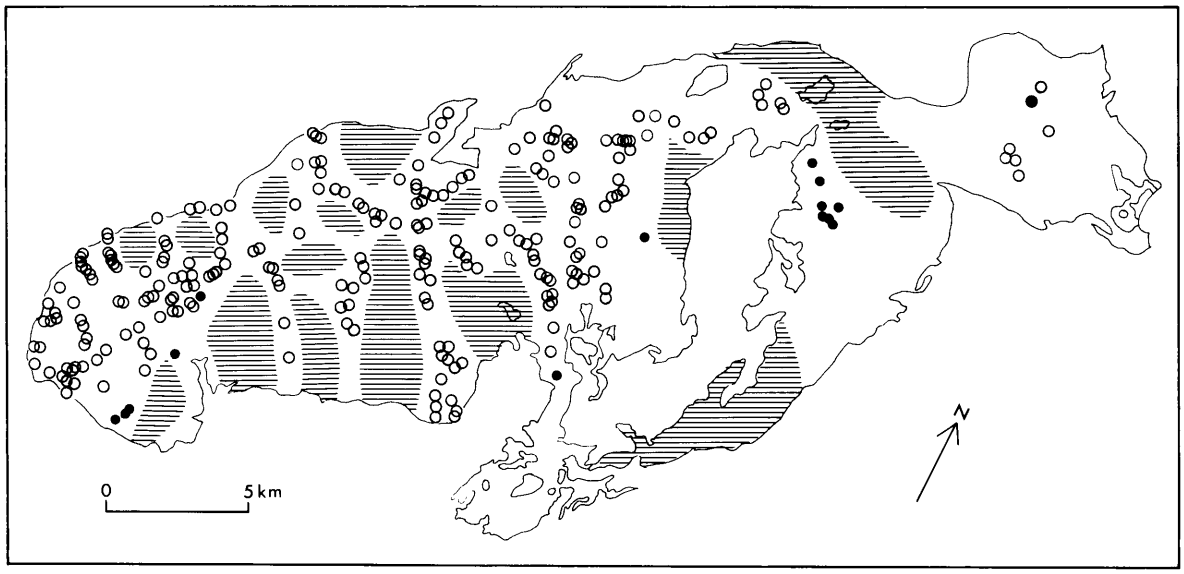

Figure 2-4. Distribution of mafic layers in the Ronda massif. Open circles, magmatic-type; solid circles, chromian pyroxenites. No data in shaded area.

Figure 2-5. Structure of the Ronda massif defined by mafic layering and compositional banding of the peridotite.

ALGATOCIN

BENARRABA

JUBRIQUE

Rio Genal

IGUALEJA

Rio Verde

TOLOX

Rio Grande

ISTAN

BENAHAVIS

Rio Guadalmansa

Rio del Castor

Rio del Velerin

Rio del Portugo

Guadalmina

C339

Rio Guadaiza

Rio Verde

ESTEPONA

N340

SAN PEDRO

MARBELLA

0 1 2 3 4 5 Km

MEDITERRANEAN SEA

N

Attitude:

- mafic layers
- chromian pyroxenite layers
- foliation in peridotite

NE-SW strike predominates. In places, the dip changes abruptly, suggesting presence of faults or isoclinal folds. The structural pattern changes abruptly in a narrow zone between two big streams cutting across the massif, Rio Guadalmansa and Rio Guadalmina (see Fig. 2-5). This is a zone where faults and metasedimentary dikes are abundant and is thought to be close to the base of the peridotite. East of this zone a general NW-SE strike predominates. The structural discontinuity may be better seen in the stereo projection of the layered structures of the two areas (Fig. 2-6). Both patterns are characterized by partial girdles with weak point maxima. The pattern of the east part may be obtained by rotating the pattern of the west part clockwise, indicating a relative block movement after the overall layered structure was fixed. This late structural disturbance has to be borne in mind in attempts of correlating petrologic and geochemical data with their geographic locations.

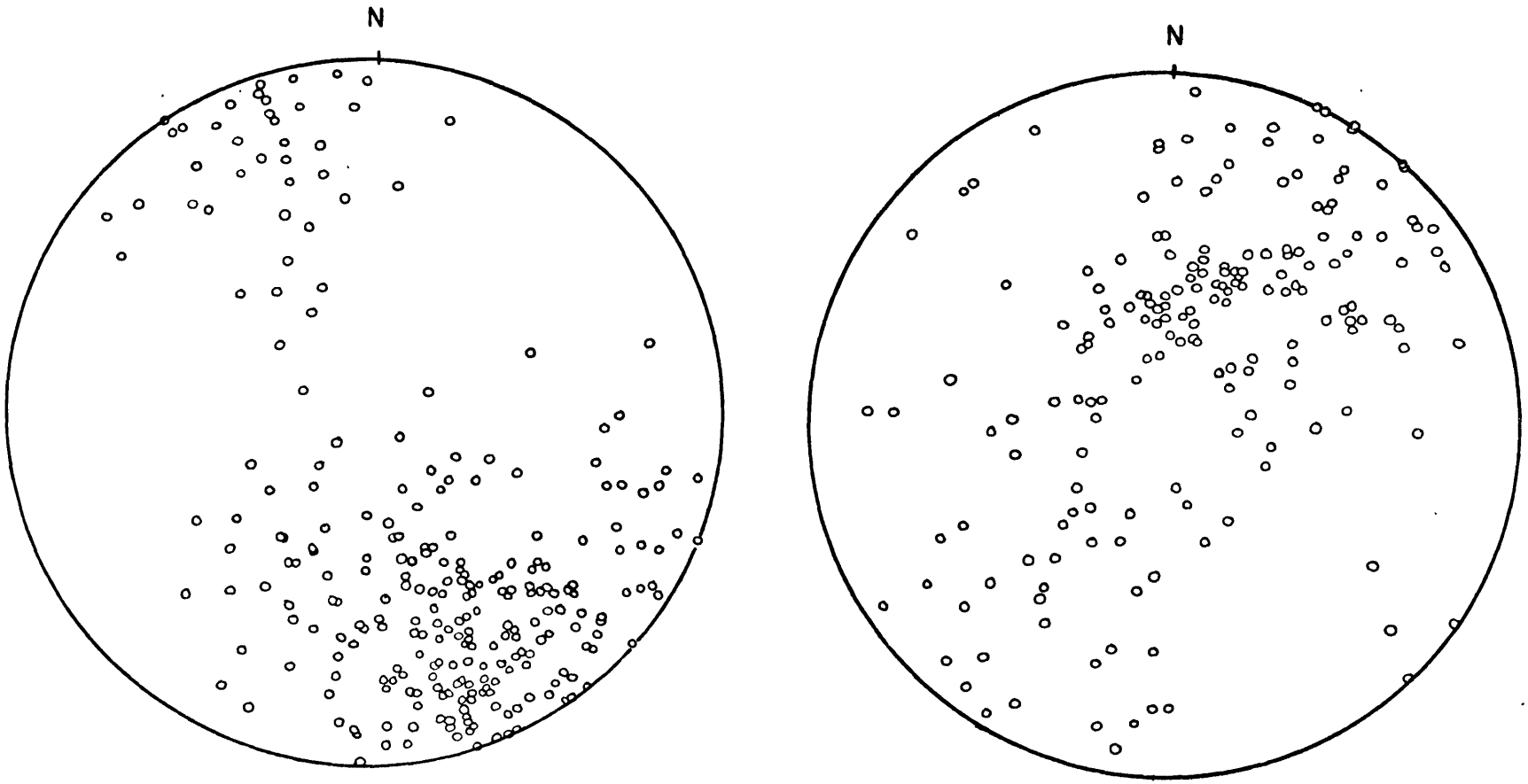

Figure 2-6. Lower hemisphere, equal area projection of mafic layering and compositional banding of the peridotite. Measurements taken west and east of a dashed line in Figure 2-5 are presented separatly left and right, respectively.

Chapter 3

PETROGRAPHY

3.1 Peridotites

The peridotite is predominantly harzburgite and lherzolite[1]. Dunite occurs locally either as narrow (<30 cm) pyroxene-poor parts of banded peridotites or, more rarely, as irregular small (∿20 cm) pods. Aside from the massive serpentines at the peridotite contacts and along sheared zones in the massif, the degree of serpentinization of the peridotite seldom exceeds 30 volume percent. The Ronda peridotite as a whole is quite anhydrous and fresh.

The aluminous phases in the peridotites are Cr-Al spinel throughout the massif, calcic plagioclase (An_{60-80}) in the eastern and the southeastern parts of the massif, and pyropic garnet which appears sporadically in the peridotites in a narrow zone of the northwestern part. Garnet and plagioclase never coexist in the peridotites. Their regional distribution, together with the mafic layers, defines mineral facies discussed later. Some peridotites show signs of transition from spinel peridotite to plagioclase peridotite, as indicated by plagioclase mantles on spinels. These are hereafter called spinel-plagioclase peridotite or simply transitional peridotite.

---

[1] Nomenclature of peridotite follows the classification system adopted by the International Union of Geological Sciences Subcommission on the Systematics of Igneous Rocks (Streckeisen, 1976).

Microscopic textures of the peridotites are variable, reflecting various stages of deformation and recrystallization. The majority of the peridotites are porphyroclastic in the sense of Mercier and Nicolas (1975). They are characterized by the presence of two habits of olivine and enstatite crystals: large, elongated, and strained grains (porphyroclasts) and small, generally polygonal, strain-free grains (neoblasts). The peridotites in the central portion of the slab are very coarse-grained (2-7 mm), little deformed, and have many features in common with the protogranular textures defined by Mercier and Nicolas (1975).

The degree of deformation, which is expressed by a) reduced grain sizes, b) enstatite porphyroclasts stretched by translation gliding, and c) development of strong foliations and lattice preferred orientations, increases toward the northwestern contact (Nicolas et al., 1971; Darot, 1973; Lundeen, 1976).

The plagioclase peridotites in the southeast have annealed after extensive shearing, as characterized by straight grain boundaries, 120° triple junctions of neoblasts, and diminishing undulose extinction and sharpening of kink boundaries of the porphyroclasts.

Pyroxenes: Most orthopyroxene porphyroclasts are zoned as suggested by slight differences of extinction angle between the core and near the rim. This is due to a decrease of Al_2O_3 from core to rim as shown by microprobe data in the chapter on

Mineral Chemistry. The orthopyroxene porphyroclasts have abundant exsolution lamellae and blebs[1] of clinopyroxene parallel to (010) and less commonly lamellae of plagioclase and amphibole. Recognition of plagioclase lamellae in the orthopyroxene porphyroclasts may be difficult because most of them are now altered to saussurite. When they are thin, they may be easily misidentified as nothing more than cleavages or partings of enstatite. Plagioclase relicts, often with albite twinning, may be found as blebs at the termination of plagioclase lamellae (Fig. 3-1).

A conspicuous feature of the orthopyroxene porphyroclasts is the presence of olivine occupying embayments in the porphyroclast margins and also occurring as inclusions within the porphyroclasts (Fig. 3-2). Spinel inclusions, in a few cases, associate with the olivine inclusions (see Fig. 4-3).

The orthopyroxene neoblasts are typically homogeneous and free from exsolution lamellae, but some are apparently zoned and have a few thin (<1μ) exsolution lamellae of probable clinopyroxene. Both neoblasts and porphyroclasts contain a few small (20-30μ) round (fluid or glass?) inclusions of lower refractive indices than the pyroxenes. These are also common in olivines.

In contrast to the olivine and orthopyroxene, the distinction between clinopyroxene porphyroclasts and neoblasts is not

---

[1] Blebs, as distinguished from lamellae, are small (<0.02 mm) irregular inclusions which are optically irrational to the host pyroxenes.

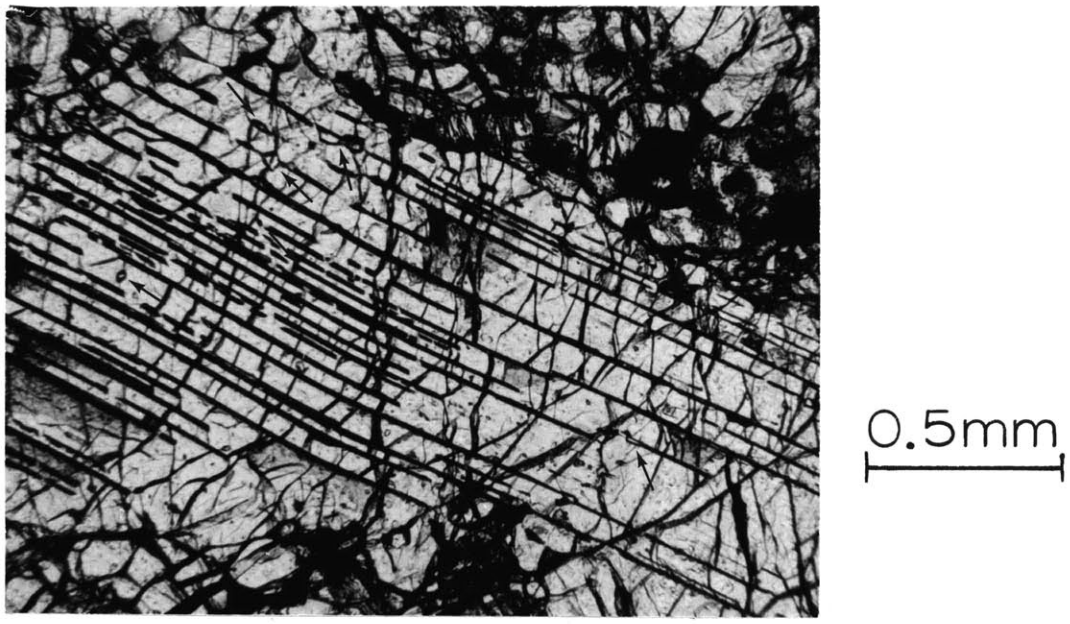

Figure 3-1. Plagioclase lamellae and blebs (indicated by arrows) in orthopyroxene in sample R37.

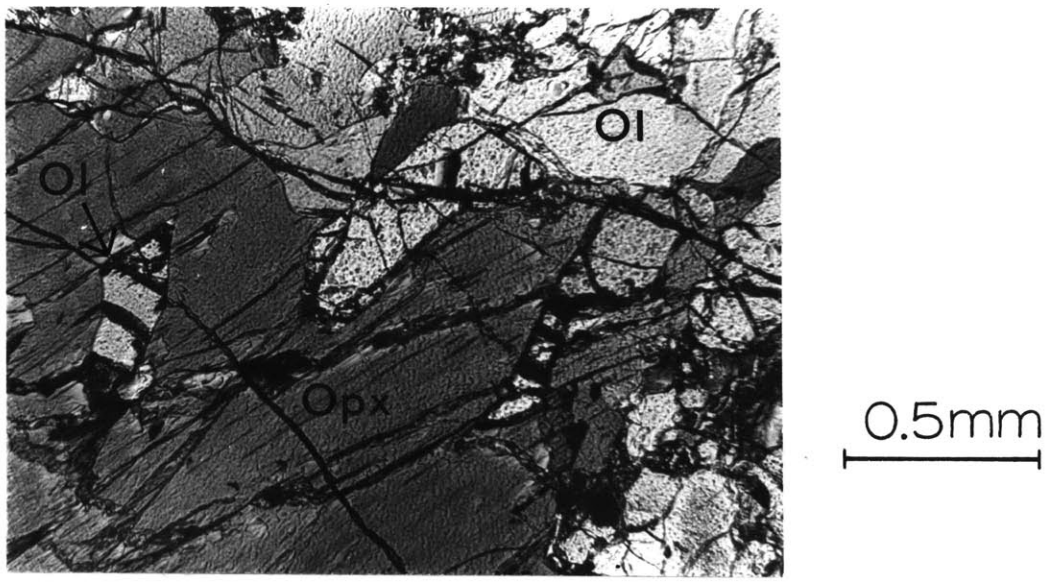

Figure 3-2. Olivine inclusions and embayments in orthopyroxene in sample R243.

clear. The grain size distribution is more or less continuous from 3 mm to 0.2 mm. In general, small clinopyroxene grains appear as small (∿0.2 mm) polygonal grains adjacent to, or near, the orthopyroxene porphyroclasts, and as mosaics of clinopyroxene-rich aggregates (Fig. 3-3). Such aggregates are typically 2-3 mm in diameter and may represent single clinopyroxene grains which were polygonized during deformation.

Most clinopyroxenes have 1 set of orthopyroxene exsolution lamellae parallel to (100), but some grains have 2 sets of lamellae (pyroxene?) of different orientations. Plagioclase lamellae are present in some coarse clinopyroxene grains and are often, as in the orthopyroxene grains, saussuritized. Tiny (∿10μ) brown spinel grains are present in the saussurites. Some clinopyroxenes in spinel lherzolites look turbid (Fig. 3-4) inside due to numerous, subrectangular inclusions (<4μ) of lower reflective indices. The long axes of the subrectangular inclusions are parallel to the c axis of the host pyroxene. These inclusions are too small to be identified optically or with the microprobe.

Spinel: The size, shape, and color of the spinels are quite variable depending on the rock type and location of the peridotite. In spinel lherzolite, it appears as pale greenish-brown, irregular, interstitial grains (0.2 to 1 mm). Coarse, vermicular intergrowths (0.07 to 0.2 mm thick) of spinel and clinopyroxene have been found in orthopyroxene porphyroclasts in a coarse spinel lherzolite by Lundeen (1976). Perhaps much

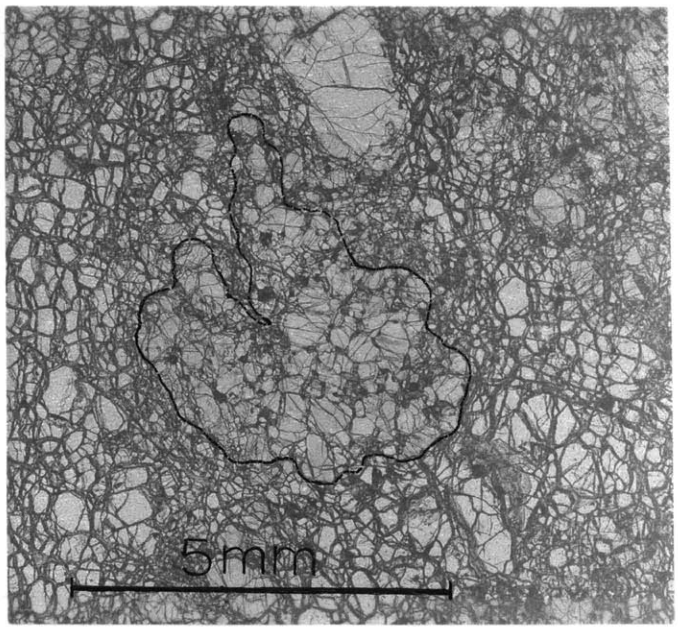

Figure 3-3. Clinopyroxene mosaic in sample R131.

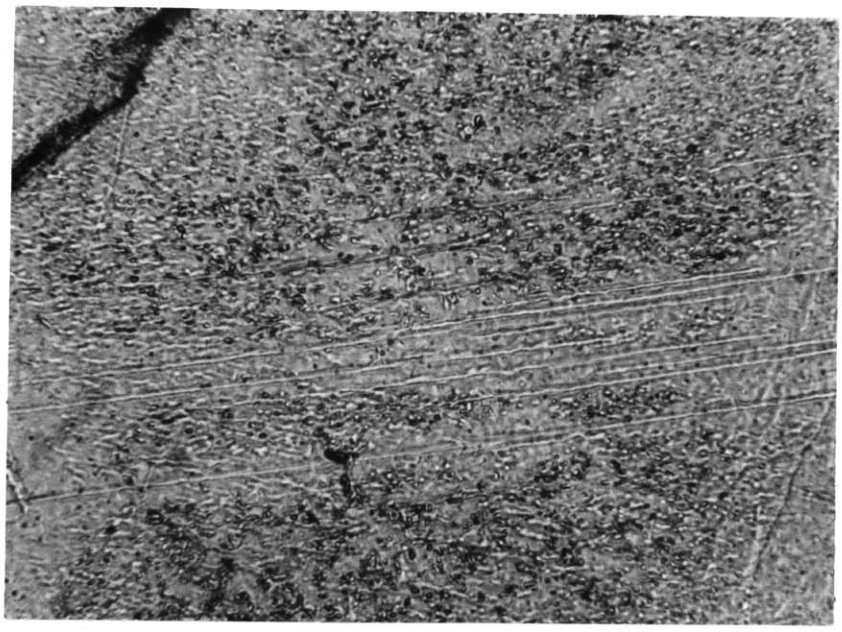

Figure 3-4. Turbid clinopyroxene with orthopyroxene lamellae in sample R243.

of the spinel in these rocks originated by exsolution from aluminous pyroxenes. In the spinel-plagioclase transitional peridotites, larger spinels (1 to 1.5 mm) are distinctively zoned from pale brown or pale greenish brown cores to reddish brown rims. Outlines of the grains are often irregular and they are invariably surrounded by plagioclase. Small (0.1 to 0.2 mm) spinel grains are reddish-brown or nearly opaque and are mounted in plagioclase matrices. The aluminous spinels are obviously reacting with pyroxenes to form plagioclase and olivine, leaving the chromium behind in residual spinels (see Green, 1964, p. 169). Spinels in the plagioclase peridotites are small (<0.4 mm), irregular and scarce (typically <1%). They are rather homogeneous dark brown or nearly opaque and are surrounded by calcic plagioclase. Their textures resemble those of the smaller spinels in the spinel-plagioclase transitional peridotites. Spinels in garnet peridotite occur as brown, irregular-shaped grains (0.3-0.7 mm) and as tiny, pale brown grains (∿20μ). There are typically only a few big grains in a thin section, but the tiny spinels, which are dispersed in serpentine matrices, are numerous. Under reflected light, many tiny spinels are observed to contain fine sulfide (pyrrhotite?) veins (∿1μ) (Fig. 3-5). The rims of some big spinel grains are slightly lighter-colored than the cores due to an increase of the Al/Cr ratio. The tiny spinels are considerably more aluminous than the big spinels (see p. 82 in Mineral Chemistry). In pyroxene-poor harzburgites and dunites, spinels are dark reddish brown and tend to be coarse

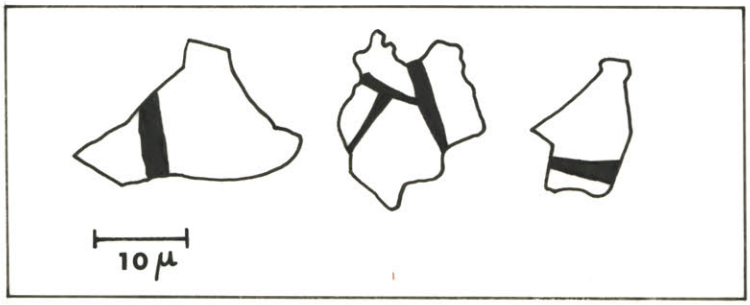

Figure 3-5. Tiny spinels (white) with sulfide (Pyrrhotite?) veins (black) in sample R501. Sketch under reflected light.

Figure 3-6. Garnet "beads" in foliated peridotite.

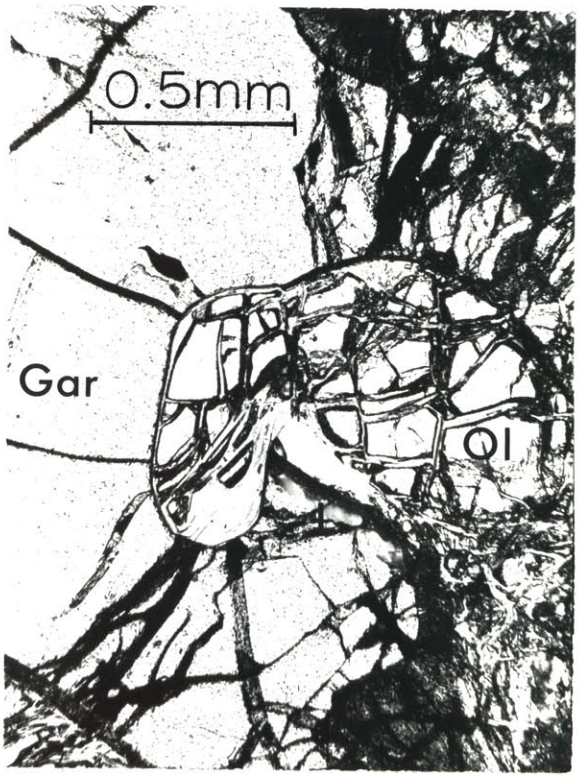

Figure 3-7. Olivine-garnet contact in sample R501.

(up to 1 mm) and euhedral.

Garnets: Garnet peridotites have never been recognized as a rock type before in the Ronda massif, so they are discussed in some detail. Pink to red pyrope-rich garnets occur sporadically in the peridotites in the northwestern part of the massif (see Fig. 3-15). They tend to align parallel to the foliation of the peridotite. The garnets are now partly or completely replaced by kelyphite and because of the resistance of the kelyphitic garnet pseudomorphs to weathering, they stick out of the host peridotite in a conspicuous fashion resembling "rosary beads" (Fig. 3-6). Green chromian diopside is commonly concentrated around the garnet as is clearly seen on weathered surfaces of the peridotite. At the northwest contact, the garnets are smaller and more evenly distributed in the sheared peridotite. Locally, however, the grains have grown to 1 cm, like metamorphic porphyroclasts.

The following petrographic description refers to specimen R501. The garnets (0.3 mm to 5 mm) are round, cracked, and invariably surrounded by kelyphite rims (0.2 to 0.4 mm thick). Some kelyphitic rims are concentrically zoned from dark inner zones to straw yellowish outer zones. Most garnets are separated from serpentinized harzburgite matrices by fresh pyroxene-rich equigranular mosaics (individual grain, $\sim$0.2 mm). Direct contacts of olivine with garnet without any reaction, however, are frequently observed (Fig. 3-7). This indicates garnet-olivine equilibration. Small (0.07 to 0.4 mm), round inclu-

sions of olivine, orthopyroxene, clinopyroxene, spinel, and sometimes amphibole are common in the garnets, but rutile inclusions, which are common in garnets of the mafic layers, are absent. Spinels or pyroxenes are surrounded by kelyphite in some garnet peridotites (Fig. 3-8). Perhaps these spinels or pyroxenes were once inclusions in garnet which, having been completely replaced by kelyphite, has left the inclusions behind. (The bulk composition of such kelyphite obtained by defocused beam microprobe analyses closely matches pyropic garnet.)

Similar garnets in peridotite were found in the peridotite at Beni Bouchera, Morocco (Millard, 1959). Kornprobst (1966), however, based on his textural observations, suggested that the garnets had been mechanically derived from garnet pyroxenite layers and were not in equilibrium with the host peridotites. He named such rock "pseudo-garnetiferous peridotite." This interpretation was also accepted in the Ronda peridotite (Dickey, 1970; Darot, 1973).

The present field observations, textural relationships between the garnet and olivine, and the pyropic compositions (see Mineral Chemistry, p. 95) indicate that the garnets are chemically in equilibrium with the host peridotite. These (and perhaps also the Beni-Bouchera peridotite) are true garnet peridotites which belong to the garnet lherzolite facies.

Amphibole: Pleochroic (pale brown to colorless) pargasitic hornblende is a common accessory in the garnet peridotites and some spinel peridotites. The amphibole occurs in the form of

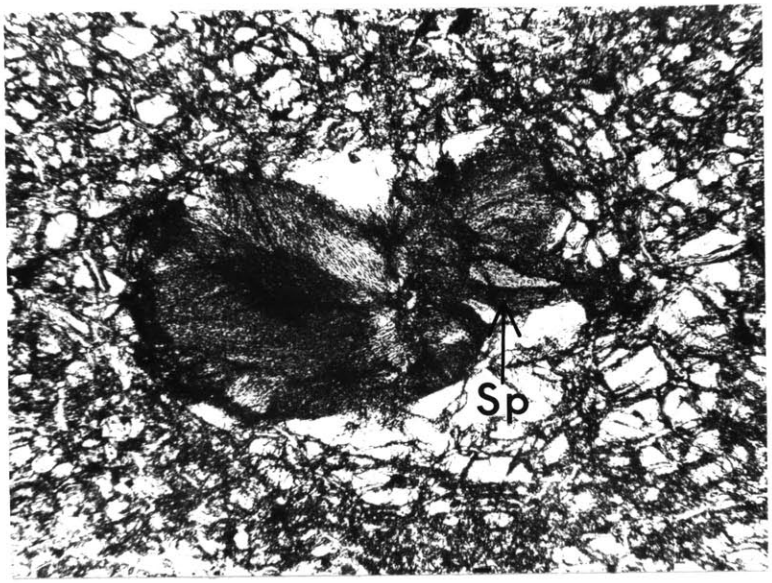

Figure 3-8. Spinel in kelyphite in garnet peridotite R740.

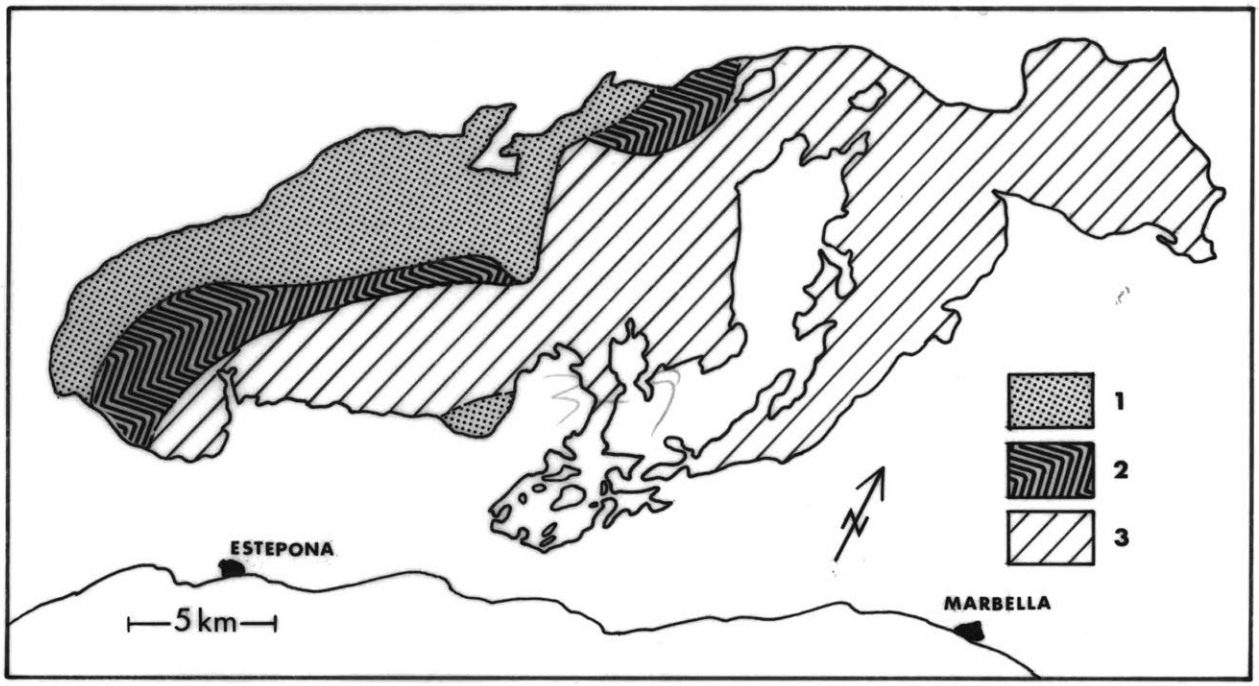

Figure 3-9. Distribution of garnet pyroxenites (1), spinel pyroxenites (2), and olivine gabbros (3) in the Ronda massif.

small (0.1 to 0.2 mm) prisms or thin (∿20μ) lamellae in orthopyroxene porphyroclasts. Undeformed and free from exsolution lamellae or any inclusions, this phase is apparently a recrystallization product and is not primary.

Others: Opaque minerals in the peridotites are pyrrhotite, ilmenite, and magnetite in serpentine. These minerals have not been examined in detail. Low grade metamorphic minerals are talc after enstatite, sericite, chrolite, and some carbonates developing along fractures.

3.2 Mafic Layers

Five mineral assemblages have been recognized in the magmatic-type mafic layers (Dickey, 1970):

I. Gar + Cpx ± green Sp (ceylonite)

II. Gar + Cpx + Plag ± green Sp

III. Cpx + Plag + green Sp + Opx

IV. Cpx + Plag + Ol + Opx + brown Sp (picotite)

V. Cpx + Plag + Ol + Opx + chromite

Garnet websterite and quartz-bearing garnet granulite (Gar + Cpx + Plag + Qz) have been newly found in this study. The stable mineralogy of the magmatic mafic layers thus has been redefined in terms of three major groups characterized by the presence or absence of garnet and olivine:

Garnet pyroxenite group:

a. Cpx + Gar + Plag

b. Cpx + Opx + Gar

c. Cpx + Gar

d. Cpx + Gar + Plag + Qz

e. Cpx + Opx + Gar + green Sp (ceylonite)

Spinel pyroxenite group:

a. Cpx + Opx + green Sp

b. Cpx + Opx + green Sp + Plag

c. Cpx

Olivine gabbro group:

a. Cpx + Ol + Plag + Opx + brown Sp (picotite)

b. Cpx + Ol + Plag + Opx + opaque Sp (chromite)

In each group, the mineral assemblages are arranged in the order of decreasing abundance. Common accessory minerals are brown amphibole (paragasite), pyrrhotite, rutile, and ilmenite. Layers of the three groups are distributed in the massif generally from west to east corresponding (with a few exceptions near the south contact) to an easterly decrease in pressure (Fig. 3-9). Most of the layers have complex textures owing to incomplete sub-solidus reactions and solid deformation. Garnets typically have kelyphite rims; pyroxenes have exsolution lamellae, and Al-rich pyroxenes are breaking down to fine-grained mixtures of olivine, plagioclase, spinel, and Al-poor pyroxenes. The textures of the mafic layers have been previously described by Dickey (1970) and Lundeen (1976), particularly from a structural point of view by the latter author. Only general features

of the mafic layers are described here, mainly from the point of interest of defining stable mineral assemblages.

Garnet pyroxenite group: The most abundant rock types in this group are garnet granulites (Gar + Cpx + Plag), garnet websterites (Gar + Opx + Opx) and bimineralic garnet clinopyroxenites (Gar + Cpx). Small amounts of interstitial quartz appear parallel to the gneissic foliation in some garnet granulites. The texture indicates equilibration of the quartz altogether with garnets, clinopyroxene, and plagioclase (An_{40-60}) (Fig. 3-10). Green spinel (ceylonite) joins garnet websterite near the south end of the garnet pyroxenite zone (ariegites defined by Lacrox, 1900 and 1917).

The garnets are colorless in thin section. They are typically bimodal in grain size and surrounded by greenish kelyphite. The following description of the kelyphites refers specifically to plagioclase-garnet-clinopyroxenite R127, but most kelyphites in the mafic layers are similar.

Inside, next to the garnets, the kelyphites are extremely fine (<10μ), radial, graphic intergrowths of enstatite, green spinel, plagioclase, and minor ilmenite. The outer rims are similar intergrowths of olivine, spinel, plagioclase, and minor ilmenite. The boundary between the inner and outer zones are zig-zagged but appear to be sharp (Fig. 3-11). No hydrous phase, such as amphibole, has been found in the kelyphites. The plagioclase may be coarser and more abundant at the margins of the kelyphitic rims. The kelyphites are typically separated from adjacent pyroxenes and plagioclase by a narrow (0.1 mm)

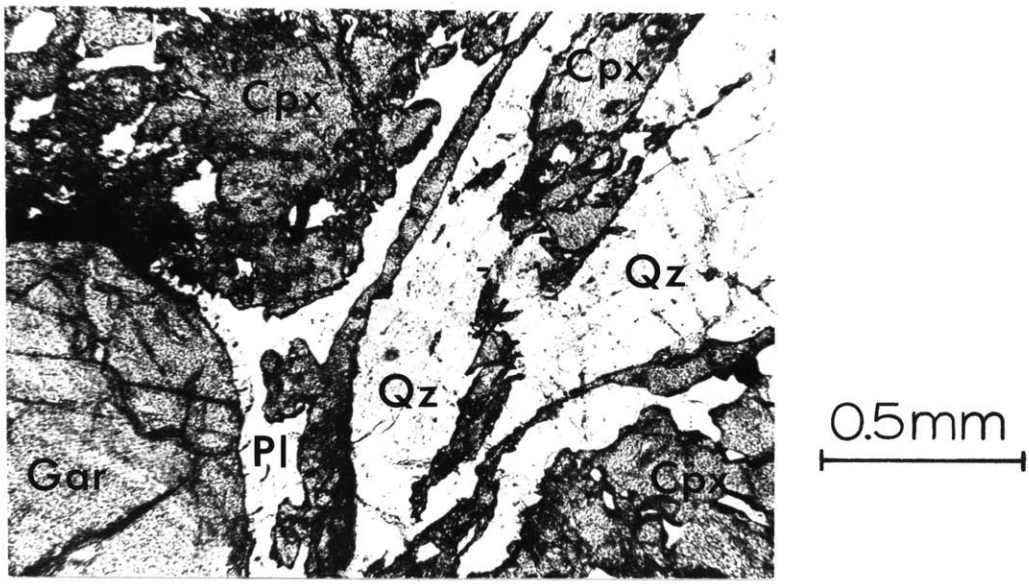

Figure 3-10. Qz - Plag - Cpx - Gar equilibration texture in sample R410.

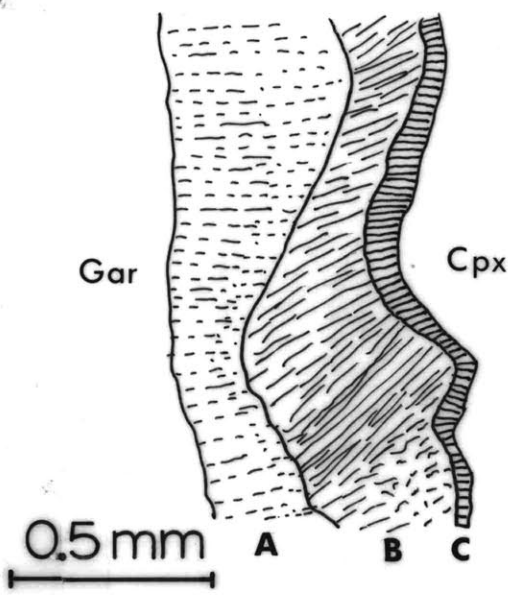

Figure 3-11. Zoned Kelyphite in sample R127. A, Opx-Sp-Plag; B, Ol-Sp-Plag-ilmenite; C, Ol-Plag-ilmenite.

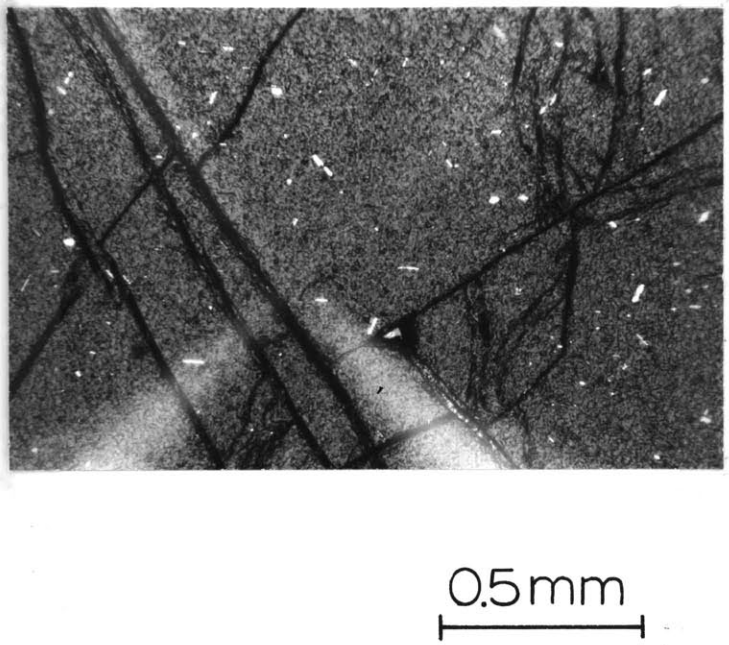

Figure 3-12. Rutile needles in garnet in sample R127.

zone of intergrown coarse (∿20μ) plagioclase (An_{90}) and olivine (Fo_{60}) crystals perpendicular to the layer boundaries.

Clinopyroxene and plagioclase inclusions are common in large (2 to 4 mm) garnets. Numerous rutile needles (4μ x 50μ) or prisms (15μ x 40μ) lie along crystallographic directions in the garnets (Fig. 3-12). The small (<0.5 mm) garnets lack inclusions, and, in some foliated rocks, are strung out as "rosary beads" (Lundeen, 1976) or rarely as continuous lamellae in pyroxene matrices, suggesting their formation by exsolution from aluminous pyroxenes (see Beeson and Jackson, 1970; Shervais et al., 1973).

The clinopyroxenes (0.2 to 1 mm in size) are pale brown or colorless in thin sections. Thin plagioclase(?) lamellae (<2μ thick) are present in some clinopyroxenes in the granulites, and orthopyroxene lamellae are common in the clinopyroxenes in garnet websterites. Some medium-sized clinopyroxenes of websterite are turbid within due to numerous tiny inclusions. These pyroxenes are similar to the turbid clinopyroxenes in the spinel lherzolite (see p. 28). The orthopyroxenes (0.8-0.2 mm) are colorless in thin section. As in the peridotites, the big grains are strained and kinked, revealing fine (∿1μ) clinopyroxene exsolution lamellae. The small grains, though still kinked in some cases, are generally strain-free and have no exsolution lamellae. Both ortho- and clinopyroxenes are reduced to 0.2 to 0.4 mm near the peridotite contact, forming equigranular mosaic textures.

The plagioclase ($\sim An_{40}$) in the granulite, which is always interstitial, constitutes up to 20% of the rocks. The grains are deformed and show undulose extinction, polysynthetic twins, and dismemberment of single grains into aggregates of interlocking smaller grains.

Besides rutile, ilmenite, and sulfides, some garnet clinopyroxenites contain interstitial or round (1-2 mm) grains of graphite near the peridotite contact. Mineralogical bonding is apparent in some layers. Observed sequences within single layers are 1) Cpx + Gar → Cpx + Plag + Gar → Cpx + Opx + Gar + Sp, and 2) Cpx + Plag + Gar → Cpx + Plag + Gar + Qz → Cpx + Opx + Gar.

Spinel pyroxenite group: These rocks, which are black or dark green in hand specimen, consist of pale brown or colorless deformed clinopyroxene grains (3-5 mm), smaller ($\sim$1 mm) kinked orthopyroxenes with interstitial green spinel (<3 mm), and calcic plagioclase ($\sim An_{70}$). The orthopyroxene and clinopyroxene ratio varies from 1:1 to nearly zero. The clinopyroxenes have abundant lamellae of plagioclase + olivine + ilmenite parallel to (100) (see Fig. 7 in Dickey, 1970) and less commonly lamellae of plagioclase + orthopyroxene + green spinel parallel to (100) (Fig. 3-13).

Fine scale ($\sim$20μ) intergrowths or aggregates of the plagioclase + olivine + ilmenite assemblages have developed along the clinopyroxene grain boundaries. The local small-scale plagioclase + olivine assemblages were apparently formed by the breakdown of Al-rich pyroxenes after the coarse grained

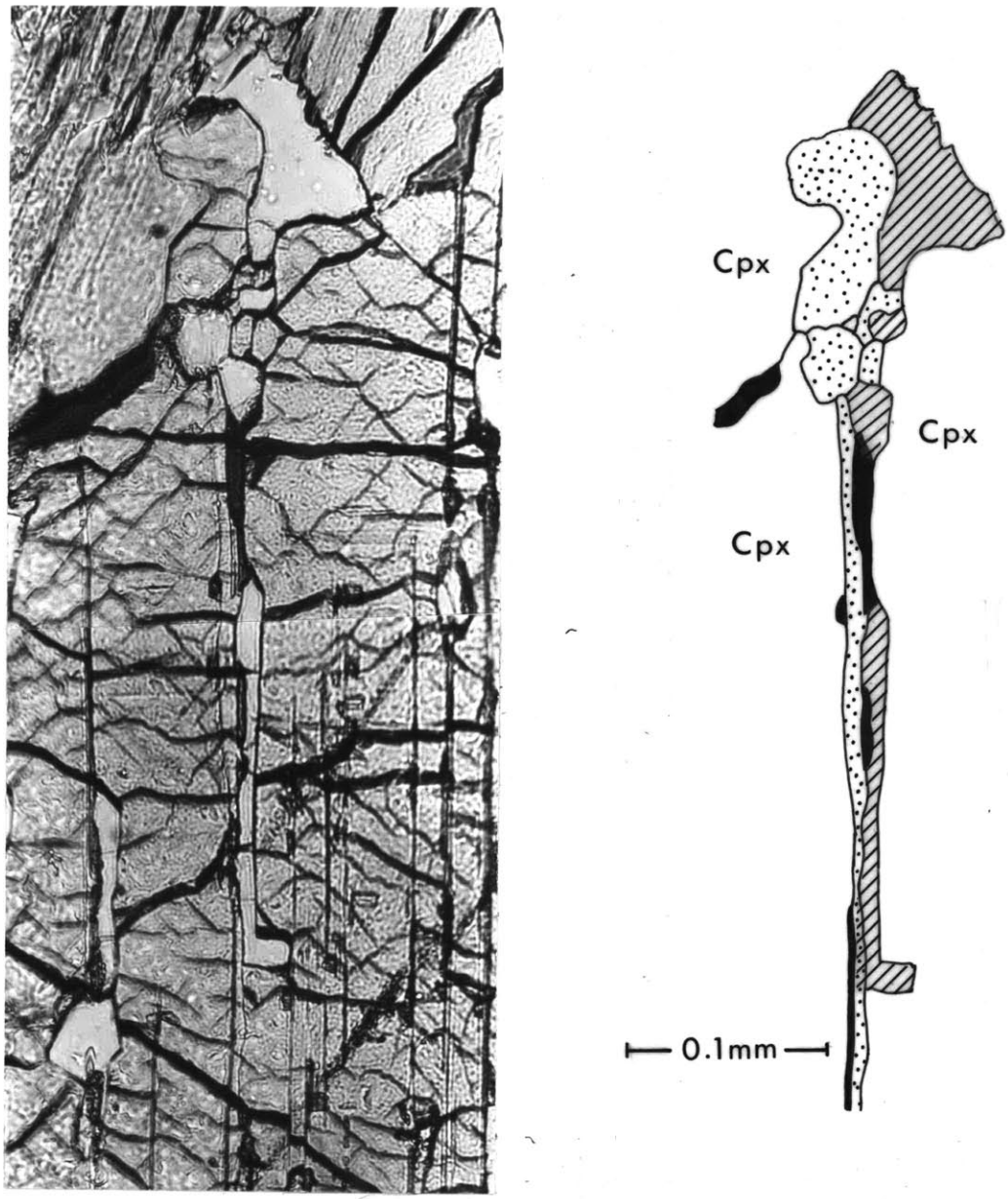

Figure 3-13. Complex lamellae of Opx-Plag-Sp in clinopyroxene in sample R251. Photomicrograph (left) and its sketch (right). Dotted is orthopyroxene; black is spinel; shaded is plagioclase.

crystals were formed. One fascinating texture in this group is a well-developed spinel-pyroxene symplectite (2 to 5 mm diameter) (Fig. 3-14). This symplectite consists of two domains of different mineral assemblages: a) fine grained (∿30μ) mosaic of olivine, irregular, green, or brownish green spinel and interstitial plagioclase; and b) graphic intergrowth of orthopyroxene, minor clinopyroxene, worm-like green spinels (∿20μ) and interstitial plagioclase, which shows undulose extinction and polysynthetic twinning. The orthopyroxenes in the second domain type are optically continuous over some 1.5 mm and are sometimes optically continuous with large (∿2 mm) adjacent single orthopyroxene grains.

The symplectite is thought to be a breakdown product of aluminous enstatite. Although the mineralogy is identical to that of the kelyphites after garnet, the symplectite is distinctly coarser grained. There is no ambiguity in distinguishing "symplectite" and "kelyphite" even when garnets are completely kelyphititized. These two kinds of breakdown reaction products (i.e. coarse symplectite and kelyphite) coexist in some spinel-garnet websterites (ariegites).

Olivine gabbro group: This is the most abundant rock type of the mafic layers. Coexistence of medium-sized (0.3-0.6 mm) olivine and plagioclase as essential phases rather than as minor fine-grained reaction products is the definitive characteristic of this group. In thin section, deformed pyroxenes (1 to 3 mm) lie in a mosaic of medium-grained (∿0.4 mm) xenomorphic granular olivine, plagioclase, clinopyroxene, ortho-

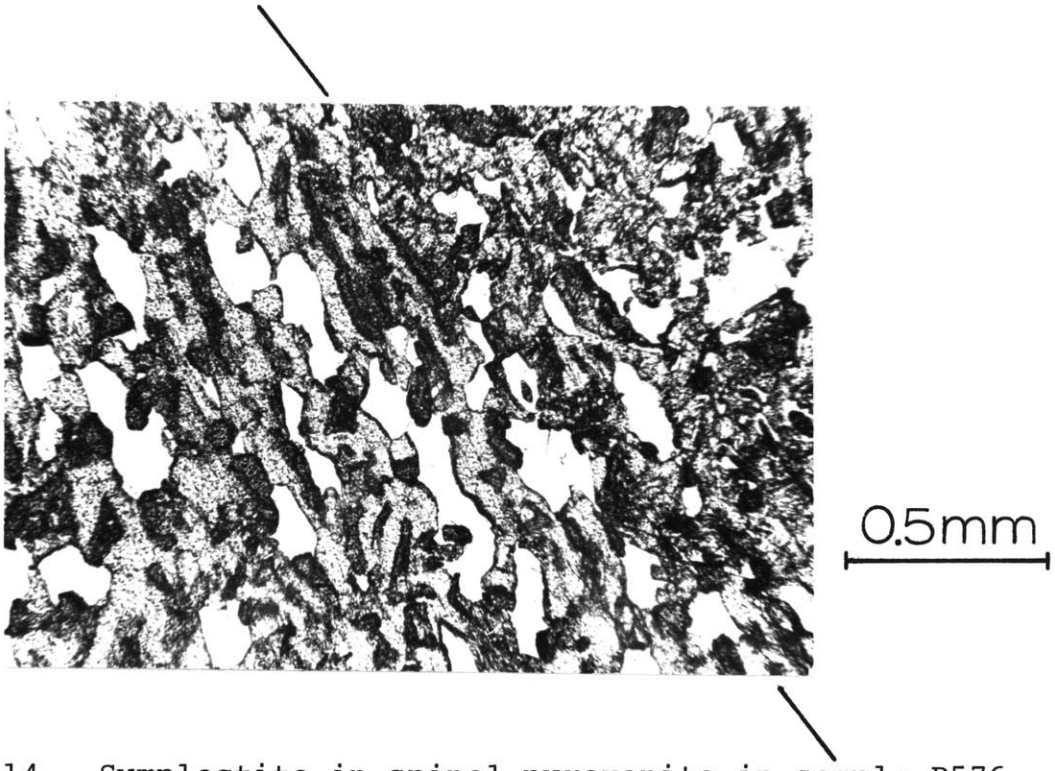

Figure 3-14. Symplectite in spinel pyroxenite in sample R576. Ol-Plag-Sp domain (upper right) and Opx-Cpx-Plag-Sp domain (the rest).

pyroxene, and minor brown spinel. The brown spinels are surrounded by plagioclase rims. As the rims grow, the spinels shrink and become more opaque, like those in the plagioclase peridotites. The big clinopyroxenes have abundant thick (∿10μ) exsolution lamellae of orthopyroxene and sometimes of plagioclase, and they are, in some rocks, breaking down from outside inwards to polygonal aggregates of small (∿0.1mm) olivine plagioclase, clinopyroxene, and orthopyroxene.

3.3 Mineral Facies and Zonal Mapping

From the previous petrographic observations it can be concluded that the peridotites and the mafic layers have undergone substantial recrystallization and metamorphism, and that none of the rocks contain their original, igneous, mineral assemblages. The variation of the mineralogy can be rigorously treated in terms of bulk chemical composition and the pressure-temperature conditions of crystallization. It is now possible to map the massif as a metamorphic terrain in terms of several zones of different mineral facies.

All the available critical mineral assemblages of both the peridotites and the mafic layers are plotted together in the map (Fig. 3-15). The late stage recrystallized assemblages such as in the kelyphites and the exsolution textures are not considered here. By looking at data for the peridotites and the mafic layers together, four zones of the following mineral facies emerge:

Figure 3-15. Mineralogical and mineral facies map of the Ronda massif.

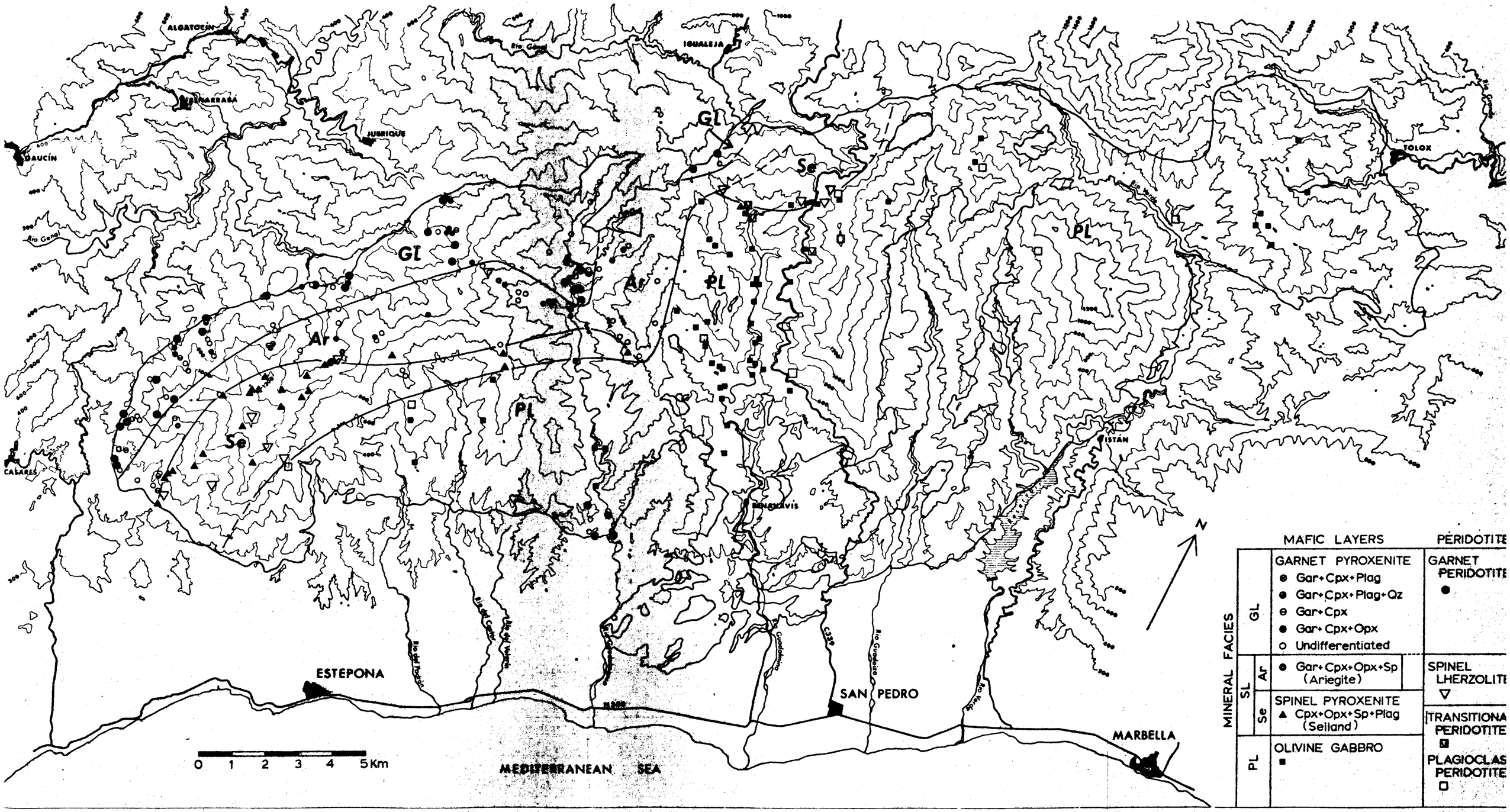
ALGATOCÍN
ALPANDEIRE
JUBRIQUE
BENAOCAZ
IGUALEJA
Río Genal
TOLOX
ISTÁN
CASARES
Benalmádena
Benaoxavis
ESTEPONA
SAN PEDRO
MARBELLA
MEDITERRANEAN SEA
Río del Castillo
Río del Hidalgo
Río del Valle
Río Guadalmina
Río Guadaiza
Río Verde
C339
Gl
Ar
Se
Pl
0 1 2 3 4 5Km
N
MINERAL FACIES
MAFIC LAYERS
PERIDOTITE
GL
GARNET PYROXENITE
Gar+Cpx+Plag
Gar+Cpx+Plag+Qz
Gar+Cpx
Gar+Cpx+Opx
Undifferentiated
GARNET PERIDOTITE
SL
Ar
Gar+Cpx+Opx+Sp (Ariegite)
SPINEL LHERZOLITE
Se
SPINEL PYROXENITE
Cpx+Opx+Sp+Plag (Seiland)
TRANSITIONAL PERIDOTITE
PL
OLIVINE GABBRO
PLAGIOCLASE PERIDOTITE

1) Garnet lherzolite facies[1]: Pyrope garnet is stable in the peridotite; spinel-garnet websterite (ariegite) is not stable in mafic layers.

2) Ariegite sub-facies[1] of spinel lherzolite facies: Spinel garnet websterite (ariegite) is stable; spinel lherzolite is stable.

3) Seiland sub-facies[1] of spinel lherzolite facies: Plagioclase spinel pyroxenite (seiland) is stable; spinel lherzolite is stable; garnet is not stable in mafic layers.

4) Plagioclase lherzolite facies[1]: Olivine-plagioclase assemblage is stable in both peridotite and mafic layers; plagioclase may not appear in depleted harzburgites or dunites.

The relationship of the mineral assemblages and the bulk chemical composition of the rocks in each mineral facies may be easily visualized by a graphic method in a projection from the diopside apex to the $CaAl_2SiO_6$-SiO_2-Mg_2SiO_4 triangle in a model system CaO-MgO-Al_2O_3-SiO_2 in Figure 3-16. These mineral facies are defined by the following reactions:

$$Cpx_{ss} + Opx_{ss} + \text{spinel} = \text{olivine} + \text{garnet} \qquad (1)$$

for the boundary between the ariegite facies (left hand side of the reaction (1)) and the garnet lherzolite facies (right hand side),

$$Cpx_{ss} + Opx_{ss} + \text{spinel} + \text{plagioclase} = \text{garnet} \qquad (2)$$

for the boundary between the seiland facies (left hand side) and the ariegite facies (right hand side),

---

[1] The facies are named and defined according to O'Hara (1967).

Figure 3-16. Graphic presentations of mineral parageneses in model system $CaO-MgO-Al_2O_3-SiO_2$; projection from diopside to $CaAl_2SiO_6-Mg_2SiO_4-SiO_2$ plane. All minerals are treated as pure phases for simplicity. Chemographic relation is shown in upper left. P-T phase diagram in the system $CaO-MgO-Al_2O_3-SiO_2$ after Kushiro and Yoder (1966) and the mineral facies map of the Ronda massif are put together for comparison. C, corundum; K, kyanite. PL, plagioclase lherzolite facies; Se, seiland subfacies of spinel lherzolite facies; Ar, ariegite subfacies of spinel lherzolite facies; GL, garnet lherzolite facies. Compositions of peridotite and mafic layers are indicated by "p" and "m", respectively, in paragenesis diagrams.

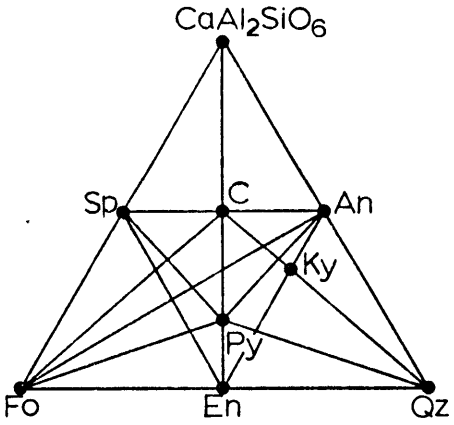
$CaAl_2SiO_6$
Sp
C
An
Ky
Py
Fo
En
Qz

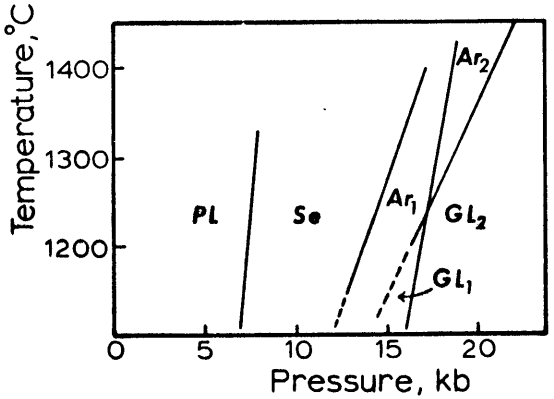
Temperature, °C
1400
1300
1200
PL
Se
Ar_1
Ar_2
GL_2
GL_1
0
5
10
15
20
Pressure, kb

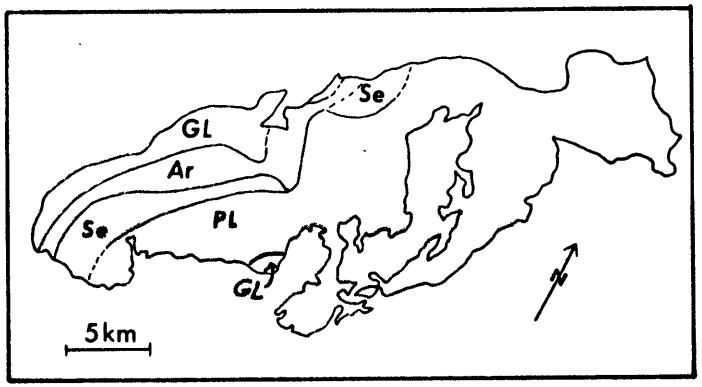
Se
GL
Ar
Se
PL
GL
5km

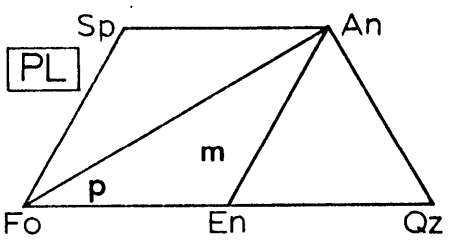
PL
Sp
An
m
p
Fo
En
Qz

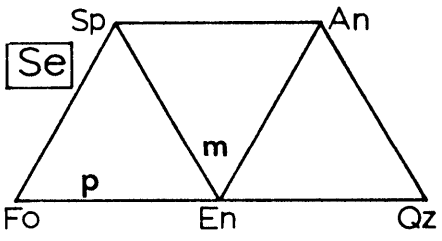
Se
Sp
An
m
p
Fo
En
Qz

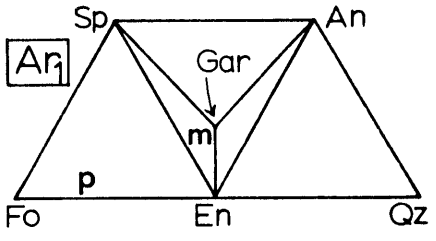
Ar_1
Sp
An
Gar
m
p
Fo
En
Qz

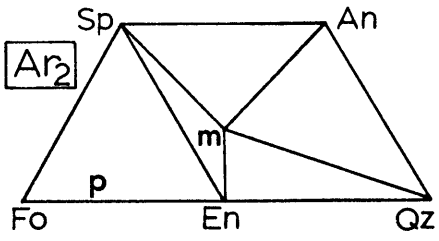
Ar_2
Sp
An
m
p
Fo
En
Qz

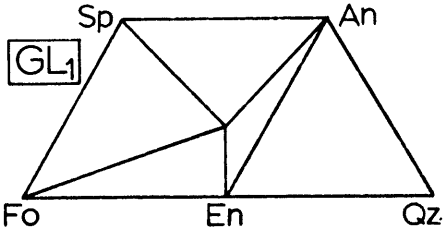
GL_1
Sp
An
Fo
En
Qz

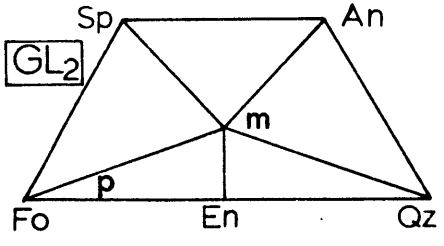
GL_2
Sp
An
m
p
Fo
En
Qz

olivine + plagioclase = Cpx_{ss} + Opx_{ss} + spinel (3)

for the boundary between the plagioclase lherzolite facies (left hand side) and the seiland facies (right hand side).

These reactions have been studied experimentally both in simple systems [e.g. on reaction (1): MacGregor, 1964; Kushiro and Yoder, 1966; O'Hara et al., 1971; on reaction (2) and (3): Kushiro and Yoder, 1966] and in natural complex systems [on reaction (1): Green and Ringwood, 1967; MacGregor, 1970; O'Hara et al., 1971; on reaction (3): Emslie, 1970; Green and Hibberson, 1970; Herzberg, 1976].

It is well established by the experimental work that these four mineral facies are primarily manifestations of different pressures. The massif is clearly zoned from higher pressure facies in the west to low pressure facies in the east (see Fig. 3-15). The facies boundaries generally strike NE-SW. The narrow zone of the seiland facies is disconnected in the middle, where the zones of ariegite and garnet lherzolite facies locally invade lower pressure zones toward the south-east. There is a small area of the garnet lherzolite facies attached to the plagioclase lherzolite facies zone at its south end at the contact (see Fig. 3-15). There are no intermediate zones of the ariegite or seiland facies between the two. This may indicate a direct transition of plagioclase peridotite to garnet peridotite as predicted by Kushiro and Yoder (1966). In the field, however, this small area of garnet lherzolite is separated from the plagioclase lherzolite by a 200 m thick metasedimentary dike (cordierite sillimanite gneiss) and the contact is probably tectonic, formed after the perido-

tite was metamorphosed. The attitude of the compositional layering of the peridotite also changes abruptly across the metasedimentary dike (see Fig. 2-5). Boulders of garnet pyroxenites and olivine gabbros are found mixed together in the peridotite breccia near Benahavis.

Although it was concluded that the zonal structure of the massif was primarily due to pressure variation, a problem arises when the actual magnitude of pressure variation required by experimentally determined phase equilibria is considered. In Fig. 3-17, relevant reaction curves experimentally determined in anhydrous conditions are drawn and compared to each other. It should be noted that most of the experiments were done above 1100°C except O'Hara et al. (1971). Obata (1976) extrapolated the high temperature data of Kushiro and Yoder (1966) to lower temperatures by thermodynamic calculations and concluded that reaction boundaries (1), (2), and (3) do not intersect at one point at low temperature (<700°C) as proposed by Kushiro and Yoder (1966). The P-T field of the spinel lherzolite which is bounded by reactions (1) and (3) in the simple system, however, may vary to some extent by adding other components: The introduction of Na_2O, for example, will stabilize the left hand side of reaction (3), thus shifting the reaction boundary to higher pressures. The introduction of FeO does not affect the position of the reaction boundary (3) (Green and Hibberson, 1970). The introduction of Cr_2O_3 and Fe_2O_3, however, stabilizes the right hand side of the same reaction because these two elements are strongly partitioned in the spinel phase, and thus

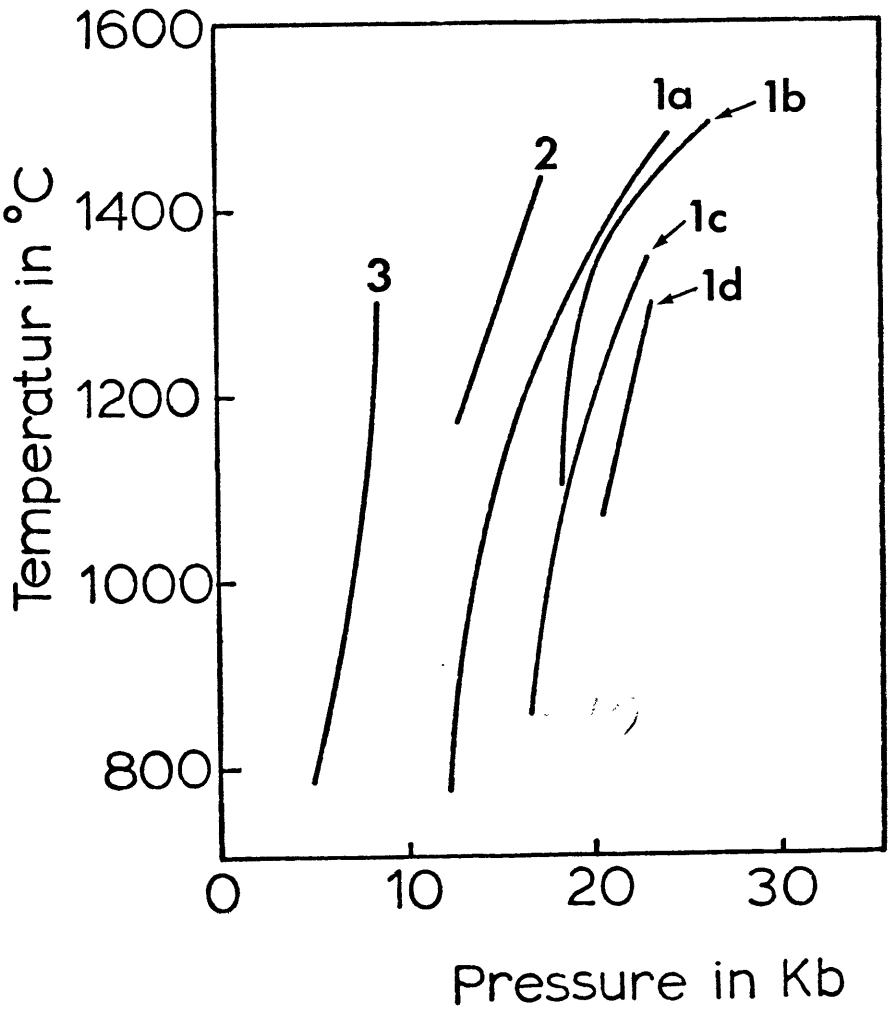

Figure 3-17. P-T phase diagram of mineral reactions (1), (2) and (3) in the text. 1a and 3, Obata's interpretation of Kushiro and Yoder's (1966) experiment; 2, Kushiro and Yoder (1966); 1b and 1c, O'Hara et al (1971) in synthetic four-component system and natural system, respectively; 1b, Green and Ringwood (1970) for Pyrolite III.

shift the boundary to lower pressures. For the same reason, reaction boundary (1) will shift to higher pressures with the introduction of Cr_2O_3 and Fe_2O_3, as experimentally demonstrated by MacGregor (1970). An introduction of FeO may stabilize garnet peridotite relative to spinel peridotite and shift reaction boundary (1) to lower pressures, considering the fact that the Fe/Mg partition coefficient between garnet and clinopyroxene rapidly increases as temperature decreases (Banno and Matsui, 1965). The reaction boundaries determined for natural peridotite (O'Hara et al., 1971) or for a multicomponent synthetic system (pyrolite III by Green and Ringwood, 1967) are all located at higher pressures than those in simple systems. Therefore, it could be concluded that the spinel lherzolite facies field extends over at least 6 kbar.

Returning to the field, the maximum width of the zone of spinel lherzolite facies is no more than 3 km assuming that the surfaces of the facies boundaries are vertical. Obviously, this distance is too small to account for the pressure difference of 6 kbar by lithostatic pressure. The field versus laboratory discrepancy may suggest the following possibilities: 1) the phase diagrams, particularly at low temperatures, are wrong, or 2) the rocks are not in chemical equilibrium, or 3) the time of the metamorphism was different in different parts of the massif, and the pressure changed during metamorphism. Such a situation might be realized if the peridotite was metamorphosed during its ascent to the crust.

The presence of quartz in garnet pyroxenite bears the following implications: The quartz-plagioclase-garnet-clinopyroxene rocks are restricted to the zone of garnet lherzolite facies (subfacies GL_2 in Fig. 3-16) and are never found in the zone of ariegite facies (Ar_2 in Fig. 3-16). This rock would be converted to plagioclase-orthopyroxene-clinopyroxene-garnet (typical granulite assemblage) at lower pressures in a subfacies of the garnet lherzolite facies (Gl_1 in Fig. 3-16) which corresponds to the high pressure side of the reaction, Cpx + Opx + Sp = Gar + Ol, but to the low pressure side of the reaction, An + Opx = Gar + Qz (Kushiro and Yoder, 1966). The assemblage plagioclase-orthopyroxene-clinopyroxene-garnet has not been found in either the garnet peridotite zone or the spinel peridotite zone. This field evidence may suggest that as pressure increases in natural rocks, plagioclase-orthopyroxene assemblages become unstable before the garnet-olivine assemblage becomes stable, and that the subfacies denoted as GL_1 in Fig. 3-16 may not exist at all. To the author's knowledge, a natural association of plagioclase-orthopyroxene-clinopyroxene-garnet rocks and garnet peridotite assemblages has never been reported. The P-T conditions in which the natural quartz-plagioclase-orthopyroxene-clinopyroxene assemblages occur together with the ariegite (Gar + Opx + Cpx + Sp) or the spinel lherzolite (Ar_2 in Fig. 3-16) assemblages may

then extend to lower pressures than in the simple system. The absence of such rock associations in the Ronda massif may be either due to the low equilibration temperatures of the massif, at which the P-T field of Ar_2 narrows (see Fig. 3-16), and so there is very little chance of finding the quartz-plagioclase-orthopyroxene-clinopyroxene rock in the ariegite facies zone, or due to bulk chemical compositions or both.

According to Figure 3-16, it is apparent that the mafic layers in the zone of the garnet lherzolite facies are on the silica-rich side of the garnet-pyroxene plane, while the mafic layers in the zone of the ariegite facies are on the silica-poor side of the plane. As the garnet pyroxene plane is a thermal barrier at high pressure (O'Hara and Yoder, 1967), the fact that the bulk compositions of the mafic layers lie on both sides of this potential thermal barrier will be critical in questions of petrogenesis.

Chapter 4

MINERAL CHEMISTRY

Minerals were analyzed with a fully automated electron microprobe analyzer (MAC Model 5). Detailed analytical procedures are described in Appendix 1.

The fact that many rocks are not in chemical equilibrium and that there are many features of chemical disequilibrium, such as zoning or drastic differences in chemical compositions between grains of the same mineral in single thin sections caused difficultly during microprobe analyses. As an example, almost the whole compositional range of pyroxenes from the Ronda peridotites may be found in some peridotite samples within a single pyroxene grain. Careful studies of such chemical inhomogeneities and some understanding of the petrologic processes which are responsible for them are essential for estimating the equilibrium conditions of the rocks.

4.1 Peridotites

For detailed studies of mineral chemistries, 12 peridotite samples were selected, covering a large area of the massif and all of the important mineralogical variations (sample location map in Fig. 4-1). The coexisting pyroxenes, spinels, garnets, amphiboles, and olivines were analyzed. The modal compositions and brief petrographic descriptions of the 12 peridotites are listed in Tables 4-1a and 4-2b, respectively.

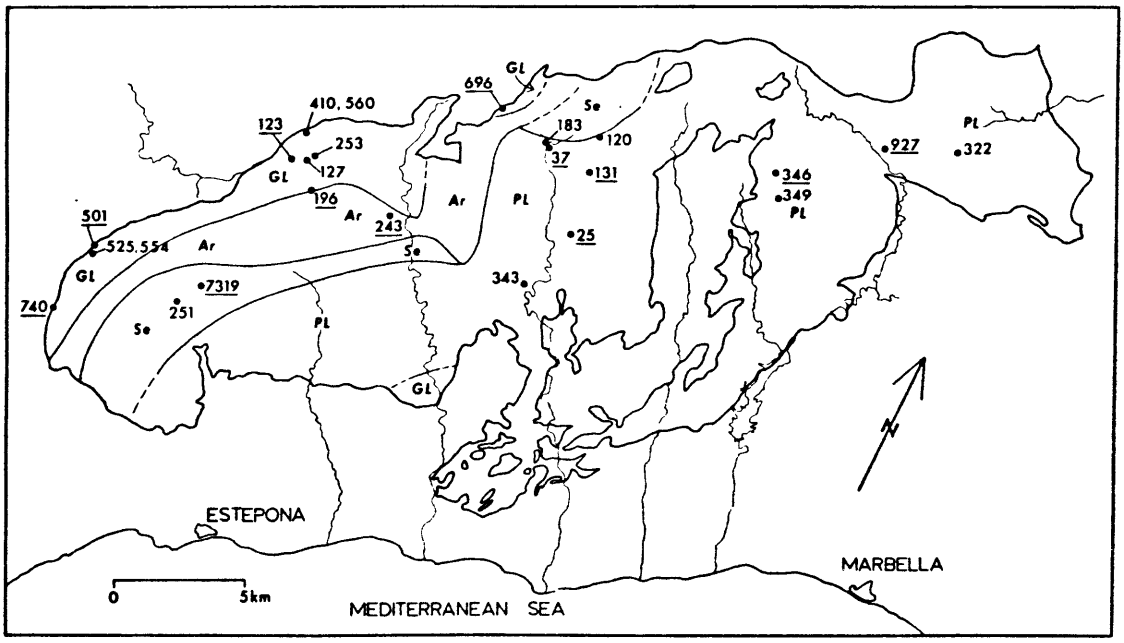

Figure 4-1. Sample locations of the Ronda peridotite (underlined) and mafic layers (others). All sample numbers start with prefix "R" except "7319", which was donated by M. Lundeen.

Table 4-1a. Mode of peridotites.

	Ol	Serp	Opx	Cpx	Sp	Gar	Plag	Amph	Opaque	Fo
R501	40	31	17	2	1	7	—	1	1.7	90.1
R740	58	18	13	1	1	7	—	1.3	1	90.6
R696	43	30	13	4.3	1	4	—	1.3	3	89.4
R123	46	11	18	10	0.6	12.3	—	1.8	1	87.8
R196	77	2	16	3	1.7	—	—	tr	tr	90.6
R243	60	—	23	15	3	—	tr	tr	tr	89.8
7319	68	18	12	1.6	1	—	—	tr	tr	91.7
R37	63	4	26	2.5	1	—	3.7	—	tr	90.6
R131	70	3	17	7	0.2	—	3	tr	tr	89.9
R25	61	15	16	2.2	1.3	—	4.4	—	tr	90.7
R346	72	2	16	1.6	1	—	7.8	—	tr	90.6
R927	59	20	12	0.7	0.6	—	6.9	—	tr	90.6

	Rock name	Texture	Grain sizes
R501	Garnet harzburgite	Cataclastic, weakly foliated.	Ol,0.06-0.2; Opx,0.1-0.2; Cpx,0.1-0.2; Gar,0.3-1.5; Sp,$<$0.7; Amph,0.1-0.2.
R740	Garnet harzburgite	Cataclastic, moderately foliated.	Ol,0.1-0.3; Opx,0.1-10; Cpx,0.1-0.2; Gar,0.4-4; Sp,0.03-1; Amph,0.1-0.2.
R696	Garnet harzburgite	Cataclastic, moderatery foliated.	Ol,0.1-1.5; Opx,0.1-10; Cpx,0.2-1; Gar, 0.15-2;Sp,0.02-1; Amph,0.1-0.2.
R123	Garnet lherzolite	Porphyroclastic, moderately foliated.	Ol,0.2-2; Opx,0.2-2; Cpx,0.4-1.5; Gar, 0.4-3; Sp,0.05-0.5; Amph,0.07-0.3.
R196	Spinel harzburgite	Porphyroclastic, moderately foliated.	Ol,0.2-2; Opx,0.2-3; Cpx,0.4-1.2; Sp, 0.08-0.8.
R243	Spinel lherzolite	Porphyroclastic.	Ol,2-3; Opx,0.2-4; Cpx,0.1-0.8; Sp,0.1-0.8.
7319	Spinel harzburgite	Coarse granular.	Ol,1-7; Opx,0.3-4; Cpx,0.4-1; Sp,0.2-1.4.
R37	Spinel-plagioclase harzburgite	Porphyroclastic, sheared & annealed.	Ol,0.1-4; Opx,0.2-3; Cpx,0.2-3; Sp,0.1-1.5; Plag,$\sim$0.3.
R131	Spinel-plagioclase lherzolite	Porphyroclastic to polygonal mosaic.	Ol,0.2-1.6; Opx,0.2-3; Cpx,0.2-0.7; Sp, 0.2-1; Plag,$\sim$0.3.
R25	Plagioclase harzuburgite	Porphyroclastic to xenomorphic granular.	Ol,0.2-3; Opx,0.1-3; Cpx,0.4-1.5; Plag, $\sim$0.3; Sp,0.2-0.4./Plag, altered.
R346	Plagioclase harzuburgite	Porphyroclastic to xenomorphic granular.	Ol,0.8-1.7; Opx,0.2-3; Cpx,0.2-1.2; Plag, $\sim$0.3; Sp,$<$0.3.
R927	Plagioclase harzuburgite	Porphyroclastic to cataclastic.	Ol,0.2-2; Opx,0.2-1.7; Cpx,0.2-0.8; Plag, $\sim$0.3; Sp,$<$0.3. /Plag, altered.

Table 4-1b. Petrographic notes of peridotites. Grain sizes are in millimeter.

Pyroxenes

The pyroxenes are quite variable in composition and record the most information about the P-T history of the peridotite. Much effort was devoted to analyzing these inhomogeneous pyroxenes. The chemical inhomogeneities of pyroxenes are illustrated (Fig. 4-2) in the Al_2O_3-CaO diagrams for the orthopyroxenes, in the Al_2O_3-Na_2O diagrams for the clinopyroxenes in each rock. The samples are arranged in a general geographic order. These parameters were chosen because they are the most variable and are thought to reflect equilibrium conditions of the peridotite most sensitively.

The pyroxene analyses were classified into 6 categories according to textures:

1) cores of porphyroclasts, excluding exsolution lamellae
2) cores of porphyroclasts, including exsolution lamellae
3) rims of porphyroclasts, which lack exsolution lamellae
4) cores of neoblasts
5) rims of neoblasts
6) exsolution lamellae in porphyroclasts.

Pyroxene Porphyroclasts

The porphyroclastic pyroxenes are more aluminous than the neoblastic pyroxenes, and they typically reveal complex patterns of chemical zoning. A result of detailed microprobe work on a single orthopyroxene porphyroclast in a transitional peridotite is illustrated in Fig. 4-3 and Fig. 4-4. The concentration of Al_2O_3 ranges from 6.2 weight percent in the core

Figure 4-2. Al_2O_3-CaO wt% relations of orthopyroxenes (left) and Al_2O_3-Na_2O wt% relations of clinopyroxenes (right) of 12 peridotites. Symbols: open circles = core of neoblasts; zoning is indicated by arrows; open squares = host of cores of porphyroclasts; stars = exsolution lamellae in the porphyroclasts; solid circles with white stars = averages of cores of porphroclasts obtained by defocused electron microprobe analyses; the "primary compositions" are indicated by "Pr"; Solid squares = rim of porphyroclasts. Open circles with solid stars for R243 clinopyroxenes are averages of "turbid" grains (see text).

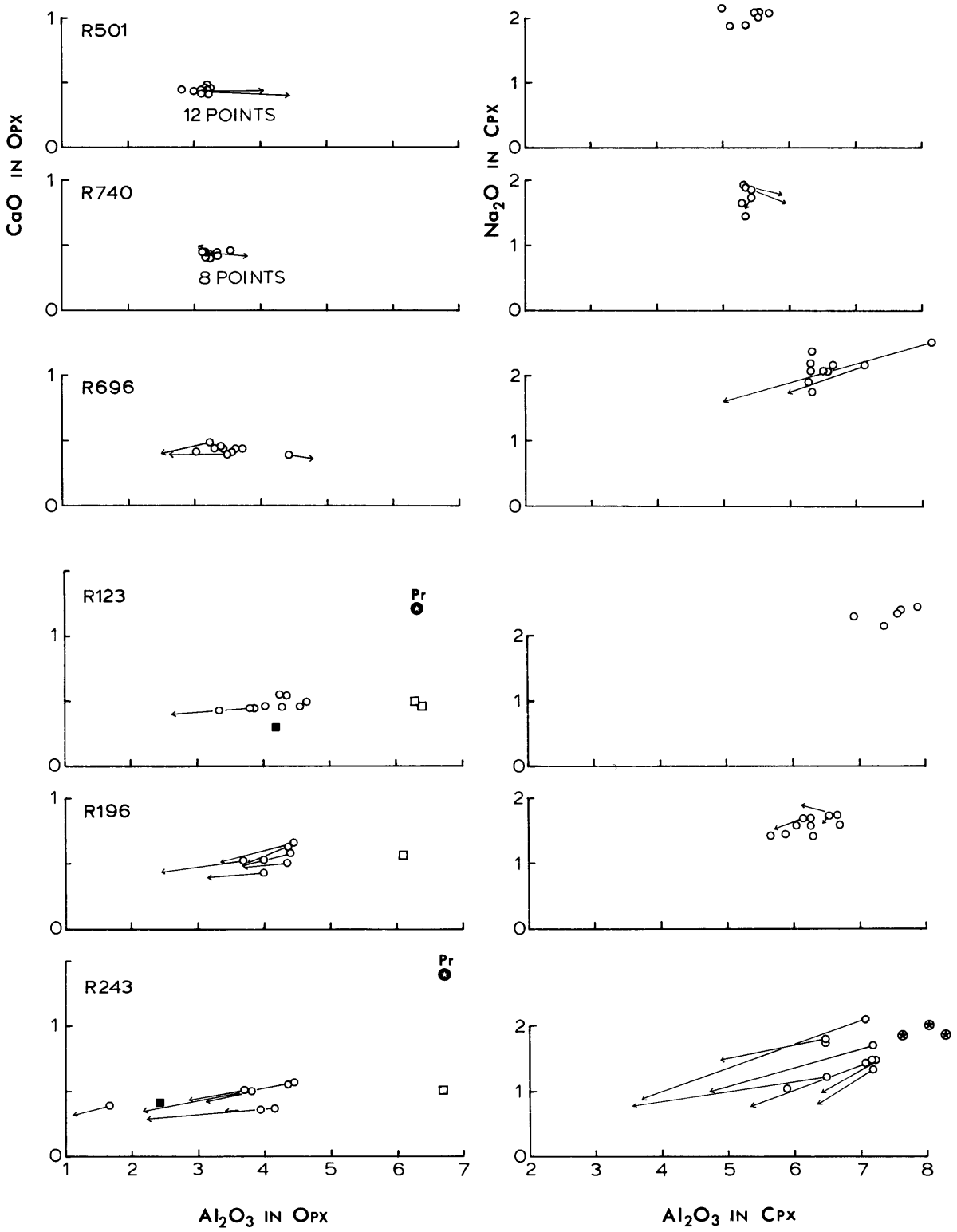
R501
12 POINTS
R740
8 POINTS
R696
R123
Pr
R196
R243
Pr
CaO IN OPX
Na2O IN CPX
Al2O3 IN OPX
Al2O3 IN CPX

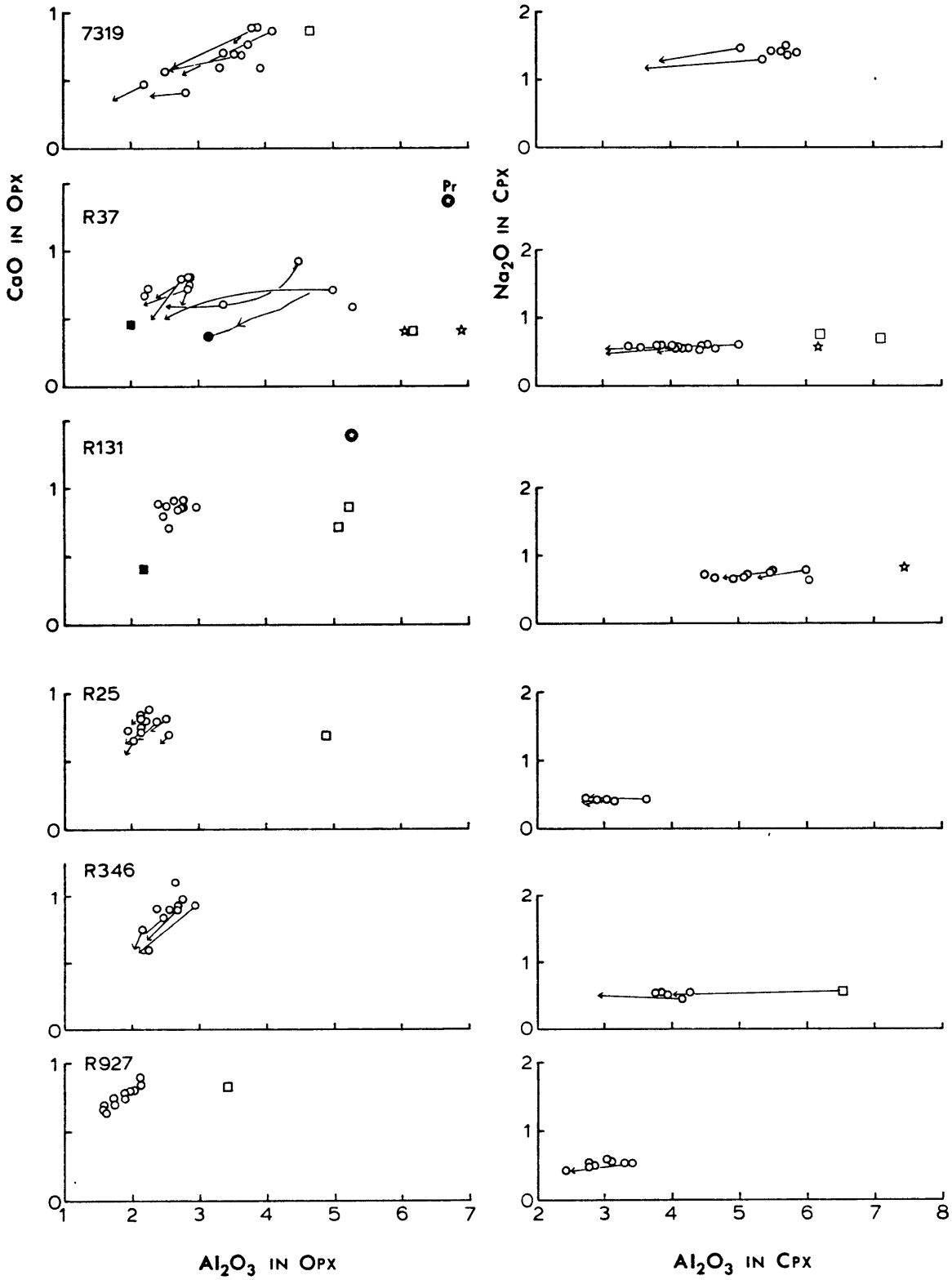
7319
R37
R131
R25
R346
R927
Pr
CaO IN OPX
Na2O IN CPX
Al2O3 IN OPX
Al2O3 IN CPX

Figure 4-3. Al_2O_3 contour map of a single orthopyroxene porphyroclast in spinel-plagioclase transitional peridotite, R37. Numerous exsolusion lamellae and blebs of clinopyroxene, which are omitted in the illustration, were avoided in microprobe analyses by using a tightly focused electron beam. The Al_2O_3 content in the orthopyroxene neoblasts are all between 2 and 3 in weight percent. Direction of C crystallographic axis is indicated in upper right. Detail microprobe traverses across the grain along lines a-a' and b-b' are shown in Figure 4-4.

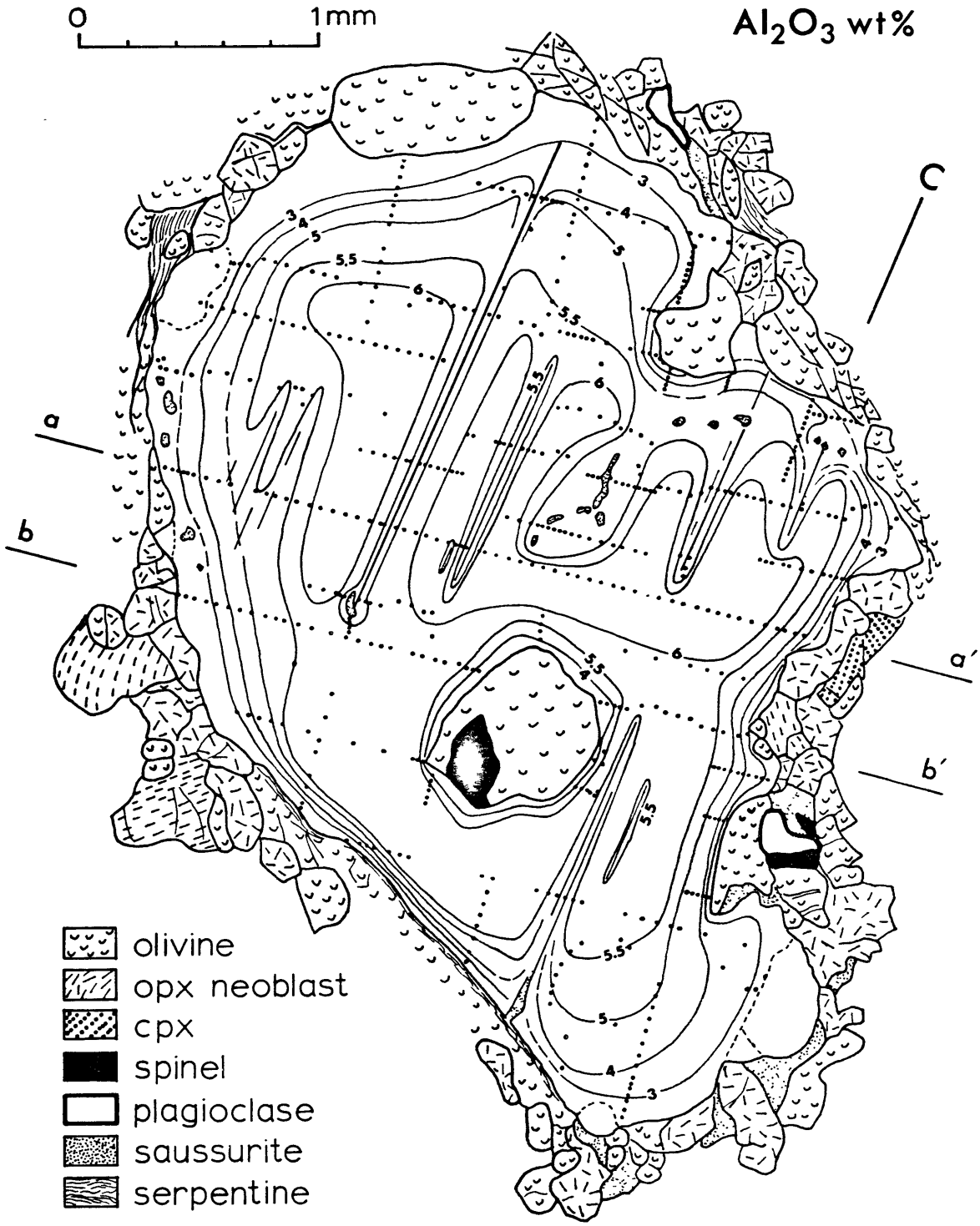
0
1mm
Al_2O_3 wt%
C
a
b
a'
b'
3
4
5
5.5
6
olivine
opx neoblast
cpx
spinel
plagioclase
saussurite
serpentine

Figure 4-4. Microprobe traverses of orthopyroxene porphyroclast along lines a-a' and b-b' in Figure 4-3. Locations of saussurite lamellae are indicated by arrows.

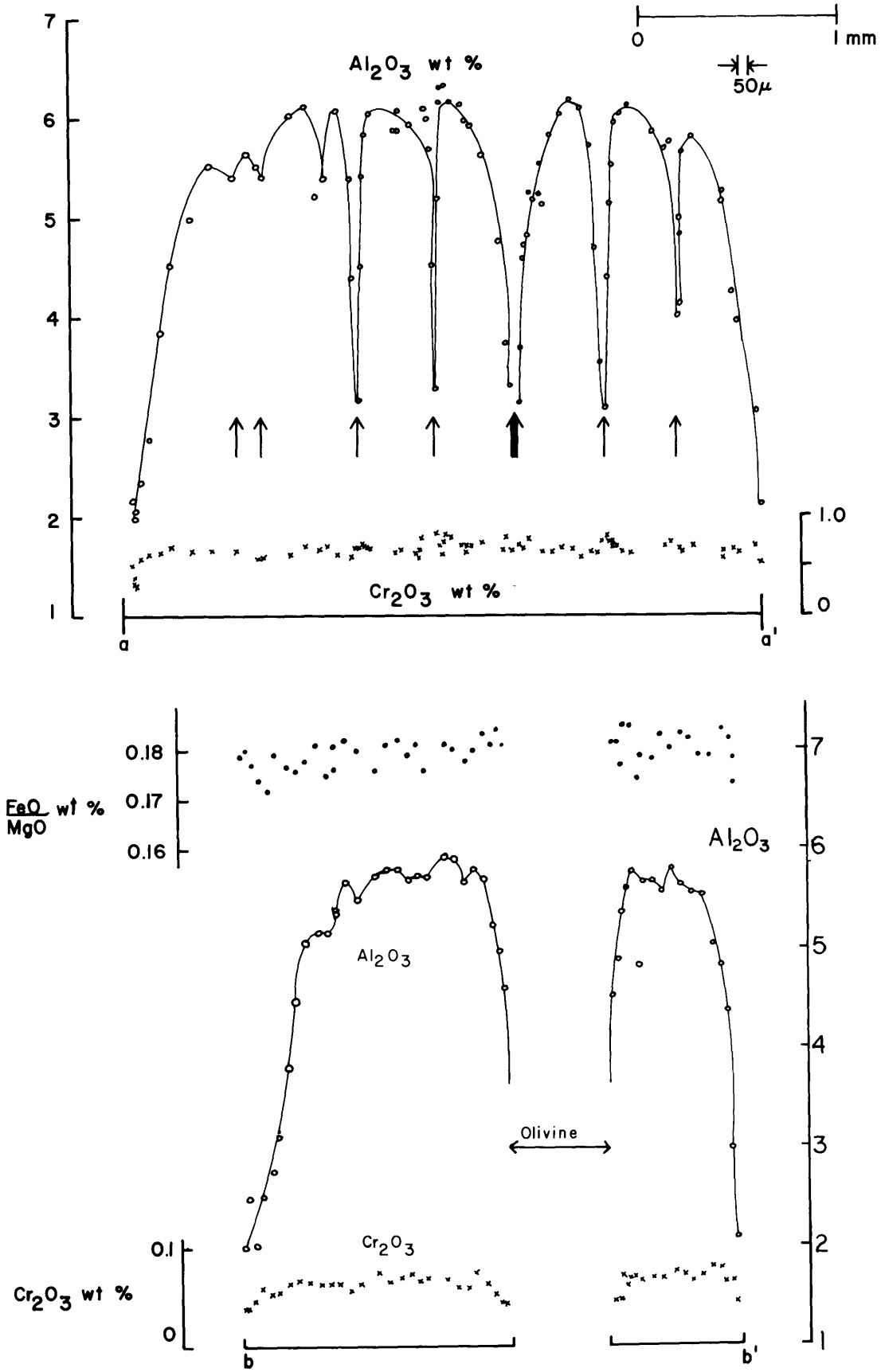
0
1 mm
50μ
Al_2O_3 wt %
7
6
5
4
3
2
1
Cr_2O_3 wt %
1.0
0
a
a'
FeO/MgO wt %
0.18
0.17
0.16
Al_2O_3
Olivine
Cr_2O_3
0.1
0
Cr_2O_3 wt %
b
b'

to 2 weight percent at the rim of the grain. The zoning pattern is complicated by depressions of the Al_2O_3 content around lamellae and blebs of plagioclase, which are now altered to saussurite, and around olivine and spinel inclusions. Near the periphery of the grain, the concentration gradient of Al_2O_3 is less pronounced in the direction of elongation of the grain, which corresponds to foliation of the peridotite, than in the other directions. The gradients are very steep near the saussurite lamellae (Fig. 4-4). The Cr_2O_3 content, however, is nearly constant throughout the grain except very near the margin, where it is slightly depressed. The FeO/MgO ratio is constant (within the range of analytical precision) (Fig. 4-4). It should be emphasized that despite the complexity of the chemical pattern, there is an irregular, but well-defined area of a maximum and uniform Al_2O_3 content, 6 to 6.2 wt. %, in the center of the grain but away from the saussurite lamellae or from the spinel inclusions. An interpretation of the inhomogeneities in the pyroxene is as follows: The pyroxenes were once coarse-grained, homogeneous and thoroughly equilibrated in the peridotite. The peridotite was then deformed and recrystallized under different physical conditions at which the original aluminous and subcalcic enstatite was no longer stable in the peridotite. The original big orthopyroxene grains were deformed, and new small orthopyroxene grains (neoblasts) formed either by nucleation or polygonization of the peripheries of the big grains with their compositions reflecting the new

physical conditions. Meanwhile, the composition of the porphyroclasts was modified by diffusion processes including exsolution of diopside and perhaps of plagioclase. Based on this interpretation, it may be concluded that the area of the Al_2O_3 plateau is the part in which the original composition of the orthopyroxene is still preserved, and that the new pyroxene compositions may be found in the pyroxene neoblasts.

The bulk chemical composition of the Al_2O_3 plateau, including fine clinopyroxene lamellae, was obtained by averaging defocused beam (30-50 mm) microprobe analyses of the area. This composition is called a primary composition in the sense that it represents the composition of the pyroxene of the last stage in which pyroxenes were homogeneous and the peridotite was totally in equilibrium. The primary compositions of orthopyroxenes (Table 4-2) are interestingly similar to each other although the peridotites are now of different mineral facies: the primary Al_2O_3 concentrations are 6.3 wt. % in a garnet peridotite, 6.7 wt. % in a spinel peridotite and 6.2 wt. % in a spinel-plagioclase peridotite. The primary CaO concentrations are 1.21, 1.4, and 1.36 wt. %, respectively, in the same peridotites. This uniformity of the primary compositions indicates that prior to the last recrystallization and re-equilibration, which must be related to the intrusion of the massif, the peridotites were homogeneous not just in hand specimens but also, perhaps, throughout the massif.

Not all porphyroclasts have Al_2O_3 plateaus. A few, particularly those in the plagioclase peridotites from the east part of

Table 4-2. Primary compositions of orthopyroxenes.

	R123	R243	R37
SiO_2	52.90	53.0	53.5
TiO_2	0.22	0.14	0.06
Al_2O_3	6.32	6.7	6.2
Cr_2O_3	0.41	0.5	0.66
FeO*	7.10	6.5	5.74
MnO	0.12	0.1	0.12
MgO	31.66	32.0	32.15
CaO	1.21	1.4	1.36
Na_2O	0.16	n.d.	0.10
Total	100.10	100.3	99.89
Cations per 6 oxygens			
Si	1.840	1.834	1.853
Ti	0.006	0.004	0.002
Al	0.259	0.273	0.253
Cr	0.011	0.014	0.018
Fe	0.207	0.188	0.166
Mn	0.004	0.003	0.004
Mg	1.641	1.651	1.660
Ca	0.045	0.052	0.050
Na	0.011	n.d.	0.007
Total	4.024	4.019	4.013
Ca	2.4	2.7	2.7
Mg	86.7	87.3	88.4
Fe	10.9	10.0	8.9
$Mg/_{(Mg+Fe)}$	0.888	0.898	0.909

the massif, do not retain their primary compositions, perhaps because of pervasive recrystallization and re-equilibration.

Clinopyroxene Porphyroclasts

An attempt to obtain primary compositions of clinopyroxene which could be paired with the primary composition of the orthopyroxenes failed because of the scarcity of clinopyroxene porphyroclasts and their apparent tendency to recrystallize more completely than the orthopyroxenes. An example of detailed microprobe work on a single clinopyroxene porphyroclast is shown in Figure 4-5. In the single clinopyroxene grain, Al_2O_3 varies from 7 to 3 wt. % and Na_2O varies from 0.9 to 0.5 wt. %. The compositional zoning has been much disrupted by extensive precipitation of plagioclase and spinel from the aluminous pyroxene. There is no area which can be called a high Al_2O_3 plateau and thus no area of "primary composition." The CaO concentration is remarkably constant (21 to 22 wt. %) throughout the grain. An attempt to reconstruct the CaO content prior to the orthopyroxene exsolution was hampered because the orthopyroxene lamellae tend to be thick ($\sim$30μ) and not evenly distributed in the grain.

Pyroxene Neoblasts

The pyroxene neoblasts are chemically distinct from the pyroxene porphyroclasts and span rather narrow ranges of compositions in single thin sections (Fig. 4-2). Some neoblasts are chemically uniform and others are zoned, typically from Al-rich cores to Al-poor rims. Zoning of the neoblasts

Figure 4-5 Al_2O_3 contour map (left) and Na_2O contour map (right) of clinopyroxene porphyroclast in sample R37. Exsolution lamellae of orthopyroxene are coarser and more widely spaced than those of clinopyroxene in orthopyroxene porphyroclasts. Only big blebs of orthopyroxene and saussurite[1] are illustrated. Direction of $\underline{c}$ crystallographic axis is indicated upper left.

---

1. It is tentatively called saussurite because it is optically similar to the saussurites in orthopyroxene porphyroclasts. A preliminary microprobe analyses is 39%SiO_2, 31%Al_2O_3 13%CaO, 3.5%Na_2O with no significant amount of TiO_2, Cr_2O_3, FeO, MnO, MgO making up total 87% only. Therefore it may be a fine grained aggregate of several minerals including carbonates and/or hydrous minerals. Tiny brown spinels ($\sim 30\mu$) are also common in the saussurite blebs.

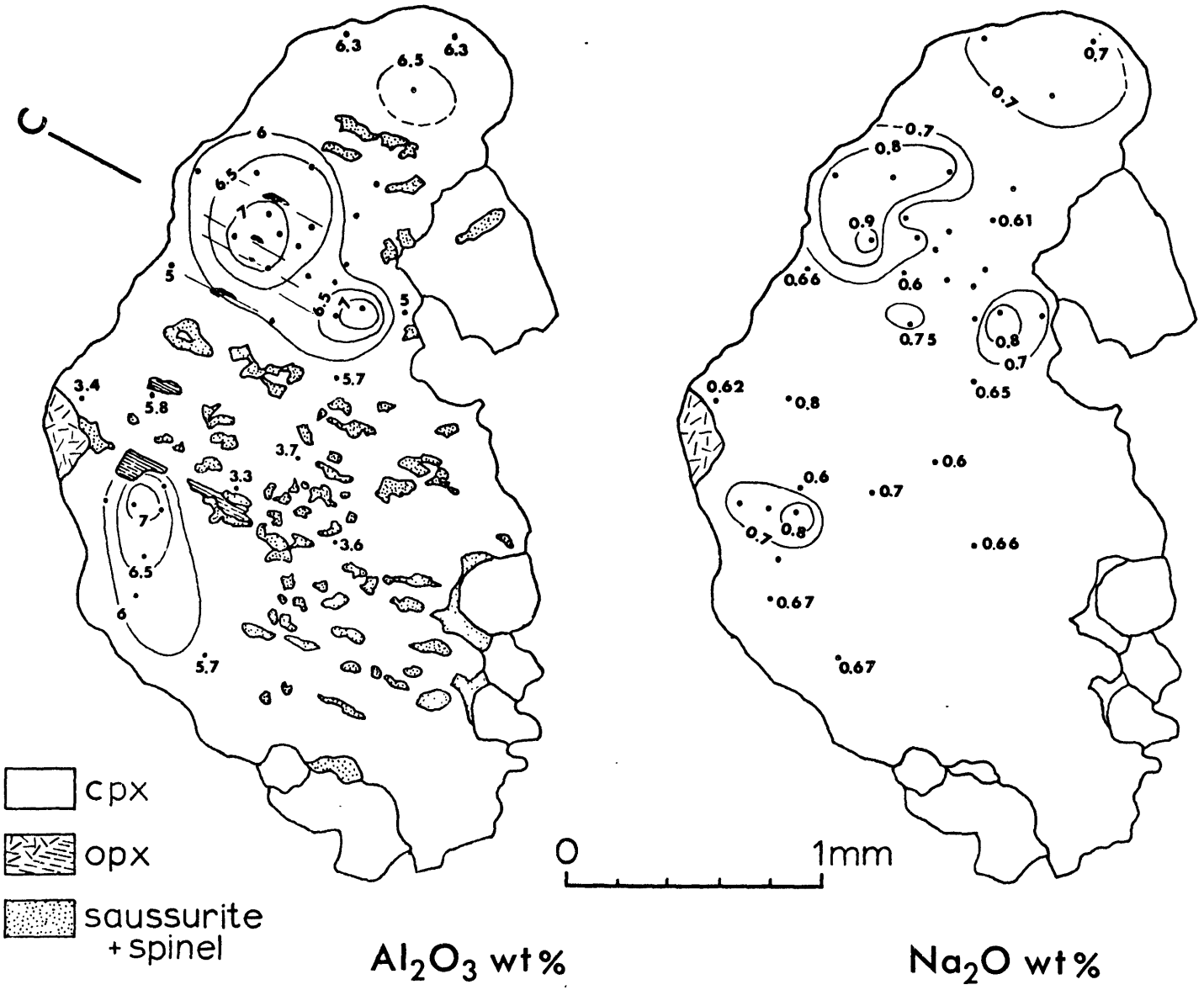
6.3
6.5
6.3
6
6.5
7
5
6.5
5
3.4
5.8
5.7
3.7
3.3
7
6.5
6
3.6
5.7
0.7
0.7
0.7
0.8
0.9
0.61
0.66
0.6
0.75
0.8
0.7
0.62
0.8
0.65
0.6
0.6
0.7
0.7
0.8
0.66
0.67
0.67
cpx
opx
saussurite
+ spinel
0
1mm
Al2O3 wt%
Na2O wt%

is particularly noticeable in some spinel peridotites. CaO drops with Al_2O_3 in the zoned orthopyroxene neoblasts, and in the zoned clinopyroxene neoblasts Na_2O drop with Al_2O_3. Al_2O_3 in the orthopyroxene and the clinopyroxene neoblasts in the two garnet peridotites increases toward garnet without significant drop of CaO content at the pyroxene/garnet contacts.

The unusual "turbid" clinopyroxene grains (0.2 to 1.5 mm) in spinel lherzolite R243 (see descriptions, page 28) were analyzed with a defocused electron beam (30μ) averaging the centers of the grains including numerous tiny inclusions and orthopyroxene exsolution lamellae. These turbid grains are distinctly more aluminous and less calcic than the smaller clean clinopyroxenes in the same thin section (Fig. 4-2 and Cpx^+ in Table 4-3). The larger "turbid" grains are thought to be relicts of early high-temperature pyroxenes. The smaller clean clinopyroxenes are considered to be in equilibrium with the orthopyroxene neoblasts.

Rims of orthopyroxene porphyroclasts are typically less calcic than cores of neoblasts. Apparently the compositions of the neoblasts have also been partly modified by diffusion processes from their initial compositions, responding to the thermal history of the massif. The compositions of the cores of the pyroxene neoblasts, which may represent the compositions of the initial neoblasts, could therefore be used to estimate

the physical conditions of the recrystallization of the peridotites.

In contrast to the uniformity of pyroxene porphyroclasts throughout the massif, there are clear correlations between the compositions of the cores of pyroxene neoblasts and the mineral facies of the peridotites and hence, their geographic locations. The relationships are illustrated in frequency diagrams in Fig. 4-6. The Al_2O_3 content of the orthopyroxene neoblasts is highest in spinel peridotites (4 wt. %) and decreases both toward garnet peridotites (3 wt. %) and toward plagioclase peridotites (2 wt. %). CaO content in the orthopyroxene neoblasts increases steadily from 0.4 wt. % in garnet peridotite to 0.9 wt. % in plagioclase peridotites. The Al_2O_3 content of clinopyroxene neoblasts generally parallels that of the orthopyroxene neoblasts, together with the Al/Al+Cr ratio of coexisting spinel. Chemistry of the spinel is discussed later (p. 87). The Na_2O content in the clinopyroxene neoblasts is highest in the garnet peridotites (2 wt. %) and lowest in plagioclase peridotites (0.5 wt. %). Cr_2O_3 is an important minor element in pyroxenes and inverse relations with Al_2O_3 may be seen within each mineral facies.

Average values of the coexisting ortho- and clinopyroxene neoblasts in the 12 peridotites are listed in Table 4-3.

Pyroxene Exsolution Lamellae

Some pyroxene exsolution lamellae, blebs, or inclusions in the pyroxene porphyroclasts were analyzed in two transitional

Figure 4-6. Summary of core compositions of pyroxene neoblasts in 12 peridotites compared with compositions of coexisting spinels. Each symbols represents average compositions of one grain. Solid squares in sample R243 is for turbid clinopyroxenes. Solid circles for spinels in samples R501 and R696 are for tiny grains,and those in R37 and R131 are for small grains mounted in plagioclase.

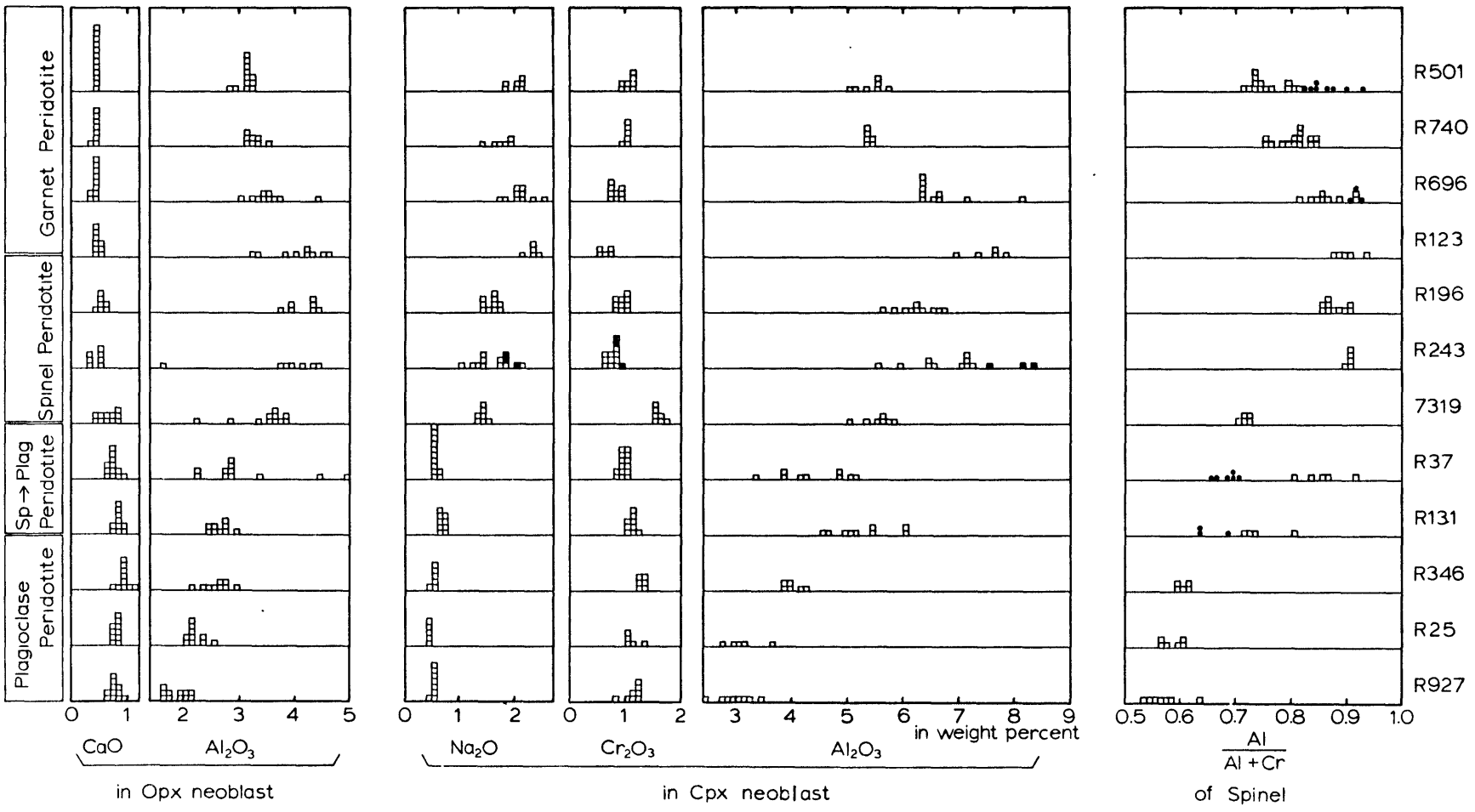
Garnet Peridotite
Spinel Peridotite
Sp → Plag Peridotite
Plagioclase Peridotite
R501
R740
R696
R123
R196
R243
7319
R37
R131
R346
R25
R927
0 1 2 3 4 5
CaO
Al2O3
in Opx neoblast
0 1 2 0 1 2 3 4 5 6 7 8 9
Na2O
Cr2O3
Al2O3
in weight percent
in Cpx neoblast
0.5 0.6 0.7 0.8 0.9 1.0
Al / Al + Cr
of Spinel

Table 4-3. Average analyses of cores of pyroxene neoblasts.

	R501		R740		R696	
	Opx	Cpx	Opx	Cpx	Opx	Cpx
SiO_2	55.67	53.25	55.26	52.79	54.86	52.36
TiO_2	0.07	0.50	0.12	0.46	0.14	0.85
Al_2O_3	3.13	5.40	3.28	5.38	3.43	6.52
Cr_2O_3	0.35	1.07	0.33	1.03	0.28	0.83
FeO*	6.55	2.51	6.69	2.48	7.43	2.78
MnO	0.15	0.08	0.17	0.09	0.17	0.05
MgO	34.00	15.58	34.15	15.87	33.64	14.72
CaO	0.44	19.87	0.43	20.86	0.43	20.08
Na_2O	0.05	2.04	n.d.	1.75	n.d.	2.07
Total	100.41	100.30	100.43	100.71	100.38	100.26
	Cations per 6 oxygens					
Si	1.918	1.916	1.906	1.898	1.900	1.889
Ti	0.002	0.014	0.003	0.012	0.004	0.023
Al	0.127	0.229	0.133	0.228	0.140	0.277
Cr	0.010	0.030	0.009	0.029	0.008	0.024
Fe	0.189	0.076	0.193	0.075	0.215	0.084
Mn	0.004	0.002	0.005	0.003	0.005	0.002
Mg	1.745	0.836	1.755	0.850	1.736	0.791
Ca	0.016	0.766	0.016	0.804	0.016	0.776
Na	0.003	0.142	n.d.	0.122	n.d.	0.145
Total	4.014	4.012	4.020	4.022	4.023	4.010
Mg/(Mg+Fe)	0.902	0.917	0.901	0.919	0.890	0.904
Ca	0.8	45.7	0.8	46.5	0.8	47.0
Mg	89.5	49.8	89.4	49.2	88.3	47.9
Fe	9.7	4.5	9.8	4.3	10.9	5.1

Table 4-3. (continued)

	R123		R196		R243		
	Opx	Cpx	Opx	Cpx	Opx	Cpx	Cpx^t
SiO_2	54.91	51.84	55.14	51.81	54.64	51.60	52.24
TiO_2	0.17	1.08	0.08	0.44	0.10	0.55	0.53
Al_2O_3	4.06	7.49	4.19	6.25	4.04	6.84	8.00
Cr_2O_3	0.28	0.64	0.47	0.95	0.29	0.75	0.89
FeO*	7.48	3.07	6.26	2.41	6.84	2.87	3.11
MnO	0.09	0.10	0.18	0.10	0.16	0.13	0.12
MgO	33.17	14.27	33.65	15.09	34.38	15.20	15.74
CaO	0.47	19.77	0.56	20.81	0.48	20.40	18.86
Na_2O	0.06	2.32	n.d.	1.58	n.d.	1.55	1.92
Total	100.69	100.58	100.53	99.44	100.93	99.89	101.41
	Cations per 6 oxygens						
Si	1.894	1.866	1.896	1.885	1.878	1.870	1.858
Ti	0.004	0.029	0.002	0.012	0.003	0.015	0.014
Al	0.165	0.318	0.170	0.268	0.164	0.292	0.335
Cr	0.008	0.018	0.013	0.027	0.008	0.021	0.025
Fe	0.216	0.092	0.180	0.073	0.197	0.087	0.093
Mn	0.003	0.003	0.005	0.003	0.005	0.004	0.004
Mg	1.705	0.766	1.724	0.818	1.761	0.821	0.834
Ca	0.017	0.763	0.021	0.811	0.018	0.792	0.719
Na	0.004	0.162	n.d.	0.111	n.d.	0.109	0.132
Total	4.017	4.017	4.011	4.011	4.033	4.012	4.014
$Mg/_{(Mg+Fe)}$	0.888	0.892	0.905	0.918	0.900	0.904	0.900
Ca	0.9	47.1	1.1	47.6	0.9	46.6	43.7
Mg	88.0	47.2	89.6	48.1	89.2	48.3	50.7
Fe	11.1	5.7	9.4	4.3	10.0	5.1	5.6

Cpx^t : Average analysis of "turbid" clinopyroxene (see p. 73).

Table 4-3.(continued)

	7319		R37		R131	
	Opx	Cpx	Opx	Cpx	Opx	Cpx
SiO_2	54.56	52.18	56.24	51.88	55.73	50.19
TiO_2	0.07	0.33	0.09	0.34	0.43	1.44
Al_2O_3	3.69	5.54	2.63	4.19	2.63	5.32
Cr_2O_3	0.67	1.61	0.54	1.00	0.48	1.12
FeO*	5.61	2.41	6.13	2.46	6.79	3.07
MnO	0.14	0.10	0.15	0.08	0.13	0.11
MgO	34.54	15.66	34.14	16.62	33.54	16.29
CaO	0.74	21.01	0.74	22.81	0.82	21.91
Na_2O	n.d.	1.41	0.03	0.56	0.02	0.70
Total	100.02	100.25	100.69	99.94	100.57	100.15
	Cations per 6 oxygens					
Si	1.885	1.887	1.930	1.889	1.922	1.832
Ti	0.002	0.009	0.002	0.009	0.011	0.040
Al	0.150	0.236	0.106	0.180	0.107	0.229
Cr	0.018	0.046	0.015	0.029	0.013	0.032
Fe	0.162	0.073	0.176	0.075	0.196	0.094
Mn	0.004	0.003	0.004	0.002	0.004	0.003
Mg	1.779	0.844	1.746	0.902	1.724	0.886
Ca	0.027	0.814	0.027	0.890	0.030	0.857
Na	n.d.	0.099	0.002	0.040	0.001	0.050
Total	4.028	4.012	4.008	4.017	4.008	4.023
$Mg/_{(Mg+Fe)}$	0.916	0.921	0.908	0.923	0.898	0.904
Ca	1.4	47.0	1.4	47.7	1.6	46.7
Mg	90.4	48.8	89.6	48.3	88.4	48.2
Fe	8.2	4.2	9.0	4.0	10.0	5.1

Table 4-3. (continued)

	R25		R346		R927	
	Opx	Cpx	Opx	Cpx	Opx	Cpx
SiO_2	55.93	53.10	55.54	52.47	56.18	52.16
TiO_2	0.08	0.31	0.17	0.32	0.11	0.38
Al_2O_3	2.22	3.10	2.55	4.01	1.86	2.98
Cr_2O_3	0.51	1.09	0.55	1.27	0.46	1.16
FeO*	6.30	2.68	6.42	2.56	6.20	2.49
MnO	0.15	0.12	0.15	0.06	0.13	0.09
MgO	34.84	17.95	34.58	17.18	35.06	17.31
CaO	0.77	21.37	0.89	21.57	0.76	22.78
Na_2O	n.d.	0.42	n.d.	0.52	n.d.	0.53
Total	100.80	100.14	100.85	99.96	100.76	99.88
	Cations per 6 oxygens					
Si	1.921	1.921	1.910	1.903	1.929	1.903
Ti	0.002	0.008	0.004	0.009	0.003	0.010
Al	0.090	0.132	0.103	0.171	0.075	0.128
Cr	0.014	0.031	0.015	0.036	0.012	0.033
Fe	0.181	0.081	0.185	0.078	0.178	0.076
Mn	0.004	0.004	0.004	0.002	0.004	0.003
Mg	1.784	0.968	1.772	0.929	1.794	0.941
Ca	0.028	0.828	0.033	0.838	0.028	0.891
Na	n.d.	0.029	n.d.	0.037	n.d.	0.038
Total	4.025	4.003	4.027	4.003	4.024	4.024
$Mg/_{(Mg+Fe)}$	0.908	0.923	0.906	0.923	0.910	0.925
Ca	1.4	44.1	1.6	45.4	1.4	46.7
Mg	89.5	51.6	89.1	50.3	89.7	49.3
Fe	9.1	4.3	9.3	4.2	8.9	4.0

peridotites, R37 and R131. The analyses are listed in Table 4-4, together with analyses of some host pyroxenes. The orthopyroxene lamellae are more aluminous and slightly less calcic than the orthopyroxene neoblasts (see R37 in Fig. 4-2). Similarly, the clinopyroxene lamellae are more aluminous than the clinopyroxene neoblasts (see R131 in Fig. 4-2). The element partitioning between the exsolved phases and the host phases are better depicted in the A-C-F diagram (Fig. 4-7), in which the points of the exsolved phases are connected with those of their host pyroxene phases. The pyroxene lamellae appear to be optically homogeneous single phases. The compositions are constant and are thought to represent equilibrium compositions. Clinopyroxene inclusions in the center of an orthopyroxene porphyroclast in R131 are compositionally identical to the lamellae or blebs. The host orthopyroxenes, however, contain many micro-scale exsolution lamellae (<1μ) of clinopyroxenes which are too closely spaced (<1μ) to resolve with the electron beam of the microprobe. Therefore, the analyses of the host phases, particularly the CaO content, should be regarded as average compositions of physical mixtures of the ortho- and clinopyroxenes, whose compositions may have been further modified by micro-scale exsolution. The pyroxene exsolution took place presumably during the cooling of the peridotites. The Al_2O_3 contents in the center of the pyroxene porphyroclasts, however, did not decrease from the primary concentrations. The equilibrium state for such highly aluminous pyroxene compositions at low pressure would be olivine + spinel

Table 4-4. Analyses of pyroxene exsolution lamellae.

	1	2	3	4	5
SiO_2	53.80	50.92	n.d.	50.96	51.99
TiO_2	n.d.	0.35	n.d.	0.30	0.15
Al_2O_3	6.07	6.21	6.9	7.09	4.75
Cr_2O_3	0.76	1.05	0.8	1.07	0.82
FeO*	6.30	2.36	6.3	2.40	2.20
MnO	0.10	0.10	n.d.	0.1	0.09
MgO	33.80	16.44	n.d.	15.79	16.85
CaO	0.40	22.44	0.4	22.94	23.29
Na_2O	0.04	0.75	n.d.	0.71	0.65
Total	101.27	101.12	---	101.37	100.79
	Cations per 6 oxygens				
Si	1.840	1.835		1.830	1.877
Ti	n.d.	0.009		0.008	0.004
Al	0.245	0.264		0.300	0.202
Cr	0.021	0.030		0.030	0.023
Fe	0.180	0.071		0.072	0.066
Mn	0.003	0.003		0.003	0.003
Mg	1.723	0.883		0.845	0.907
Ca	0.015	0.886		0.883	0.901
Na	0.003	0.052		0.049	0.046
Total	4.029	4.034		4.021	4.029
Ca	0.8	48.1		49.0	48.1
Mg	89.8	48.0		47.0	48.4
Fe	9.4	3.9		4.0	3.5
$Mg/_{(Mg+Fe)}$	0.905	0.925		0.921	0.932

Table 4-4 (continued)

	6	7	8
SiO_2	54.72	49.20	49.52
TiO_2	0.29	1.67	1.12
Al_2O_3	5.09	7.41	7.57
Cr_2O_3	0.68	1.09	1.08
FeO*	6.52	2.78	3.04
MnO	0.13	0.09	0.13
MgO	33.22	15.14	15.08
CaO	0.72	22.18	22.23
Na_2O	n.d.	0.79	0.80
Total	101.37	100.35	100.57
	Cations per 6 oxygens		
Si	1.870	1.791	1.799
Ti	0.007	0.046	0.031
Al	0.205	0.318	0.324
Cr	0.018	0.031	0.031
Fe	0.186	0.085	0.092
Mn	0.004	0.003	0.004
Mg	1.692	0.821	0.817
Ca	0.026	0.865	0.866
Na	n.d.	0.056	0.056
Total	4.010	4.016	4.020
Ca	1.4	48.8	48.8
Mg	88.8	46.4	46.0
Fe	9.8	4.8	5.2
$Mg/_{(Mg+Fe)}$	0.901	0.907	0.898

Table 4-4. Keys

1, Opx lamella in Cpx (2) R37

3, Opx lamella in Cpx (3) R37

5, Cpx bleb in Opx R37

7, Cpx lamella in Opx (6) R131

8, Cpx inclusion in Opx R131

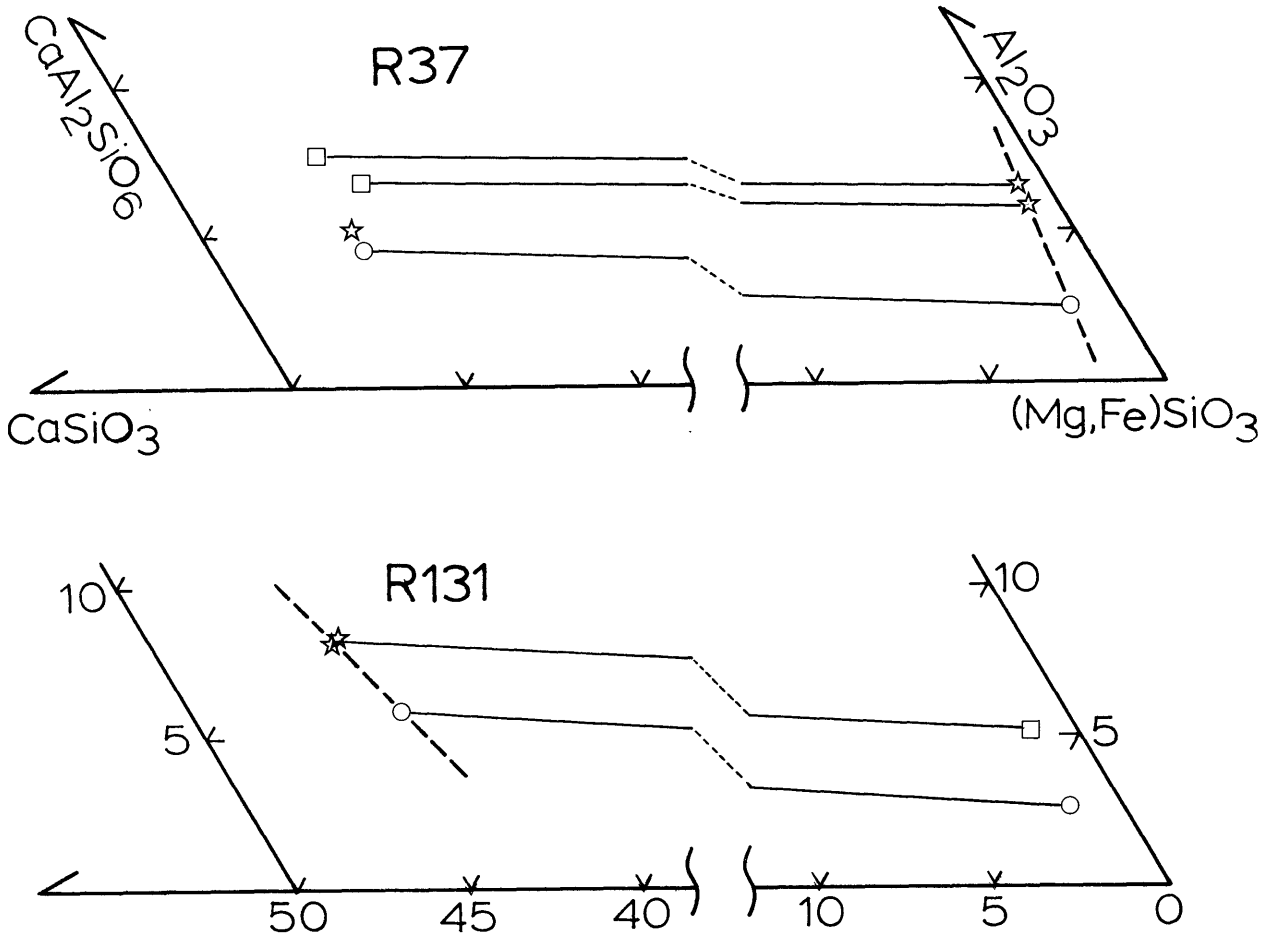

Figure 4-7. A-C-F plots of pyroxene exsolution lamellae and blebs (stars), their hosts (squares) and averages of neoblasts (circles) from samples R37 and R131.

(or plagioclase) + Al-poor pyroxenes as represented by the neoblasts assemblages. For some kinetic reasons, however, olivine, spinel, or plagioclase did not nucleate inside the pyroxene grains[1]. Instead, the primary Al_2O_3 content was simply partitioned between the host pyroxene phase and the exsolved pyroxene phases in such a way that the Gibbs free energy is locally minimized, in other words, the host pyroxenes and the pyroxene lamellae are in metastable equilibrium in the anomalously high-alumina environment.

There are currently controversial opinions among experimentalists about the effect of Al_2O_3 on the enstatite-diopside solvus (see page 118). This is an important problem because direct application of the enstatite-diopside solvus to Al-bearing natural pyroxenes without proper correction for the effects of Al_2O_3 would result in erroneous temperature estimates. In this context, it is interesting to compare the CaO contents of the pyroxene lamellae and the pyroxene neoblasts, which are thought to represent true equilibrium conditions, because one could draw a metastable pyroxene solvus in the A-C-F diagram (dashed lines in Fig. 4-7) by connecting the points of the lamellae and the neoblasts if the exsolution and the neoblast formation were more or less contemporaneous (therefore, isothermal and isobaric). The metastable pyroxene solvus thus defined in the natural rocks is

---

[1] Plagioclase and perhaps olivine may be nucleating in the center of the "turbid" clinopyroxene. See Petrography (p. 28).

quantitatively in harmony with the experiments by O'Hara and Schairer (1963), Herzberg and Chapman (1976), and Mori (1977) , all of whom claim that diopside solubility in enstatite and enstatite solubility in diopside decrease as Al_2O_3 increases at constant pressure and temperature.

Alternative explanation for the differences of the CaO content is that the pyroxene lamellae have re-equilibrated at lower temperatures than the neoblasts by solid diffusion, preserving the high Al_2O_3 content for the same reason mentioned above.

Spinel

The spinels in the peridotites span a wide range of compositions which correlate with the mineral facies of the peridotites. The analyses are plotted in the Fe^{3+}-Cr-Al triangles (Fig. 4-8) for each rock and are arranged in the same order as adopted for the presentation of the pyroxene analyses. Chemical inhomogeneities are apparent particularly in the garnet peridotites and the transitional peridotites. Medium-sized (∿0.5 mm) spinels in the garnet peridotites are more chromiferous than those in the spinel peridotites except a harzburgite 7319, which in terms of the pyroxene contents is one of the most depleted peridotites investigated (see mode in Table 4-1). The "tiny" spinel grains (∿20μ, see p. 30 for description) are considerably more aluminous than the medium-sized grains. The medium-sized spinel grains are fairly uniform in composition. Zoning, from chromian core to aluminous rim, is recognized only within a few tens of microns

Figure 4-8. Fe^{3+}-Cr-Al plots of spinel analyses from 12 peridotites. Open circles = cores; triangles = core of tiny grains; solid squares = small grains mounted in plagioclase; direction of zoning is indicated by arrows.

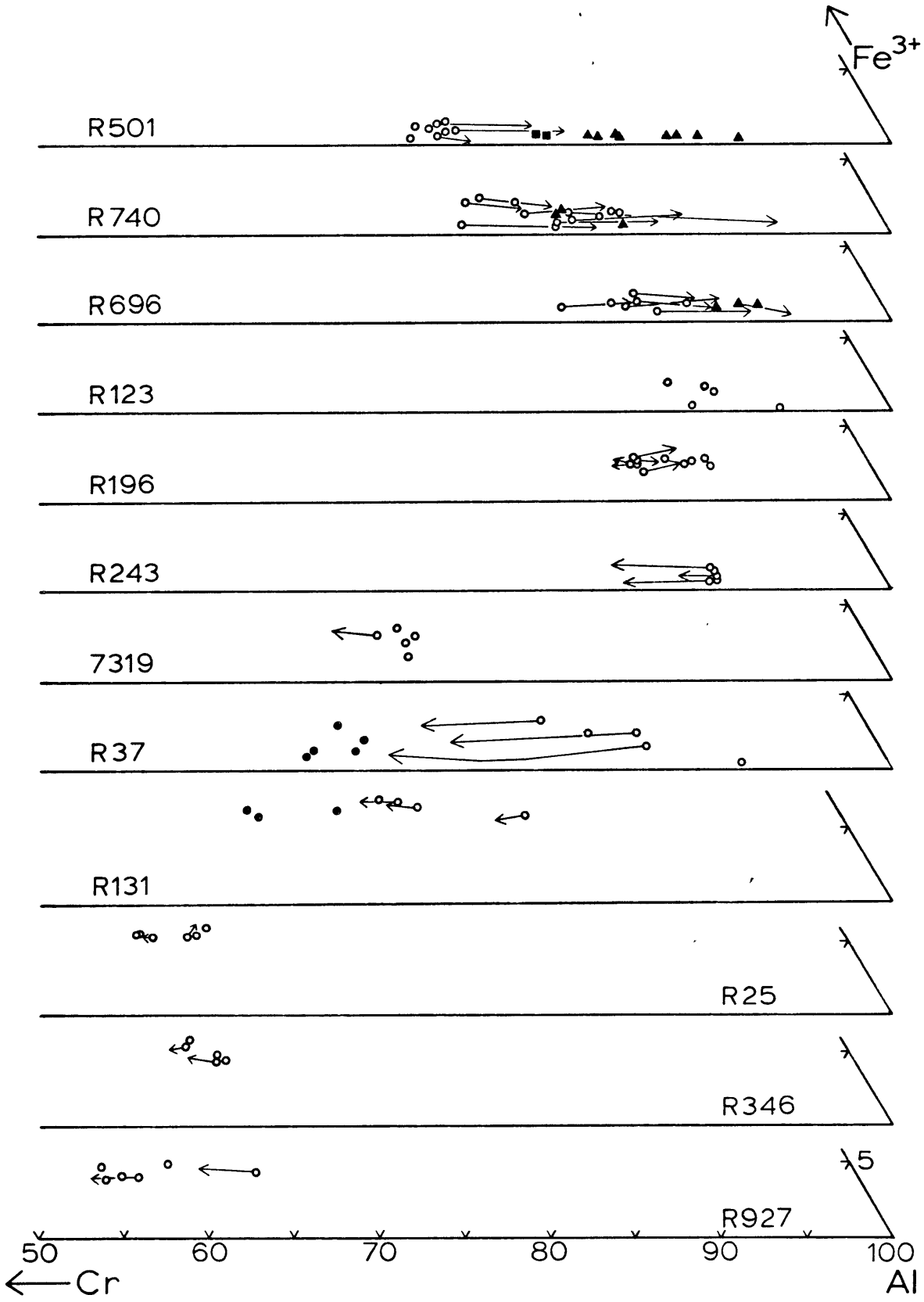
Fe3+
R501
R740
R696
R123
R196
R243
7319
R37
R131
R25
R346
5
R927
50
60
70
80
90
100
Cr
Al

of the rims. The cores of the medium-sized spinels are considered to be chemically equilibrated in the garnet lherzolite facies. The "tiny" spinels are of younger generations as inferred from their intimate intergrowths with sulfides, the extremely small grain sizes (∿20 m), and their high Al/Cr ratios, and therefore, they may not be in equilibrium with garnets.

The zoning pattern is reversed for the other peridotite facies; i.e., the spinels are zoned from aluminous cores to chromiferous rims in some spinel peridotites, the 2 transitional peridotites, and the 3 plagioclase peridotites.

The spinels from the transitional peridotites define wide ranges of chemical composition from very aluminous cores of big (7 to 1.5 mm) grains to chromiferous small (0.1 to 0.2 mm) grains which are mounted in plagioclase matrices, well documenting the chemical changes of spinels in the course of the transition from spinel- to plagioclase-peridotiteS. Spinels from plagioclase peridotites, are, as expected, the most chromiferous.

The ranges of the Fe^{3+} content in octahedral sites are 0 to 2.5 atomic percent for the garnet peridotites, 0 to 3 for the spinel peridotites, and 4 to 6 for the plagioclase peridotites.

The spinel analyses were averaged on different textural bases in each rock and are listed in Table 4-5.

Garnet

Compared with the pyroxenes and spinels, garnets are

Table 4-5. Average analyses of spinels from peridotites.

Rock no.	R501			R740	
	1	2	3	4	5
TiO_2	0.06	---	---	0.05	0.02
Al_2O_3	45.3	50.3	55.7	50.2	51.7
Cr_2O_3	24.2	19.1	13.1	18.4	17.5
FeO*	13.1	12.5	11.3	11.8	11.7
MnO	0.26	0.18	0.11	0.20	---
MgO	17.7	18.6	19.8	19.3	19.6
Total	100.6	100.7	100.0	100.0	100.4
Cations per 32 oxygens					
Al	11.63	12.62	13.69	12.62	12.86
Cr	4.17	3.22	2.16	3.10	2.91
Fe^{3+}	0.19	0.16	0.15	0.28	0.23
Ti	0.01	---	---	0.01	---
Sum Al to Ti	16.00	16.00	16.00	16.00	16.00
Fe^{2+}	2.20	2.06	1.83	1.83	1.84
Mg	5.76	5.91	6.16	6.14	6.16
Mn	0.05	0.03	0.02	0.04	---
Sum $^{+2}$ ions	8.00	8.00	8.00	8.00	8.00
$Al/(Al+Cr+Fe^{3+})$ %	72.8	78.9	85.5	78.9	80.0
$Cr/(Al+Cr+Fe^{3+})$ %	26.1	20.1	13.5	19.4	18.2
$Fe^{3+}/(Al+Cr+Fe^{3+})$%	1.2	1.0	0.9	1.7	1.4
$Mg/(Mg+Fe^{2+})$ %	72.4	74.1	77.1	77.0	77.0

* Total Fe as FeO.

Fe^{3+} was calculated assuming perfect stoichiometry of spinel.

Sums and the four parameters at the bottom of the columns were calculated before rounding off the numbers of each cations.

Table 4-5. (continued)

R696		R123	R196	R243	7319
6	7	8	9	10	11
0.04	---	0.06	0.05	0.09	0.09
54.5	60.0	58.4	55.7	58.7	43.1
14.1	8.3	9.8	11.8	9.7	25.3
12.0	11.1	12.1	11.0	11.0	13.1
0.22	0.17	0.15	0.20	0.13	0.35
19.4	20.5	19.6	20.8	20.3	18.3
100.2	100.1	100.2	99.6	99.9	100.1

Cations per 32 oxygens

13.47	14.48	14.23	13.65	14.26	11.15
2.33	1.35	1.60	1.94	1.57	4.39
0.19	0.17	0.15	0.40	0.15	0.44
0.01	---	0.01	0.01	0.01	0.02
16.00	16.00	16.00	16.00	16.00	16.00
1.92	1.73	1.94	1.51	1.75	1.96
6.05	6.25	6.03	6.45	6.23	5.97
0.04	0.03	0.03	0.04	0.02	0.07
8.00	8.00	8.00	8.00	8.00	8.00
84.2	90.5	89.0	85.4	89.2	69.8
14.6	8.4	10.0	12.1	9.8	27.5
1.2	1.1	0.9	2.5	0.9	2.7
75.9	78.3	75.6	81.0	78.1	75.3

Table 4-5. (continued)

R37		R131		R25	R346	R927
12	13	14	15	16	17	18
0.06	0.15	0.36	0.59	0.27	0.38	0.33
54.4	39.9	43.2	36.4	32.0	34.0	31.5
13.9	28.7	21.8	29.1	35.1	33.2	35.4
11.1	14.4	14.3	17.3	17.1	16.1	17.5
0.19	0.42	0.32	0.46	0.62	0.52	0.53
20.4	16.4	19.6	16.6	15.9	16.5	14.9
100.1	99.9	99.6	100.5	100.9	100.6	100.1

Cations per 32 oxygens

13.38	10.58	11.10	9.71	8.69	9.14	8.69
2.29	5.10	3.77	5.19	6.38	5.99	6.54
0.33	0.29	1.06	0.98	0.87	0.79	0.71
0.01	0.03	0.06	0.10	0.05	0.07	0.06
16.00	15.99	15.99	15.98	15.99	15.98	15.99
1.62	2.41	1.56	2.30	2.43	2.29	2.72
6.35	5.50	6.38	5.60	5.45	5.61	5.17
0.03	0.08	0.06	0.09	0.12	0.10	0.11
8.00	8.00	7.99	7.99	7.99	7.99	7.99
83.7	66.3	69.7	61.1	54.5	57.4	54.5
14.3	31.9	23.6	32.7	40.0	37.6	41.1
2.0	1.8	6.6	6.2	5.5	5.0	4.5
79.7	69.5	80.4	70.9	69.2	71.0	65.6

Table 4-5. Keys

1; Average of 8 medium-sized (~0.5mm) grains.

2; Average of 2 smaller (~0.1mm) grains.

3; Averages of 8 tiny grains (~20μ). 1, 2 and 3 all from garnet peridotite R501.

4; Average of 5 medium-sized grains (~1mm) and 6 small grains (~0.1mm).

5; Average of 4 tiny grains (~20μ). 4 and 5 from garnet peridotite R740.

6; Average of 7 medium-sized grains (0.3 1mm).

7; Average of 3 tiny grains (~30μ). 6 and 7 from garnet peridotite R696.

12; Average of 5 large garins (~1.5mm).

13; Average of five small grains (~0.1mm). 12 and 13 from transitional peridotite R37.

14; Average of 4 large grains (~1mm).

15; Average of 3 small (~0.2mm) grains. 14 and 15 from transitional peridotite R131.

The rest is averages of all grains in each sample.

relatively homogeneous. There are some compositional differences grain by grain, but, except for chromium, individual grains are rather homogeneous. The Fe/Mg ratio tends to slightly increase near the edges of the grains and Cr_2O_3 varies erratically as much as 20% (relative). There is no systematic difference in composition between larger (∿1 mm) and smaller (∿0.3 mm) grains. The average analyses for the four garnet peridotites are listed in Table 4-6. The garnets contain up to 70 mole percent pyrope. Their compositions are similar to those of garnets in peridotites found as nodules in kimberlite pipes and as massifs in Europe (references in Table 5-3). Among garnets in the four peridotites, CaO content varies from 4.6 wt. % to 5.1 wt. % and Cr_2O_3 content from 0.5 wt. % to 1.4 wt. %, and these two elements seem to vary sympathetically (see Table 4-6).

A question is whether the observed variation of the CaO content in the garnets is due to variation of physical conditions or due to the compositions of the rocks.

Theoretically, the CaO content in garnets which coexist with both ortho- and clinopyroxenes in the system $CaSiO_3$-$MgSiO_3$-Al_2O_3 is invariant at constant temperature and pressure (e.g. Boyd, 1970). This invariant relationship is valid even in the presence of small amounts of iron. Garnet coexisting with 2 pyroxenes will become pyrope-rich or less calcic as pressure increases because the volume change of the reaction:

$$1/3\ Ca_3Al_2Si_3O_{12} + Mg_2Si_2O_6 = 1/3\ Mg_3Al_2Si_3O_{12} + CaMgSi_2O_6$$

gar. opx. gar. cpx

Table 4-6. Analyses of garnets from peridotites.

Rock no.	R501	R740	R696	R123
SiO_2	42.37	42.42	42.64	41.79
TiO_2	0.17	0.17	0.15	0.30
Al_2O_3	22.46	22.58	22.83	22.90
Cr_2O_3	1.38	1.10	0.71	0.53
FeO*	8.50	8.01	9.23	9.22
MnO	0.41	0.35	0.37	0.32
MgO	20.56	20.27	20.06	19.82
CaO	5.04	5.01	4.74	4.65
Total	100.89	99.91	100.73	99.53
	Cations per 12 oxygens			
Si	2.994	3.014	3.015	2.991
Ti	0.009	0.009	0.008	0.016
Al	1.870	1.891	1.902	1.932
Cr	0.077	0.062	0.040	0.030
Fe*	0.502	0.476	0.546	0.552
Mn	0.025	0.021	0.022	0.019
Mg	2.165	2.147	2.114	2.115
Ca	0.382	0.381	0.359	0.357
Total	8.024	8.001	8.006	8.012
Ca	12.5	12.7	11.9	11.8
Mg	71.0	71.5	70.0	69.9
Fe	16.5	15.8	18.1	18.3
100Mg/(Mg+Fe)	81.2	81.9	79.5	79.3

is negative (Kushiro et al., 1967). It is not likely, however, that there is enough pressure difference among the four garnet peridotites from the Ronda massif to account for the apparent variation of the CaO contents in the garnets.

Natural garnet may contain significant amounts of Cr_2O_3 and this may affect the CaO content of the garnet. The Cr_2O_3 contents are quite variable in the garnets in peridotite nodules in kimberlites. Positive correlations between Cr_2O_3 and CaO contents in garnets which coexist with 2 pyroxenes have been noted by Sobolev et al. (1973) for Yakutian kimberlite nodules. The positive correlation is also apparent for South African kimberlite nodules (Fig. 4-9). The garnets from massif peridotites including the Ronda massif are more uniform in Cr_2O_3 and CaO contents than those from the kimberlite nodules, but they seem to fall on the general trend defined by the kimberlite nodules (Fig. 4-9). This correlation of CaO contents with Cr_2O_3 contents in garnets suggests that the observed CaO variation of the garnets is due to some coupling of the Ca atoms with the Cr atoms in the garnet structures and does not necessarily reflect a variation in the physical condition.

Amphibole

Chemical analyses of the amphiboles from 4 garnet peridotites and 2 spinel peridotites are listed in Table 4-7. Little variation was found in the probe analyses, although the study was not as thorough as that done of other minerals. These

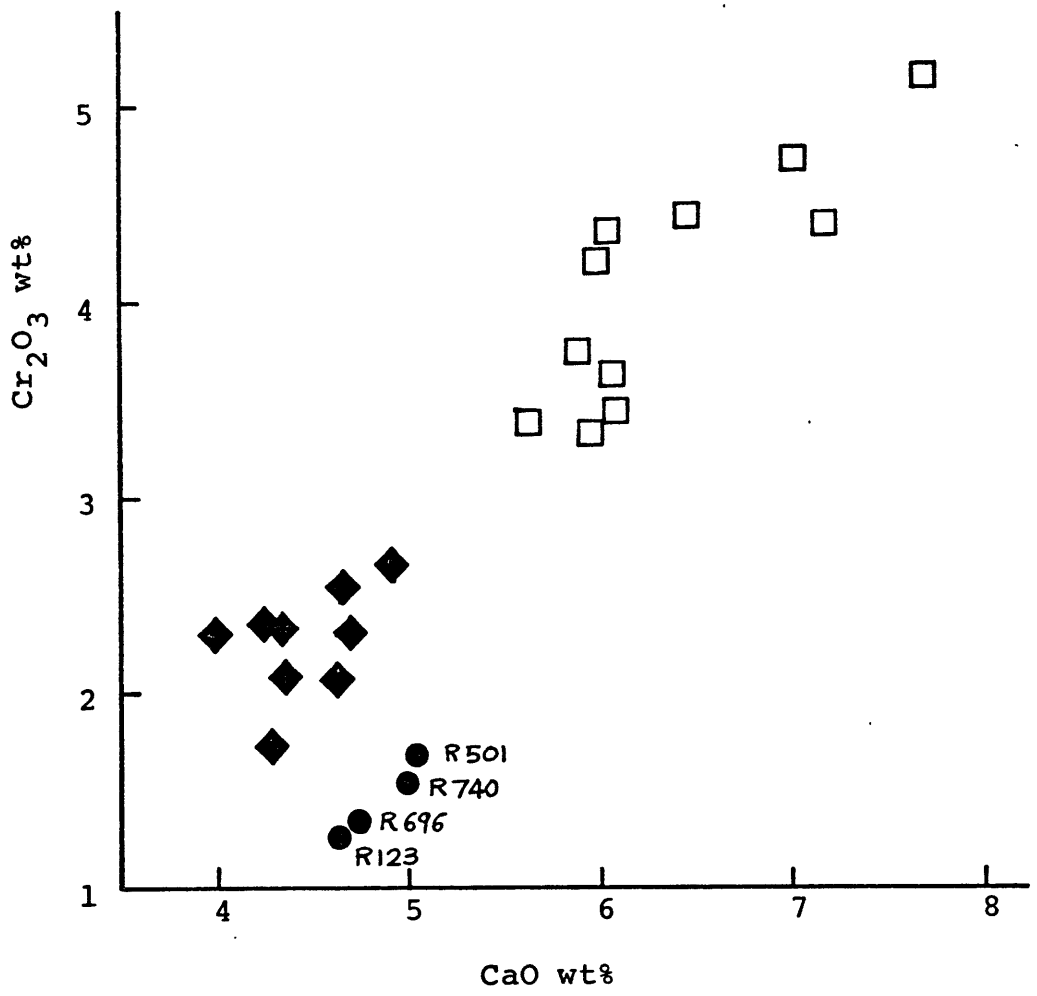

Figure 4-9. CaO-Cr_2O_3 relation of garnets coexisting with ortho- and clinopyroxenes. Open squares = granular nodules in kimberlites; solid diamonds = sheared nodules in kimberlites (Nixon and Boyd, 1974); solid cirles = Ronda peridotite.

Table 4-7. Average analyses of amphiboles from peridotites.

	R501	R740	R696	R123	R243	7319
SiO_2	43.65	43.58	43.65	43.34	44.27	42.58
TiO_2	1.96	2.35	2.72	2.95	2.87	1.87
Al_2O_3	15.15	14.62	13.81	15.08	14.03	14.11
Cr_2O_3	1.20	1.05	1.03	0.84	0.97	1.86
FeO*	3.45	3.40	4.16	4.24	3.70	3.12
MnO	0.05	0.07	0.06	0.07	0.09	0.07
MgO	17.68	18.20	17.70	16.99	17.35	18.55
CaO	11.28	11.49	11.12	11.19	11.99	11.96
Na_2O	3.68	3.47	3.25	4.06	3.20	3.64
K_2O	0.00	n.d.	n.d.	n.d.	n.d.	n.d.
Total	98.10	98.23	97.50	98.76	98.47	97.76
	Cations per 23 oxygens					
Si	6.145	6.131	6.197	6.092	6.216	6.053
Ti	0.207	0.249	0.290	0.312	0.303	0.200
Al	2.514	2.425	2.311	2.499	2.323	2.365
Cr	0.134	0.117	0.116	0.093	0.108	0.209
Fe	0.406	0.400	0.494	0.498	0.435	0.371
Mn	0.006	0.008	0.007	0.008	0.011	0.008
Mg	3.710	3.816	3.745	3.559	3.631	3.930
Ca	1.701	1.732	1.692	1.685	1.804	1.822
Na	1.004	0.947	0.895	1.107	0.871	1.003
K	0.000	n.d.	n.d.	n.d.	n.d.	n.d.
Total	15.827	15.823	15.747	15.854	15.701	15.962
Al^4	1.855	1.869	1.803	1.908	1.784	1.947
Al^6	0.659	0.555	0.508	0.590	0.539	0.417
$Mg/_{(Mg+Fe)}$	0.901	0.905	0.883	0.877	0.893	0.914

amphiboles are all composed of paragasitic hornblende with rather high titanium and chromium contents. Pargasitic hornblende is a common accessory mineral in recrystallized spinel peridotite massifs; e.g., Tinaquilo, Venezuela (MacKenzie, 1960), Lizard, England (Green, 1963), St. Paul's Rock in the South Atlantic (Melson et al., 1967), S.W. Oregon, U.S. (Medaris, 1975), and in some garnet peridotite massifs; e.g. Norway (O'Hara and Mercy, 1963; Carswell, 1968), Czeckoslavakia (Kopecky, 1966), Switzerland (Möckel, 1969). Although it is not as common as in massif peridotites, pargasitic hornblende does occur in some peridotite nodules with metamorphic textures (Varne, 1970; Griffin, 1973; Aoki, 1973; Best, 1974; Frey and Green, 1974; Francis, 1976).

In the peridotite nodules in kimberlite, pargasitic hornblende has been found only in symplectic intergrowth with spinel (Boyd, 1971) and euhedral amphiboles are potassic richterite (Erlank and Finger, 1970; Erlank, 1973; Aoki, 1974). The pargasites in kimberlite xenoliths invariably contain small amounts of K_2O (typically 0.1 to 0.5 wt. %). The pargasites from the Ronda peridotite, however, do not have detectable amounts of K_2O (i.e. below 0.01 wt. %).

Olivine

The Mg/(Mg+Fe) ratios of olivines from the 12 peridotites are given in Table 4-1a. Individual olivine grains are homogeneous (within the analytical precision). There are no systematic differences in terms of Fo content between big grains and

small grains. This may mean either that the olivines were homogenized by diffusion during recrystallization or that they were homogeneous initially and the Fo content did not change with physical conditions. The second possibility may be correct because the Fe-Mg partitioning between olivine and orthopyroxene, which is the second most abundant phase in the peridotites, is not sensitive to temperature (Matsui and Nishizawa, 1974). The 12 microprobe analyses (Table 4-1) and 30 olivine analyses (Dickey, 1970) determined by x-ray diffraction method are summarized in a frequency diagram in Fig. 4-10. The Fo content ranges from 91.5 to 87 in mole per cent. As pointed out by Dickey (1970), the olivines from the peridotites associated with the mafic layers (i.e. within a few meters from the mafic layers) are statistically slightly more Fe-rich than the olivines from the peridotites away from the mafic layers.

4.2 Mafic Layers

Coexisting minerals were analyzed in 3 plagioclase-garnet clinopyroxenites (R127, R253, R560), 1 quartz-bearing plagioclase clinopyroxenite (R410), 1 garnet websterite (R554), 1 garnet clinopyroxenite (R525), 1 spinel pyroxenite (R251), and 2 olivine gabbros (R120, R343) (sample locations in Fig. 4-1). The analyses are listed in Table 4-8. Where 2 analyses of the same mineral with different compositions from the same thin section are reported, they are numbered in chronological order of recrystallization, cpx-1, cpx-2, etc., based on

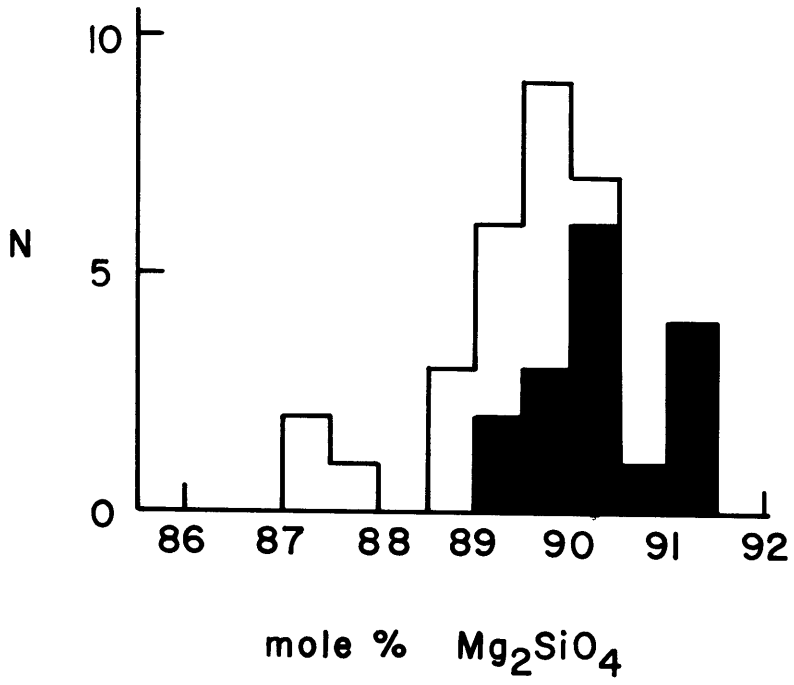

Figure 4-10. Compositions of olivines from peridotite with no magmatic mafic layers (black), peridotite with magmatic mafic layers (white).

Table 4-8. Average analyses of minerals in mafic layers.

Rock no.	R127			
Minerals	Cpx-1	Gar-1	Cpx-2	Gar-2
SiO_2	48.79	40.77	48.30	40.50
TiO_2	1.50	0.16	1.00	0.0
Al_2O_3	8.17	22.46	9.50	23.00
Cr_2O_3	0.13	0.12	0.10	0.10
FeO*	7.04	16.73	4.70	17.50
MnO	0.14	0.36	0.10	0.40
MgO	12.66	12.62	12.90	13.00
CaO	20.60	7.42	22.50	6.00
Na_2O	1.02	0.0	0.70	n.d.
Total	100.05	100.64	99.80	100.50

Numbers of cations for n oxygens

n=	6	12	6	12
Si	1.803	3.007	1.777	2.989
Ti	0.042	0.009	0.028	0.0
Al	0.356	1.953	0.412	2.002
Cr	0.004	0.007	0.003	0.006
Fe^{3+}	---	---	---	---
Fe^{2+}	0.218	1.032	0.145	1.080
Mn	0.004	0.022	0.003	0.025
Mg	0.697	1.387	0.707	1.430
Ca	0.816	0.586	0.887	0.475
Na	0.073	0.0	0.050	n.d.
Total	4.012	8.004	4.012	8.007
$Mg/_{(Mg+Fe)}$	76.2	57.3	83.0	57.0

Table 4-8. (continued)

Rock no.	R253				
Minerals	Cpx-1	Gar	Opx	Cpx-2	Ol
SiO_2	49.49	39.99	52.84	52.13	33.70
TiO_2	1.27	0.26	0.12	0.41	n.d.
Al_2O_3	7.97	22.01	2.89	2.90	n.d.
Cr_2O_3	0.15	0.05	0.0	0.0	n.d.
FeO*	7.35	19.85	19.69	6.81	42.30
MnO	0.06	0.50	0.51	0.22	1.10
MgO	13.04	11.67	23.68	14.48	23.70
CaO	19.28	5.75	0.70	22.48	n.d.
Na_2O	1.27	n.d.	0.02	0.48	n.d.
Total	99.88	100.08	100.45	99.91	100.80

Number of cations for n oxygens

n=	6	12	6	6	4
Si	1.825	3.001	1.934	1.931	0.970
Ti	0.035	0.015	0.003	0.011	n.d.
Al	0.347	1.947	0.125	0.127	n.d.
Cr	0.004	0.003	0.001	0.0	n.d.
Fe^{3+}	---	---	---	---	---
Fe^{2+}	0.227	1.246	0.603	0.211	1.018
Mn	0.002	0.032	0.016	0.007	0.027
Mg	0.717	1.305	1.292	0.799	1.016
Ca	0.762	0.462	0.027	0.892	n.d.
Na	0.091	n.d.	0.001	0.034	n.d.
Total	4.009	8.010	4.001	4.012	3.030
$Mg/_{(Mg+Fe)}$	76.0	51.2	68.2	79.1	50.0

Table 4-8. (continued)

Rock no.	R554			R525		
Minerals	Opx	Cpx	Gar	Cpx	Gar-1	Gar-2
SiO_2	55.04	53.35	41.25	52.13	39.17	39.42
TiO_2	0.07	0.93	0.10	0.55	0.13	0.12
Al_2O_3	2.89	6.98	23.32	5.16	22.45	22.49
Cr_2O_3	0.01	0.14	0.11	0.10	0.11	0.09
FeO*	11.51	4.47	14.80	7.87	21.76	20.56
MnO	0.20	0.08	0.55	0.08	0.54	0.52
MgO	29.29	13.65	15.53	13.00	9.38	10.10
CaO	0.51	17.95	4.23	18.54	6.08	6.40
Na_2O	0.10	2.87	0.09	2.02	0.05	0.05
Total	99.62	100.42	99.98	99.45	99.67	100.05
Number of cations for n oxygens						
n=	6	6	12	6	12	12
Si	1.949	1.919	3.007	1.929	2.983	2.996
Ti	0.002	0.025	0.005	0.015	0.007	0.007
Al	0.121	0.296	2.004	0.225	2.016	2.000
Cr	0.000	0.004	0.006	0.003	0.007	0.005
Fe^{3+}	---	---	---	---	---	---
Fe^{2+}	0.341	0.134	0.902	0.244	1.386	1.297
Mn	0.006	0.002	0.034	0.003	0.035	0.033
Mg	1.546	0.732	1.687	0.717	1.065	1.135
Ca	0.019	0.692	0.330	0.735	0.496	0.517
Na	0.007	0.200	0.013	0.145	0.007	0.007
Total	3.992	4.006	7.989	4.015	8.002	7.998
$Mg/_{(Mg+Fe)}$ %	81.9	84.5	65.2	74.6	43.4	46.7

Table 4-8. (continued)

Rock no.	R410		R560			
Mineral	Cpx	Gar	Cpx-1	Gar	Opx	Cpx-2
SiO_2	50.33	41.73	49.78	41.94	53.89	52.42
TiO_2	0.38	0.03	0.25	0.03	0.05	0.27
Al_2O_3	11.29	23.15	10.54	24.13	4.10	4.93
Cr_2O_3	0.16	0.16	0.20	0.23	0.16	0.43
FeO*	2.52	9.66	2.59	8.89	10.79	2.62
MnO	0.08	0.22	0.02	0.16	0.20	0.06
MgO	13.27	16.04	14.00	18.93	30.53	16.00
CaO	21.07	9.24	21.22	6.47	0.46	22.05
Na_2O	1.86	n.d.	1.44	n.d.	0.02	1.02
Total	100.96	100.23	100.04	100.78	100.20	99.80
Number of cations for n oxygens						
n=	6	12	6	12	6	6
Si	1.801	3.004	1.799	2.968	1.896	1.904
Ti	0.010	0.002	0.007	0.002	0.001	0.007
Al	0.476	1.965	0.449	2.013	0.170	0.211
Cr	0.005	0.009	0.006	0.013	0.004	0.012
Fe^{3+}	---	---	---	---	---	---
Fe^{2+}	0.075	0.582	0.078	0.526	0.318	0.080
Mn	0.002	0.013	0.001	0.010	0.006	0.002
Mg	0.707	1.721	0.754	1.996	1.601	0.866
Ca	0.808	0.713	0.822	0.491	0.017	0.858
Na	0.129	n.d.	0.101	n.d.	0.001	0.072
Total	4.013	8.008	4.017	8.018	4.016	4.013
$Mg/_{(Mg+Fe)}$ %	90.4	74.7	90.6	79.1	83.4	91.6

Table 4-8. (continued)

Rock no.	R251					
Monerals	Opx-1	Cpx-1	Sp-1	Opx-2	Cpx-2	Sp-2
SiO_2	53.49	48.51	0.15	53.80	49.22	0.58
TiO_2	0.33	1.37	0.16	0.25	1.35	0.16
Al_2O_3	5.19	10.28	64.21	3.07	5.48	61.58
Cr_2O_3	0.06	0.05	0.39	0.04	0.08	0.32
FeO*	12.78	5.03	18.75	12.92	5.13	21.71
MnO	0.25	0.11	0.15	0.25	0.14	0.13
MgO	27.01	12.66	16.83	29.36	15.23	14.81
CaO	0.61	21.28	0.02	0.89	21.29	0.24
Na_2O	0.04	1.03	n.d.	0.04	0.74	0.0
Total	99.76	100.32	100.66	100.62	98.66	99.53
Number of cations for n oxygens						
n=	6	6	32	6	6	32
Si	1.904	1.772	0.031	1.908	1.836	0.122
Ti	0.009	0.038	0.025	0.007	0.038	0.025
Al	0.218	0.443	15.490	0.128	0.241	15.229
Cr	0.002	0.001	0.063	0.001	0.002	0.053
Fe^{3+}	---	---	0.378	---	---	0.534
Fe^{2+}	0.380	0.154	2.830	0.383	0.160	3.275
Mn	0.008	0.003	0.026	0.008	0.004	0.023
Mg	1.433	0.689	5.132	1.551	0.846	4.630
Ca	0.023	0.833	0.004	0.034	0.851	0.054
Na	0.003	0.073	n.d.	0.003	0.054	n.d.
Total	3.979	4.005	23.979	4.022	4.032	23.945
$Mg/_{(Mg+Fe)}$ %	79.0	81.8	64.5	80.2	84.1	58.6

Table 4-8. (continued)

Rock no.	R120				R343	
Minerals	Opx	Cpx	Ol	Amp	Opx	Cpx
SiO_2	55.04	51.65	41.07	42.47	54.63	52.85
TiO_2	0.37	1.20	n.d.	3.95	0.04	0.11
Al_2O_3	2.57	3.93	n.d.	12.71	2.04	3.02
Cr_2O_3	0.21	0.45	0.01	1.05	0.43	0.71
FeO*	8.90	3.75	13.50	6.17	10.49	4.55
MnO	0.28	0.17	0.28	0.10	0.28	0.18
MgO	31.84	16.41	46.36	17.04	31.14	16.74
CaO	0.77	22.62	0.01	11.14	0.85	20.42
Na_2O	0.02	0.63	n.d.	3.41	0.01	0.38
Total	100.00	100.81	101.26	98.04	99.91	98.96
Number of cations for n oxygens						
n=	6	6	4	23	6	6
Si	1.927	1.876	1.009	6.087	1.931	1.943
Ti	0.010	0.033	n.d.	0.426	0.001	0.003
Al	0.106	0.168	n.d.	2.147	0.085	0.131
Cr	0.006	0.013	0.000	0.119	0.012	0.021
Fe^{3+}	---	---	---	---	---	---
Fe^{2+}	0.261	0.114	0.277	0.740	0.310	0.140
Mn	0.008	0.005	0.006	0.012	0.008	0.006
Mg	1.661	0.888	1.697	3.640	1.640	0.917
Ca	0.029	0.880	0.000	1.711	0.032	0.804
Na	0.001	0.044	n.d.	0.948	0.001	0.027
Total	4.008	4.023	2.991	15.828	4.020	3.992
$Mg/_{(Mg+Fe)}$ %	86.4	88.6	86.0	83.1	84.1	86.8

Description of Analyses

R127, plagioclase-garnet clinopyroxenite; Mode[1]: 5% gar, 11% kelyphite, 61% Cpx, 23% Plag. The texture is xenomorphic granular with garnets (0.2 to 5 mm), pale brown clinopyroxene (∿0.4 mm) and interstitial plagioclase (An_{40}). Both clinopyroxenes and plagioclases are strained. The clinopyroxenes lack apparent exsolution lamellae. Kelyphite rims on the garnets are described in Petrography (p. 37). "Cpx-1" and "Gar-1" are average analyses of the clinopyroxenes and the garnets. At rare direct contacts of Cpx/Gar grain boundaries at which no kelyphite has developed Al_2O_3 and the Mg/Fe ratio increase, and CaO in the garnet decreases toward the contacts. The compositions, "Cpx-2" and "Gar-2" represent an equilibrium pair, determined by extrapolation of microprobe point traverses extending toward but not actually to the boundary.

R253, plagioclase garnet clinopyroxenite; Mode: 4% Gar, 23% Cpx, 7% Plag, 1% opaques, 66% fine-grain matrix. The texture is mylonitic. Pale brown pleochroic clinopyroxenes (0.2 to 0.4 mm) and colorless garnets (∿0.8 mm) float in a fluid groundmass which is banded with plagioclase layers and extremely fine grained (∿10μ) aggregates of orthopyroxene, clinopyroxene, olivine, plagioclase, and sulfides parallel to

---

[1] Mode of R127, R251, R120, and R343 are from Dickey (1970); R554, R525 from Lundeen (1976).

the layer. The garnets do not have kelyphite rims. Some clinopyroxenes have thin plagioclase lamellae (<5μ). "Cpx-1" and "Gar" are average analyses of the larger grains and "Opx", "Cpx", and "Ol" are analyses of small (∿10μ) orthopyroxene, clinopyroxene, and olivine which coexist in a small area (<0.1 mm) of the groundmass.

R554, garnet websterite; Mode: 23% Gar, 58% pyroxenes, 3% opaques, 17% sedimentary alterations. The texture is xenomorphic granular with a foliation due to flattening of garnet and pyroxene grains. Big garnets (3-4 mm) lie mounted in a mosaic matrix of medium-sized (0.2-0.4 mm) colorless garnet, orthopyroxene, and clinopyroxene. The garnets do not have kelyphite rims. The pyroxenes are typically free from exsolution lamellae. Grain boundaries are fuzzy due to late stage recrystallization. Small interstitial brown pleochroic amphiboles (0.05 to 0.2 mm) are ubiquitous. Other accessories are ilmenite, rutile, and sulfides. The ilmenite and the rutile closely contact each other. "Opx", "Cpx", and "Gar" are average analyses of orthopyroxene, clinopyroxene, and garnet. There is no compositional difference between the big grains and the small grains of the garnets. High Na_2O content in the clinopyroxene is noticeable.

R525, garnet clinopyroxenite; Mode: 20% Gar, 80% Cpx, tr opaques. Texture and grain sizes are similar to that of R554. Garnets are free from kelyphitic rims. The grain boundaries in the matrix are clear and straight. Pyroxene inclusions and rutile needles are common in the big garnets.

The matrix is an equigranular mosaic of garnet and clinopyroxene with accessory rutile, ilmenite, and sulfides. Neither orthopyroxene nor amphibole are present. "Cpx" and "Gar-2" are average analyses of the clinopyroxene and the small garnet in the matrix. "Gar-1" is an average analysis of the big garnets. The small garnets are slightly more iron-rich and less calcic than the big ones. The "Gar-2" is paired with "Cpx" in discussions of element partitioning below. The Na_2O is also high in the clinopyroxene.

R410, quartz-bearing plagioclase garnet clinopyroxene, light grey, medium-sized granulite; Mode: 5 % Gar, 15% kelyphite, 52% Cpx, 15% Plag, 5% Qz, tr opaque, 8 % secondary recrystallization. The garnet is pinkish in hand specimen. The texture is xenomorphic granular with weak foliation due to plagioclase concentrations, parallel to the layering. Medium-sized (∿0.8 mm) colorless garnets are evenly distributed in a fine-grained (∿0.2 mm) matrix of garnet, clinopyroxene, plagioclase, and minor quartz. The textural relationship of the quartz was described in Petrography (p. 37).

The garnets have kelyphite rims (up to 0.2 mm thick), and have no inclusions. "Cpx" and "Gar" are average analyses of the clinopyroxenes and the garnets. Both the garnets and the clinopyroxenes are rather homogeneous, although the plagioclases are inhomogeneous (An_{40-56}).

R560, plagioclase garnet clinopyroxenite; Mode: 3 % Gar, 27 % kelyphite, 57% Cpx,13 % Plag, tr opaque. Appearance of the hand specimen and the microscopic texture are similar to

R410. The texture is xenomorphic granular with almost completely kelyphititized garnet (0.2 mm to 1 mm), clinopyroxene (0.2 mm to 0.4 mm), and interstitial plagioclase ($\sim An_{55}$), without quartz. The pyroxenes are locally recrystallized to a fine-grained (<40μ) mosaic of Al-poor clinopyroxenes and orthopyroxenes. The clinopyroxenes are typically zoned from Al- and Na-rich cores to Al- and Na-poor rims. "Cpx-1" is an average analysis of the cores of several big clinopyroxenes, and "Gar" is an average of the garnet analyses. "Opx" and "Cpx-2" are analyses of small (∿20μ), later-recrystallized ortho- and clinopyroxenes next to each other. Much reduction of Al_2O_3 in the clinopyroxenes during recrystallization is noticeable.

R251, spinel plagioclase pyroxenite, dark colored coarse pyroxenite; Mode: 78% Cpx, 3% Opx, 8% Sp, 7% Plag, 4% Ol, tr ilmenite. This rock was described in Petrography (p. 40). "Opx-1" is an analysis of a core of sparce medium-sized orthopyroxene (2 mm); "Cpx-1" is an analysis of a core of big clinopyroxene (∿1 cm) away from plagioclase lamellae; "Sp-1" is an analysis of a big interstitial (∿1 mm) green spinel. "Opx-2" and "Sp-2" are average analyses of the lamellae of orthopyroxene and spinel, which are closely associated together with a plagioclase (An_{70}) in a big clinopyroxene (see Fig. 3-13. on p. 41). The clinopyroxene is strongly zoned in Al_2O_3. "Cpx-2" is an analysis of the host clinopyroxene close to the lamellae. Thus, "Opx-2", "Cpx-2", "Sp-2", and An_{70} for plagioclase are thought to be the equilibrium compositions. The lamellae spinels have slightly higher SiO_2, CaO, Fe^{3+},

and lower Al_2O_3 than the larger interstitial spinels. The large orthopyroxenes are very inhomogeneous but the lamellae orthopyroxenes are homogeneous.

R120, olivine gabbro; Mode: 23% Cpx, 33% Plag, 27% Ol, 3% Sp, 12% Opx, 2% secondary alterations. The texture is gneissic, with plagioclase and pyroxene-rich bands parallel to the layering. Pale brown, large elongated clinopyroxenes (up to 4 mm long) lie subparallel to the foliation in a mosaic matrix of equigranular (∿0.3 mm) olivine, plagioclase (An_{76}), orthopyroxene, clinopyroxene, and greenish brown to brown spinel. The large clinopyroxenes are strongly deformed and either contain thick orthopyroxene exsolution lamellae (∿40μ) or are split apart by lamellae or aggregates of olivine and plagioclase. The small pyroxenes are free from exsolution lamellae. Accessories are small (∿0.2 mm) interstitial brown hornblende and some opaques including sulfides. "Opx", "Cpx", "Ol", and "Amph" are average analyses of the small orthopyroxene, clinopyroxene, olivine, and amphibole, which closely equilibrated in a small area (<2 mm) of the matrix.

R343, olivine gabbro, dark green massive rock with bright green chromian diopside; Mode: 24% Ol, 23% Cpx, 15% Opx, 36% Plag, <1% chromite. The texture is xenomorphic granular (0.05-1.3 mm) with olivine (Fo_{79}), plagioclase (An_{88}), orthopyroxene, clinopyroxene, and small and trace amounts of dark-brown spinel. No amphibole is present. Both ortho- and clinopyroxenes have thin exsolution lamellae of each other. "Opx" and "Cpx" are an equilibrium pair of homogeneous pyroxenes in contact.

Garnet-Pyroxene Relations

The compositions of minerals are quite variable, reflecting the variation of the bulk compositions of the host rocks and of the equilibrium conditions. The compositions of the coexisting garnets and pyroxenes are graphically expressed in A-C-F and Ca-Mg-Fe diagrams (Fig. 4-11 and 4-12), and compared with average garnet and pyroxenes of the 4 garnet peridotites. Additional 28 garnets, hand-picked from various types of garnet pyroxenites, were analyzed to examine the range of chemical compositions of the garnet pyroxenite group. They are also plotted in the Ca-Mg-Fe triangles in Fig. 4-12. Some garnet-clinopyroxene tie lines cross each other, probably due to the oversimplified graphical method. The garnets from the mafic layers cover a wide range of Mg/(Mg+Fe) ratio (0.83 to 0.42). Some mafic layers are more magnesian than the peridotites. The Ca value of the garnets which coexist with both ortho- and clinopyroxenes are more or less constant around 11% over a wide range of Mg/(Mg+Fe) ratio. The garnets which do not coexist with orthopyroxenes are all more calcic than those in the websterites. There is no apparent systematic chemical difference between the two groups, Gar + Cpx and Gar + Cpx + Plag $\pm$ Qz.

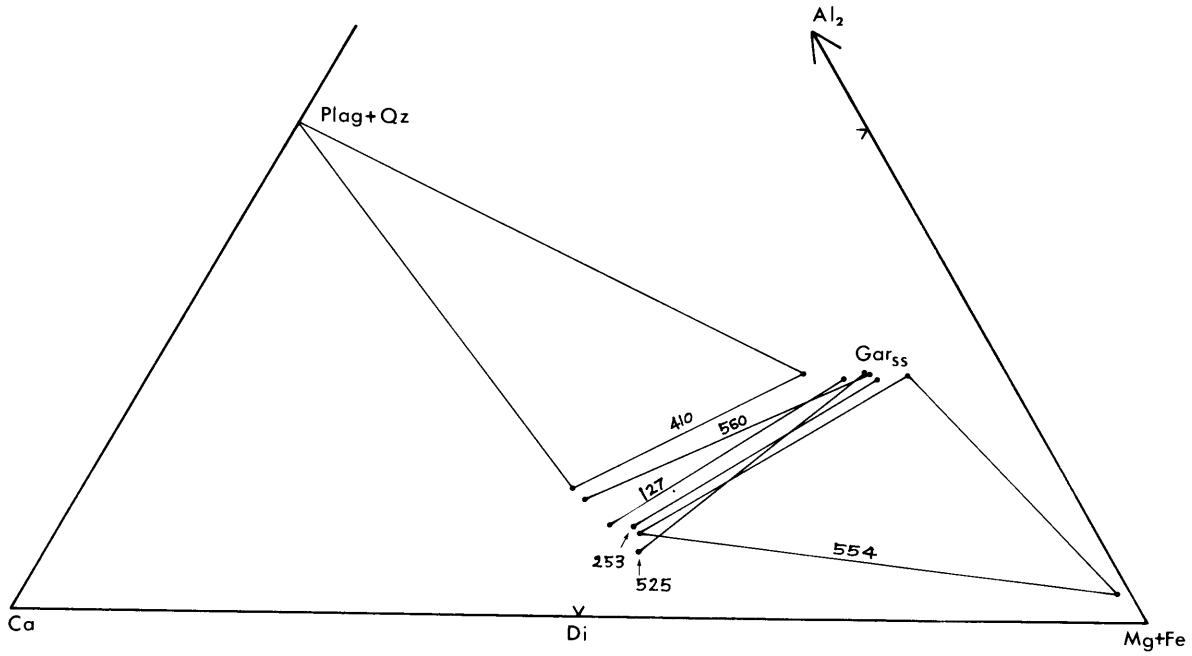

Figure 4-11 A-C-F plot of garnets and pyroxenes of mafic layers.

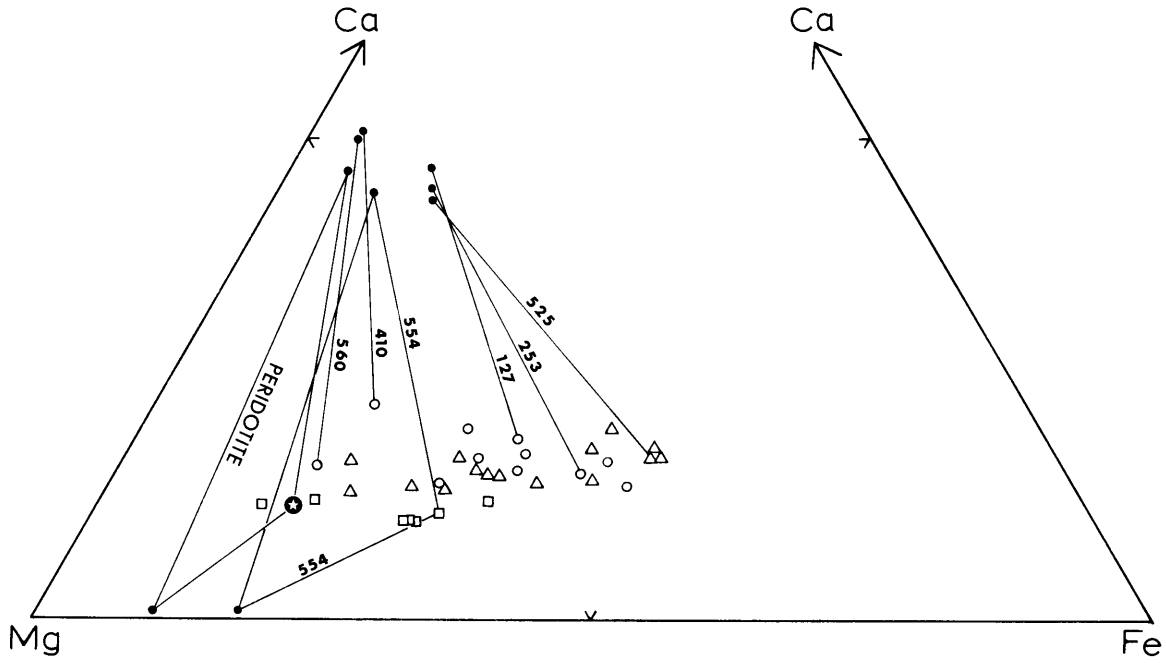

Figure 4-12. Ca-Mg-Fe plot of garnets and pyroxenes of mafic layers and average garnet peridotites.

Chapter 5

EQUILIBRIUM CONDITIONS

In this chapter, equilibrium conditions of the peridotites and mafic layers are discussed on the basis of the petrography and mineral chemistry. A single rock may record more than one P-T condition, and this may provide useful information about the P-T history of the massif. Latest recorded P-T conditions may be obtained from neoblast compositions. Earlier P-T conditions may be obtained from compositions of porphyroclasts in the same rocks.

5.1 Temperatures of Recrystallization

Current methods of estimating equilibration temperatures of peridotites and related rocks may be classified in the following categories[1]:

1) Mutual solubilities of diopside and enstatite.

2) Solubility of Al_2O_3 in pyroxenes in spinel lherzolites.

3) Fe-Mg partitioning between minerals.

4) Cr-Al partitioning between pyroxenes.

With the equilibration temperatures estimated, the equilibration pressure may be obtained from the Al_2O_3 content in orthopyroxenes in garnet peridotites (Boyd, 1970) or in plagioclase peridotites (Obata, 1976).

---

[1] References will appear later in each discussion.

1) Mutual solubilities of enstatite and diopside

The mutual solubilities of enstatite and diopside increase primarily with temperature (Boyd and Schairer, 1964). The solubility of enstatite in diopside solid solution, particularly, has been much used as a geothermometer (e.g. Boyd, 1973). However, recent refinements of the phase diagram of the enstatite-diopside system at high pressures (Warner and Luth, 1974; Nehru and Wyllie, 1974; Mori and Green, 1975, 1976; Lindsley and Dixon, 1976) demonstrate larger pressure effects on the pyroxene solvus than had previously been assumed by Boyd (1973).

The observed steady increase of CaO content in the orthopyroxene neoblasts from the garnet peridotites to the plagioclase peridotites going east across the Ronda massif (Fig. 4-6) may thus be attributed either to a steady increase of temperature or a decrease of pressure, or both.

The solubility of enstatite in clinopyroxene as expressed by Ca/(Ca+Mg), however, does not parallel the variation of CaO in the coexisting orthopyroxenes (see Table 5-1). The Ca/(Ca+Mg) ratio of the clinopyroxenes is quite constant in the spinel peridotites in the middle of the massif and decreases slightly in some garnet- and plagioclase peridotites.

In order to interpret the variation of these parameters in terms of temperature and/or pressure, we must know the effects of other components present in the natural rocks, particularly

the effects of FeO and Al_2O_3 on the enstatite-diopside solvus. The enstatite limb of the solvus in the system $CaSiO_3$-$MgSiO_3$-$FeSiO_3$ is nearly parallel to the enstatite-ferrosilite join over a wide range of Fe/Mg ratios at 810°C to 1200°C (Lindsley et al., 1974a,b; Mori and Green, 1977a) so the Ca/(Ca+Mg+Fe) ratio (Table 5-1) may be substituted for the Ca/(Ca+Mg) ratio in the Fe-free system. The effect of Al_2O_3 is less well known: The Ca/(Ca+Mg) ratio in orthopyroxene coexisting with garnet and clinopyroxene in the system $CaSiO_3$-$MgSiO_3$-Al_2O_3 (Boyd, 1970; Akella, 1974) is nearly equal to that of orthopyroxene coexisting with diopside solid solution in the Al-free system at 1200 to 1300°C, 26 to 38 kb. Herzberg and Chapman (1976) and Mori (1977) , however, experimentally demonstrated that the CaO content in the orthopyroxene in spinel lherzolite in the system CaO-MgO-Al_2O_3-SiO_2 was significantly reduced from the value in the Al-free system at the same physical condition. It appears, therefore, that the effect of Al_2O_3 upon the CaO content in orthopyroxene coexisting with clinopyroxenes may also be a function of pressure and temperature. Because of the present uncertainty, the Ca/(Ca+Mg+Fe) ratios were chosen for direct comparisons of the natural rocks with the phase diagrams in the enstatite-diopside system.

CaO isopleths of orthopyroxene coexisting with clinopyroxene were constructed in a pressure-temperature diagram in Fig. 5-1, based on recent experiments on the enstatite-diopside system (Mori and Green, 1975; Lindsley and Dixon, 1976). A value of

Table 5-1. Geothermometers.

	Opx	Cpx						
	$\frac{Ca}{Ca+Mg+Fe}$	$\frac{Ca}{Ca+Mg}$	$\frac{Ca}{Ca+Mg+0.5Al}$	$K^{opx/cpx}_{Fe/Mg}$	$K^{gar/cpx}_{Fe/Mg}$	$K^{ol/cpx}_{Fe/Mg}$	$K^{opx/cpx}_{Al/Cr}$ ($T^{\circ}C$)	Ol-Sp($T^{\circ}C$)
R501	0.82	47.8	44.6	1.20	2.57	1.21	1.77 (949)	800-900
R740	0.82	48.6	45.5	1.25	2.53	1.17	1.90 (922)	800-900
R696	0.81	49.5	45.5	1.17	2.44	1.12	1.56(1000)	850-950
R123	0.88	49.9	45.2	1.05	2.16	1.16	1.24(1105)	800-950
R196	1.09	49.8	46.0	1.16	---	1.16	1.36(1060)	900-1000
R243	0.91	49.1	45.0	1.05	---	1.07	1.53(1008)	800-900
7319	1.37	49.1	45.8	1.06	---	1.05	1.60(989)	800-900
R37	1.39	49.7	47.3	1.21	---	1.25	1.16(1138)	800-850
R131	1.54	49.2	46.1	1.07	---	1.05	1.15(1143)	850-900
R25	1.41	46.1	44.5	1.21	---	1.22	1.53(1008)	900-950
R346	1.66	47.4	45.2	1.25	---	1.24	1.47(1025)	900-950
R927	1.40	48.6	47.0	1.23	---	1.28	1.57(997)	850-900

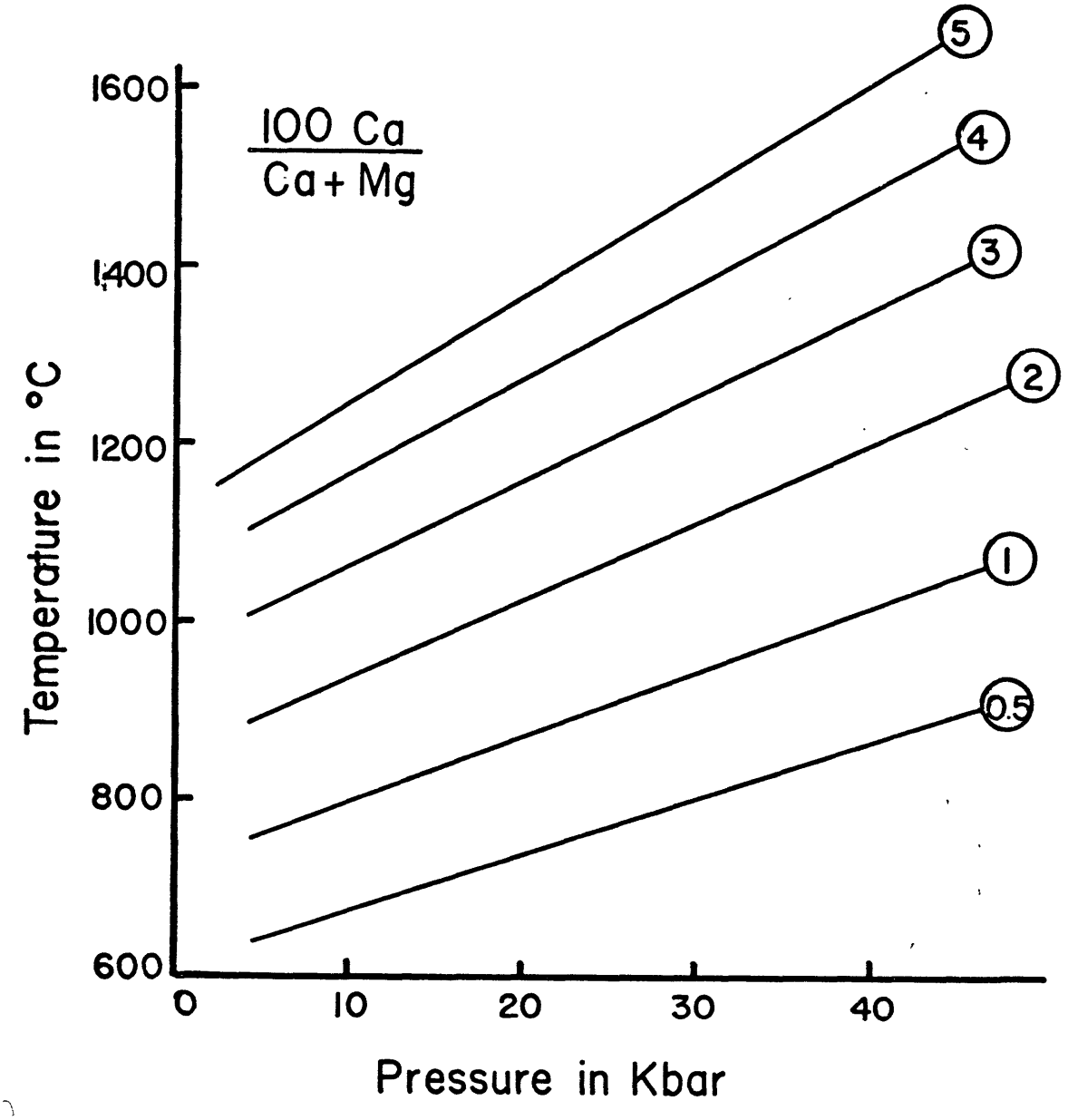

Figure 5-1. Isopleths of 100 Ca/(Ca+Mg) of enstatite coexisting with diopside in the $MgSiO_3$- $CaMgSi_2O_6$ system. Constructed from Mori and Green (1975),and Lindsley and Dixon (1976).

0.8 for 100 Ca/(Ca+Mg+Fe) of the orthopyroxene neoblasts in the garnet peridotite corresponds to temperatures around 900°C at 30 kbar or 1100°C at 10 kbar. A pressure difference of 20 kbar results in as much as 200°C difference in the temperature estimation. A value of 1.5, which is an average for orthopyroxenes in the plagioclase peridotites, corresponds to 1000°C and 900°C at 30 kbar and 10 kbar, respectively. A pressure difference of 20 kbar may account for the whole range of CaO content in the orthopyroxenes from garnet to plagioclase peridotites at more or less constant temperature (900°C).

The estimated temperature may bear large uncertainties, however, because the diopside solubility in enstatite becomes so insensitive to temperatures at these low temperatures that the analytical uncertainty and erroneous correction of the Al_2O_3-effect on the geothermometer may propagate into significant errors.

In the case of clinopyroxene, there are more ambiguities in the application of phase diagrams of simple systems to natural rocks because the chemistry of clinopyroxenes is more complex than that of orthopyroxenes. Unlike the orthopyroxene limb of the solvus, the solubility of enstatite in clinopyroxene as expressed by the Ca/(Ca+Mg+Fe) ratio increases markedly as Fe/Mg increases at constant T and P (Lindsley et al., 1974a,b; Mori and Green, 1977a). It would be more accurate, therefore, to apply the Ca/(Ca+Mg) ratio rather than the Ca/(Ca+Mg+Fe) ratio---in other words, to project clinopyroxene compositions

back to the enstatite-diopside join from the $FeSiO_3$ composition as was done by Boyd (1973).

The effect of Al_2O_3 appears to be stronger on the diopside limb of the solvus. There is currently disagreement among experimentalists concerning the nature of this effect. Some experiments suggest that the Ca/(Ca+Mg) ratio of clinopyroxene drastically increases as Al_2O_3 increases in the garnet peridotite (O'Hara and Schairer, 1963) and spinel peridotite stability fields (O'Hara and Schairer, 1963; Herzberg and Chapman, 1976). The Ca/(Ca+Mg+0.5Al) ratio (Table 5-1) may thus be more appropriate than the Ca/(Ca+Mg) ratio to apply data from Al-free synthetic systems to the natural rocks - in other words, to assume that the clinopyroxene limb of the solvus parallels the $CaMgSi_2O_6$-$CaAl_2SiO_6$ join. Mori and Green (1977b) suggest, however, that increasing Al_2O_3 content is accompanied by <u>decreasing</u> Ca/(Ca+Mg) ratio at constant T and P in the garnet peridotite field!

The solubility of enstatite in clinopyroxene has been more frequently used as a geothermometer than the solubility of diopside in orthopyroxene because the former was thought to be more temperature-sensitive than the latter (Boyd, 1973). The revised diopside solvus, however, turned out to be steeper than that of Davis and Boyd (1966) (see Fig. 3 in Mori and Green, 1975), and the temperature sensitivities are about the same for both diopside and enstatite limbs below 1000°C, which unfortunately seems to be the equilibration temperature range of the recrystallized Ronda peridotites. In contrast to the majority clinopyroxenes

in garnet peridotite nodules in kimberlite (e.g. Boyd and Nixon, 1973), the clinopyroxenes of the Ronda peridotote are very aluminous (more than 5 wt. % in the garnet and spinel peridotites), so the erroneous correction of the Al_2O_3-effects would cause large errors in the temperature estimation. Moreover, the pressure effect on the diopside limb is greater than that on the enstatite limb (Mori and Green, 1975). Considering these problems, it is concluded that for the Ronda peridotites, the geothermometer based on the diopside limb is no more accurate than that based on the enstatite limb.

Until more is known about pyroxene subsolidus phase equilibria in multicomponent systems, a semi-empirical thermodynamic approach, such as that of Wood and Banno (1973), cannot provide more accurate temperature estimates because they are entirely dependent on the accuracy of the experimental data.

2) Solubility of Al_2O_3 in pyroxenes in spinel lherzolites

The solubilities of Al_2O_3 in orthopyroxene and clinopyroxene in spinel lherzolites are primarily functions of temperature (Wood, 1975; Obata, 1976; Herzberg and Chapman, 1976; Fujii, 1977) and are not much affected by pressure as suggested by O'Hara (1967) and MacGregor (1974). Several geothermometers based on these parameters have been proposed for spinel lherzolite by Obata (1976), Herzberg and Chapman (1976), and Mori (1977).

A garnet lherzolite R123, a spinel harzburgite R196, and a spinel lherzolite R243, all of which have the most aluminous

spinels among the 12 peridotites studied, were chosen for application of the geothermemeters. Using the average compositions of the pyroxene neoblasts, spinels and olivines in these rocks, the apparent equilibrium constants K_2 and K_3 for the reactions:

$$\underset{\text{cpx}}{CaMgSi_2O_6} + \underset{\text{sp}}{MgAl_2O_4} = \underset{\text{cpx}}{CaAl_2SiO_6} + \underset{\text{ol}}{Mg_2SiO_4} \qquad (2)$$

$$\underset{\text{opx}}{Mg_2Si_2O_6} + \underset{\text{sp}}{MgAl_2O_4} = \underset{\text{opx}}{MgAl_2SiO_6} + \underset{\text{ol}}{Mg_2SiO_4} \qquad (3)$$

were calculated (Table 5-1) by equations (9) (10) in Mori (1977):

$$K_2 = \frac{[X_{Ca}^{M2}.MIN(X_{Al}^{M1},X_{Al}^{T})]^{cpx}.[(X_{Mg})^2]^{ol}}{(X_{Ca}^{M2}.X_{Mg}^{M1})^{cpx}.[X_{Mg}.(X_{Al})^2]^{sp}} \qquad (9)$$

$$K_3 = \frac{[X_{Mg}^{M2}.MIN(X_{Al}^{M1},X_{Al}^{T})]^{opx}.[(X_{Mg})^2]^{ol}}{(X_{Mg}^{M2}.X_{Mg}^{M1})^{opx}.[X_{Mg}.(X_{Al})^2]^{sp}} \qquad (10)$$

where $MIN(X_{Al}^{M1},X_{Al}^{T})$ represents the smaller value between Al concentrations in M1 site and in tetrahedral site of the pyroxenes.

Several methods have been proposed to convert the $\underline{K}$ values to temperatures. Here, two temperatures, T_1 and T_2, were calculated for each orthopyroxene (Table 5-2) using two methods expressed by equations (15) and (18) in Mori (1977), respectively:

$$\frac{10^4}{T_1°K} = -2.061 \ln K_3 + 3.454 \qquad (15)$$

Table 5-2. Equilibrium constants of reaction (2) and (3), and calculated temperatures based on different methods. See text for explanations.

	Orthopyroxene			Clinopyroxene		
	K_3	T_1	T_2	K_2	T_3	T_4
R123	0.091	1038	1058	0.249	1313	1236
R196	0.110	1109	1122	0.214	1273	1200
R243	0.063	919	938	0.231	1293	1219

$$\frac{10^4}{T_2°K} = 0.357\ (\ln K_3)^2 - 0.177\ \ln K_3 + 5.04 \qquad (18)$$

Equation (15) was derived from Obata's (1976) thermodynamic calculation expression for Al concentration in orthopyroxene in the $MgO\text{-}Al_2O_3\text{-}SiO_2$ system, and equation (18) is Mori's empirical modification of the expression in the 3-component system based on his experiment in a natural multicomponent system at 1200°C and 16 kbar. For the clinopyroxenes, also, 2 temperatures T_3 and T_4 were calculated (Table 5-2), using equations (13) and (17) in Mori (1977):

$$\frac{10^4}{T_3°K} = -1.083\ \ln K_2 + 4.80 \qquad (13)$$

$$\frac{10^4}{T_4°K} = -1.083\ \ln K_2 + 5.12 \qquad (17)$$

Equation (13) was derived by Herzberg and Chapman (1976) based on their experiment in the $CaO\text{-}MgO\text{-}Al_2O_3\text{-}SiO_2$ system. Equation (17) is Mori's (1977) empirical modification of equation (13) to satisfy his experiment in a natural multicomponent system at 1200°C and 16 kbar. As is seen in Table 5-2, the clinopyroxene geothermometers give us systematically 100°C to 300°C(!) higher temperatures than the orthopyroxene geothermometers do for the same rocks. Possible reasons for such discrepancies are 1) the natural rocks are in chemical disequilibrium; 2) the way to apply the experiments to the natural rocks, particularly expression of activities, is not correct; or 3) the laboratory experiments are in error.

It is obvious that the natural rocks are to some extent in chemical disequilibrium. The chemical inhomogeneities of the pyroxene neoblasts and the spinels as described in Chapter 4 may be explained by a succession of recrystallizations during cooling. In the process of choosing the average values of the mineral analyses, it was implicitly assumed that all the minerals which are anticipated in reaction (2) and (3) were recrystallized simultaneously. In reality, however, the clinopyroxene may have frozen-in earlier (at higher temperatures) than the orthopyroxenes. Although the textures of the rocks indicate the simultaneous formation of the ortho- and clinopyroxene neoblasts, it is difficult to prove this by textural relations alone.

For the calculation of activities, the Temkin-type formula (Wood, 1975) was used throughout. All sites in the minerals were assumed to be ideal and no interaction between cations was assumed (Wood and Banno, 1973). This may cause some errors, particularly in chemically complex clinopyroxenes. Tetrahedral Al of pyroxenes was assumed to equal 2-Si, which totally depends on the precision of the Si analyses. The remaining Al was assigned to the M1 site, and the smaller of the 2 values was used to calculate the activities of the aluminous pyroxene component as proposed by Mori (1977). To use total Al/2 in the calculation as proposed by Wood and Banno (1973) would systematically raise the temperature estimations. Frost (1976) suggested that pressure discrepancies observed for the spinel-plagioclase peridotite transition between natural

Cr-bearing metamorphic peridotites and simple synthetic Cr-free peridotites might be due to nonideality of the spinel phase. If the $MgAl_2O_4$-$MgCr_2O_4$ solid solution is positively non-ideal, that is, if the activity coefficient is greater than one, the activity of $MgAl_2O_4$ component as expressed in equations (9) and (10) are underestimated; therefore, the temperatures derived from equations (15), (18), (13) and (17) are all overestimated.

The third possibility that the experimental data are in error should be evaluated either by further experiments or by other independent methods, such as thermodynamic calculations, using accurate calorimetric data (Charlu et al, 1975). This is not a problem which can be resolved by examining the natural rocks until problems 1) and 2) are resolved. This argument, of course, applies to all the other geothermemeters and geobarometers.

3) Fe-Mg partitioning between minerals

Among the 5 ferromagnesian minerals orthopyroxene, clinopyroxene, spinel, garnet, and olivine, there are 4 independent mineral pairs. Here, orthopyroxene-clinopyroxene, garnet-clinopyroxene, olivine-clinopyroxene, and olivine-spinel pairs are chosen for geothermometers, since these 4 are the best studied in natural and/or in synthetic systems, ~~and they have been studied in natural and/or synthetic systems,~~ and they have been demonstrated to be temperature-sensitive[1].

[1]References appear later in each discussion.

In general, for an exchange reaction of ferrous iron and magnesium between mineral α and β:

$$Mg_{\alpha} + Fe^{2+}_{\beta} = Fe^{2+}_{\alpha} + Mg_{\beta} \quad (4)$$

an apparent partition coefficient $K_{Fe/Mg}^{\alpha/\beta}$ may be defined as follows:

$$K_{FeMg}^{\alpha/\beta} = \left(\frac{X_{Fe^{2+}}}{X_{Mg}}\right)^{\alpha} \Big/ \left(\frac{X_{Fe^{2+}}}{X_{Mg}}\right)^{\beta} \quad (5)$$

where $X_{Fe^{2+}}$ and X_{Mg} are the mole fractions of Fe^{2+} and Mg end-members of the relevant minerals. In the following discussions all the iron in the minerals, except spinel, was assumed to be in a ferrous state, partly because of the inability of the electron microprobe to determine the oxidation state of iron and also because the oxidation state of iron, determined by conventional wet chemical analysis of natural rocks may not necessarily reflect the original oxidation state of the rocks at the time of their formations. Shortcomings of this simplification will be discussed later. The volume changes of such exchange reactions generally very small (e.g. Kretz, 1963; Banno, 1970; Evans and Frost, 1975), and hence the pressure effect on the geothermometer is slight and, as a first approximation, it can be neglected for crustal and upper-most mantle rocks.

Orthopyroxene-clinopyroxene and garnet-clinopyroxene pairs: The values of $K^{opx/cpx}$ for the average analyses of the pyroxene neoblasts of the peridotites are calculated and listed in Table 5-1. They fall between 1.05 and 1.25. The spinel

peridotites have slightly smaller values than the garnet- and plagioclase peridotites. This may indicate higher equilibration temperatures for the spinel peridotites than the others. It is also possible that this slight variation of the K value is due to some compositional variation of the pyroxenes, particularly the Al content and/or oxidation state of iron (the Al content is highest for pyroxenes in the spinel peridotites). The K values for coarse pyroxenes in 4 mafic layers, a garnet websterite R554; a spinel pyroxenite R251; and two olivine gabbros R120 and R343, are 1.20, 1.24, 1.22 and 1.24, respectively. They are very close to each other in spite of the different mineral facies and fall in the middle of the range defined by the peridotites, which may indicate uniform equilibration temperatures of the peridotites and the mafic layers. On the other hand, small interstitial recrystallized pyroxene pairs in 2 garnet clinopyroxenites R560 and R253 (Opx/Cpx-2 pairs in Table 4-8) have distinctively higher values than the coarse pyroxenes discussed above: 2.16 and 1.77, respectively, indicating lower equilibration temperatures. This is in harmony with the low CaO content of the smaller orthopyroxenes.

The values of $K^{gar/cpx}$ of the four garnet peridotites and the five garnet pyroxenites are illustrated in Fig. 5-2. Despite large compositional ranges of pyroxenes and garnets of the mafic layers (Fe/Mg ratio of cpx: 0.1 to 0.4, Al_2O_3 in cpx: 3 to 11 wt. %, CaO in garnet: 4 to 10 wt. %), the $K^{gar/cpx}$ values are fairly uniform among the mafic layers and

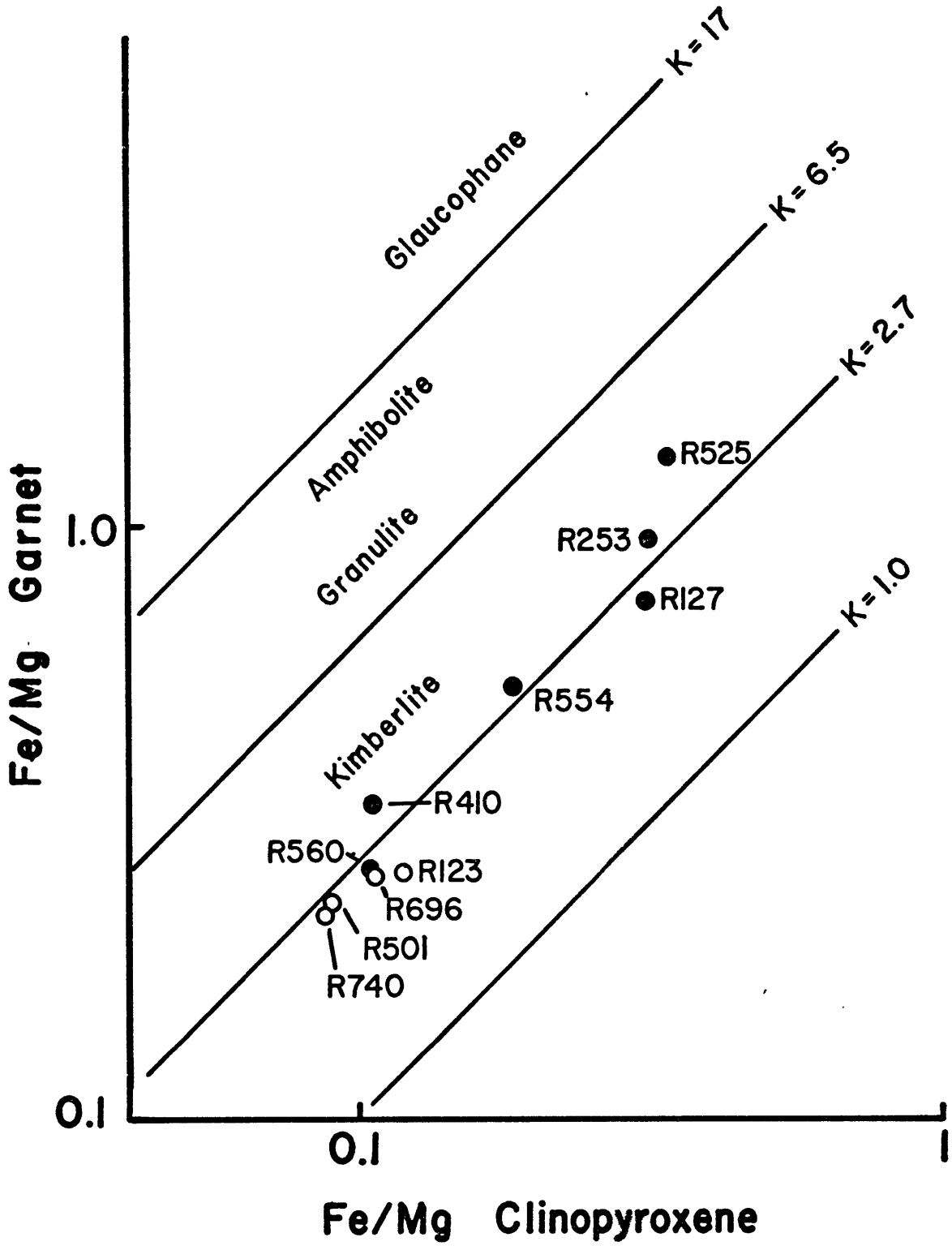

Figure 5-2. Plot of atomic ratios Fe/Mg for coexisting clinopyroxenes and garnets in 6 mafic layers and 4 garnet peridotites of the Ronda massif. Fields of eclogites in glaucophane schist-amphibolite- and granulite metamorphic terrain, and those in kimberlite eclogite nodules are indicated after Banno (1970).

are close to those of the peridotites, which again argues for rather uniform equilibration temperatures of the peridotites and the mafic layers. The values of $K^{opx/cpx}$ and $K^{gar/cpx}$ of the Ronda rocks are compared with those of the other occurrences in a log-log plot (Fig. 5-3) which was first used by Mori and Banno (1973). The use of the Gar-Opx-Cpx assemblages only minimizes possible effects of random variations of Al_2O_3 and CaO in the garnet and the pyroxenes on the partition coefficients because the compositions of pyroxenes and garnets are, at constant temperatures and pressures, more restricted in this mineral assemblage than in Gar-Cpx assemblages. If, by analogy to the case of the ideal solution, the logarithm of the partition coefficient is proportional to the reciprocal of temperature for the 2 pairs of Opx/Cpx and Gar/Cpx, then a linear relationship should hold between the two logarithms of the partition coefficients. The temperature dependencies of these partitionings have recently been investigated experimentally by Mori and Green (1977b) with a pyrolite composition in a temperature range of 950-1500°C, and a pressure range of 30-40 kbar. Their calibrations are:

$$\ln K^{opx/cpx} = 1500/T°K - 1.07 \quad (6)$$

$$\ln K^{gar/cpx} = 2800/T°K - 1.19 \quad (7)$$

By combining equations (6) and (7), the following relation between the two K values may be obtained:

$$1.24 \ln K^{gar/cpx} - 2.31 \ln K^{opx/cpx} = 1 \quad (8)$$

which is graphically expressed by a straight line in the diagram in Fig. 5-3. A temperature scale by Mori and Green

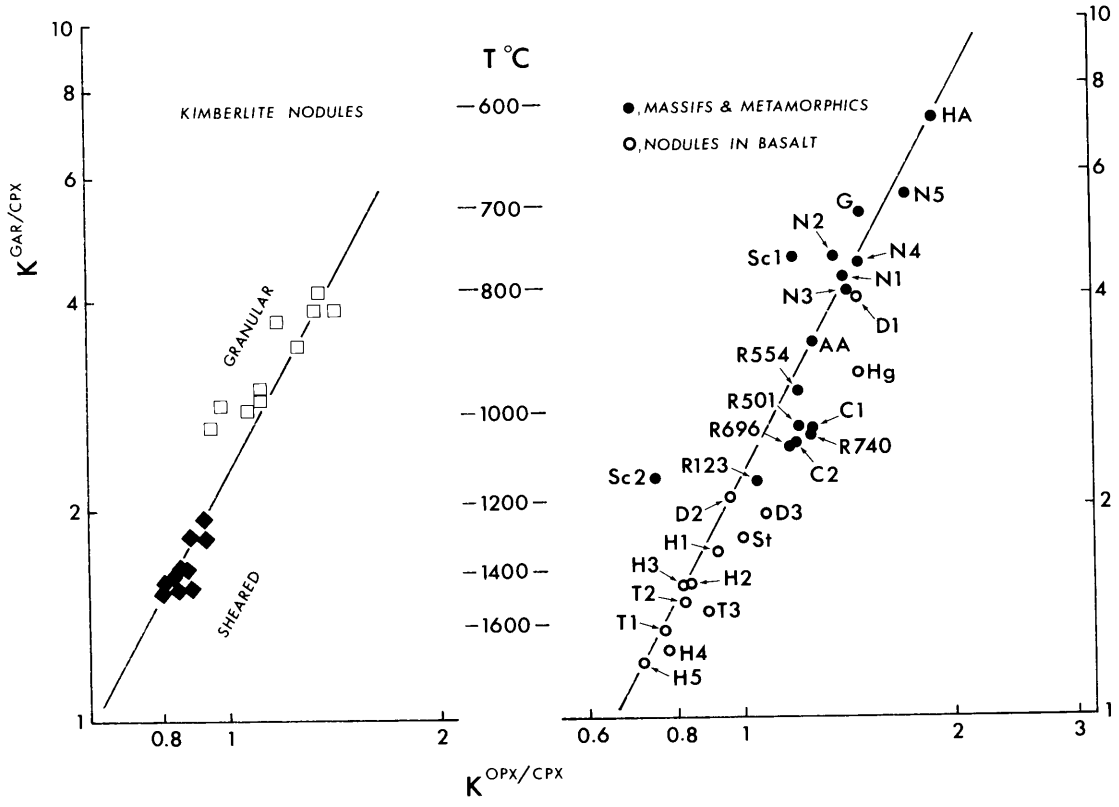

Figure 5-3. $K^{opx/cpx}_{Fe/Mg}$ versus $K^{gar/cpx}_{Fe/Mg}$ for natural coexisting Opx-Cpx-Gar rocks in massifs and metamorphics, nodules in basalts (right diagram), and for kimberlite nodules (left diagram). R123, R501, R554, R696 and R740 are Ronda samples. Sample locations and data sources other than of the Ronda samples are listed in Table 5-3. Temperature scale is after Mori and Green (1977b).

Table 5-3.

Occurences	Symboles in Fig.5-3	Original sample no. ; References
Peridotite Massifs		
Mt. Higasi-Akaisi	HA	--- average; Mori & Banno(1973)
Norway (Almklovdalen and Kalskalet)	N1,N2	---N69,N70; O'Hara & Mercy(1963a)
	N3	---T96; Carswell(1968a)
(Ugelvik)	N4	---U8; Carswell(1968b)
	N5	---U95; Carswell(1973)
Switzerland (Alpe Arami)	AA	---A2; O'Hara & Mercy(1963a)
Czechoslovakia	C1,C2	---1,2; Fiala(1966)
Metamorphic Rocks		
Scotland		
(Glenelg)	G	O'Hara(1960)
(Scorie)	Sc1,Sc2	---X646,X819; O'Hara(1961)
Inclusions in Basaltic Lavas and Tuffs		
Hawaii	H1,H2,H3,H4	---AL-24,AL-26,AL-6,AL-7; Beeson & Jackson(1970)
	H5	--- AL-7(reconstructed)
Australia (Delegate)	D1,D2	--- R804,R394; Lovering & White(1968)
	D3	--- 69-27; Irving(1975)
Austria (Tobaj)	T1,T2,T3	---#362,#363,#364; Richter (1971)
Styria	St	Kurat(1971)
Sahara (Hoggar)	Ho	Girod(1967)
Inclusions in Kimberlites		
South Africa		Nixon & Boyd(1974)

is also shown in the same diagram. Other experimental data on the Gar-Opx-Cpx assemblages by Akella (1973, 1974) at 1100°C to 1300°C and by Hensen (1973) at 1110°C to 1410°C agree well with Mori and Green's calibration. The linear relationship between the two parameters for natural rocks, and furthermore, their agreement with the experimentally determined line are remarkable (Fig. 5-3). Direct application of the temperature scale to the natural rocks, however, results in temperature estimations which are systematically somewhat higher than generally thought: 600°C vs. 550°C (Mori and Banno, 1973) for Japanese peridotite, 800°C vs. 700°C (O'Hara and Mercy, 1963) for Norwegian peridotite, and for some Hawaiian xenoliths (Beeson and Jackson, 1970), above 1700°C!

This apparent discrepancy may derive from the different oxidation state of iron between natural and synthetic pairs. All the experiments were done in reduced conditions and almost all iron in the reaction products is considered to be ferrous according to Mori and Green (1977b). Natural rocks, on the other hand, almost certainly contain some ferric iron, in concentrations decreasing from clinopyroxene to orthopyroxene, and then to garnet judging from published analyses. If the ferric/ferrous ratio in the natural minerals were accurately determined and only the ferrous ions were used in the calculation of the K values in equation (5) instead of total iron, the K values would increase and thus somewhat lower temperatures would be obtained. Therefore, the temperature range

950°C to 1100°C for the Ronda garnet peridotites and garnet websterite may be regarded as an upper limit of recrystallization temperatures.

Olivine-clinopyroxene pairs: The partition coefficient $K_{Fe/Mg}^{Ol/cpx}$ increases markedly as temperature decreases, particularly at low temperatures, due to the non-ideal behavior of olivine (Obata et al., 1974). The calculated values of $K_{Fe/Mg}^{Ol/cpx}$ for the peridotites in Table 5-1 are all close to the $K_{Fe/Mg}^{opx/cpx}$ values for each peridotite and the 2 coefficients parallel each other, which means the partition coefficients of Fe and Mg between olivine and orthopyroxene are constant and close to unity for all the peridotites (Table 5-1). The variation of the $K^{ol/cpx}$ values, like the variation of $K^{opx/cpx}$, could also be due to variation of the ferric to ferrous ratio of clinopyroxenes instead of temperature variation.

Olivine-spinel pairs: The Fe^{2+}-Mg partitioning between spinel and olivine was first treated theoretically and suggested as a potential geothermometer by Irvine (1965). Subsequently this geothermometer was calibrated by Jackson (1969) using then available thermochemical data. Repeated applications of this calibration to natural rocks, however, have resulted in much higher equilibration temperatures than obtained by other methods of temperature estimation (Evans and Frost, 1975). This systematic deviation is probably due to inaccuracies and errors in the thermochemical data used by Jackson (1969). The calibration was recently revised by Evans and Frost (1975)

using natural assemblages of metamorphic peridotites and volcanic rocks, crystallization temperatures of which were already known by other independent methods. An advantage of the olivine-spinel geothermometer compared to other geothermometers, such as those based on the mutual solubilities of ortho- and clinopyroxenes or Fe^{2+}-Mg partitioning between silicate pairs involving pyroxene is that the chemistries of both olivine and spinel are relatively simple: Olivine is a binary solution of forsterite and fayalite, and the tetrahedral site of the spinel can be dealt with as a binary solution between Mg and Fe^{2+} and the octahedral site as a ternary solution of Cr-Al-Fe^{3+}. The concentrations of other minor elements such as Mn, Al, Ca, Fe^{3+}, Ni in olivines, and Ti, Mn, Ni, Ca in the spinels are so low that their effects upon the temperature estimation will be practically negligible. Inaccuracies involved in assigning total iron to tetrahedral and octahedral sites of the spinel structure assuming perfect stoichiometry could be a source of the error in the temperature estimation. Complete and accurate analyses of the spinels are thus required to minimize the error.

The K_D values were calculated (Table 5-1) by pairing all the spinel analyses with the average compositions of olivine (Table 5-1) for each peridotite and are plotted in the $\ln K_D$ vs. Y_{Cr} diagram of Evans and Frost (1975) in Fig. 5-4. The use of the average olivine composition for different spinel compositions in each rock may be justified by the argument made

Figure 5-4. ln K_D versus Y_{Cr} plot for spinel-olivine pairs from 4 garnet peridotites (top), and from other peridotites (bottom). Y_{Cr} = Cr/(Al+Cr+Fe^{3+}) atomic ratio of spinels. Solid symbols are tiny spinels in garnet peridotites, and small spinels in transitional peridotites. Direction of zoning is indicated by arrows.

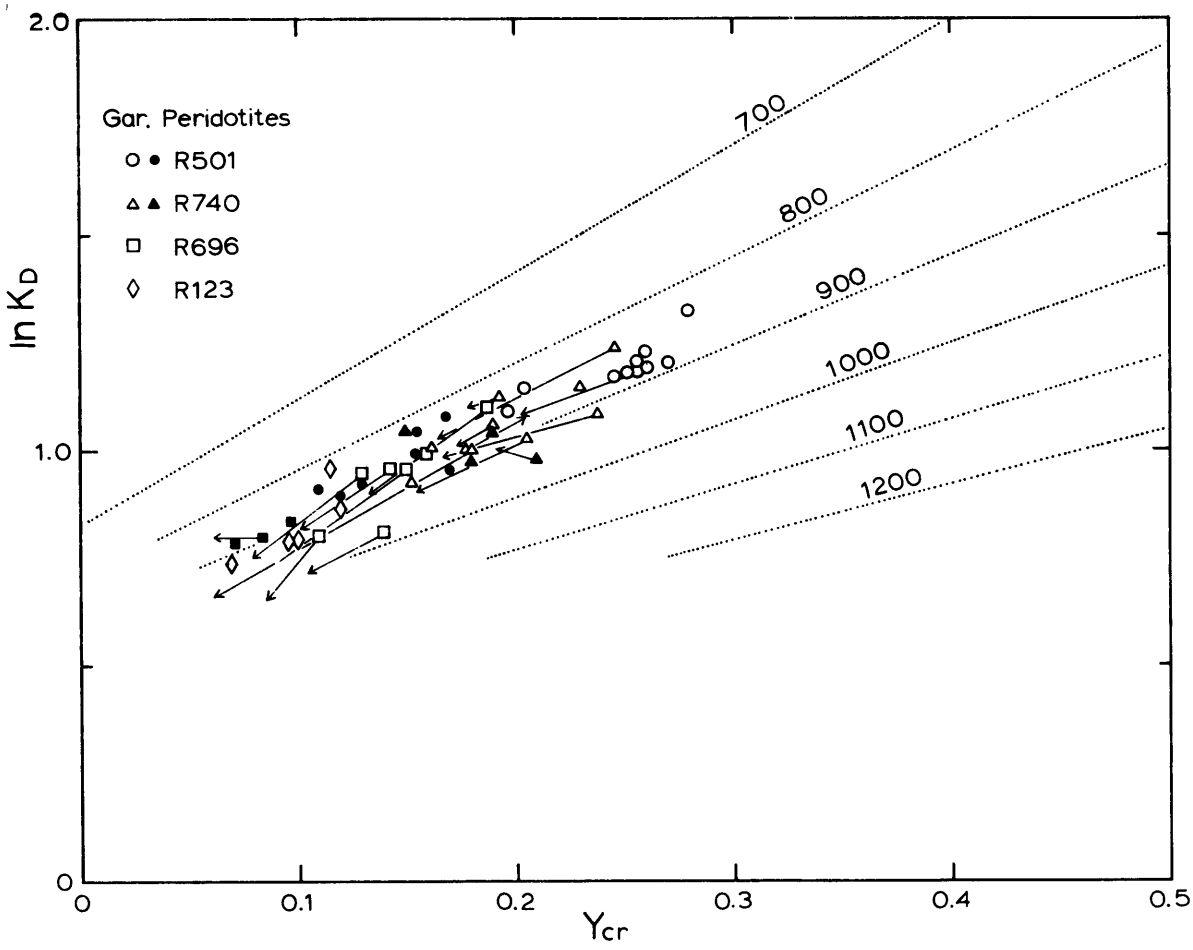
Gar. Peridotites
R501
R740
R696
R123
700
800
900
1000
1100
1200
ln K_D
Y_cr
2.0
1.0
0
0.1
0.2
0.3
0.4
0.5

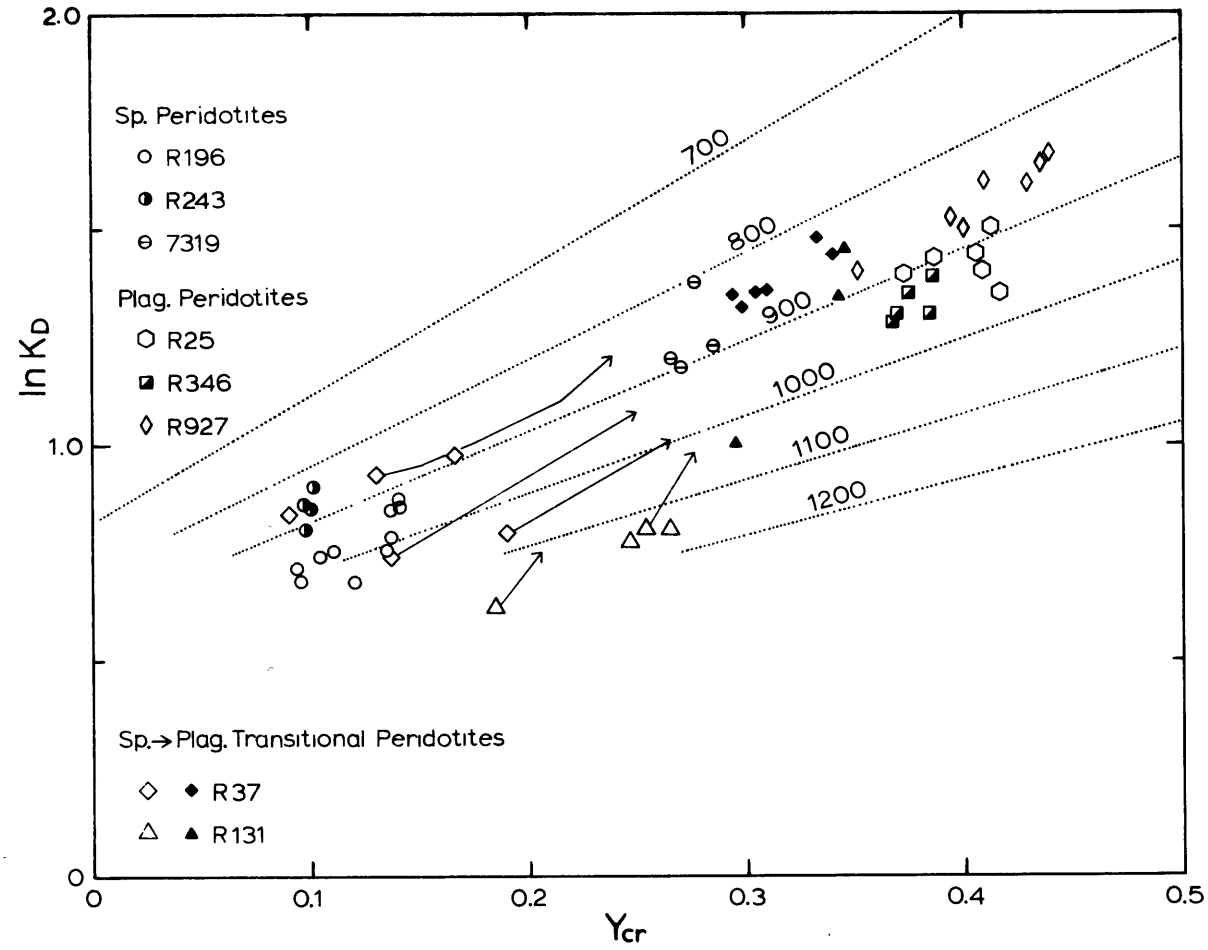
Sp. Peridotites
R196
R243
7319
Plag. Peridotites
R25
R346
R927
Sp.→Plag. Transitional Peridotites
R37
R131
700
800
900
1000
1100
1200
ln K_D
Y_cr
2.0
1.0
0
0.1
0.2
0.3
0.4
0.5

in Mineral Chemistry (p.139). Isopleths of 700°C and 1200°C are from Evans and Frost (1975), and the intervening isopleths were spaced out in proportion to 1/T. The lnK was not normallized to $X_{Fe^{3+}} = 0.05$ as suggested by Evans and Frost because the uncertainty of the correction factor, which was derived from thermochemical data by Irvine (1965), is thought to be too large.

The isotherms in Fig. 5-4, however, would not shift significantly, even if the un-normallized values were used because the $X_{Fe^{3+}}$ values of the spinels used by Evans and Frost have a maximum frequency around 0.05. (This is the reason for their choice of this number, so that the error derived from the uncertainty of the correction factor may be avoided (Evans, personal communication)).

Interestingly, for the garnet peridotites (Fig. 5-4) there are no systematic temperature differences between spinels of different compositions and textures, and all the garnet peridotites seem to have been formed between 800°C and 950°C. Some spinels in the transitional peridotites (See Fig. 5-4) have memories of temperatures up to 1200°C in the centers of big grains, and they are zoned outwards to lower temperatures. Small grains in the same rocks lie in a temperature range of 800 to 900°C. The spinel peridotites' range is 800 to 1100°C and the plagioclase peridotites' range is 850°C to 950°C. The olivine-spinel temperatures for each rock are compared with other parameters discussed before in Table 5-1.

4) Al-Cr partitioning between pyroxenes

Mysen and Boettcher (1975) proposed a geothermometer based on the partitioning of the octahedrally coordinated Al and Cr between orthopyroxene and clinopyroxene. Total Al/2 was used for the octahedrally coordinated Al as suggested by Mysen and Boettcher (1975). The partition coefficients were defined as:

$$K_{Al/Cr}^{opx/cpx} = \left(\frac{X_{Al}^{VI}}{X_{Cr}}\right)^{opx} / \left(\frac{X_{Al}^{VI}}{X_{Cr}}\right)^{cpx} \qquad (3)$$

and the corresponding temperatures were calculated by equation (3) in Mysen (1976):

$$\frac{10^3}{T} = 0.26\ \ln K + 0.6$$

The results for the 12 Ronda peridotites are listed in Table 5-1. These temperatures tend to be higher than the Ol-Sp temperatures. No monotonic geographic correlation is apparent as is observed for the CaO content of the orthopyroxene neoblasts.

Summary of Recrystallization Temperature

In summary, internal agreement of the different geothermometers is not very satisfactory. The pyroxene solvus method is subject to much uncertainty in the temperature range of the recrystallization of the Ronda peridotites (i.e. below 1000°C). From the Al_2O_3 content, clinopyroxene neoblasts appear to have formed at higher temperatures than orthopyroxene neoblasts. According to Fe-Mg partitioning among garnet, pyroxenes and olivine, both peridotites and mafic layers of different mineral

facies appear to have recrystallized together in a narrow temperature range. Some variations of the $K_{Fe/Mg}$ values may be due to compositional variation of pyroxenes.

The olivine-spinel geothermometer seems to work well for peridotites and indicates that the majority of peridotites last equilibrated at 800° to 900°C. The Al-Cr geothermometer gives temperatures higher than the olivine-spinel geothermometer. The use of total Al/2 for the 6-coordinated Al may be a problem, particularly for clinopyroxene which contains other aluminous components, such as $NaAlSi_2O_6$, $CaTiAl_2O_6$ and $CaCrAlSiO_6$.

There is another independent temperature estimation: The composition of the clinopyroxene in a natural plagioclase garnet clinopyroxenite layer sampled from the zone of the garnet lherzolite facies was experimentally duplicated at 800° to 900°C as shown in Chapter 6 (p. 164). This temperature estimate agrees well with the temperature range of the olivine-spinel geothermometer and of the orthopyroxene geothermometers for the garnet peridotites, although the latter are, of course, subject to much uncertainty. The plagioclase peridotite appears to have equilibrated in the same temperature range as the garnet peridotites, although the spinel peridotites may have equilibrated some 100°C higher. Perhaps this is the most we could say about equilibration temperatures of the recrystallization at this moment.

5.2 Pressures of Recrystallization

For the estimation of the equilibrium pressure of the garnet peridotites, the average composition of orthopyroxenes in

R501 was used because among the 4 garnet peridotites this rock is the most thoroughly equilibrated (see Fig. 4-2). Pressures of 15 kbar and 12 kbar were obtained for estimated temperatures of 900° and 800°C, respectively, by the method of Wood and Banno (1973) using the revised ΔG values (Wood, 1974). It should be noted that these conditions are outside of the garnet peridotite field of O'Hara et al. (1967) but still within the garnet peridotite field of Obata (1976) (Fig. 5-5).

The pressures of the plagioclase peridotites were estimated to be 5 to 7 kbar by the method of Obata (1976) for the same temperature range as the garnet peridotites. This is near the plagioclase/spinel peridotite field boundary calculated by Obata (1976) in the CaO-MgO-Al_2O_3-SiO_2 system. Equilibration pressures of the spinel peridotites must lie between those of plagioclase and garnet peridotites. Currently, however, there is no method to pinpoint the pressure value of the spinel peridotites (Obata, 1976). The pressure difference between the garnet and plagioclase peridotites is, as a minimum estimate, 5 kbar. This is still too large a value to be accounted for by lithostatic pressure differences across the massif. The conclusion reached in the discussion in Mineral Facies is now supported by the mineral chemistry here.

5.3 Primary Condition

The equilibrium condition at which the orthopyroxenes of the "primary composition" (see Mineral Chemistry, p. 68) were stable in the peridotites may be called the "primary condition". The "primary composition" of the orthopyroxene is 6 to 7 wt. % Al_2O_3 and 1.3 to 1.5 wt. % CaO. In Fig. 5-5, Al_2O_3 isopleths (6.5 to 7 wt.%) of orthopyroxene in the spinel peridotite (Obata, 1976) and the garnet peridotite (Akella, 1976) in the Al_2O_3-CaO-MgO-SiO_2 system, and the CaO isopleth (1.4 to 1.5 wt.%) of orthopyroxene coexisting with clinopyroxene in the enstatite-diopside system (Fig. 5-1) are drawn. The primary condition has to lie at or above the temperatures of the appropriate Al_2O_3 isopleth depending on whether or not the peridotites were saturated with the aluminous phases.

The CaO isopleths for the primary composition pass through the intersection of the two sets of Al_2O_3 isopleths for the spinel and the garnet peridotites, indicating that the primary peridotite was once equilibrated near the spinel/garnet peridotite boundary at 1100°C and 1200°C and 20 to 25 kbar. This also coincides the maximum temperatures recorded in cores of big spinels in the transitional peridotites. Of course, there may be much uncertainty in this T,P estimate due to the uncertainties of the phase diagrams and the ambiguities of the effect of Al_2O_3 on CaO in the orthopyroxene as discussed above. It is clear,

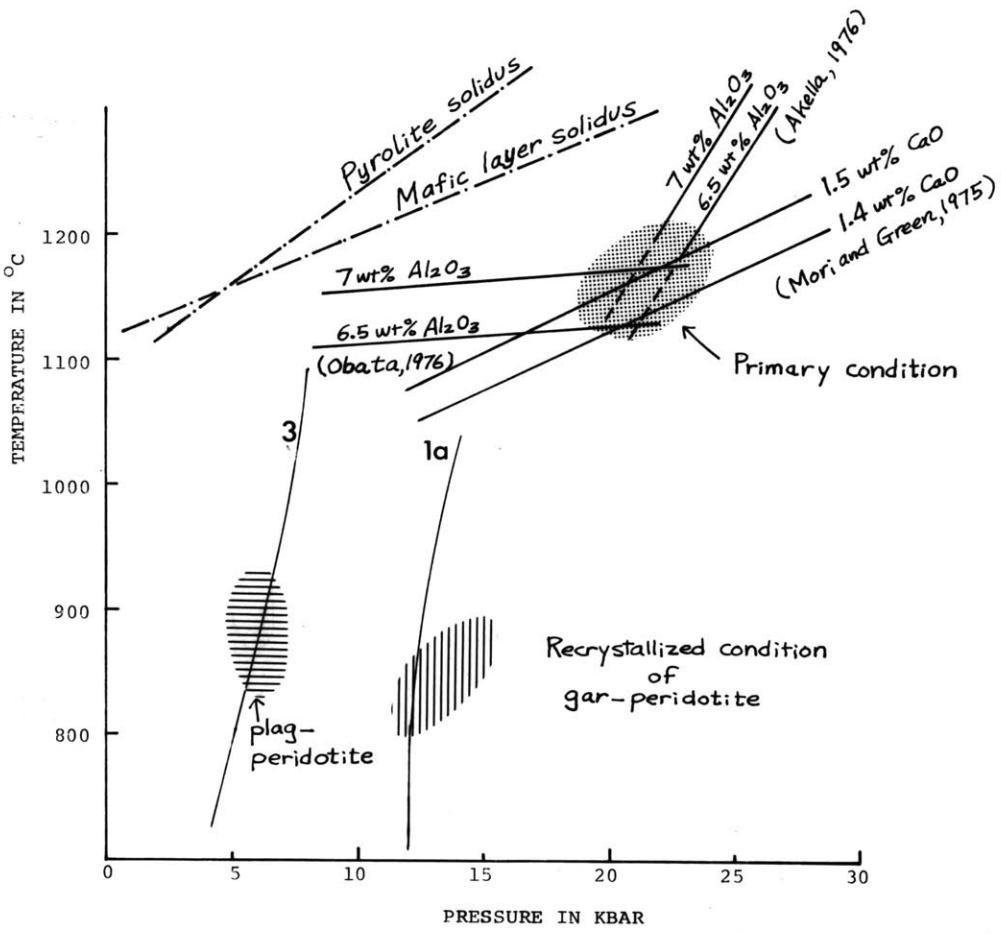

Figure 5-5. Primary and recrystallized conditions of the Ronda massif.

however, that the primary condition was at much higher temperatures and pressures than the recrystallized condition. Now, how may the "primary condition" be linked to the recrystallized conditions in terms of thermal history?

5.4 Pressure - Temperature Trajectories

Theoretically, there are a number of ways to connect the primary condition to the recrystallized condition, but geophysical and geological constraints restrict the number of realistic trajectories. A model of a hot peridotite diapir as sketched in Fig. 5-6, may provide us an aid to draw trajectories of the peridotite in P-T space.

A hot peridotite body (1100°C to 1200°C) starts to rise from around 70 km depth. The peridotite is solid but mobile and continues to flow by syntectonic recrystallization and plastic deformation under the shear stress at high temperatures (Carter and Ave'Lallemant, 1970; Ave'Lallemant and Carter, 1970; Nicolas et al., 1971). The outer part of the body loses heat to the cooler surroundings faster than the inside. There would be a certain lower limit of temperature of syntectonic recrystallization, so as the peridotite cools, the recrystallization would stop successively from the outer part to the inside of the body. Because the body rises while cooling, the "frozen-in" mineralogy of the peridotites and the mafic layers changes from high-presure assemblages at the margin of the body to low-pressure assemblages inside, resulting in a mineralogically-zoned structure.

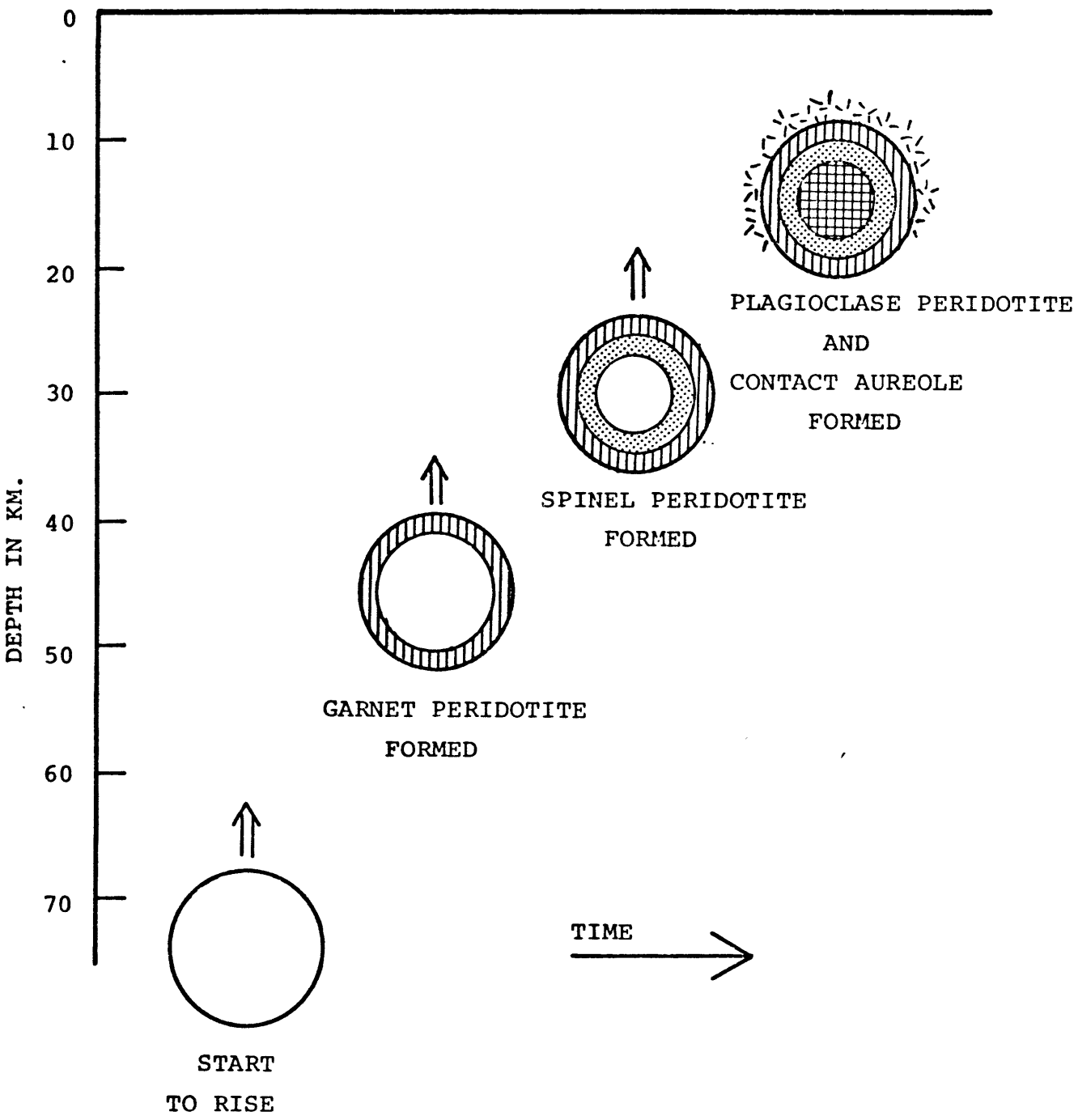
0
10
20
30
40
50
60
70
DEPTH IN KM.
PLAGIOCLASE PERIDOTITE
AND
CONTACT AUREOLE
FORMED
SPINEL PERIDOTITE
FORMED
GARNET PERIDOTITE
FORMED
START
TO RISE
TIME

Figure 5-6.

The zone of the garnet lherzolite facies would be thus the outer-most part of the body which stopped recrystallizing at 800-900°C and 12 to 15 kbar (40 to 50 km depth). Deep inside of the body the cooling would be nearly adiabatic ($\sim$0.3°C/km). When the peridotite intrudes into the crust, it will heat up and metamorphose the surrounding sediments by the heat flowing out from inside of the peridotite body. By the time the peridotite penetrated into the crust, the out-most part of the body was already frozen-in as garnet peridotite and spinel peridotite, and only superficial retrogressive reaction would affect the peridotite; (i.e., kelyphitization of garnet, symplectization of aluminous pyroxene, exsolution and chemical zoning of pyroxenes, and perhaps formation of the "tiny" spinels in the garnet peridotites). This mechanism explains the large pressure gap between the garnet peridotites ($\sim$15 kb) and the garnet cordierite gneiss at the peridotite contact ($\sim$4 kb according to Loomis, 1972). The thickness of the zones of different mineral facies is controlled by combinations of the cooling rate and the rising rate of the peridotite body. The cooling rate depends on the thermal diffusivities of the peridotite and the temperature differences between the body and the surroundings, which also depends on rising rate. If the body rises infinitesimally slowly, the entire body will eventually follow the ambient geotherm and no zonal pattern will appear in the body. On the other hand, if the body rises rapidly

and stops at some level and cools slowly, it will be recrystallized in a low-pressure mineralogy leaving no record of earlier high-pressure, high-temperature mineralogies. If the cooling is fast, however, due to very effective heat conduction, the high-pressure mineralogies survive just as spinel or garnet peridotite nodules are brought to the surface by volcanic eruptions. Between these extremes, there are numbers of intermediate cases, but generally the geometry of the P-T trajectories from the primary condition to the recrystallized conditions will resemble those drawn in Fig. 5-7. Judging from the textural relations of spinels (inclusions of spinel in garnet and plagioclase mantling spinels) the peridotites were perhaps once all spinel peridotites. The garnets and plagioclases grew upon cooling at the expense of the spinel in the garnet lherzolite facies zone and the plagioclase lherzolite facies zone, respectively. The peridotite which cooled along an intermediate path (PL-1 in Fig. 5-7) would have gained more quantities of spinel in the middle and later partially transformed to plagioclase peridotite. The transition was incomplete, as is apparent in the textures of the transitional peridotites (see Petrography, p. 24), because when this part entered the plagioclase lherzolite field it was too cold to react completely. The diverse mineralogies of the mafic layers, varying from eclogite to gabbroic, are also the result of the different P-T paths, perhaps starting from a uniform lithology at high P,T.

In order to see the lithology of the mafic layers at

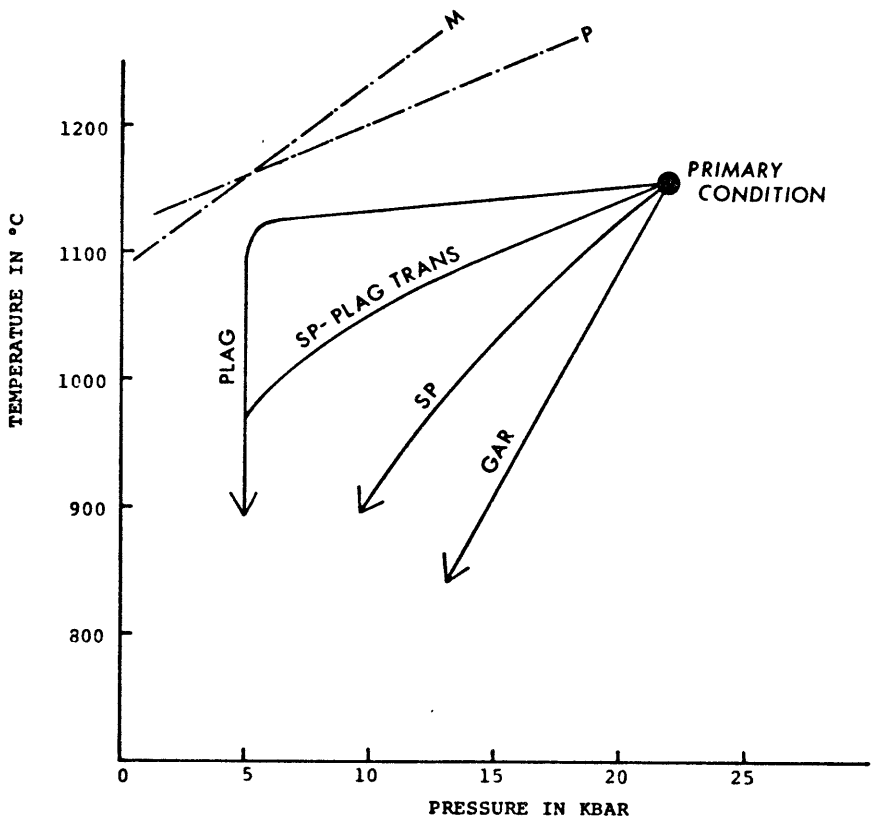

Figure 5-7. P-T trajectories of garnet, spinel, transitional and plagioclase peridotites of the Ronda massif.

the "primary condition," the mantle norm of Kushiro and Kuno (1963) was calculated for the 7 "magmatic-type" mafic layer compositions (Dickey, 1970) in Table 5-4. The $CaAl_2SiO_6$ component was split into Al_2O_3 and $CaSiO_3$. Interestingly, the compositions of all the magmatic mafic layers are nearly 90% accounted for by pyroxene components. They are projected to the Al_2O_3-$CaSiO_3$-$(Mg,Fe)SiO_3$ plane from other pyroxene components and quartz or olivine (Fig. 5-8), and compared with a subsolidus phase diagram at 1200°C, 20kb, which is constructed from experimental data by Boyd (1973), Mori and Green (1975), Herzberg and Chapman (1976), and Akella (1976). The garnet to pyroxene volume proportion would vary depending on temperature and pressure. At higher temperatures or at lower pressures, in the field of ariegite facies, olivine-garnet assemblages become unstable and so spinel would replace olivine by the reaction olivine + garnet = orthopyroxene + clinopyroxene + spinel.

In summary, the Ronda peridotite massif was, before the intrusion, spinel or garnet peridotite with thin layers of pyroxenite or garnet pyroxenite with minor amounts (<10%) of olivine, spinel, or quartz. The mineralogically zoned structure of the massif has resulted from a combination of different cooling rates in different parts of the rising peridotite body. There are <u>infinite</u> numbers of P-T trajectories in a <u>single</u> body depending on the distances from the surface of the body toward the inside. Although the sketch in Figure 5-6 may imply a diapir case, it must be emphasized that these

Table 5-4. Compositions of mafic layers in the Ronda massif (Dickey, 1970) and mantle norms.

	R127	R251	R183	R120	R322	R343	R349
SiO_2	47.73	44.09	46.67	46.68	48.33	48.91	53.21
TiO_2	0.73	1.12	0.24	0.19	0.31	0.06	0.09
Al_2O_3	16.16	14.51	17.71	12.91	11.83	11.61	5.17
Cr_2O_3	0.00	0.06	0.09	0.25	0.47	0.35	0.82
Fe_2O_3	0.94	2.47	0.96	0.99	0.48	0.53	0.63
FeO	7.84	4.97	6.15	5.43	4.43	5.81*	5.42
MnO	0.15	0.14	0.14	0.17	0.12	0.15	0.14
MgO	9.88	14.80	12.16	20.81	22.38	20.01	29.81
CaO	14.15	16.44	14.16	10.33	9.86	11.27	3.92
Na_2O	1.89	0.89	1.30	0.96	0.77	0.53	0.18
K_2O	<0.01	0.01	<0.01	0.00	0.01	0.00	0.00
H_2O+	0.35	0.24	0.37	1.03	0.52	0.56	0.33
H_2O-	0.06	0.09	0.06	0.10	0.11	0.09	0.11
P_2O_5	0.00	0.00	0.00	0.00	0.00	0.00	0.00
NiO	<0.01	0.03	0.03	0.08	0.11	0.06	0.02
$O_3=$	0.00	0.04	0.00	0.12	0.06	0.00	0.05
Total	99.88	99.90	100.04	100.05	99.79	99.94	99.90
			Mantle Norms (wt %)				
$NaAlSi_2O_6$	12.4	5.9	8.5	6.3	5.0	3.5	1.2
$CaTiAl_2O_6$	2.2	3.3	0.8	0.6	0.9	0.2	0.2
Al_2O_3	12.1	11.8	15.3	11.4	10.6	11.8	5.7
$CaSiO_3$	29.4	32.7	29.4	21.7	20.6	23.3	8.1
$MgSiO_3$	24.6	25.8	30.4	39.4	48.1	48.5	71.1
$FeSiO_3$	16.3	9.4	13.2	9.0	7.8	11.6	10.8
Mg_2SiO_4	---	8.0	---	9.2	5.7	0.9	2.6
Fe_2SiO_4	---	3.2	---	2.4	1.0	0.2	0.4
SiO_2	3.1	---	2.4	---	---	---	---
Mg/(Mg+Fe) %	67.0	78.4	75.6	85.4	89.1	85.0	88.9

All iron was assumed to be ferrous in the norm calculation.
Sample locations are in Fig. 4-1.
Norm calculation method, after Kushiro and Kuno (1963).

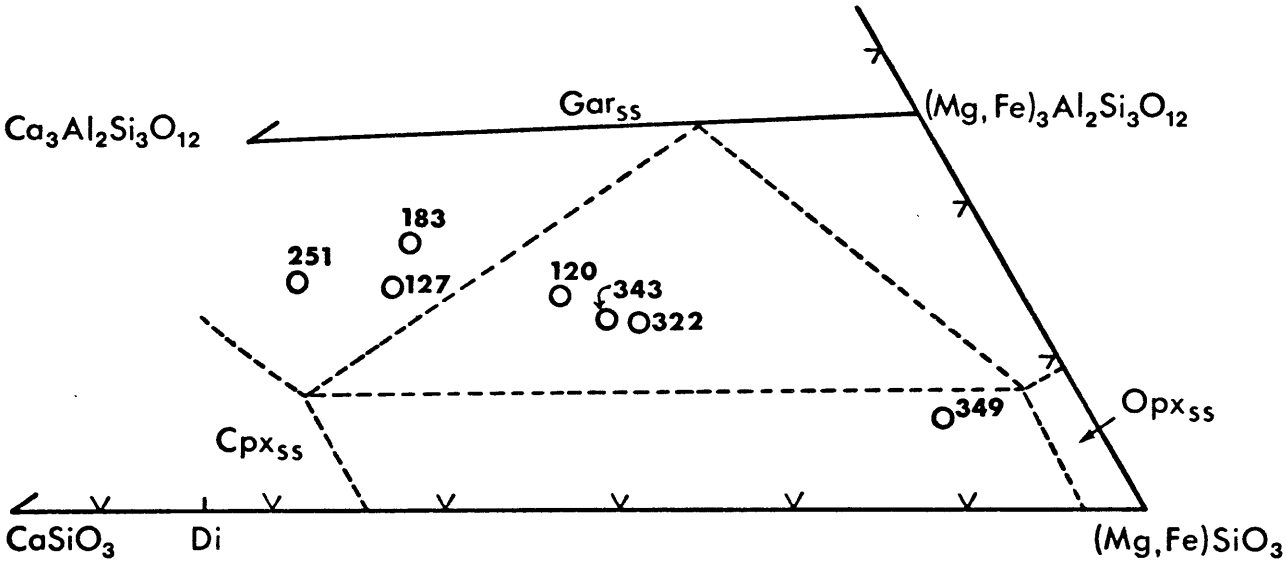

Figure 5-8. Projection of 7 mafic layer compositions from olivine or quartz apeces to garnet-pyroxene plane; in weight percent.

multiple P-T trajectories of a single body will appear in any tectonic situation where the cooling rate is not homogeneous in the body while the pressure keeps changing.

According to Ave'Lallement and Carter (1970), syntectonic recrystallization is a dominant mechanism of flow in the upper mantle and the lower temperature limit of the syntectonic recrystallization depends on the strain rate. The temperature range 800 to 900°C as recorded in the Ronda recrystallized peridotites may mean that this is the lower temperature limit of syntectonic recrystallization of cooling peridotite. It is interesting to note that many alpine-type peridotites seem to have equilibrated in this temperature range (Evans and Frost, 1975). There are, however, abnormally low-temperature peridotites in metamorphic terrains such as garnet peridotite lenses in the Caledonian basement of Norway and Japanese peridotites in the Sanbagawa metamorphic belt (see Fig. 5-3). For the equilibrations of such low-temperature peridotites, other mechanisms rather than syntectonic recrystallization upon cooling have to be considered. Another implication of the P-T trajectories of the peridotite is that when the P-T paths are compared with published peridotite solidi (Fig. 5-7), the peridotite, even in the center, is not hot enough to melt during rising. If the peridotite is presumed to start rising at higher temperatures, considering the inaccuracies of the temperature estimate of the "primary condition", then the P-T trajectories well inside of the body may cross cut the

dry peridotite solidus at lower pressures, and the inner part of the peridotite body may begin to melt. As it cools, it will crystallize as plagioclase peridotite with gabbro layers. The field evidence is somewhat opposed to this possibility. That is, there are, on the average, more mafic layers in the high pressure part of the massif (outer part) than in the low pressure part (inner part) as is seen in Fig. 2-4. Moreover, it would be very difficult for the primary compositions of the enstatite to survive through the melting episode. It can be concluded therefore that the peridotite was essentially solid during intrusion and already had layered structures at the primary condition ($\sim$1100-1200°C, $\sim$22 kb). The origin of the peridotite and the mafic layers (that is, the differentiation of the massif), therefore, must be sought beyond the stage of the "primary condition."

CHAPTER 6

PETROGENESIS

The initial differentiation of the peridotite is assumed to be igneous; however, not only the present mineralogies of the peridotite and the mafic layers, but also the reconstructed mineralogies at the "primary condition" (1100-1200°C, 20-25 Kb) are not necessarily igneous. The "primary condition" may itself refer to a metamorphic equilibrium condition in the upper mantle. Considering the high temperatures and mobilities of the upper mantle, it is reasonable to suppose that the original igneous mineralogies and textures of the Ronda rocks were destroyed during metamorphism and flow in the mantle. The discussion of petrogenesis, therefore, must rely on properties which were created by igneous processes (crystallization and/or fusion) and have not been modified by subsequent metamorphism. Bulk chemical compositions are such properties, provided metasomatic processes do not predominate in the mantle.

The regional distribution pattern and abundance of the mafic layers were perhaps defined by the igneous processes. Parallelism of the compositional banding of the peridotite and the mafic layering may also date back to the igneous stage, although the original shape and thickness of the layers may have been modified by solid state flow in the mantle.

Dickey (1970) proposed a model for the igneous differentiation of the Ronda peridotite in the light of recent knowledge of igneous petrology. According to this model the peridotite is

a residue of partial fusion in the upper mantle, and the magmatic mafic layers are solidified primary magma generated by the partial fusion. If this is correct, the liquids of the mafic layer compositions must be in equilibrium with mantle rock at the physical conditions of their origin.

A study of petrogenesis, therefore, was initiated with high P-T experiments in order to examine the phase relationships of the mafic layers.

6.1 Experiment

A plagioclase garnet clinopyroxenite (R127) that occurs as a thick layer (∿60 cm) in the garnet lherzolite facies zone (see Fig. 4-1. for the sample location) was chosen for the experimental study[1].

The experiments were conducted in graphite crucibles in a 1/2-inch diameter, solid-media, high-pressure apparatus (Boyd and England, 1960), using the piston-out technique. Sealed $Pt_{95}Au_5$ crucibles were also used for long runs near solidus temperatures to avoid possible introduction of water by the dehydration of the assembly parts. The analyzed rock powder, which contained garnet, plagioclase, and clinopyroxene ($\sim 10\mu$) was used for liquidus runs. Glass prepared from the rock powder (by fusion in $Pt_{95}Au_5$ foil in N_2 gas at 1 atm and 1400°C), mixtures of 70 wt % glass and 30 wt % rock powder, or mixtures of 95 wt % glass and 5 wt % garnet that had been separated from

---

[1]The following paragraph on the experimental method is from Obata and Dickey (1976).

the rock were used for subsolidus runs. Except for a few low-temperature runs in which the charge was slightly moistened (breathed on) before loading, the loaded capsules were dried by heating to glowing red with a gas torch for 30 seconds immediately prior to the run. Run times ranged from 20 minutes to 12 hours. Run products were identified by optical, X-ray diffraction, and electron microprobe methods.

The experimental results are summarized in Tables 6-1 and Fig. 6-1. At pressures up to 8 kbar, olivine (Fo_{85}), clinopyroxene, and plagioclase all crystallize within 25°C of the liquidus, but above 8 kbar clinopyroxene is the sole liquidus phase. From 8 to 20 kbar, clinopyroxene is followed by plagioclase with decreasing temperature. Olivine is not stable above 9 kbar. Garnet first appears above the solidus at about 18 kbar and expands its field toward higher pressure. The plagioclase field decreases with increasing pressure and pinches out at 29 kbar.

Four different subsolidus assemblages have been identified: clinopyroxene + plagioclase + olivine; clinopyroxene + plagioclase; clinopyroxene + plagioclase + garnet; and clinopyroxene + garnet + quartz. The olivine of the first assemblage disappears at the boundary A (Fig. 6-1) by reacting with plagioclase to form aluminous pyroxene components. Garnet appears at boundary B and increases in abundance with pressure toward the boundary C, where plagioclase disappears. Boundaries A and B are established on the basis of marked changes in the kind and abundance of

Table 6-1. Results of experiments on pyroxenite R127.

Run no.	P(kb)	T(°C)	Run dur. (min.)	Cap.	Starting material	Products
36	5	1250	90	G	A	Gl,q-Cpx
32	5	1225	120	G	A	Cpx,Plag,Ol,Gl
64	7	1250	120	G	A	Cpx,Plag,Ol
41	8	1175	150	G	B	Ol,Cpx,Plag
54	8.6	1000	240	G	C	Ol,Cpx,Plag
42	9	1175	150	G	B	Cpx,Plag
73	9.5	950	480	G	D	Cpx,Plag,Gar(?trace)
56	9.6	1000	260	G	C	Cpx,Plag
13	10	1300	120	G	A	Gl
16	10	1275	150	G	A	Cpx,Plag,Gl
25	10	1250	180	G	A	Cpx,Plag,Gl
46	10	1225	120	G	A	Cpx,Plag,Gl
40	10	1175	135	G	C	Cpx,Plag,Sp(?trace)
72	11	950	360	G	D	Cpx,Plag,Gar
69	13	1050	250	G	D	Cpx,Plag,Gar
43	14	1150	240	G	B	Cpx,Plag
8	15	1375	90	G	A	Gl
7	15	1350	90	G	A	Cpx,Gl,q-Cpx
9	15	1325	90	G	A	Cpx,Plag,Gl
11	15	1300	150	G	C	Cpx,Plag(?),Gl
21	15	1275	150	G	A	Cpx,Plag,Gl
31	15	1250	190	G	B	Cpx,Plag,Gl(trace), Sp(?)
47	15	1175	210	G	D	Cpx,Plag
48	15	1150	240	G	D	Cpx,Gar,Plag
63	15	1050	255	G	D	Cpx,Gar,Plag

Run no.	P(kb)	T(°C)	Run dur. (min.)	Cap.	Starting material	Products
61	15	950	360	G	D	Cpx,Gar,Plag
65	15	850	480	G	D	Cpx,Gar,Plag
44	16	1225	180	G	B	Cpx,Plag
71	16	1175	180	G	D	Cpx,Gar,Plag, Gl(?)
67	16	1125	240	G	D	Cpx,Gar,Plag
59	16	950	360	G	D	Cpx,Gar,Plag
51	17	1200	180	G	D	Cpx,Gar,Plag
50	17	1175	230	G	D	Cpx,Gar,Plag
57	17	1125	250	G	D	Cpx,Gar,Plag
55	17.8	1255	190	G	D	Cpx,Gar,Plag
53	18	1300	150	G	A	Cpx,Plag,Gar(trace)
1	20	1400	60	G	A	Cpx,Gl,q-Cpx
2	20	1375	100	G	A	Cpx,Gl
3	20	1350	90	G	A	Cpx,Gl
6	20	1325	120	G	A	Cpx,Gar,Plag,Gl
20	20	1300	240	G	B	Cpx,Plag,Gl(trace)
23	20	1250	240	G	C	Cpx,Gar,Plag
75-1	24	1250	375	G	C	Cpx,Gar,Plag(An_{46})
17	25	1500	16	G	A	Gl,q-Cpx
14	25	1475	20	G	A	Cpx,Gl
12	25	1450	30	G	A	Cpx,Gl
30	25	1425	60	G	A	Cpx,Gar,Gl
15	25	1400	60	G	A	Cpx,Gar,Gl
19	25	1375	90	G	A	Cpx,Gar,Gl
26	25	1350	180	G	B	Cpx,Plag(?),Gar,Gl

Table 6-1. (continued)

Run no.	P(kb)	T(°C)	Run dur. (min.)	Cap.	Starting material	Products
49	25	1250	360	G	D	Cpx,Gar,Plag
75-6	27	1350	180	PA	C	Cpx,Gl
75-7	27	1325	300	PA	C	Cpx,Gar(?), Plag(?),Gl(?)
75-3	27	1250	320	G	C	Cpx,Gar,Plag(An_{48})
75-11	27	1200	390	PA	E	Cpx,Gar,Qz(?)
75-10	28.5	1300	300	PA	E	Cpx,Gar,Qz(trace)
75-5	29	1350	210	G	C	Cpx,Gar,Qz(trace)
28	30	1475	60	G	A	Cpx,Gar,Gl
27	30	1450	60	G	A	Cpx,Gar,Gl
29	30	1425	130	G	B	Cpx,Gar,Gl(?)
52	30	1250	340	G	D	Cpx,Gar,Qz(trace)

Table 6-1. Keys

Abbreviations: Cap., capsule; G, graphite; PA, sealed $Pt_{95}Au_5$ capsule. Starting materials, A, original rock powder; C, glass prepared from the rock powder (see text); B, mixture of 95% C+5% A; D, mixture of 70% C+30% A; E, mixture of 95% C+5% garnet. Gl, glass; q-, quenched product, question mark indicates uncertain phases. When the amount of phase is trace, it is indicated in parentheses. Compositions of plagioclase are indicated in parentheses when they were determined by electron microprobe.

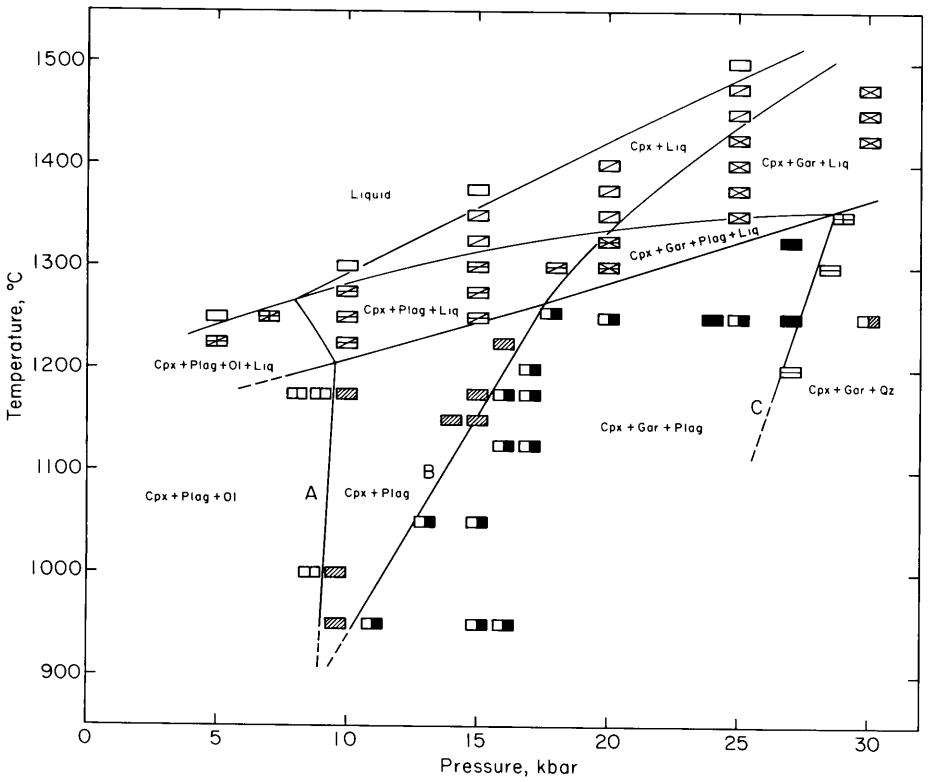

Figure 6-1. Pressure-temperature diagram for the composition of plagioclase-garnet clinopyroxenite R127. Symbols in the subsolidus region: open rectangles with vertical line, Cpx + Plag + Ol formed from glass when seeded with a small amount of rock powder; shaded rectangles, Cpx + Plag formed from glass when seeded with a small amount of rock powder; half-solid rectangles, Cpx + Gar + Plag formed from glass when seeded with a small amount of rock powder; solid rectangles, Cpx + Gar + Plag formed from glass; open rectangles with horizontal line, Cpx + Gar + Qz from glass; crossed open rectangles, Cpx + Gar + Qz formed from glass when seeded with a small amount of garnet; half-shaded rectangles, Cpx + Gar + Qz formed from glass when seeded with a small amount of rock powder.

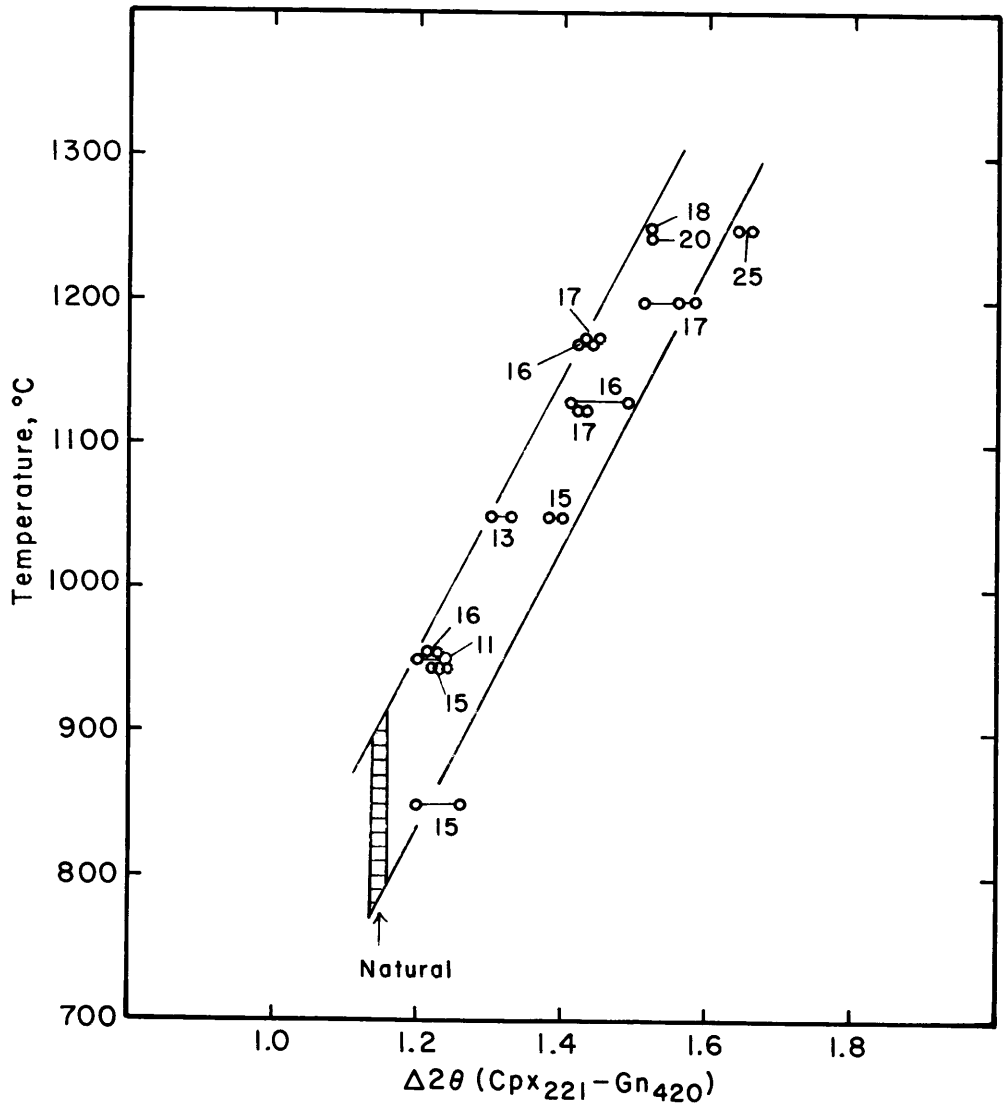

Figure 6-2. Temperature versus $\Delta 2\theta$ (Cpx_{221} - Gar_{420}) diagram for garnets and clinopyroxenes coexisting with plagioclase in experimental run products synthesized from the composition of plagioclase-garnet clinopyroxenite R127. Numbers on data points are pressures in kilobars. Each point is a single measurement.

phases. Boundary C was difficult to locate precisely because plagioclase is too sparse to be detected by X-ray powder diffraction and must be identified by optical and electron microprobe methods. Plagioclase (An_{40-50}) in addition to clinopyroxene and garnet was formed from glass up to 27 kbar at 1250°C. Trace amounts of quartz were identified by scanning electron microscopy in some of the runs beyond boundary C.

The mineral assemblage of the original rock, plagioclase + garnet + clinopyroxene is apparently stable over a broad P-T interval, and it is expected that the phases vary in composition throughout this field. However, because of the fine grain size of the subsolidus run products and their complex textural intergrowths, the phases could rarely be analyzed with the electron microprobe. As an alternative, the compositional changes have been monitored indirectly by X-ray diffraction methods, by measuring the 2θ differences between the (221) peak of clinopyroxene and the (420) peak of garnet. The results of (Fig. 6-2) indicate that this 2θ changes systematically over the temperature-pressure field of the assemblage and that the natural rock equilibrated at a temperature of 800°-900°C. This is an additional, independent estimate of the recrystallization temperatures for the garnet lherzolite facies zone (see p. 141)

A successful electron microprobe analysis was obtained for a clinopyroxene formed with garnet at 1250°C and 30 kbar (5.7 hours), and the result is compared in Table 6-2 with an analysis of the pyroxene in the original rock. The synthetic pyroxene

Table 6-2. Clinopyroxene compositions

	a	b	c
SiO_2	49.6 (0.8)†	48.8	51.99
TiO_2	0.8 (0.04)	1.5	0.28
Al_2O_3	15.8 (0.4)	8.2	15.75
Cr_2O_3	0.1	0.1	0.03
FeO*	6.5 (0.5)	7.0	1.98
MnO	0.1	0.1	tr
MgO	9.0 (0.2)	12.7	10.72
CaO	15.5 (0.5)	20.6	14.75
Na_2O	2.8 (0.1)	1.0	4.22
Total	100.0	100.1	100.09
	Cations per 6 oxygens		
Si	1.787	1.803	1.828
Ti	0.021	0.042	0.008
Al	0.669	0.356	0.654
Cr	0.002	0.004	0.001
Fe^{2+}	0.202	0.218	0.059
Mn	0.003	0.004	tr
Mg	0.481	0.697	0.561
Ca	0.598	0.816	0.555
Na	0.193	0.073	0.287
Total	3.956	4.012	3.961

Table 6-2. (continued)

	Norm in wt%		
$NaAlSi_2O_6$	18.0	6.6	27.5
$CaTiAl_2O_6$	2.3	4.5	0.9
$CaAl_2SiO_6$	21.9	9.9	18.2
$Ca_2Si_2O_6$	19.2	34.8	20.5
$Mg_2Si_2O_6$	22.3	31.2	26.7
$Fe_2Si_2O_6$	12.5	13.1	3.7
SiO_2	3.8	0.0#	2.5

* Total Fe calculated as FeO

† Standard deviation of six averaged analyses.

With total Fe calculated as FeO this calculation shows a silica deficiency. Ferric iron is present, however, (cf. Table 5-4), and the silica deficiency is artificial.

a. Clinopyroxene formed at 30 kbar, 1250°C (Run no. 52).

b. Natural clinopyroxene in R127 (from Table 4-8).

c. Natural clinopyroxene in kyanite eclogite, Z52, from a kimberlite pipe in Yakutia (Sobolev, Kuznetsova and Zyuzin, 1968).

is exceptionally high in Al_2O_3, and the sum of cations per 6 oxygens is unusually low. Expressed in terms of end-member components with all iron as FeO, the analysis shows 3.8 wt % excess silica. If any of the iron is ferric, the silica excess is even larger. Excess silica is not common in pyroxenes but has previously been reported in both natural and synthetic clinopyroxenes formed at high pressures (Sobolev, Kuznetsova, and Zyuzin, 1968; Kushiro, 1969a; Wood, 1976).

6.2 Partial fusion and fractional crystallization

Unlike nonporphyritic volcanic rocks, there is an additional question to be considered for the origin of plutonic rocks such as the mafic layers: Do the mafic layers represent compositions of liquid or cumulate? If the mafic layers are regarded as frozen liquids, the experimental results give the following constraints to the P-T conditions of their origin: 1) the liquid was formed by partial fusion of peridotite without subsequent fractional crystallization at less than 8 kbar (24 km), which is the maximum pressure at which olivine is a liquidus phase. The liquid would crystallize initially to olivine gabbro but might be later metamorphosed, under increasing pressure, to the assemblage garnet + plagioclase + clinopyroxene. 2) if the liquid was formed by partial fusion of dry peridotite at pressures greater than 8 kbar, it must have been subsequently displaced from the olivine field by fractional crystallization. This is possible because, as demonstrated by Kushiro and Yoder

(1974) such liquids have reaction relationships with olivine at pressures between 17 and 30 kbars.

At solidus temperatures below 8 kbar the peridotite would be plagioclase peridotite and so plagioclase would have been involved in the melting and crystallization in Case 1. Rare earth element data (Suen, personal communication), however, eliminate this possibility, that is, neither the peridotites nor the mafic layers have Eu anomalies, which are symptomatic of plagioclase fractionation (by crystallization or fusion).

If the original composition of the liquid had been modified by fractional crystallization as in Case 2, the liquidus temperature of the fractionated liquid would be lower than the solidus of the peridotite with which the original liquid was in equilibrium. Fig. 6-3 compares the liquidus of the mafic layer with published solidus curves of 4 peridotites. The liquidus of the mafic layer coincides with the solidus of spinel lherzolite determined by Kushiro et al. (1968), and lies above those of pyrolite III by Green and Ringwood (1967) and garnet peridotite by Ito and Kennedy (1968). It lies below the solidus of a garnet lherzolite kimberlite nodule determined by Kushiro (1973). Neither spinel nor garnet are present in Kushiro's Kimberlite lherzolite on the solidus, however, so the comparison may not be valid. The drop of the liquid's temperature during the early fractional crystallization may not be detectable by the experimental method, and the mafic layer could be a

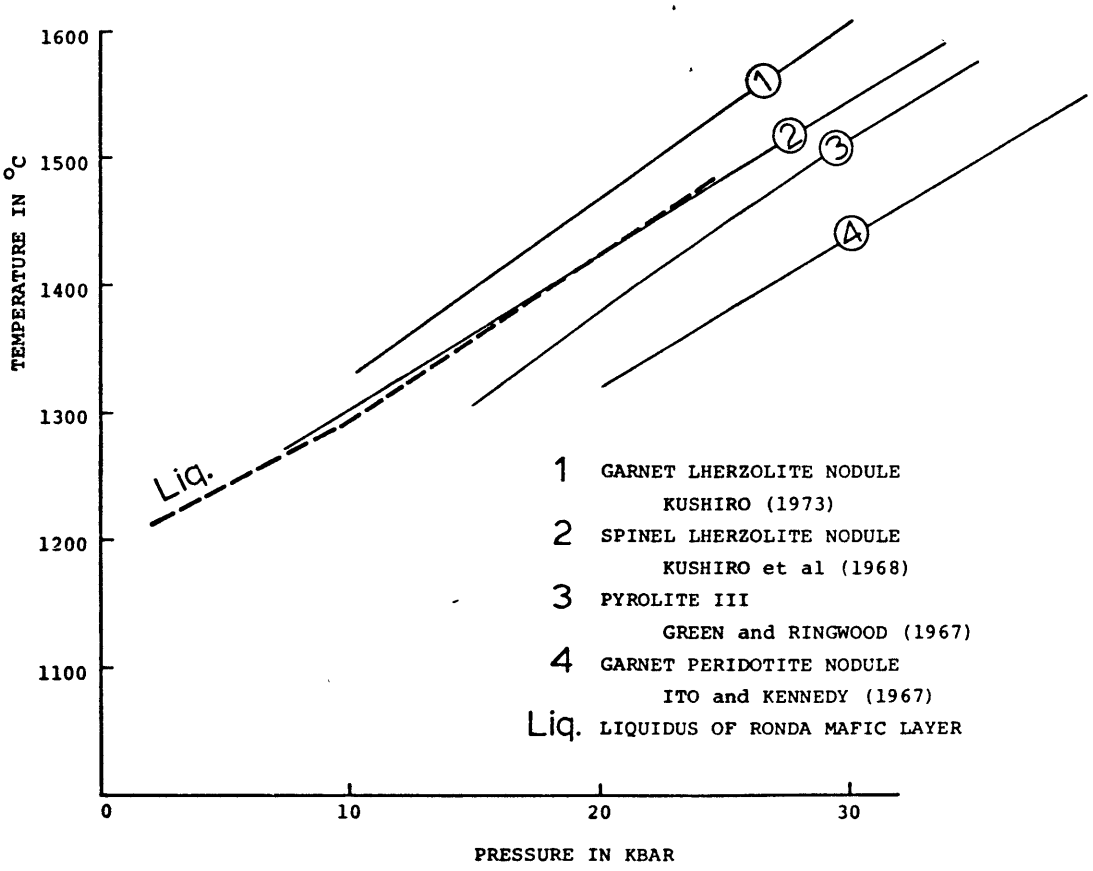

Figure 6-3. Liquidus of R127 compared with 4 published peridotite solidi.

fractionated liquid which was originally derived by partial fusion of peridotite similar to the spinel lherzolite examined by Kushiro et al. (1968). Considering the existence of peridotites with lower solidus curves, however, the liquidus of the mafic layer is thought to be too high for this origin.

The experimental result may be interpreted in different ways if the mafic layer represents a cumulate composition instead of a liquid composition: varieties of cumulate may be obtained by fractional crystallizations due to different liquidus relationships at different pressures. In order to visualize the fractional crystallization trend graphically, the liquidus relations in a model system CaO-MgO-Al_2O_3-SiO_2 at various pressures are summarized in Fig. 6-4 in a projection form, which was employed in Mineral Facies (see the chemographic relation in Fig. 3-16.

Four invariant points in this system were experimentally determined in P-T space by Kushiro and Yoder (1966):

An + Fo + Cpx + Opx + Sp + Liquid at 9 kb, 1350°C

Cpx + Opx + An + Sp + Gar + Liquid at 17 kb, 1400°C

An + Opx + Gar + Cpx + Qz + Liquid at 19 kb, 1450°C

Cpx + Opx + Fo + Sp + Gar + Liquid at 25 kb, 1450°C

The anorthite-enstatite-diopside plane is a thermal barrier above 5 kbar (O'Hara, 1967) and this must break down at some pressure below 19 kbar, at which anorthite-enstatite assemblage is replaced by garnet-quartz. The garnet-pyroxene plane is a

Figure 6-4. Liquidus relations in the system $CaO-MaO-Al_2O_3-SiO_2$ at various pressures , summarized from litteratures. Projection from diopside apex to the $CaAl_2SiO_6-Mg_2SiO_4-SiO_2$ plane. Dioside is always present on the liquidi. Direction of falling temperature are indicated by arrows where they are known.

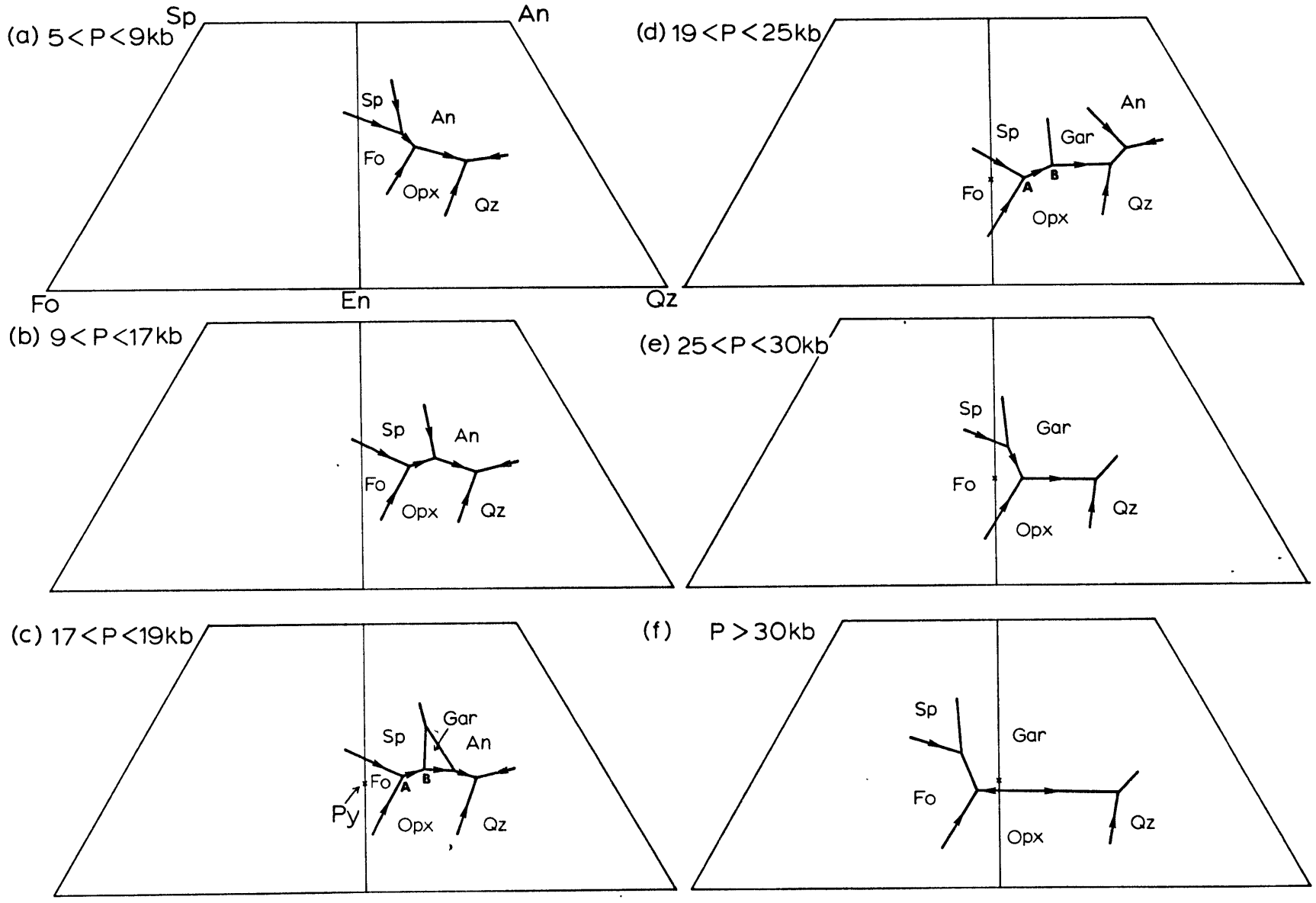
(a) 5<P<9kb
Sp
An
Fo
En
Qz
Sp
An
Fo
Opx
Qz
(d) 19<P<25kb
An
Sp
Gar
A
B
Fo
Opx
Qz
(b) 9<P<17kb
Sp
An
Fo
Opx
Qz
(e) 25<P<30kb
Sp
Gar
Fo
Opx
Qz
(c) 17<P<19kb
Gar
Sp
An
Fo
A
B
Py
Opx
Qz
(f) P>30kb
Sp
Gar
Fo
Opx
Qz

thermal barrier above 30 kbar (O'Hara and Yoder, 1967). Topologies of the liquidus relations change around these pressures as is shown in the series of diagrams in Fig. 6-4, (a) to (f). At pressures between 17 and 25 kbar, for example, a reaction relation, Fo + Liq $\rightarrow$ Sp + Opx + Cpx exists (Kushiro, 1968). Therefore, a liquid A [Fig. 6-4 (c) or (d)], which may be generated by partial fusion of spinel lherzolite, will leave the forsterite field as temperature decreases due to the reaction relation, and change its composition along the spinel - opx - Cpx phase boundary toward B by precipitating orthopyroxene, clinopyroxene and spinel. The geometry requires point B to be another reaction point at which spinel reacts out. There are two possibilities for the reaction relations depending on the compositions of the liquid and the garnet: if the composition of the garnet lies inside the Sp-Opx-Liquid triangle, the reaction would be Sp+Opx+Liq$\rightarrow$Gar+Cpx. If, on the other hand, the composition of the garnet lies outside of the Sp-Opx-Liquid triangle, the reaction would be Sp+Liq$\rightarrow$Gar+Opx+Cpx. In either case, as temperature decreases, the liquid will be displaced from the spinel field and may follow the cotectic line of garnet-orthopyroxene-clinopyroxene. At some point the liquid will be further displaced from the orthopyroxene field by the reaction relation Opx+Liq$\rightarrow$Gar+Cpx, which was found to exist at 30 kbar (O'Hara and Yoder, 1967) and at 20 kbar (Tilley and Yoder, 1963). The sequence of cumulates obtained in this course of fractional crystallization is, therefore, Sp+Opx+Cpx, Gar+Opx+Cpx and Gar+Cpx. The Gar+Opx+Cpx cumulate may not appear at all if the

reaction Opx+Liq→Gar+Cpx takes place as soon as garnet appears at point B.

It should be noted that the first cumulate is undersaturated with silica in the mantle norm due to the presence of spinel and the second and the third cumulates are either on the garnet-pyroxene compositional plane or may be slightly oversaturated with silica if some trapped melt exists because the liquids in equilibrium with the crystals are oversaturated with silica. The mafic layers from the Ronda massif seem to be divided at least into two subgroups of chemical compositions (see Fig. 5-8). They may be called "subcalcic group" for R120, R343, and R322 and "calcic group" for R127, R251, and R183. As pointed out in the previous chapter (p.150), the mafic layers of the "subcalcic group" are undersaturated with silica and two of the "calcic group" are oversaturated with silica in the mantle norm. Therefore, the "subcalcic group" could be early stage cumulates (igneous mineralogy of, Sp + Opx + Cpx + trapped melt) and the "calcic group" could be late stage cumulates (igneous mineralogy of, Gar + Cpx + trapped melt). This model is in harmony with the order of the Fe/Mg ratio, i.e. the mafic layers of the "calcic group" have higher Fe/Mg ratios than those of the "subcalcic group" (see Table 5-4). At pressures between 25 kbar and 30 kbar, a series of cumulates, Gar + Opx + Cpx and Gar + Cpx may similarly be obtained by fractional crystallization as discussed by Kushiro and Yoder (1974). In this case, however, it is impossible to generate

any cumulate or liquid which is undersaturated with silica like the "subcalcic group" mafic layers. Above 30 kbar, at which the garnet-pyroxene plane is a thermal barrier, it is impossible to generate liquids or cumulates oversaturated with silica by partial fusion and fractional crystallization. Below 17 kbar, plagioclase should appear in the late cumulates. Plagioclase fractionation was already ruled out, however, by the rare earth element argument.

Considering the above constraints of the phase equilibria of the natural and the synthetic systems, I should like to propose an alternative model for the genesis of the mafic layers: the mafic layers are not solidified liquids as proposed by Dickey (1970), but are a series of cumulates which were generated by fractional crystallization of melts at pressures between 17 kbar and 25 kbar. The actual pressure range, which is based upon a simple synthetic system, may be different for the natural rocks, particularly because the spinel contains chromium, but quantitative evaluation of such effects is not yet possible. The extremely low concentration of K_2O (less than 0.01 wt%) and P_2O_5 (nil) (see Table 5-4) and the high melting temperature of R127 may be understood by this model. The fractionated liquids apparently escaped from the peridotite. Such liquids would be reactive with olivine and must have reacted in part with the olivine in the peridotite, producing spinel pyroxenite walls along the channels of the escaping liquids. Some chromian pyroxenite layers may be such wall rock reaction products.

There are a few field indications of the in situ fractional crystallization. A transition from undersaturated "subcalcic" (Opx + Cpx + Gar + Sp) assemblage as a metamorphic mineralogy to an oversaturated "calcic" (Plag + Cpx + Gar) assemblage within a thick single layer has been found in the zone of the ariegite facies (Fig. 6-5). A symmetric zoning from undersaturated subcalcic outside to calcic inside in single layer as observed by Kronprobst (1970) in the Beni-Bouchera peridotite (Fig. 6-5) could also be evidence for in situ fractional crystallization.

Composition of peridotite

If the peridotite is a residue of the partial fusion, there must be some systematics in the variation of the peridotite compositions. In order to test the partial fusion hypothesis, 21 peridotites were point-counted under microscope (Appendix 2). The observed modes, however, are metamorphic and, therefore, prohibit direct comparison between different mineral facies. The aluminous phases such as garnet or plagioclase, for example, must have grown at the expense of pyroxenes. Growth of spinel, however, should not have changed the amount of pyroxenes substantially but only compositions of pyroxenes. For the same bulk chemical composition therefore, the metamorphic garnet or plagioclase peridotites contain less pyroxene than the spinel peridotites.

In order to compare bulk composition of the peridotites of different mineral facies, minerals other than olivine

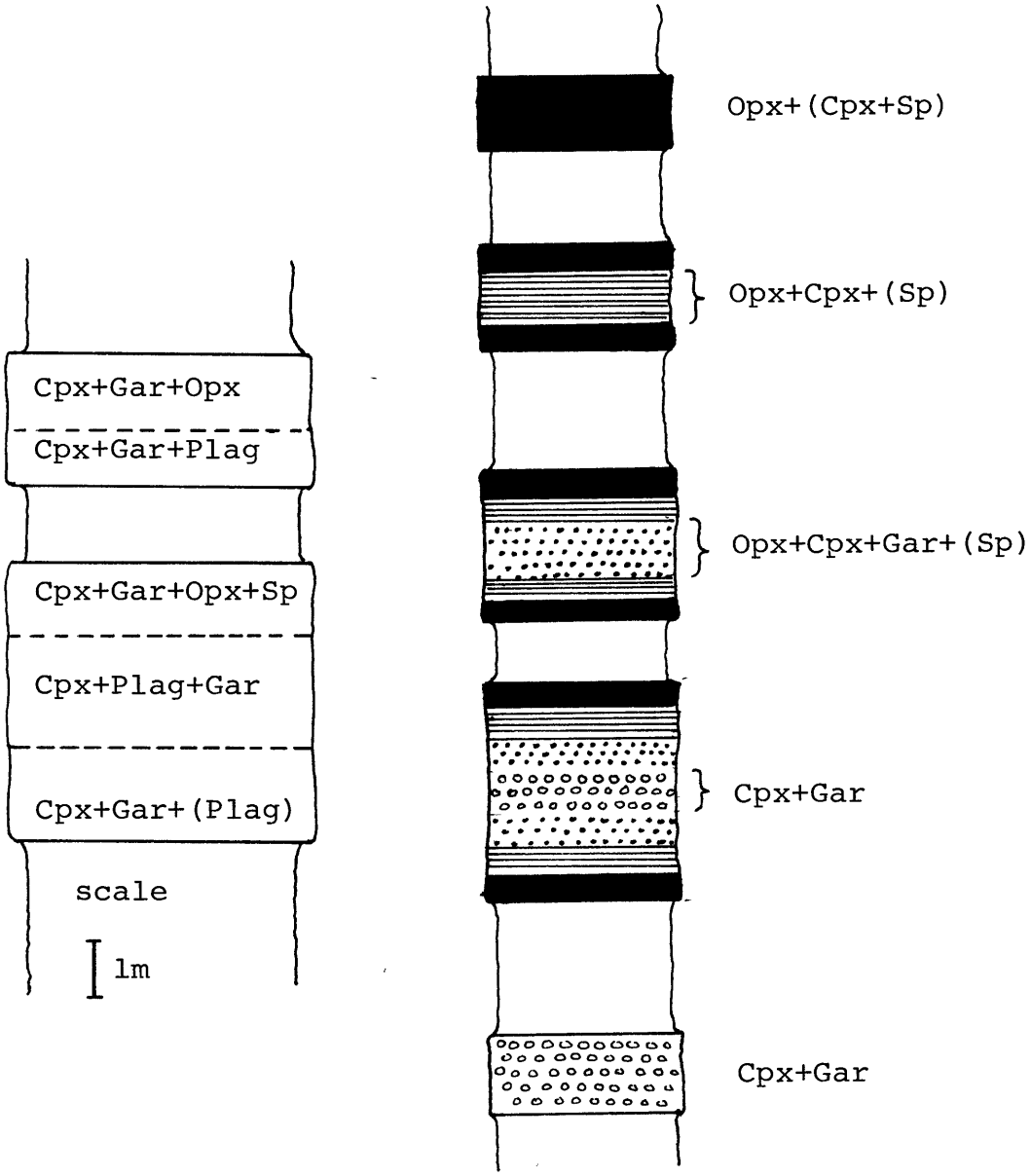

Figure 6-5. Zoned mafic layers in the Ronda massif (left) and in the Beni Bouchera massif (right). The Beni Bouchera column is after Kornprobst (1969). Scale is for the Ronda layers only.

(+ serpentine), orthopyroxene, and clinopyroxene, i.e. garnet, spinel, plagioclase and amphibole (pargasite) were mathematically broken down into olivine and pyroxene components[1], and added to the observed mode of olivine and pyroxenes as follows:

$$ol^* = ol + \text{serpentine} + Sp - Plag + 0.67\ \text{pargasite}$$

$$Opx^* = Opx + Plag + 0.12\ Gar - 0.17\ \text{pargasite}$$

$$Cpx^* = Cpx + Plag + 0.88\ Gar + \text{pargasite}$$

---

1. Garnet, spinel, plagioclase and pargasite may be expressed in terms of olivine and pyroxene components as follows:

$$\underset{\text{gar}}{(Ca_{0.12}Mg_{0.88})_3Al_2Si_3O_{12}} = 0.82\ \underset{\text{opx}}{Mg_3Al_2Si_3O_{12}} + 0.18\ \underset{\text{cpx}}{Ca_2MgAl_2Si_3O_{12}}$$

$$\underset{\text{sp}}{MgAl_2O_4} + \underset{\text{opx}}{Mg_2Si_2O_6} = \underset{\text{opx}}{MgAl_2SiO_6} + \underset{\text{fo}}{Mg_2SiO_4}$$

$$\underset{\text{plag}}{CaAl_2Si_2O_8} + \underset{\text{fo}}{Mg_2SiO_4} = \underset{\text{cpx}}{CaAl_2SiO_6} + \underset{\text{opx}}{Mg_2Si_2O_6}$$

$$\underset{\text{plag}}{NaAlSi_3O_8} + \underset{\text{fo}}{Mg_2SiO_4} = \underset{\text{cpx}}{NaAlSi_2O_6} + \underset{\text{opx}}{Mg_2Si_2O_6}$$

$$\underset{\text{pargasite}}{NaCa_2Mg_4Al_3Si_6O_{22}(OH)_2} + 0.5\ \underset{\text{opx}}{Mg_2Si_2O_6} = \underset{\text{cpx}}{CaMgSi_2O_6} + \underset{\text{cpx}}{CaAl_2SiO_6} + \underset{\text{cpx}}{NaAlSi_2O_6} + 2\underset{\text{fo}}{Mg_2SiO_4} + \underset{\text{vapor}}{H_2O}$$

On this olivine-pyroxene normalized basis, the bulk compositions of the peridotites from the garnet lherzolite, spinel lherzolite and plagioclase lherzolite facies zones are plotted in the Ol*-Opx*-Cpx* triangle in Fig. 6-6. The three groups of peridotites overlap each other, and they define a definite narrow compositional trend from lherzolite to harzburgite and dunite. This is exactly a trend which residual peridotites would follow in the course of partial fusion (c.f. Carter, 1970). A very similar trend has been observed for the Beni-Bouchera peridotite by Kornprobst (1970). No geographic correlation of the depletion of the peridotites is apparent, but the data are not conclusive because the peridotites are typically banded in pyroxene-rich and pyroxene-poor layers and a wide range of compositions may be obtained from a small area in the field.

During the partial fusion, the Mg/Fe ratio of the residual peridotite would increase as the degree of melting increases and the peridotite would become more and more depleted in pyroxenes. The Fo contents of the olivines are chosen as an index of the Mg/Fe ratio of the peridotite and they are plotted against the calculated amount of pyroxenes (Opx* + Cpx*) in Fig. 6-7. The Fo content is insensitive to subsolidus metamorphism (excluding metasomatism) as discussed in Mineral Chemistry (p.101) and may not have been significantly modified since the magmatic stage. There is a weak but definite correlation between Fo content and the pyroxene content as expected from the partial fusion model.

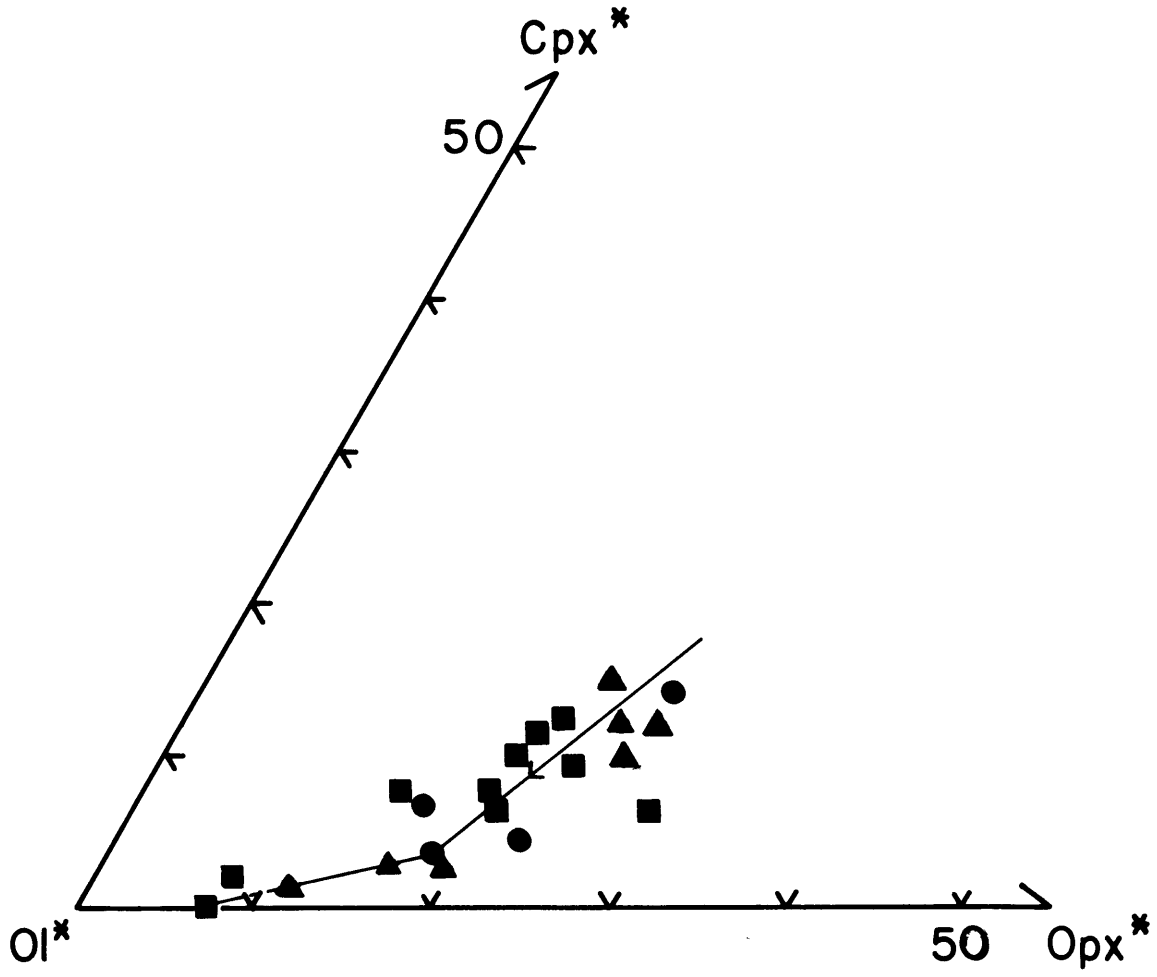

Figure 6-6. Normalized mode of the Ronda peridotite from garnet lherzolite facies zone (circles), spinel lherzolite facies zone (triangle), and plagioclase lherzolite facies zone (squares).

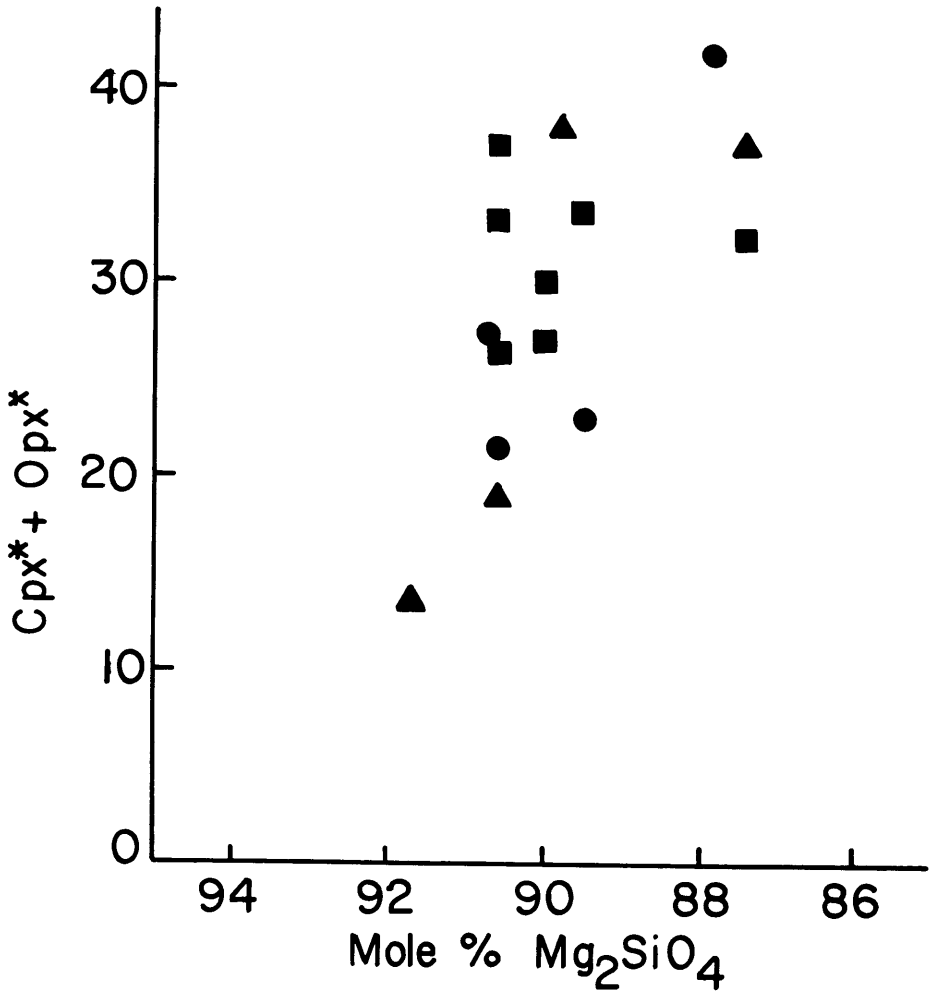

Figure 6-7. Plot of % forsterite in olivines versus total amount of pyroxenes in normalized mode of the Ronda peridotite. Symbols are same as in Figure 6-6.

P-T conditions of partial fusion and fractional crystallization

If the mafic layer R127 did not contain any trapped melt, the solidus of the layer defines the upper limit of the temperature of crystallization. If, on the other hand, it contained trapped melt, which is very likely, the experimentally determined solidus should be slightly lower than that of the pure cumulate, and so the crystallization temperature could be higher than the determined solidus. But, of course, it still should be lower than the peridotite solidus. In the phase diagram in Fig. 6-1, the temperature range of the Gar+Cpx+Liquid field is 1350 to 1425°C at 25 kbar, and narrows down and pinches out around 1350°C at 22 kbar, which coincides with the estimated pressure value for the "primary condition" (20-25 kbar). The liquids coexisting with garnet and clinopyroxene are saturated with silica, and some of them must resemble in composition the liquid which precipitated the cumulate and presumably escaped from the peridotite.

These cumulates cooled together with the surrounding peridotites, perhaps without much pressure change, and re-equilibrated under the "primary condition". The pressure at which partial fusion occurred, however, is not necessarily restricted to the pressure range of fractional crystallization. If the liquid was generated by partial fusion of garnet lherzolite above 25 kbar (>83 km) it must have risen with the host peridotite without cooling, preventing crystallization of the liquid until the pressure was low enough for spinel to appear in early cumulates. (Spinel is necessary to account for the silica deficiencies of the "subcalcic" group.) This situation is possible in a mantle diapir.

Because of the low thermal conductivity of silicates, vertical movements in the mantle are generally considered to be adiabatic. As a diapir rises from deep in the mantle, the adiabatic cooling curve of the diapir will intersect the peridotite solidus at some depth, because the melting temperature curve of the peridotite decreases with pressure faster than the adiabatic temperature curve. As discussed earlier (p. 145), however, the diapir is not really a thermally isolated system, and the outer part will lose some heat by conduction to the surroundings. Partial melting, therefore, begins inside of the diapir. As the melting proceeds, the liquid droplets coalesce into thin sheets, local pockets or lenses (Dickey, 1970). The geometry and orientation of the liquid lenses must be governed by stress and the flow direction of the peridotite. The liquids thus formed are gravitationally and mechanically unstable, and they tend to migrate upward. Considering the reduction of viscosity of magma at high pressures (Kushiro, 1977) the migration of the melt must be fast, especially if the host peridotite is deforming under shear stress. Before the liquid escapes out the diapir, it must traverse the outer cooler zone. There the liquid will be cooled in its channels. This could be the region in which fractional crystallization takes place. After the fractionated liquids escape, the "barren" diapir body is now compositionally zoned from depleted inside without much cumulate matter, through relatively undepleted intermediate zones with spinel websterite cumulate layers (undersaturated "subcalcic group") to undepleted outer-most zones with eclogite cumulate

layers (oversaturated "calcic group").

In the field, it has been observed that mafic layers are concentrated in the west half of the massif, and the east half has very few mafic layers (see Fig. 2-4). Furthermore, the mafic layers in the low and medium pressure zones are undersaturated "subcalcic group", and those in the high pressure zone are "calcic group" with or without excess silica. Perhaps the Ronda massif was, in the upper mantle, very close to the cool "skin" of the mantle diapir, and the flow direction of the melt was from the eastern part to the western part. It must be emphasized that, in this model, the composition of the melt generated by partial fusion of peridotite is inevitably modified by fractional crystallization even before the melt separates from the diapir. If this mechanism is typical of magma formation in the upper mantle, it follows that we have very little chance to sample magmas whose composition has not been modified; i.e., primary magma!

In summary, the present chemical data of the peridotites are consistent with the partial fusion model, and those of the mafic layers and their regional distribution pattern are explained by in situ fractional crystallization of the partial melts in a mantle diapir. Most of the fractionated liquid probably escaped from the peridotite. From the geometry of the mafic layers and the regional pattern of the chemical composition, we may define the shape and the flow direction of the liquid in the upper mantle. Since this model bears important implications in magma genesis in general, it must further be tested with more bulk chemical data

for both major and trace elements.[1]

If this model is correct, where did the fractionated liquid go? What kind of liquid is it? When and where did the partial fusion and the fractional crystallization happen? Because the partial fusion or fractional crystallization are results of upper mantle dynamics and this must be, in some way, coupled with surface phenomena, for example, plate tectonics and volcanism, these questions must be answered in a regional tectonic and geologic framework.

---

[1]This is currently undertaken by C. J. Suen for a Ph.D. thesis at MIT.

Chapter 7

PERIDOTITE INTRUSION AND PLATE TECTONICS

In this chapter, an attempt is made to correlate the petrologic events in the mantle with geologic events in the crust. The intrusion of the peridotite massif is discussed in the context of circum-Mediterranean plate tectonics.

Petrogenetic constraints and the P-T history of the peridotite indicate that the displacement of the peridotite and associated materials from the mantle into the crust may have been a three-step process:

Step 1. A mantle diapir rose from deep in the mantle. ← The peridotite was differentiated by partial fusion followed by fractional crystallization of the partial melts. Most of the fractionated liquids escaped upwards. After the igneous differentiation, the peridotite cooled at about 70 km below the surface and completely re-equilibrated below the solidus at 1100 to 1200°C ("primary condition").

Step 2. The peridotite with mafic segregations or layers rose again as a solid and penetrated the lower crust. The P-T trajectories deduced in Chapter 5 apply to this stage.

Step 3. Part of the peridotite, together with the Casares unit, was thrust as a 2 km thick sheet over the Blanca unit in the Betic zone. The Blanca unit was metamorphosed by the residual heat of the peridotite at this stage.

The timing of steps 1, 2, and 3 is of great significance. Direct dating of the igneous differentiation of the massif, perhaps by the whole rock Rb-Sr isotope method, has not yet been done. Another way to date Step 1 would be by identifying consequences of the mantle diapir such as volcanism in the geologic record. In the history of the Betic-Rif system, the youngest volcanic rocks which may have been related to the intrusion are: calc-alkaline volcanics of Middle Miocene to Early Pliocene age in south-eastern Spain (Almeria to Alicante) (Arana and Vergas, 1974), the basalt-andesite-rhyolite complex of Late Miocene to post-Pliocene age in northern Morocco (Fuster, 1956) and andesite tuffs of probable Miocene age forming Alboran Island (Hernandes-Pachco and Ibarrola, 1970). These volcanic eruptions were interpreted by Loomis (1975) as anatexic melts from the lower crust, which was heated by a hot peridotite diapir. These volcanics are, however, too acidic and are located too far east or south of the peridotite to be derivatives of the igneous differentiation of the diapir.

Prior to the Neogene eruptions, the next youngest volcanics are rather extensive basic submarine volcanic eruptions in the Late Triassic (Rondeel and Simon, 1974). Volcanism was not restricted to the Betic zone in the Late Triassic but was wide-spread in the western Mediterranean and on the east coast of North America. This Late Triassic volcanism is thought

to signal the initiation of the opening of the present Atlantic ocean (c.f. Dewey et al, 1973). Note that the stratigraphic succession of the Betic Zone ends with Late Triassic sediments. These Late Triassic geologic features may be linked with the mantle diapirism of Step 1. The uplift of the upper mantle may have caused a broad welt of the geosynclinal floor (haut fond) creating a non-depositional environment as suggested by Lundeen (1976). Whether the mantle diapirism was a result of the mantle forces which broke up Gondwanaland or a cause of them is, of course, unknown. The diapir did not reach the crust in Step 1 but apparently stopped in the upper mantle. A sufficiently long time interval between Step 1 and 2 would be required for the peridotite to be thoroughly re-equilibrated as a solid at the primary condition. It was concluded before (p. 68) that the peridotite body had to be thermally equilibrated in order to explain the apparent homogeneity of the "primary compositions" of the orthopyroxenes from different parts of the massif. The time required for a 10 km thick diapir to cool from the solidus temperature would be of the order of a million years. On the other hand, the pyroxenes would respond to the temperature change in the order of a thousand years (supposing a pyroxene grain size of 1 cm and using experimentally measured diffusivity of Al in diopside at

1250°C (Seitz, 1973)). Therefore, heat conduction is the rate determining step for pyroxene homogenization in the diapir. It may be awkward to suppose such a pause in the midst of the diapirism. The buoyancy of the diapir would have been reduced when the melt, which was a low density constituent of the partially molten diapir, escaped from the peridotite. The buoyancy would be further reduced if the escaping melts precipitated garnet pyroxenites within the residual peridotite (eclogites are more dense than the peridotites). It is doubtful, however, that such density increases would stop the rising diapir. Probably the diapir encountered some sudden change of the physical properties of the mantle such as an increase in density or an increase in viscosity or both. This situation might obtain when the diapir encountered the base of the lithosphere.

Once the diapir cooled to the regional geotherm, it would be very difficult for the peridotite to rise again by itself unless it was substantially reheated. There is no adequate source of heat in the residual peridotite, and there is no petrologic evidence for such re-heating. The second rise of the peridotite, therefore, must have been caused by an external tectonic force.

Pitman and Talwani (1972) reconstructed the relative movements of the African and European plates, based on

sea-floor magnetic anomalies in the Atlantic ocean. According to their analysis, from the beginning of the opening of the Atlantic (Late Triassic) until early Jurassic, North America, Spain and Europe were on the same plate, and only the African plate, rotating counter-clockwise, moved eastward away from the American-European plate. Vector analyses of the relative plate motions suggests that the Iberian/African plate boundary is not a pure transform fault, and that the African continent was separated from Iberia. In order to account for this separation, Dewey et al (1973) introduced a ridge-transform fault system deriving from the mid-Atlantic ridge and running into the Tethian plate through the Strait of Gibraltar (see Fig. 10 of Dewey et al, 1973.) If new oceanic crust was accreted between Africa and Iberia at this time, there would be geologic evidences for it in or around the Alboran Sea. Geophysical observations, however, (gravity work by Bonini et al, 1972, seismic work by WGDSS, 1977) suggest that the present Alboran basin does not have typical oceanic structure but may consist of a thin continental crust. (The mean Pn crustal velocity lies between 6.0 and 6.3km/s. No layer of higher velocity could be detected in the lower crust.) Garnet-cordierite gneiss which is similar to rocks of the contact aureoles of the Ronda and Beni-Bouchera peridotites have been cored from the Alboran basin (DSDP Hole 121, Ryan et al, 1973). In the Betic-Rif system there appear to

be no Mesozoic ophiolites or even oceanic tholeiites. Such remnants of oceanic crust are widespread further east in the Mediterranean. Considering these geophysical and geologic observations, the introduction of accreting plate margins in the Alboran Sea area by Dewey et al is difficult to accept. If the plates were not accreted during the relative plate motion, a considerable extensional field would have been developed at the plate boundary. A possible consequence of this would be either lithospheric thinning or fracturing or both. This would be a suitable environment for peridotite near the base of lithosphere to become mechanically unstable.

In the Late Cretaceous (80m.y.) there was a drastic change in the relative plate motion as a consequence of the beginning of the separation of Europe from North America. Africa began to move westward with respect to Europe but continued its relative counter-clockwise rotation. The extensional tectonic environment was then perhaps replaced by a north-south compressional environment with right-lateral shearing at the plate boundary. The first major phase of the Alpine thrusting in the Betic-Rif system may have taken place in this compressional environment. If the Blanca contact aureole was due to the residual heat of the overthrusted peridotite slab, the Step 3 lateral emplacement must have

taken place before the hot peridotite had cooled. This thermal constraint does not allow more than 10^6 years between Steps 2 and 3.

This tectonic model for the emplacement of the mantle diapir may explain not only the Ronda peridotite but also certain other peridotite massifs in the Alpine fold belts in the Mediterranean. As pointed out by Nicolas and Jackson (1972), peridotites in the western Mediterranean are dominantly lherzolite or wehrlite, and those in the eastern Mediterranean are harzburgite or dunite (Fig. 7-1). These depleted peridotites in the eastern Mediterranean lack magmatic mafic layers (Dickey, 1970) and are typically associated with sheeted dikes, pillow lavas and marine sediments (ophiolite complexes). On the other hand, the lherzolite massifs in the western Mediterranean have magmatic layers similar to those in the Ronda massif: Garnet pyroxenites, particularly ceylonite-bearing garnet pyroxenites (ariegites) occur as layers in the spinel lherzolite massifs at Etang de Lherz (Lacrox, 1900, 1917); Beni Bouchera (Kornprobst, 1969), in the serpentinites at Totalp (Peters, 1963; Peters and Niggle, 1964); Malenco Valley (Del Vesco, 1953) and in the garnet peridotite at Alpe Arami (Möckel, 1969). Medium pressure mafic layers (granulite) are common in the spinel lherzolite massifs in Ivria zone (Lensh, 1968, 1971) and low-pressure mafic layers such as gabbro are common in the plagioclase lherzolite massifs in the Piemont Alps (Nicolas, 1966; Boudier, 1976). It is interesting to note that in

the Italian-Swiss Alps, the sequence of mineral facies of the peridotite massifs is, generally from south to north, plagioclase, spinel, and garnet lherzolites. Perhaps these are disintegrated tectonic pieces of an originally mineralogically zoned, large high-temperature peridotite intrusion before its tectonic re-emplacement in the Alpine fold belts.

Chapter 8

CONCLUSIONS

Metamorphism, igneous differentiation and intrusion tectonics of the Ronda high-temperature peridotite intrusion have been discussed. The history of the Ronda massif may be organized in terms of 5 stages (Fig. 8-1): Stage I is defined by Step 1 motion of the peridotite (mantle diapir). This results in igneous differentiation of the peridotite in the upper mantle. The present peridotite is a residue of the partial fusion; the mafic layers are cumulates from the partial melts. The fractional crystallization took place when the liquids passed through the colder margins of the diapir before the liquids escaped. The suggested sequence of cumulates is Cpx + Opx + Sp $\longrightarrow$ (Cpx + Opx + Gar) $\longrightarrow$ Cpx + Gar. It is not certain whether the Cpx + Opx + Gar cumulate ever appeared. The pressure during fractional crystallization was probably close to that of the "primary condition" (i.e., 20 - 25 Kbar). The partial fusion, however, may have started at higher pressure.

Stage II is a pause in the peridotite's movement between Step 1 and 2. The hot differentiated peridotite body cooled slowly and re-equilibrated at the "primary condition" (1100 - 1200°C, 20 - 25 Kb). Upon cooling, the pyroxenes became less aluminus, the peridotite gained more spinel, and the mafic layers gained more garnets. It is not certain whether garnet appeared in the peridotite at this stage. The original

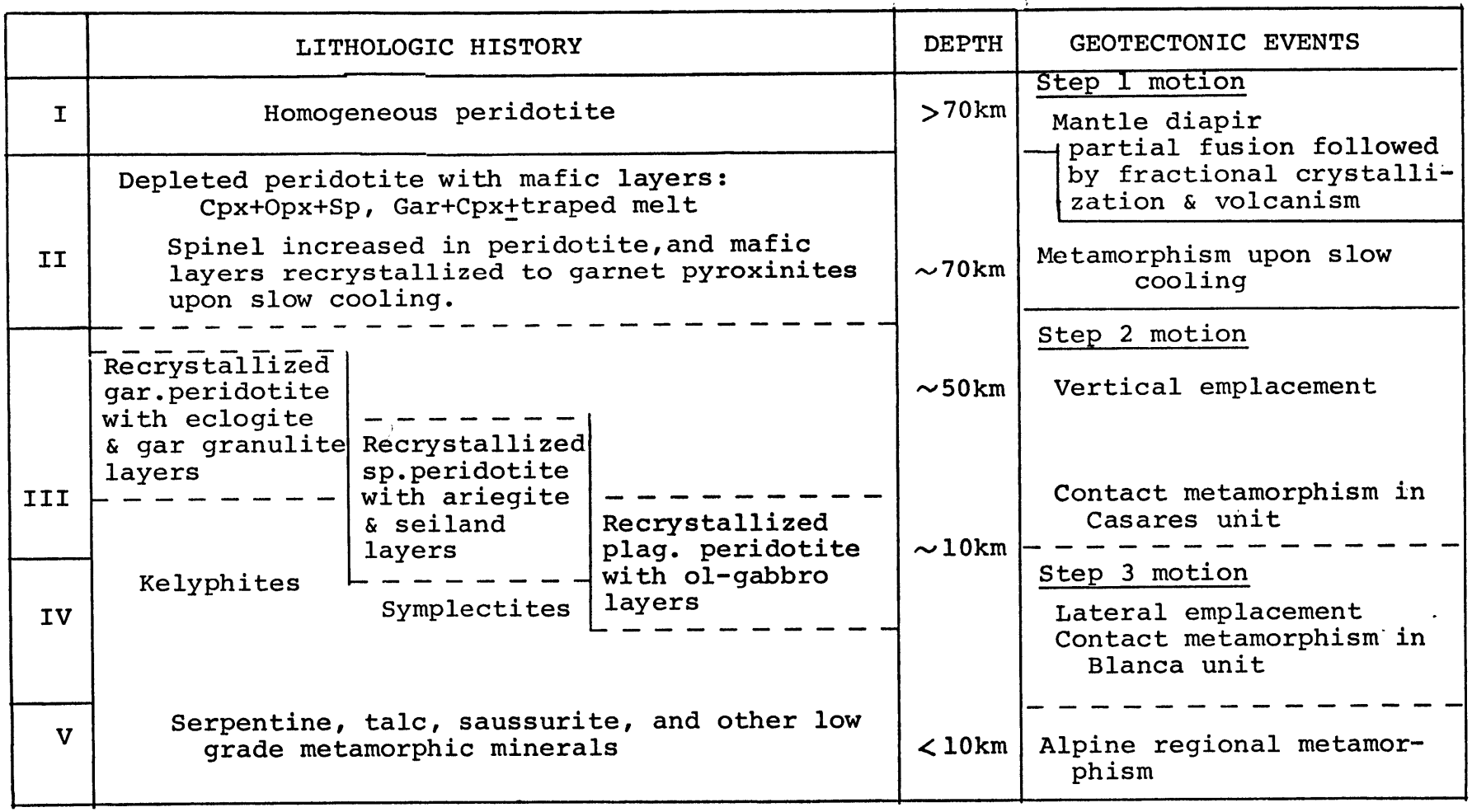

Figure 8-1. History of the Ronda massif.

igneous mineralogy was completely destroyed at this stage. The "primary condition" should not be confused with the original igneous condition.[1]

Stage III is the time of Step 2 motion. Due to the thermal gradient of an ascending peridotite body, the peridotite was frozen-in successively from outside to inside, resulting in mineralogical zoning from garnet peridotites with garnet pyroxenite layers to plagioclase peridotites with olivine gabbro layers. Crustal sediments (now in the Casares unit) were metamorphosed to garnet-cordierite gneiss by the peridotite at 700 - 800°C, $\sim$4 Kb.

Stage IV is defined by the northward thrusting (Step 3 motion) of the peridotite slab, together with the Casares unit, over the Blanca unit. The Blanca unit was metamorphosed to cordierite-sillimanite gneiss. The interior of the peridotite slab might still have been hot ($>$1000°C), and some plagioclase peridotite might have been recrystallizing at this stage. Kelyphitization of garnets and decomposition of aluminus pyroxenes may have taken place in the pressure range of plagioclase lherzolite facies either at the end of Stage III or at Stage IV.

---

[1]Green (1964) defined the primary stage of the Lizard peridotite in a similar sense; however, he considered the possibility that the primary stage was the stage of igneous accumulation.

Stage V is a time of low-grade metamorphism of probable alpine age. This may be further subdivided but this low-grade metamorphism was not studied.

There are still ambiguities about the age of the peridotite emplacement. Suggested ages are Late Triassic for Stage I, Late Mesozoic to Miocene for Stage III and IV.

From the present petrologic study of the Ronda peridotite massif the following general conclusions and remarks may be drawn:

1) Different parts of a single, cooling and rising geologic unit such as a mantle diapir may follow multiple P-T trajectories. Apparent large pressure ranges in some alpine-type peridotites have been emphasized by Wilshire and Jackson (1975) although their pressure estimates are very uncertain. Careful studies of the mineralogical and chemical inhomogenuities of other alpine-type peridotites and interpretations based on dynamic cooling models as developed for the Ronda massif clarify the mechanism of mantle intrusions, and their place in regional tectonics.

2) The thermal gradient within a mantle diapir may significantly affect magma genesis. Fractional crystallization of the partial melts driven from the hot center of the diapir was proposed for the origin of the magmatic mafic layers. This mechanism may be called in situ fractional crystallization because fractional crystallization takes place inside of

the diapir. The composition of the magma is inevitably modified before it separates from the diapir. It was suggested that if this mechanism is typical in the process of magma formation in the upper mantle, we have little chance to sample primary magmas.

Although much progress has been made in recent years in high pressure phase equilibria concerning magma genesis, our knowledge of actual mechanism of magma segregation from the liquid - droplet stage to the magma-resevoir stage is still limited. The Ronda peridotite massif contains field evidence of partial fusion and in situ fractional crystallization of the upper mantle. Further study both in the field and in the laboratory would improve our knowledge of both chemical and physical processes of magma genesis.

ACKNOWLEDGEMENTS

I would gracefully acknowledge my supervisor, John Dickey, for guiding me to the Ronda project, and for his continuous help, advice and encouragement throughout this work, without which this thesis would not have been completed.

I would like to thank Dr. H.S. Yoder for giving me an opportunity to work in the Geophysical Laboratory as a guest investigator in 1974. Dr. I. Kushiro supervised me in the high pressure experiments and kindly made a few supplemental runs.

Thanks are also due to Fred Frey, who inspired me in geochemistry and shared a memorable hard-working week with us in the field in summer 1975, Stan Hart for instructing me in geochemical kinetics, and Chris Goetze in rock mechanics.

My field assistants were Eiko Obata in 1974, and Dorian Nicole in 1975.

Tony Irving kindly donated microprobe standards.

Alan Parkes assisted me in microprobe and computer techniques.

I learned much through discussions with friends and colleagues. Especially I would like to thank Meg Lundeen (Wellesley College) for her cooperation in the project and for instructing me in geology of the Betic, John Suen for cooperation in the field and laboratory work and discussions on geochemistry, and Takeshi Mori (Kobe University) for discussions on high pressure phase equilibria. Close

correspondence with Takeshi was always a source of inspiration and encouragement.

The manuscript was typed by Department secretaries. Mark Sneeringer proofread the typescript. Thanks for their efforts.

My studies were supported by the Earth Sciences Division of the National Science Foundation (Grant Nos. GA-41072, DES 73-00264 and EAR 76-84067).

Lastly I would like to thank my wife Eiko for her help, constant encouragement at home and patience throughout my work.

REFERENCES CITED

Akella, J., 1973. Effect of pressure on the composition of coexisting pyroxenes and garnet in the system $CaSiO_3$-$MgSiO_3$-$FeSiO_3$-$CaAlTi_2O_6$. Carnegie Inst. Wash. Year Book, 72, 523-526.

Akella, J., 1974. Solubility of Al_2O_3 in orthopyroxene coexisting with garnet and clinopyroxene for compositions on the diopside-pyrope join in the system $CaSiO_3$-$MgSiO_3$-Al_2O_3. Carnegie Inst. Wash. Year Book, 73, 273-278.

Akella, J., 1976. Garnet pyroxene equilibria in the system $CaSiO_3$-$MgSiO_3$-Al_2O_3 and in a natural mineral mixture. Amer. Mineral., 61, 589-598.

Aoki, K., 1975. Origin of phlogopite and potassic richterite bearing peridotite xenoliths from South Africa. Contrib. Mineral. Petrol., 53, 145-156.

Araña, V. and Vargas, R., 1974. Plate tectonics and volcanism in the Gibraltar Arc. Tectonophys., 24, 197-212.

Ave'Lallemant, H.G. and Carter, N.L., 1970. Syntectonic recrystallization of olivine and modes of flow in the upper mantle. Geol. Soc. Amer. Bull., 81, 2203-2220.

Banno, S., 1970. Classification of eclogites in terms of physical conditions of their origin. Phys. Earth Planet. Inter., 3, 405-421.

Banno, S. and Matsui, Y., 1965. Eclogite types and partition of Mg, Fe, and Mn between clinopyroxene and garnet. Proc. Japan Acad., 41, 716-721.

Beeson, M.H. and Jackson, E.D., 1970. Origin of garnet pyroxenite xenoliths at Salt Lake Crater, Oahu. Mineral. Soc. Amer. Spec. Paper No. 2, 95-112.

Best, M.G., 1974. Mantle-derived amphibole within inclusions in alkalic-basaltic lavas. Jour. Geophys. Res., 79, 2107-2113.

Boudier, F., 1976. Le massif lherzolitique de Lanzo (Alps Piemontaises) etude structurale et petrologique. Thesis, Nantes, 163 p.

Boyd, F.R., 1970. Garnet peridotites and the system $CaSiO_3$-$MgSiO_3$-Al_2O_3. Mineral. Soc. Amer. Spec. Paper 3, 63-75.

Boyd, F.R., 1971. Pargasite-spinel peridotite xenolith from the Wesselton Mine. Carnegie Inst. Wash. Year Book, 70, 138-142.

Boyd, F.R., 1973. A pyroxene geotherm. Geochim. Cosmochim. Acta, 37, 2533-2546.

Boyd, F.R. and England, J.L., 1960. Apparatus for phase-equilibrium measurements at pressures up to 50Kb and temperatures up to 1750 C. Jour. Geophys. Res. 65, 741-748.

Boyd, F.R. and Schairer, J.F., 1964. The system $MgSiO_3$-$CaMgSi_2O_6$. Jour. Petrol., 5, 275-309.

Bonini, W.E., Loomis, T.P., and Robertson, J.D., 1973. Gravity anomalies, ultramafic intrusions, and the tectonics of the region around the Strait of Gibraltar. Jour. Geophys. Res., 78, 1372-1382.

Carswell, D.A., 1968a. Picritic magma-residual dunite relationships in garnet peridotite at Kalskaret near Tafjord, South Norway. Contr. Mineral. Petrol., 19, 97-124.

Carswell, D.A., 1968b. Possible primary upper mantle peridotite in Norwegian basal gneiss. Lithos, 1, 322-355.

Carswell, D.A., 1973. Garnet pyroxenite lens within Ugelvik layered garnet peridotite. Earth Planet. Sci. Lett., 20, 347-352.

Carter, J.L., 1970. Mineralogy and chemistry of the Earth's upper mantle based on the partial fusion-partial crystallization model. Geol. Soc. Amer. Bull., 81, 2021-2034.

Carter, N.L. and Ave'Lallemant, H.G., 1970. High temperature flow of dunite and peridotite. Geol. Soc. Amer. Bull., 81, 2181-2202.

Charlu, T.V., Newton, R.C., and Kleppa, O.J., 1975. Enthalpies of formation at 970°K of compounds in the system MgO-Al_2O_3-SiO_2 from high temperature solution chemistry. Geochim. Cosmochim. Acta, 39, 1487-1497.

Darot, M., 1973. Methods d'analyse structurale et cinematique. Applications a l'étude du massif ultrabasique de la Sierra Bermeja. Thesis, Nantes, 120 p.

Davis, B.T.C. and Boyd, F.R., 1966. The join $Mg_2Si_2O_6$-$CaMgSi_2O_6$ at 30 kb and its application to pyroxenes from kimberlite. Jour. Geophys. Res., 71, 3567-3576.

Del Vesco, E., 1953. Genesi e metamorfosi delle rocce basiche e ultrabasiche nell'ambiente mesozonale dell'orogene pennidico. Schweiz. Mineral. Petrogr. Mitt., 33, 173-480.

De Roever, W.P. and Nijhuis, H.J., 1964. Plurifacial alpine metamorphism in the eastern Betic Cordilleras (SE Spain) with special reference to the genesis of glaucophane. Geol. Rundsch., 53, 324-336.

Dewey, J.F., Pitman, W.C., III, Ryan, W.B.F., and Bonnin, J., 1973. Plate tectonics and the evolution of the Alpine system. Geol. Soc. Amer. Bull., 84, 3137-3180.

Dickey, J.S. Jr., 1970. Partial fusion products in alpine-type peridotites: Serrania de la Ronda and other examples. Mineral. Soc. Amer. Spec. Paper 3, 33-49.

Dickey, J.S. Jr. and Obata, M., 1974. Graphic hornfels dikes in the Ronda high-temperature peridotite massif. Amer. Mineral., 59, 1183-1189.

Didon, J., Durand Delga, M., and Kornprobst, J., 1973. Homologies géologiques entre les deux rives du detroit de Gibraltar. Bull. Soc. Géol. France, Sér. 7, 15, 77-105.

Dürr, S.H., 1967. Geologie de Serrania de Ronda und ihrer südwestlichen Auslaufer. Geologica Romana, 6, 1-73.

Egeler, C.G. and Simon, Q.J., 1969. Sur la tectonique de la Zone Betique (Cordillères Bétiques, Espagne). Kgl. Akad. Wetensch. Verh. Natuurk, ser. 1, 25, 90 p.

Emslie, R.F., 1970. Liquidus relations and subsolidus reactions in some plagioclase-bearing systems. Carnegie Inst. Wash. Year Book, 69, 148-155.

Erlank, A.J., 1973. Kimberlitic potassic richterite and the distribution of potassium in the mantle. Inter. Kimberlite Conference, abstract, 103-106.

Erlank, A.J. and Finger, L.W., 1970. The occurrence of potassic richterite in a mica nodule from the Wesselton kimberlite, South Africa. Carnegie Inst. Wash. Year Book, 68, 320-324.

Evans, B.W. and Frost, B.R., 1975. Chrome-spinel in progressive metamorphism - a preliminary analysis. Geochim. Cosmochim. Acta, 39, 959-972.

Fallot, P., 1948. Les cordillères bétique. Cons. Sup. Invest. Cient., Inst. Lucas Mallada, 8, 83-172.

Fiala, J., 1966. The distribution of elements in mineral phases of some garnet peridotites from the Bohemian Massif. Krystallinikum, 4, 31-53.

Francis, D.M., 1976. The origin of amphibole in lherzolite xenoliths from Nunivak Island, Alaska. Jour. Petrol., 17, 357-378.

Frey, F.A. and Green, D.H., 1974. The mineralogy and origin of lherzolite inclusions in Victorian basanites. Geochim. Cosmochim. Acta, 38, 1023-1059.

Fujii, T., 1976. Solubility of Al_2O_3 in enstatite coexisting with forsterite and spinel. Carnegie Inst. Wash. Year Book, 75, 566-571.

Fuster, J., 1956. La provinica volcánica de la Gueleya (Marreucos español). Estudios geológicos, 29, 59-94.

Girod, M., 1967. Données pétrographiques sur des pyroxenolites a granat en enclaves dans des basalt du Hoggan (Sahara central). Bull. Soc. Franc. Mineral. Crist., 90, 202-213.

Green, D.H., 1964. The petrogenesis of the high-temperature peridotite intrusion in the Lizard area, Cornwall. Jour. Petrol., 5, 134-188.

Green, D.H. and Ringwood, A.E., 1967. The stability fields of aluminous pyroxene peridotite and garnet peridotite and their relevance in upper mantle structure. Earth Planet. Sci. Lett., 3, 151-160.

Green, D.H. and Hibberson, W., 1970. The instability of plagioclase in peridotite at high pressures. Lithos, 3, 209-221.

Griffin, W.L., 1973. Lherzolite nodules from the Fen alkaline complex, Norway. Contr. Mineral. Petrol., 38, 135-146.

Hensen, B.J., 1973. Pyroxenes and garnets as geothermometers and barometers. Carnegie Inst. Wash. Year Book, 72, 527-534.

Hernandez-Pacheco, A. and Ibarrola, E., 1970. Nuevos datos sobre la petrologia y geoquimica des las rocas volcánicas de Alboran (Mediterraneo occidental, Almeria). Estudios Geologicos, 26, 93-103.

Herzberg, C.T. and Chapman, N.A., 1976. Clinopyroxene geothermometry of spinel-lherzolites. Amer. Mineral., 61, 626-637.

Irvine, T.N., 1967. Chromian spinel as a petrogenetic indicator. Part 2. Petrologic application. Canad. Jour. Earth Sci., 4, 71-103.

Irving, A.J., 1974. Geochemical and high pressure experimental studies of garnet pyroxenite and pyroxene granulite xenoliths from the Delegate basaltic pipes, Australia. Jour. Petrol., 15, 1-40.

Ito, K. and Kennedy, G.C., 1967. Melting and phase relations in a natural peridotite to 40 kilobars. Amer. Jour. Sci., 265, 519-538.

Jackson, E.D., 1969. Chemical variation in coexisting chromite and olivine in chromite zones of the Stillwater Complex. Econ. Geol., 4, 41-71.

Kornprobst, J., 1966. A propos des peridotites du massif des Beni-Bouchera (Rif serpentrional, Maroc). Bull. Soc. Franc. Mineral. Cristallogr., 89, 399-404.

Kretz, R., 1963. Distribution of magnesium and iron between orthopyroxene and calcic pyroxene in natural mineral assemblages. Jour. Geol., 71, 773-785.

Kurat, G., 1971. Granat-Spinell-Websterit und Lherzolith aus dem Basalttuff von Kapfenstein, Steiermark. Tschermaks Mineral. Petrogr. Mitt., 16, 192-214.

Kushiro, I., 1968. Compositions of magmas formed by partial zone melting of the earth's upper mantle. Jour. Geophys. Res., 73, 619-634.

Kushiro, I., 1969a. Clinopyroxene solid solutions formed by reactions between diopside and plagioclase at high pressures. Mineral. Soc. Amer. Spec. Paper 2, 179-191.

Kushiro, I., 1969b. The system forsterite-diopside-silica with and without water at high pressures. Amer. Jour. Sci., Schairer Vol. 267A, 269-294.

Kushiro, I., 1973. Partial melting of garnet lherzolites from kimberlite at high pressures. In: P.H. Nixon, ed., Lesotho Kimberlites, Lesotho National Development Corporation, Maseru, Lesotho, pp. 294-299.

Kushiro, I. and Kuno, H., 1963. Origin of primary basalt magmas and classification of basaltic rocks. Jour. Petrol., 4, 75-89.

Kushiro, I. and Yoder, H.S. Jr., 1966. Anorthite-forsterite and anorthite-enstatite reactions and their bearing on the basalt-eclogite transformation. Jour. Petrol., 7, 337-362.

Kushiro, I., Syono, Y., and Akimoto, S., 1967. Effect of pressure on garnet-pyroxene equilibrium in the system $MgSiO_3$-$CaSiO_3$-Al_2O_3. Earth Planet. Sci. Lett., 2, 460-464.

Kushiro, I., Syono, Y., and Akimoto, S., 1968. Melting of a peridotite at high pressures and high water pressures. Jour. Geophys. Res., 73, 6023-6029.

Kushiro, I. and Yoder, H.S., 1974. Formation of eclogite from garnet lherzolite liquidus relations in a portion of the system $MgSiO_3$-$CaSiO_3$-Al_2O_3 at high pressures. Carnegie Inst. Wash. Year Book, 73, 266-269.

Kushiro, I., Yoder, H.S. Jr., and Mysen, B.O., 1976. Viscosities of basalt and andesite melts at high pressures. Jour. Geophys. Res., 81, 6351-6356.

Kopecký, L. and Sattran, V., 1966. Buried occurrence of pyrope-peridotite and the structure of the crystalline basement in the extreme south-west of the Ceske Stredohori mountains. Krystalinikum, 4, 65-86.

Lensch, G., 1968. Die Ultramafitite der Zone von Ivrea und ihre geologische Interpretation. Schweiz. Mineral. Petrogr. Mitt., 48, 91-102.

Lensch, G., 1971. Die Ultramafitite der Zone von Ivrea. Ann. Univ. Saraviensis, 9, 5-146.

Lindsley, D.H., King, H.E. Jr., and Turnock, A.C., 1974a. Compositions of synthetic augite and hypersthene coexisting at 810°C: application to pyroxenes from lunar highland rocks. Geophys. Res. Lett., 1, 134-136.

Lindsley, D.H., King, H.E. Jr., Turnock, A.C., and Grover, J.E., 1974b. Phase relations in the pyroxene quadrilateral at 980°C and 15 kbar. Geol. Soc. Am. Abstracts with Programs, 6, 846.

Lindsley, D.H. and Dixon, S.A., 1976. Diopside-enstatite equilibria at 850°C to 1400°C, 5 to 35 kb. Amer. Jour. Sci., 276, 1285-1301.

Lacrox, A., 1900. Les roches basiques accompagnant les lherzolites et les ophites des Pyrénées. Rept. 8th Intern. Geol. Congr., Paris, 806-838.

Lacrox, A., 1917. Les peridotites des Pyrénées et les autres roches intrusives non-feldspathiques qui les accompagnant. C.R. Acad. Sci., Paris, 165, 381-387.

Lundeen, M.T., 1976. Structural evolution of the Ronda peridotite and its tectonic position in the Betic Cordilleras, Spain. Thesis, Harvard Univ., 177 p.

Lundeen, M.T., 1977. Emplacement of the Ronda peridotite, Sierra Bermeja, Spain. Geol. Soc. Amer. Bull. (in press).

Loomis, T.P., 1972a. Contact metamorphism of pelitic rock by the Ronda ultramafic intrusion, southern Spain. Geol. Soc. Amer. Bull., 83, 2449-2474.

Loomis, T.P., 1972b. Diapiric emplacement of the Ronda high-temperature ultramafic intrusion, southern Spain. Geol. Soc. Amer. Bull., 83, 2475-2496.

Loomis, T.P., 1975. Tertiary mantle diapirism, orogeny, and plate tectonics east of the Strait of Gibraltar. Amer. Jour. Sci., 275, 1-30.

Lovering, J.F. and White, A.J.R., 1969. Granulitic and eclogite inclusions from basic pipes at Delegate, Australia. Contr. Mineral. Petrol., 21, 9-52.

MacGregor, I.D., 1964. The reaction 4 enstatite + spinel = forsterite + pyrope. Carnegie Inst. Wash. Year Book, 63, 157.

MacGregor, I.D., 1970. The effect of CaO, Cr_2O_3, Fe_2O_3, and Al_2O_3 on the stability of spinel and garnet peridotites. Phys. Earth Planet. Inter., 3, 372-377.

MacGregor, I.D., 1974. The system $MgO-Al_2O_3-SiO_2$: solubility of Al_2O_3 in enstatite for spinel and garnet peridotite compositions. Amer. Mineral., 59, 110-119.

MacKenzie, D.B., 1960. High-temperature alpine-type peridotite from Venezuela. Bull. Geol. Soc. Amer., 71, 303-318.

Matsui, Y. and Nishizawa, O., 1975. Iron(II)-magnesium exchange equilibrium between olivine and calcium-free pyroxene over a temperature range 800°C to 1300°C. Bull. Bull. Soc. fr. Mineral. Crystallogr., 97, 122-130.

Medaris, L.G. Jr., 1975. Coexisting spinel and silicates in alpine peridotites of the granulite facies. Geochim. Cosmochim. Acta, 39, 947-958.

Melson, W.G., Jarosewich, E., Bowen, V.T., and Thompson, G., 1967. St. Peter and St. Paul rocks: a high temperature, mantle-derived intrusion. Science, 155, 1532-1535.

Mercier, J-C.C. and Nicolas, A., 1975. Textures and fabrics of upper-mantle peridotites as illustrated by xenoliths from basalts. Jour. Petrol., 16, 454-487.

Millard, Y., 1959. Les massifs metamorphiques et ultrabasiques de la zone paleozoic intern du Rif. Notes Serv. Geol. Maroc, 147, 125-160.

Mökel, J.R., 1969. The structural petrology of the garnet-peridotite of Alpe Arami (Ticino, Switzerland). Leidse Geol. Mededel., 42, 61-130.

Mollat, H., 1968. Schichtenfolge und tektonischer Bau der Sierra Blanca und ihrer Umgebung (Betische Kordilleren, Südspanien). Geol. Jahrb., 86, 471-521.

Mori, T., 1977. Geothermometry of spinel lherzolites. Contrib. Mineral. Petrol., 59, 261-279.

Mori, T. and Banno, S., 1973. Petrology of peridotite and garnet clinopyroxenite of the Mt. Higasi-Akaisi Mass, Central Sikoku, Japan - subsolidus relation of anhydrous phases. Contr. Mineral. Petrol., 41, 301-323.

Mori, T. and Green, D.H., 1975. Pyroxenes in the system $Mg_2Si_2O_6$-$-CaMgSi_2O_6$ at high pressure. Earth Planet. Sci. Lett., 26, 277-286.

Mori, T. and Green, D.H., 1976. Subsolidus equilibria between pyroxenes in the CaO-MgO-SiO_2 system at high pressures and temperatures. Amer. Mineral., 61, 616-625.

Mori, T. and Green, D.H., 1977a. Experimental study on pyroxene equilibria in the system CaO-MgO-FeO-SiO_2. Jour. Petrol., (in press).

Mori, T. and Green, D.H., 1977b. Laboratory duplication of phase equilibria observed in natural garnet lherzolites. Jour. Geol., (in press).

Mysen, B.O. and Boettcher, A.L., 1975. Melting of a hydrous mantle. Part I. Phase relations of natural peridotite at high pressures and temperatures with controlled activity of water, carbon dioxide, and hydrogen. Jour. Petrol., 16, 520-548.

Nehru, C.E. and Wyllie, P.J., 1974. Electron microprobe measurement of pyroxenes coexisting with H_2O-undersaturated liquid in the join $CaMgSi_2O_6$-$Mg_2Si_2O_6$-H_2O at 30 kilobars, with applications to geothermometry. Contrib. Mineral. Petrol., 48, 221-228.

Nicolas, A., 1966. Etude pétrochimique des roches vertes et de leurs minéraux entre Dora Maira et Grand Paradis (Alpes Piémontaises). Thesis, Nantes, 178 p.

Nicolas, A., Bouchez, J.L., Boudier, F., and Mercier, J-C.C., 1971. Textures, structures and fabrics due to solid state flow in some Euopean lherzolites. Tectonophysics, 12, 55-86.

Nicolas, A. and Jackson, E.D., 1972. Repartition en deux provinces des peridotites des chaînes alpines logeant la Mediterranée: implications geotectoniques. Schweiz. Mineral. Petrogr. Mitt., 52, 479-495.

Nixon, P.H. and Boyd, F.R., 1973. Petrogenesis of the granular and sheared ultrabasic nodule suite in kimberlite. In: P.H. Nixon, ed., Lesotho Kimberlites, Cape Town, pp. 48-56.

Obata, M., 1976. The solubility of Al_2O_3 in orthopyroxenes in spinel and plagioclase peridotites and spinel pyroxenite. Amer. Mineral., 61, 804-816.

Obata, M., Banno, S., and Mori, T., 1974. The iron-magnesium partitioning between naturally occurring coexisting olivine and Ca-rich clinopyroxene: an application of the simple mixture model to olivine solid solution. Bull. Soc. fr. Mineral. Cristallogr., 97, 101-107.

Obata, M. and Dickey, J.S. Jr., 1976. Phase relations of mafic layers in the Ronda peridotite. Carnegie Inst. Wash. Year Book, 75, 562-566.

O'Hara, M.J., 1960. A garnet-hornblende-pyroxene rock from Grenelg, Inverness-shire. Geol. Mag., 97, 145-156.

O'Hara, M.J., 1961. Zoned ultrabasic and basic gneiss masses in the early Lewisian metamorphic complex at Scourie, Sutherland. Jour. Petrol., 2, 248-276.

O'Hara, M.J., 1967. Mineral paragenesis in ultrabasic rocks. In: P.J. Wyllie, ed., Ultramafic and Related Rocks, Wiley, New York, pp. 393-401.

O'Hara, M.J., 1968. The bearing of phase equilibria studies in synthetic and natural systems on the origin and evolution of basic and ultrabasic rocks. Earth Sci. Rev., 4, 69-133.

O'Hara, M.J. and Mercy, E.L.P., 1963a. Petrology and petrogenesis of some garnetiferous peridotite. Trans. Roy. Soc. Edinburgh, 65, 251-314.

O'Hara, M.J. and Schairer, J.F., 1963b. The join diopside-pyrope at atmospheric pressure. Carnegie Inst. Wash. Year Book, 62, 107-115.

O'Hara, M.J. and Yoder, H.S. Jr., 1967. Formation and fractionation of basic magmas at high pressures. Scott. Jour. Geol., 3, 67-117.

O'Hara, M.J., Richardson, S.W., and Wilson, G., 1971. Garnet peridotite stability and occurrence in crust and mantle. Contrib. Mineral. Petrol., 32, 48-68.

Peters, T., 1963. Mineralogie und Petrographie des Totalp serpentins bei Davos. Schweiz. Mineral. Petrogr. Mitt., 43, 529-685.

Peters, T. and Niggli, E., 1964. Spinellführende Pyroxenite ("Ariégite") in den Lherzolitkorpen von Lherz und Umgebung (Ariège, Pyrenäen) und der Totalp (Graubünden, Schweiz), ein Vergleich. Schweiz. Mineral. Petrogr. Mitt., 44, 513-517.

Pitman, W.C. III, and Talwani, M., 1972. Sea-floor spreading in the North Atlantic. Geol. Soc. Amer. Bull., 83, 619-643.

Richter, W., 1971. Ariegite, Spinell-Peridotite und Phlogopit-Klinopyroxene aus dem Tuff von Tobaj im südlichen Burgenland. Tschermaks Mineral. Petrogr. Mitt., 16, 227-251.

Robertson, J.D., 1970. A gravity study of the Serrania de la Ronda, Provencia Malaga Espana. Geol. Eng. Rep. 70-1, 1-41, Princeton Univ., Princeton, N.J..

Rondeel, H.E. and Simon, O.J., 1974. Betic cordilleras. In: A.M. Spencer, ed., Mesozoic-Cenozoic Orogenic Belts, Geol. Soc. London, pp. 23-35.

Ryan, W.B., et al., 1973. Western Alboran basin-site 121. Initial Rept. DSDP XIII, 43-89.

Seitz, M.G., 1973, 1973. Uranium and thorium diffusion in diopside and fluorapatite. Carnegie Inst. Wash. Year Book, 72, 586-588.

Shervais, J.W., Wilshire, H.G., and Schwarzman, E.C., 1973. Garnet clinopyroxene from Dish Hill, California. Earth Planet. Sci. Lett., 19, 120-130.

Sobolev, N.R. Jr., Kuznetsova, I.K., and Zyuzin, N.I., 1968. The petrology of grospydite xenoliths from the Zagadochnaya kimberlite pipe in Yakutia. Jour. Petrol., 9, 253-280.

Streckeisen, A., 1976. To each plutonic rock its proper name. Earth Sci. Rev., 12, 1-33.

Varne, R., 1970. Hornblende lherzolite and the upper mantle. Contrib. Mineral. Petrol., 27, 45-51.

Warner, R.D. and Luth, W.C., 1974. The diopside-orthoenstatite two phase region in the system $CaMgSi_2O_6$-$Mg_2Si_2O_6$. Amer. Mineral., 39, 98-109.

WGDSS(Working Group for Deep Seismic Sounding in the Alboran Sea 1974), 1977. Crustal seismic profiles in the Alboran Sea - preliminary results, in press.

Wilshire, H.G. and Jackson, E.D., 1975. Problems in determining mantle geotherms from pyroxene compositions of ultramafic rocks. Jour. Geophys., 83, 313-329.

Wood, J.B., 1974. The solubility of alumina in orthopyroxene coexisting with garnet. Contrib. Mineral. Petrol., 46, 1-15.

Wood, J.B., 1975. The application of thermodynamics to some subsolidus equilibria involving solid solutions. Fortschr. Mineral., 52, 21-45.

Wood, J.B., 1976. On the stoichiometry of clinopyroxenes in the system $CaO-MgO-Al_2O_3-SiO_2$. Carnegie Inst. Wash. Year Book, 75, 741-746.

Wood, B.J. and Banno, S., 1973. Garnet-orthopyroxene and orthopyroxene-clinopyroxene relationships in simple and complex systems. Contrib. Mineral. Petrol., 42, 109-124.

APPENDIX 1

Method of Microprobe Analyses

The microprobe is part of an automated system designed by Finger and Hadidiacos (1972) using a PDP11/20 mini-computer. The instrument has a take-off angle of 38.5° and employs three spectrometers with analyzing crystals of RAP, PET and LiF. Flow proportional counter are used with the first two crystals and a scintillation counter is used with the LiF crystal.

Analyses were reduced on-line with the GeoLab" program of Finger and Hadidiacos (1972) which employs the correction scheme of Albee and Roy (1970). In a standard operation set-up, a filament voltage of 15 KV was used with a beam current of 300 μA and counting time of 20 to 30 sec. per element.

Both synthetic and natural materials were used for standards:

Di65Jd35 glass for Si, Al, Mg, Ca, Na in ortho- and clinopyroxenes.

En95Al5 glass for Si, Al, Mg in orthopyroxene.

P-140 glass for Si, Fe, Mg in olivine.

Cossyrite (natural) for Fe in ortho- and clinopyroxenes.

Di-2Ti glass for Ti in ortho- and clinopyroxenes.

Di94CrCaTs6 glass for Cr in ortho- and clinopyroxenes.

An60 glass for Si, Al, Ca, Na in plagioclase.

52-NL-11 (natural chromite) for Cr in spinel.

Synthetic $MgAl_2O_4$ spinel for Mg and Al in spinel.

For garnets, a natural garnet megacryst DD-1, which was corrected by A. Irving and analyzed by J. Ito (personal communication

in 1976), was used. Ito's analysis of DD-1 is: SiO_2, 42.16; Al_2O_3, 23.05; TiO_2, 0.38; Cr_2O_3, 0.11; Fe_2O_3, 0.77; FeO, 8.98; MnO, 0.30; MgO, 19.38; CaO, 5.34, Na_2O, 0.03, K_2O, 0.0; Total, 100.50.

References

Albee, A. L., and Roy, L., 1970. Correction factors for electron probe analysis of silicates, oxides, carbonates, phosphates, and sulphates. Anal. Chem. 42, 1408-1414.

Finger, L. W., and Hadidiacos, C. G., 1972. Electron microprobe automation. Carnegie Inst. Wash. Year Book, 71, 598-600.

APPENDIX 2. Modal analyses of peridotites and olivine compositions.

	Ol	Serp	Opx	Cpx	Sp	Gar	Plag	Amph	opaque	Ol*	Opx*	Cpx*	ΣPx	Fo(mole%)
R37	63	4	26	2.5	1	--	3.7	--	tr	64.3	30.9	6.2	37.1	90.6
R131	70	3	17	7	<0.2	--	3	tr	tr	70	19	11	30	89.9
R196	77	2	16	3	1.7	--	--	tr	tr	80.7	16	3.1	19.1	90.6
R501	40	31	17	2	<1	7	--	1	1.7	72.7	22.6	4.3	26.9	90.1
R740	58	18	13	1	1	7	--	1.3	<1	77.9	17.6	3.6	21.2	90.6
R696	43	30	13	4.3	1	4	--	1.3	3	77.0	16.5	6.5	23	89.4
R243	60	--	23	15	3	--	tr	tr	tr	62	23	15	38	89.8
R25	61	15	16	2.2	1.3	--	4.4	--	tr	72.9	20.4	6.6	27	90.7
R224										66	21	12.4	33.4	89.5†
7319	68	18	12	1.6	1	--	--	tr	tr	87	12	1.6	13.6	91.7
74578	51	11	27	10	1.7	--	--	tr	tr	63.7	27	10	37	---
R927	59	20	12	0.7	0.6	--	6.9	--	tr	72.7	18.9	7.6	26.5	90.6
R346	72	2	16	1.6	1	--	7.8	--	tr	67.2	23.8	9.4	33.2	90.6
R930	33	58	7.4	--	1.1	--	--	--	--	92.5	7.4	0	7.4	---
R123	46	11	18	10	0.6	12.3	--	1.8	<1	58.8	27.8	14.0	41.8	87.8†
R180	66	6	15	6	1.8	--	5.6	--	tr	68.2	20.6	11.6	32.2	87.4†
R315	63	tr	25	12	<0.1	--	--	tr	tr	63	25	12	37	87.4†
R717	46	14	27	12	1.8	--	--	tr	tr	61	27	12	39	---
R845	70	7	20.2	2.4	0.4	--	--	tr	tr	77.4	20.2	2.7	22.9	---
R893A	66	23	8	2	0.7	--	--	--	tr	89.7	8	2	10	---
R893B	66	13	12	5	1.5	--	2.8	--	tr	77.7	14.8	7.8	22.6	---

Method of point counting is same as discribed in Table 4-1a. Cpx*, Opx*, Ol*, normalized modes (method in P. 178). ΣPx, sum of Opx* and Cpx*. Olivine compositions with "†" are by X-ray diffraction method (Dickey, 1970). R224 was not point-counted but calculated mantle norm of Kushiro and Kuno (1963) from bulk composition in Dickey (1970).

APPENDIX 3

Complete List of Microprobe Analyses of Orthopyroxenes, Clinopyroxenes and Spinels in Peridotites.

SIO2	TIO2	AL2O3	CR2O3	FEO	MNO	MGO	CAO	NA2O	K2O	TOTAL	SAMPLE	ANAL.NO
55.83	0.04	3.19	0.26	6.30	0.17	34.55	0.46	0.04	0.0	100.84	OPX R 501	000100
55.42	0.05	3.19	0.33	6.52	0.18	34.79	0.48	0.0	0.0	100.96	OPX R 501	000200
55.58	0.07	2.82	0.32	6.34	0.15	33.48	0.43	0.04	0.0	99.23	OPX R 501	000300
55.50	0.04	3.11	0.39	6.26	0.14	33.39	0.41	0.06	0.0	99.30	OPX R 501	000400
56.08	0.05	3.11	0.34	6.24	0.13	34.84	0.43	0.06	0.0	101.28	OPX R 501	000500
55.01	0.05	3.19	0.36	7.04	0.13	33.21	0.43	0.03	0.0	99.45	OPX R 501	000600
54.85	0.04	3.24	0.33	6.70	0.19	35.08	0.46	0.07	0.0	100.96	OPX R 501	000700
55.99	0.09	3.11	0.41	6.60	0.12	34.01	0.42	0.0	0.0	100.75	OPX R 501	010101
55.66	0.08	3.43	0.36	6.78	0.14	33.82	0.42	0.0	0.0	100.69	OPX R 501	010102
55.91	0.10	3.14	0.43	6.59	0.11	33.87	0.43	0.0	0.0	100.58	OPX R 501	010201
55.09	0.08	4.47	0.39	7.63	0.22	32.56	0.40	0.0	0.0	100.84	OPX R 501	010202
56.23	0.09	2.99	0.36	6.60	0.16	33.86	0.43	0.0	0.0	100.72	OPX R 501	010301
55.41	0.09	3.52	0.37	6.82	0.17	33.47	0.43	0.0	0.0	100.28	OPX R 501	010302
55.97	0.09	3.21	0.35	6.71	0.15	33.46	0.43	0.0	0.0	100.37	OPX R 501	010401
55.57	0.08	4.00	0.42	6.72	0.14	33.21	0.43	0.0	0.0	100.57	OPX R 501	010402
55.68	0.08	3.21	0.30	6.65	0.15	33.47	0.41	0.0	0.0	99.95	OPX R 501	010501
52.57	0.48	5.36	1.05	2.45	0.11	16.18	20.50	1.88	0.02	100.60	CPX R 501	000100
52.91	0.43	5.00	0.93	2.61	0.05	16.15	19.75	2.17	0.0	100.00	CPX R 501	000200
53.33	0.11	5.11	0.96	2.36	0.0	15.94	20.32	1.88	0.0	100.01	CPX R 501	000300

SIO2	TIO2	AL2O3	CR2O3	FEO	MNO	MGO	CAO	NA2O	K2O	TOTAL	SAMPLE	ANAL.NO
53.15	0.51	5.54	1.13	2.55	0.08	15.33	20.25	2.02	0.0	100.56	CPX R 501	000500
53.29	0.52	5.54	1.15	2.59	0.06	15.11	19.86	2.11	0.0	100.23	CPX R 501	000600
53.86	0.56	5.71	1.13	2.41	0.09	15.27	19.02	2.09	0.0	100.14	CPX R 501	000700
55.39	0.14	3.19	0.27	6.50	0.13	34.09	0.45	0.0	0.0	100.16	OPX R 740	020101
55.21	0.12	3.19	0.29	6.60	0.15	34.28	0.41	0.0	0.0	100.25	OPX R 740	020200
55.65	0.12	3.56	0.26	6.55	0.18	34.44	0.46	0.0	0.0	101.22	OPX R 740	020300
54.82	0.14	3.14	0.40	6.46	0.13	34.50	0.45	0.0	0.0	100.04	OPX R 740	030101
54.89	0.13	3.79	0.42	7.13	0.22	34.17	0.42	0.0	0.0	101.17	OPX R 740	030102
55.41	0.15	3.21	0.36	6.59	0.20	33.79	0.45	0.0	0.0	100.16	OPX R 740	030201
54.54	0.09	3.35	0.42	7.03	0.18	34.30	0.44	0.0	0.0	100.35	OPX R 740	030301
55.31	0.10	3.09	0.27	7.26	0.24	34.19	0.49	0.0	0.0	100.95	OPX R 740	030302
55.41	0.13	3.36	0.35	6.76	0.18	34.23	0.42	0.0	0.0	100.84	OPX R 740	030400
55.66	0.05	3.25	0.25	6.99	0.18	33.55	0.39	0.0	0.0	100.32	OPX R 740	030501
53.18	0.51	5.45	0.99	2.57	0.07	15.82	20.35	1.86	0.0	100.80	CPX R 740	020101
53.06	0.47	5.38	0.93	2.53	0.07	15.55	20.90	1.71	0.0	100.60	CPX R 740	020102
53.10	0.45	5.33	1.06	2.41	0.09	15.68	20.78	1.91	0.0	100.81	CPX R 740	020201
52.60	0.45	5.91	1.00	2.27	0.10	15.24	21.19	1.80	0.0	100.56	CPX R 740	020202
52.78	0.52	5.36	1.01	2.49	0.10	15.53	20.37	1.90	0.0	100.06	CPX R 740	020301
52.32	0.50	5.97	0.69	2.50	0.09	15.42	20.92	1.67	0.0	100.08	CPX R 740	020302

SIO2	TIO2	AI2O3	CR2O3	FEO	MNO	MGO	CAO	NA2O	K2O	TOTAL	SAMPLE	ANAL.NO
52.47	0.43	5.36	1.09	2.59	0.11	16.18	21.14	1.59	0.0	100.96	CPX R 740	030102
52.75	0.34	5.35	1.01	2.29	0.10	16.12	21.79	1.44	0.0	101.19	CPX R 740	030201
52.34	0.51	5.30	1.04	2.67	0.09	16.23	20.68	1.64	0.0	100.50	CPX R 740	030301
55.55	0.16	3.05	0.25	7.36	0.15	33.70	0.42	0.0	0.0	100.64	OPX R 696	000100
54.45	0.14	3.40	0.29	7.29	0.14	34.06	0.46	0.0	0.0	100.23	OPX R 696	010100
54.52	0.17	3.25	0.31	7.46	0.16	34.12	0.48	0.0	0.0	100.47	OPX R 696	010200
55.45	0.09	2.48	0.31	7.52	0.07	33.46	0.41	0.02	0.0	99.81	OPX R 696	010202
54.84	0.15	3.74	0.30	7.45	0.18	33.69	0.44	0.0	0.0	100.79	OPX R 696	010300
54.81	0.13	3.44	0.24	7.38	0.16	33.84	0.43	0.0	0.0	100.43	OPX R 696	010400
54.55	0.13	3.50	0.28	7.54	0.18	33.85	0.39	0.0	0.0	100.42	OPX R 696	010500
55.57	0.11	2.66	0.18	7.29	0.11	33.80	0.39	0.0	0.0	100.11	OPX R 696	010502
55.11	0.14	3.58	0.28	7.56	0.22	33.37	0.42	0.0	0.0	100.68	OPX R 696	020101
55.17	0.15	3.31	0.25	7.29	0.18	32.99	0.44	0.0	0.0	99.78	OPX R 696	020300
54.71	0.12	3.64	0.29	7.54	0.17	33.13	0.43	0.0	0.0	100.03	OPX R 696	020401
53.65	0.09	4.43	0.39	7.34	0.16	33.55	0.39	0.0	0.0	100.00	OPX R 696	020200
53.59	0.08	4.78	0.36	7.49	0.18	33.39	0.36	0.0	0.0	100.23	OPX R 696	020202
52.67	0.91	7.14	0.95	2.90	0.04	14.43	19.64	2.16	0.0	100.84	CPX R 696	010201
0.0	0.64	6.09	0.53	2.57	0.0	0.0	21.20	1.87	0.0	32.90	CPX R 696	010202
51.88	0.99	6.38	0.89	2.88	0.04	14.80	19.70	2.05	0.0	99.52	CPX R 696	010301

SIO2	TIO2	AL2O3	CR2O3	FEO	MNO	MGO	CAC	NA2O	K2O	TOTAL	SAMPLE	ANAL.NO
52.12	0.77	6.35	0.75	2.60	0.0	14.72	19.88	2.36	0.0	99.55	CPX R 696	010501
51.63	0.84	6.67	0.91	2.84	0.05	14.62	20.19	2.14	0.0	99.89	CPX R 696	010601
53.30	0.77	6.31	0.83	2.72	0.08	14.80	19.96	1.89	0.0	100.66	CPX R 696	010701
0.0	0.79	6.33	0.75	2.79	0.0	0.0	20.12	2.18	0.0	32.96	CPX R 696	020101
0.0	0.85	6.59	0.71	2.78	0.0	0.0	20.31	2.06	0.0	33.30	CPX R 696	020301
0.0	1.01	6.35	0.74	2.60	0.0	0.0	21.10	1.75	0.0	33.55	CPX R 696	020401
50.73	1.05	8.17	0.71	2.90	0.0	14.39	19.54	2.51	0.0	100.00	CPX R 696	010101
0.0	1.86	5.98	0.33	2.50	0.0	0.0	21.64	1.64	0.0	33.95	CPX R 696	010102
53.97	0.12	4.64	0.37	7.46	0.13	32.60	0.50	0.08	0.0	99.87	OPX R 123	010200
54.44	0.11	4.35	0.33	7.44	0.12	33.20	0.54	0.08	0.0	100.61	OPX R 123	010301
54.87	0.0	4.55	0.40	7.49	0.0	33.31	0.46	0.0	0.0	101.08	OPX R 123	010400
55.26	0.0	3.36	0.27	7.80	0.0	33.52	0.43	0.0	0.0	100.64	OPX R 123	010700
54.93	0.0	3.26	0.19	7.80	0.0	33.71	0.40	0.0	0.0	100.29	OPX R 123	010800
54.88	0.0	3.87	0.28	7.64	0.0	33.66	0.45	0.0	0.0	100.78	OPX R 123	010900
54.91	0.0	4.02	0.32	7.78	0.0	33.61	0.46	0.0	0.0	101.10	OPX R 123	011001
55.57	0.25	4.25	0.17	6.90	0.06	32.39	0.54	0.07	0.0	100.20	OPX R 123	030100
55.32	0.20	4.28	0.18	7.03	0.04	32.56	0.46	0.02	0.0	100.09	OPX R 123	030200
52.51	0.0	6.31	0.44	7.38	0.0	32.61	0.50	0.0	0.0	99.75	OPX R 123	010101
54.68	0.0	4.12	0.31	7.77	0.0	33.49	0.30	0.0	0.0	100.67	OPX R 123	010102

SIO2	TIO2	AL2O3	CR2O3	FEO	MNO	MGO	CAO	NA2O	K2O	TOTAL	SAMPLE	ANAL.NO
52.22	0.87	7.89	0.66	2.85	0.12	13.92	19.88	2.43	0.0	100.84	CPX R 123	020101
52.50	0.83	6.94	0.72	3.36	0.13	14.51	19.39	2.30	0.0	100.68	CPX R 123	020200
51.50	1.33	7.61	0.54	3.16	0.05	14.65	19.43	2.33	0.0	100.60	CPX R 123	030100
51.11	1.48	7.39	0.55	2.84	0.07	13.99	20.49	2.16	0.0	100.08	CPX R 123	030200
54.89	0.09	4.38	0.48	6.16	0.17	33.24	0.64	0.0	0.0	100.05	OPX R 196	010201
55.76	0.08	3.75	0.47	6.48	0.18	33.82	0.52	0.0	0.0	101.06	OPX R 196	010202
55.16	0.08	4.36	0.49	6.14	0.17	33.43	0.52	0.0	0.0	100.35	OPX R 196	010301
55.58	0.02	3.69	0.39	6.11	0.16	33.71	0.48	0.0	0.0	100.14	OPX R 196	010302
55.46	0.09	3.71	0.46	6.24	0.21	33.82	0.53	0.0	0.0	100.52	OPX R 196	010401
56.32	0.05	2.46	0.30	6.32	0.18	34.05	0.44	0.0	0.0	100.12	OPX R 196	010402
54.95	0.09	4.48	0.47	6.21	0.17	33.62	0.67	0.0	0.0	100.66	OPX R 196	010501
55.49	0.08	3.36	0.24	6.21	0.15	34.46	0.52	0.0	0.0	100.51	OPX R 196	010502
54.82	0.09	3.99	0.39	6.46	0.17	33.89	0.54	0.0	0.0	100.35	OPX R 196	010600
55.02	0.09	4.42	0.51	6.26	0.17	33.97	0.59	0.0	0.0	101.03	OPX R 196	010701
55.19	0.05	3.72	0.38	6.20	0.16	33.98	0.51	0.0	0.0	100.19	OPX R 196	010702
55.71	0.05	3.96	0.46	6.37	0.18	33.59	0.44	0.0	0.0	100.76	OPX R 196	030101
55.70	0.07	3.16	0.32	6.50	0.20	33.93	0.41	0.0	0.0	100.29	OPX R 196	030102
53.43	0.13	6.10	0.80	6.04	0.16	32.63	0.57	0.0	0.0	99.86	OPX F 196	010101
52.38	0.44	6.14	0.92	2.52	0.13	14.77	21.19	1.68	0.0	100.17	CPX R 196	000101

SIO2	TIO2	AL2O3	CR2O3	FEO	MNO	MGO	CAO	NA2O	K2O	TOTAL	SAMPLE	ANAL.NO
51.58	0.42	6.53	1.04	2.41	0.10	14.72	21.03	1.75	0.0	99.58	CPX R 196	010101
0.0	0.68	6.48	1.07	2.26	0.0	0.0	21.44	1.65	0.0	33.58	CPX R 196	010102
52.42	0.41	6.05	0.98	2.43	0.10	15.37	20.96	1.60	0.0	100.32	CPX R 196	010201
51.79	0.45	6.66	1.03	2.49	0.08	14.94	20.66	1.73	0.0	99.83	CPX R 196	010301
0.0	0.64	6.12	1.00	2.39	0.0	0.0	20.60	1.89	0.0	32.64	CPX R 196	010302
51.97	0.41	6.27	0.89	2.37	0.09	15.09	20.73	1.69	0.0	99.51	CPX R 196	010401
51.86	0.45	6.26	1.00	2.49	0.08	15.61	20.01	1.58	0.0	99.34	CPX R 196	030101
51.73	0.46	5.66	0.82	2.31	0.09	15.25	21.28	1.42	0.0	99.02	CPX R 196	030201
51.22	0.46	6.70	1.03	2.36	0.12	14.57	20.99	1.60	0.0	99.05	CPX R 196	030301
52.04	0.45	5.87	0.81	2.37	0.11	15.28	20.97	1.47	0.0	99.37	CPX R 196	030401
51.64	0.46	6.29	0.94	2.45	0.11	15.02	20.68	1.42	0.0	99.01	CPX R 196	030501
54.81	0.10	4.14	0.34	6.68	0.18	34.20	0.37	0.0	0.0	100.82	OPX R 243	030201
56.57	0.08	2.20	0.14	6.83	0.18	34.72	0.29	0.0	0.0	101.01	OPX R 243	030202
53.34	0.12	4.37	0.33	6.86	0.18	34.01	0.56	0.0	0.0	99.77	OPX R 243	030401
53.25	0.12	3.84	0.34	7.02	0.13	34.01	0.50	0.0	0.0	99.21	OPX R 243	030402
55.73	0.09	3.63	0.24	6.96	0.13	34.35	0.48	0.0	0.0	101.61	OPX R 243	030600
0.0	0.0	3.10	0.0	0.0	0.0	0.0	0.43	0.0	0.0	3.53	OPX R 243	030602
54.82	0.09	3.96	0.30	6.86	0.16	34.42	0.36	0.0	0.0	100.97	OPX R 243	030701
55.16	0.10	3.47	0.30	6.90	0.16	34.57	0.35	0.0	0.0	101.01	OPX R 243	030702

SIO2	TIO2	AL2C3	CR2O3	FEC	MNO	MGO	CAO	NA2O	K2O	TOTAL	SAMPLE	ANAL.NO
55.84	0.10	2.85	0.18	6.88	0.17	35.27	0.43	0.0	0.0	101.72	OPX R 243	040302
54.54	0.12	4.43	0.28	6.72	0.15	34.71	0.57	0.0	0.0	101.52	OPX R 243	040401
55.86	0.08	2.14	0.23	6.81	0.20	35.50	0.35	0.0	0.0	101.17	OPX R 243	040402
56.63	0.12	1.67	0.18	6.78	0.17	35.52	0.39	0.0	0.0	101.46	OPX R 243	040201
56.95	0.12	1.09	0.16	6.82	0.16	35.75	0.33	0.0	0.0	101.38	OPX R 243	040202
51.42	0.44	7.25	0.74	2.89	0.13	15.09	20.06	1.48	0.0	99.50	CPX R 243	001101
51.50	0.59	6.43	0.70	3.01	0.14	17.23	19.73	1.01	0.0	100.34	CPX R 243	001102
52.14	0.53	6.50	0.66	2.95	0.11	14.79	20.29	1.80	0.0	99.77	CPX R 243	001201
53.21	0.34	4.91	0.50	2.79	0.12	15.53	20.65	1.51	0.0	99.56	CPX R 243	001202
51.46	0.59	7.19	0.86	2.85	0.16	14.36	20.38	1.72	0.0	99.57	CPX R 243	001301
52.50	0.35	4.73	0.51	2.50	0.10	16.04	22.25	1.02	0.0	100.00	CPX R 243	001302
51.16	0.61	6.49	0.75	2.75	0.15	15.03	21.35	1.24	0.0	99.53	CPX R 243	001401
53.12	0.43	3.56	0.43	2.60	0.13	16.34	22.63	0.79	0.0	100.03	CPX R 243	001402
51.82	0.51	5.90	0.64	2.67	0.13	16.05	21.01	1.05	0.0	99.78	CPX R 243	001501
51.31	0.60	7.09	0.81	2.76	0.14	15.01	20.99	1.46	0.0	100.17	CPX R 243	001600
52.32	0.63	7.11	0.71	2.97	0.13	14.61	20.15	2.12	0.0	100.75	CPX R 243	030201
53.35	0.51	3.68	0.59	2.53	0.11	16.25	23.15	0.90	0.0	101.07	CPX R 243	030202
53.03	0.46	5.52	0.61	2.61	0.13	15.13	21.47	1.62	0.0	100.58	CPX R 243	030203
51.24	0.60	7.18	0.69	3.19	0.14	15.91	19.78	1.49	0.0	100.22	CPX R 243	030301

SIO2	TIO2	AL2O3	CR2O3	FEO	MNO	MGO	CAO	NA2O	K2O	TOTAL	SAMPLE	ANAL.NO
51.62	0.53	7.19	0.83	2.94	0.09	15.94	19.59	1.34	0.0	100.07	CPX R 243	030901
51.70	0.49	6.38	0.89	2.48	0.05	16.09	21.81	0.82	0.0	100.71	CPX R 243	030902
51.54	0.49	6.48	0.81	2.78	0.11	15.24	20.39	1.77	0.0	99.61	CPX R 243	031001
52.45	0.51	8.32	0.90	3.17	0.13	16.71	18.50	1.87	0.0	102.56	CPX R 243	000301
52.48	0.53	8.10	0.89	2.97	0.11	14.95	19.38	2.02	0.0	101.43	CPX R 243	000501
51.80	0.55	7.58	0.89	3.20	0.11	15.55	18.71	1.86	0.0	100.25	CPX R 243	001001
54.20	0.08	3.62	0.71	5.70	0.13	34.20	0.69	0.0	0.0	99.33	OPX 7319	010101
54.89	0.06	2.57	0.39	5.76	0.15	34.84	0.58	0.0	0.0	99.24	OPX 7319	010102
54.23	0.11	3.80	0.69	5.49	0.16	34.04	0.88	0.0	0.0	99.40	OPX 7319	010201
54.26	0.09	3.53	0.64	5.87	0.12	34.35	0.78	0.0	0.0	99.64	OPX 7319	010202
54.45	0.09	3.88	0.74	5.68	0.15	34.18	0.89	0.0	0.0	100.06	OPX 7319	010301
55.26	0.08	2.61	0.42	5.68	0.17	34.91	0.61	0.0	0.0	99.74	OPX 7319	010302
54.56	0.06	3.36	0.63	5.55	0.12	34.65	0.70	0.0	0.0	99.63	OPX 7319	030201
54.65	0.05	3.53	0.65	5.58	0.13	34.84	0.69	0.0	0.0	100.12	OPX 7319	030301
55.14	0.08	4.10	0.71	5.53	0.16	34.27	0.87	0.0	0.0	100.86	OPX 7319	030401
56.04	0.03	2.77	0.38	5.32	0.11	35.04	0.56	0.0	0.0	100.25	OPX 7319	030402
55.91	0.0	2.85	0.38	5.58	0.13	35.27	0.61	0.0	0.0	100.73	OPX 7319	030403
56.57	0.05	2.91	0.39	5.71	0.13	35.27	0.62	0.0	0.0	101.65	OPX 7319	030404
55.23	0.07	3.53	0.61	5.48	0.10	34.80	0.63	0.0	0.0	100.45	OPX 7319	030405

SIO2	TIO2	AL2O3	CR2O3	FEO	MNO	MGO	CAO	NA2O	K2O	TOTAL	SAMPLE	ANAL.NO
54.61	0.05	3.30	0.55	5.60	0.13	35.02	0.59	0.0	0.0	99.85	OPX 7319	030601
54.74	0.05	3.92	0.74	5.71	0.12	34.97	0.59	0.0	0.0	100.84	OPX 7319	030701
55.30	0.03	2.51	0.36	5.82	0.16	35.30	0.56	0.0	0.0	100.04	OPX 7319	000100
55.96	0.05	2.20	0.46	5.75	0.14	34.95	0.47	0.0	0.0	99.98	OPX 7319	020201
55.88	0.03	1.73	0.31	5.63	0.12	35.21	0.36	0.0	0.0	99.27	OPX 7319	020202
56.19	0.06	2.80	0.59	5.74	0.15	35.00	0.41	0.0	0.0	100.94	OPX 7319	020301
0.0	0.0	2.27	0.48	0.0	0.0	0.0	0.39	0.0	0.0	3.14	OPX 7319	020302
52.53	0.32	5.04	1.53	2.12	0.10	15.40	21.68	1.46	0.0	100.18	CPX 7319	000101
54.24	0.21	3.86	0.91	2.13	0.09	16.05	22.40	1.29	0.0	101.18	CPX 7319	000102
52.17	0.34	5.62	1.73	2.47	0.09	15.63	20.71	1.41	0.0	100.17	CPX 7319	010101
51.88	0.32	5.37	1.54	2.54	0.11	16.19	20.80	1.31	0.0	100.06	CPX 7319	010201
0.0	0.61	3.61	0.56	2.36	0.0	0.0	22.90	1.17	0.0	31.21	CPX 7319	010202
52.33	0.33	5.69	1.64	2.44	0.08	15.22	21.43	1.52	0.0	100.68	CPX 7319	010301
51.90	0.34	5.50	1.57	2.56	0.09	15.97	20.57	1.42	0.0	99.92	CPX 7319	010401
52.55	0.34	5.84	1.69	2.35	0.09	15.56	21.03	1.40	0.0	100.85	CPX 7319	020101
51.92	0.34	5.72	1.54	2.37	0.11	15.62	20.87	1.37	0.0	99.86	CPX 7319	020201
56.17	0.0	2.78	0.54	6.06	0.0	33.66	0.78	0.0	0.0	99.99	OPX R 37	010300
56.56	0.10	1.65	0.47	6.54	0.13	34.99	0.32	0.0	0.0	100.76	OPX R 37	010302
56.30	0.0	2.85	0.55	6.01	0.0	34.08	0.80	0.0	0.0	100.59	OPX R 37	010400

SIO2	TIO2	AL2O3	CR2O3	FEO	MNO	MGO	CAO	NA2O	K2O	TOTAL	SAMPLE	ANAL.NO
56.72	0.0	2.83	0.62	6.19	0.0	34.15	0.72	0.0	0.0	101.23	OPX R 37	010500
55.53	0.10	2.17	0.42	6.54	0.17	34.69	0.60	0.0	0.0	100.22	OPX R 37	010502
56.63	0.0	2.87	0.66	6.13	0.0	34.45	0.73	0.0	0.0	101.47	OPX R 37	010800
55.46	0.10	2.75	0.70	6.40	0.14	34.79	0.60	0.0	0.0	100.94	OPX R 37	010802
56.43	0.09	2.25	0.43	6.37	0.16	34.01	0.72	0.04	0.0	100.50	OPX R 37	020300
55.16	0.08	2.21	0.43	6.04	0.13	34.51	0.67	0.02	0.0	99.25	OPX R 37	040300
53.92	0.10	5.00	0.37	7.25	0.12	33.01	0.70	0.05	0.0	100.52	OPX R 37	010201
0.0	0.0	2.50	0.0	0.0	0.0	0.0	0.50	0.0	0.0	3.00	OPX R 37	010202
55.11	0.0	4.51	0.70	6.04	0.0	32.95	0.92	0.0	0.0	100.23	OPX R 37	010601
55.82	0.0	2.49	0.50	6.34	0.0	34.32	0.59	0.0	0.0	100.06	OPX R 37	010602
0.0	0.0	5.29	0.0	0.0	0.0	0.0	0.57	0.0	0.0	5.86	OPX R 37	020201
56.34	0.02	3.15	0.35	6.30	0.17	33.29	0.37	0.01	0.0	100.00	OPX R 37	010110
53.47	0.06	5.83	0.65	5.74	0.12	32.32	1.34	0.09	0.0	99.62	OPX R 37	010100
53.90	0.06	5.82	0.67	5.76	0.13	32.35	1.39	0.13	0.0	100.21	OPX R 37	020100
53.77	0.06	5.90	0.67	5.72	0.12	32.37	1.35	0.07	0.0	100.03	OPX R 37	030100
53.71	0.06	5.85	0.66	5.74	0.12	32.35	1.36	0.10	0.0	99.95	OPX R 37	000000
51.84	0.35	4.27	1.02	2.42	0.12	16.54	22.71	0.54	0.0	99.81	CPX R 37	020301
51.19	0.43	4.99	1.01	2.36	0.08	16.21	22.54	0.59	0.0	99.40	CPX R 37	020401
0.0	0.29	3.04	0.84	2.26	0.0	0.0	23.45	0.48	0.0	30.36	CPX R 37	020402

SIO2	TIO2	AL2O3	CR2O3	FEO	MNO	MGO	CAO	NA2O	K2O	TOTAL	SAMPLE	ANAL.NO
51.23	0.43	4.56	0.97	2.38	0.08	16.48	22.94	0.58	0.0	99.65	CPX R 37	020601
0.0	1.06	3.81	0.88	2.26	0.0	0.0	23.75	0.50	0.0	32.26	CPX R 37	020602
52.60	0.31	3.37	0.87	2.47	0.09	17.38	22.74	0.57	0.0	100.40	CPX R 37	040200
52.46	0.34	3.82	0.99	2.29	0.09	17.36	22.70	0.60	0.0	100.65	CPX R 37	040300
0.0	0.72	4.11	0.86	2.58	0.0	0.0	22.91	0.56	0.0	31.74	CPX R 37	040401
51.75	0.30	4.07	0.98	2.47	0.07	16.63	22.63	0.55	0.0	99.45	CPX R 37	040501
51.94	0.33	4.46	1.08	2.52	0.06	16.10	22.64	0.58	0.0	99.71	CPX R 37	050101
0.0	0.77	3.03	0.87	2.41	0.0	0.0	21.57	0.55	0.0	29.20	CPX R 37	050102
51.91	0.36	4.44	1.07	2.65	0.08	16.50	22.62	0.55	0.0	100.18	CPX R 37	050201
51.94	0.32	4.02	1.05	2.42	0.06	16.50	22.90	0.56	0.0	99.77	CPX R 37	060301
52.55	0.32	3.54	0.98	2.41	0.08	16.96	23.45	0.54	0.0	100.83	CPX R 37	060401
51.54	0.30	4.14	0.97	2.54	0.11	16.27	23.02	0.56	0.0	99.45	CPX R 37	060501
51.56	0.34	4.66	1.01	2.60	0.09	16.47	22.84	0.55	0.0	100.12	CPX R 37	060601
51.55	0.36	6.13	1.09	2.38	0.11	15.72	22.80	0.52	0.0	100.66	CPX R 37	060101
50.74	0.29	6.16	0.96	2.64	0.08	15.92	22.33	0.55	0.0	99.67	CPX R 37	020101
55.27	0.44	2.70	0.56	6.71	0.14	33.69	0.84	0.02	0.0	100.37	OPX R 131	010200
55.97	0.41	2.40	0.46	6.69	0.11	33.53	0.88	0.01	0.0	100.46	OPX R 131	010400
55.02	0.42	2.52	0.48	6.80	0.10	33.54	0.87	0.04	0.0	99.79	OPX R 131	010500
55.98	0.45	2.77	0.54	6.71	0.12	33.22	0.86	0.05	0.0	100.70	OPX R 131	010500

SIO2	TIO2	AL2O3	CR2O3	FEO	MNO	MGO	CAO	NA2O	K2O	TOTAL	SAMPLE	ANAL.NO
55.38	0.47	2.62	0.47	6.76	0.13	33.55	0.91	0.04	0.0	100.33	OPX R 131	010700
56.34	0.39	2.52	0.38	7.03	0.14	33.75	0.68	0.03	0.0	101.26	OPX R 131	020200
56.42	0.40	2.57	0.38	7.02	0.15	33.78	0.70	0.02	0.0	101.44	OPX R 131	020201
56.15	0.42	2.48	0.48	6.86	0.13	33.69	0.79	0.04	0.0	101.04	OPX R 131	020700
55.53	0.42	2.97	0.59	6.67	0.15	33.45	0.86	0.0	0.0	100.64	OPX R 131	040200
49.66	1.46	6.01	1.07	3.17	0.08	16.39	21.46	0.77	0.0	100.07	CPX R 131	010201
50.53	1.44	5.30	1.11	3.13	0.15	16.48	20.91	0.66	0.0	99.71	CPX R 131	010202
50.18	1.72	4.64	1.16	2.91	0.15	16.30	22.92	0.69	0.0	100.67	CPX R 131	010402
50.23	1.46	4.93	1.14	2.91	0.09	15.91	22.41	0.66	0.0	99.74	CPX R 131	010601
50.32	1.39	5.09	1.08	3.87	0.15	18.58	18.89	0.66	0.0	100.03	CPX R 131	020201
50.64	1.29	5.13	1.13	3.15	0.13	16.83	21.62	0.68	0.0	100.60	CPX R 131	020202
50.29	1.51	4.62	1.10	2.90	0.14	16.46	22.83	0.67	0.0	100.52	CPX R 131	020300
50.38	1.49	5.49	1.20	2.79	0.17	15.49	22.72	0.75	0.0	100.47	CPX R 131	020401
51.01	1.40	4.80	1.12	2.72	0.13	16.10	22.59	0.66	0.0	100.53	CPX R 131	020402
50.15	1.35	6.04	1.11	3.30	0.09	16.15	21.61	0.63	0.0	100.43	CPX R 131	020501
49.94	1.46	5.13	1.13	2.95	0.09	15.85	22.36	0.71	0.0	99.62	CPX R 131	020601
50.79	1.40	5.08	1.17	2.77	0.09	15.58	22.62	0.67	0.0	100.17	CPX R 131	020701
49.92	1.43	5.48	1.05	2.95	0.11	16.18	22.30	0.74	0.0	100.16	CPX R 131	021300
57.08	0.05	1.96	0.49	6.08	0.11	34.73	0.73	0.01	0.0	101.24	OPX R 25	000100

SIO2	TIO2	AL2O3	CR2O3	FEO	MNO	MGO	CAO	NA2O	K2O	TOTAL	SAMPLE	ANAL.NO
56.01	0.06	2.46	0.52	6.27	0.14	35.10	0.65	0.0	0.0	101.21	OPX R 25	010302
55.60	0.06	2.15	0.47	6.31	0.14	34.99	0.83	0.0	0.0	100.55	OPX R 25	010401
55.47	0.08	2.15	0.46	6.34	0.14	35.39	0.67	0.0	0.0	100.70	OPX R 25	010402
56.46	0.06	2.03	0.46	6.44	0.16	34.82	0.66	0.0	0.0	101.09	OPX R 25	010501
56.93	0.07	2.03	0.34	6.47	0.13	34.67	0.63	0.0	0.0	101.27	OPX R 25	010502
56.30	0.07	2.15	0.50	6.21	0.13	34.96	0.82	0.0	0.0	101.14	OPX R 25	020301
56.30	0.07	2.15	0.45	6.21	0.13	34.96	0.74	0.0	0.0	101.01	OPX R 25	020302
54.83	0.08	2.38	0.56	6.38	0.12	35.42	0.79	0.0	0.0	100.56	OPX R 25	020401
54.21	0.07	2.03	0.57	6.34	0.13	35.57	0.65	0.0	0.0	99.57	OPX R 25	020402
56.78	0.09	2.15	0.53	6.25	0.15	34.72	0.76	0.0	0.0	101.43	OPX R 25	020501
56.68	0.09	2.11	0.50	6.26	0.15	34.47	0.66	0.0	0.0	100.92	OPX R 25	020502
55.11	0.08	2.20	0.49	6.35	0.16	34.92	0.79	0.0	0.0	100.10	OPX R 25	030101
55.39	0.08	1.90	0.49	6.30	0.16	35.17	0.55	0.0	0.0	100.04	OPX R 25	030102
55.56	0.09	2.14	0.44	6.30	0.18	34.70	0.72	0.0	0.0	100.13	OPX R 25	030201
56.03	0.09	1.99	0.50	6.40	0.18	34.70	0.66	0.0	0.0	100.55	OPX R 25	030202
55.55	0.08	2.25	0.57	6.14	0.17	34.64	0.88	0.0	0.0	100.28	OPX R 25	030601
55.50	0.08	2.04	0.48	6.21	0.17	34.97	0.79	0.0	0.0	100.24	OPX R 25	030602
56.01	0.11	2.51	0.57	6.40	0.15	34.62	0.82	0.0	0.0	101.19	OPX R 25	030701
56.61	0.10	2.26	0.50	6.37	0.15	34.60	0.73	0.0	0.0	101.32	OPX R 25	030702

SIO2	TIO2	AL2O3	CR2O3	FEO	MNO	MGO	CAO	NA2O	K2O	TOTAL	SAMPLE	ANAL.NO
53.36	0.29	2.84	1.03	2.44	0.07	17.38	22.65	0.43	0.0	100.49	CPX R 25	070102
53.25	0.38	2.73	1.00	2.48	0.11	17.49	22.05	0.43	0.0	99.92	CPX R 25	070200
53.14	0.22	3.05	1.01	2.61	0.09	17.82	21.64	0.43	0.0	100.01	CPX R 25	080101
53.36	0.24	2.77	0.93	2.55	0.12	17.71	22.32	0.39	0.0	100.39	CPX R 25	080102
53.47	0.16	3.16	1.11	3.38	0.16	20.09	18.34	0.40	0.0	100.27	CPX R 25	080201
53.24	0.25	2.69	0.95	2.48	0.11	17.56	22.74	0.40	0.0	100.42	CPX R 25	080202
53.16	0.39	2.90	1.05	2.55	0.13	17.49	22.35	0.42	0.0	100.44	CPX R 25	080300
56.29	0.12	2.25	0.46	6.50	0.18	34.66	0.61	0.0	0.0	101.07	OPX R 346	010200
55.73	0.15	2.16	0.50	6.58	0.15	34.36	0.75	0.0	0.0	100.38	OPX R 346	010301
56.58	0.11	2.02	0.41	6.65	0.17	34.78	0.60	0.0	0.0	101.32	OPX R 346	010302
56.41	0.16	2.67	0.60	6.37	0.15	34.05	0.91	0.0	0.0	101.32	OPX R 346	010401
56.67	0.13	2.17	0.51	6.53	0.18	34.66	0.67	0.0	0.0	101.52	OPX R 346	010402
56.71	0.14	2.48	0.59	6.34	0.19	34.10	0.85	0.0	0.0	101.40	OPX R 346	010501
56.73	0.14	2.15	0.51	6.38	0.20	34.16	0.73	0.0	0.0	101.00	OPX R 346	010502
55.29	0.17	2.71	0.57	6.41	0.11	34.26	0.94	0.0	0.0	100.46	OPX R 346	010601
55.52	0.16	2.10	0.37	6.49	0.18	35.04	0.68	0.0	0.0	100.54	OPX R 346	010602
54.65	0.20	2.94	0.59	6.39	0.13	34.46	0.94	0.0	0.0	100.30	OPX R 346	010701
55.51	0.18	2.05	0.40	6.13	0.18	35.32	0.57	0.0	0.0	100.34	OPX R 346	010702
54.85	0.18	2.72	0.49	6.36	0.13	35.07	0.98	0.0	0.0	100.78	OPX R 346	010801

SIO2	TIO2	AL2O3	CR2O3	FEO	MNO	MGO	CAO	NA2O	K2O	TOTAL	SAMPLE	ANAL.NO
55.62	0.18	2.56	0.55	6.52	0.16	34.79	0.90	0.0	0.0	101.28	OPX R 346	011001
54.66	0.18	2.68	0.67	6.24	0.16	34.88	1.12	0.0	0.0	100.59	OPX R 346	011101
52.53	0.31	4.30	1.34	2.51	0.06	16.66	21.37	0.55	0.0	99.63	CPX R 346	020201
52.83	0.34	4.18	1.30	2.74	0.09	17.79	20.96	0.46	0.0	100.69	CPX R 346	020301
53.27	0.35	2.91	1.04	2.24	0.04	17.00	22.74	0.52	0.0	100.11	CPX R 346	020302
52.59	0.33	3.81	1.20	2.47	0.06	17.04	21.96	0.54	0.0	100.00	CPX R 346	020401
51.79	0.29	3.87	1.23	2.58	0.05	17.20	21.95	0.55	0.0	99.51	CPX R 346	020501
52.56	0.33	3.95	1.30	2.50	0.06	16.91	21.54	0.51	0.0	99.66	CPX R 346	020601
52.49	0.33	3.96	1.24	2.56	0.07	17.48	21.63	0.51	0.0	100.27	CPX R 346	020701
50.53	0.40	6.55	1.27	2.67	0.08	16.08	21.86	0.57	0.0	100.01	CPX R 346	020101
51.88	0.36	3.82	1.34	2.24	0.09	16.81	22.52	0.53	0.0	99.59	CPX R 346	020102
55.81	0.12	2.05	0.52	6.30	0.13	35.14	0.80	0.0	0.0	100.87	OPX R 927	010201
56.18	0.09	1.64	0.42	6.26	0.11	35.41	0.65	0.0	0.0	100.76	OPX R 927	010301
56.67	0.11	1.75	0.44	6.20	0.15	35.30	0.72	0.0	0.0	101.34	OPX R 927	010401
56.39	0.09	1.59	0.34	6.27	0.13	35.46	0.70	0.0	0.0	100.97	OPX R 927	010501
55.06	0.12	2.13	0.52	6.11	0.17	34.75	0.90	0.0	0.0	99.76	OPX R 927	020101
56.44	0.08	1.60	0.31	6.16	0.10	35.54	0.67	0.0	0.0	100.90	OPX R 927	020201
56.58	0.11	1.75	0.41	6.12	0.13	35.05	0.75	0.0	0.0	100.90	OPX R 927	020301
55.16	0.12	1.91	0.48	6.17	0.13	34.96	0.79	0.0	0.0	99.72	OPX R 927	020401

SIO2	TIO2	AI2O3	CR2O3	FEO	MNO	MGO	CAO	NA2O	K2O	TOTAL	SAMPLE	ANAL.NO
56.62	0.13	1.92	0.52	6.19	0.13	35.20	0.76	0.0	0.0	101.47	OPX R 927	020601
56.96	0.15	2.15	0.55	6.27	0.07	33.89	0.85	0.0	0.0	100.89	OPX R 927	020701
54.46	0.11	3.46	0.88	6.13	0.15	34.21	0.84	0.0	0.0	100.24	OPX R 927	010101
52.99	0.35	2.92	1.09	2.50	0.14	17.29	22.77	0.50	0.0	100.55	CPX R 927	020101
51.49	0.34	3.05	1.20	2.48	0.13	17.39	22.92	0.59	0.0	99.59	CPX R 927	020201
51.80	0.36	3.12	1.17	2.60	0.12	17.49	22.45	0.56	0.0	99.67	CPX R 927	020401
52.33	0.43	3.31	1.33	2.55	0.04	17.25	22.31	0.54	0.0	100.09	CPX R 927	020501
52.03	0.43	3.09	1.21	2.49	0.11	17.26	22.80	0.53	0.0	99.95	CPX R 927	020502
51.88	0.39	2.79	1.13	2.45	0.06	17.49	22.96	0.55	0.0	99.69	CPX R 927	030101
52.03	0.39	2.80	1.20	2.44	0.09	17.30	23.12	0.52	0.0	99.89	CPX R 927	030201
51.79	0.44	3.43	1.26	2.33	0.11	16.80	23.20	0.54	0.0	99.90	CPX R 927	030301
53.27	0.32	2.45	0.88	2.08	0.05	17.43	23.28	0.44	0.0	100.20	CPX R 927	030302
53.01	0.33	2.42	0.89	2.61	0.01	17.50	22.55	0.44	0.0	99.76	CPX R 927	030401
52.82	0.08	6.57	0.83	7.62	0.11	31.47	0.65	0.01	0.0	100.16	OPX R 180	000101
49.20	0.77	7.98	1.26	3.09	0.05	14.82	21.72	0.71	0.0	99.60	CPX R 180	000101

SIO2	TIO2	AL2O3	CR2O3	FEO	MNO	MGO	CAO	NA2O	K2O	TOTAL	SAMPLE	ANAL.NO
0.0	0.06	44.36	25.87	13.40	0.0	17.11	0.0	0.0	0.0	100.80	SP R 501	000101
0.0	0.10	45.66	24.27	12.94	0.0	17.72	0.0	0.0	0.0	100.69	SP R 501	000201
0.0	0.04	47.47	22.94	13.05	0.0	17.46	0.0	0.0	0.0	100.96	SP R 501	000202
0.0	0.05	45.97	23.86	12.95	0.0	17.82	0.0	0.0	0.0	100.65	SP R 501	000301
0.0	0.01	43.91	24.82	13.04	0.0	17.50	0.0	0.0	0.0	99.28	SP R 501	000401
0.0	0.0	46.33	23.02	12.85	0.29	17.95	0.0	0.0	0.0	100.44	SP R 501	010101
0.0	0.0	51.04	17.61	12.20	0.15	19.35	0.0	0.0	0.0	100.35	SP R 501	010102
0.0	0.0	47.31	21.19	12.79	0.27	18.36	0.0	0.0	0.0	99.92	SP R 501	010103
0.0	0.0	45.28	23.89	13.07	0.26	17.83	0.0	0.0	0.0	100.33	SP R 501	010200
0.0	0.0	45.55	23.47	13.38	0.23	17.95	0.0	0.0	0.0	100.58	SP R 501	010300
0.0	0.0	44.13	24.10	13.79	0.13	17.73	0.0	0.0	0.0	99.88	SP R 501	010302
0.0	0.0	45.16	24.24	12.96	0.26	17.86	0.0	0.0	0.0	100.48	SP R 501	010400
0.0	0.0	50.01	19.13	12.74	0.17	18.86	0.0	0.0	0.0	100.91	SP R 501	010402
0.0	0.01	50.19	19.50	12.51	0.0	18.52	0.0	0.0	0.0	100.73	SP R 501	000501
0.0	0.0	50.38	18.72	12.41	0.18	18.70	0.0	0.0	0.0	100.39	SP R 501	010900
0.0	0.0	57.14	12.67	10.76	0.0	20.23	0.0	0.0	0.0	100.80	SP R 501	000601
0.0	0.0	52.44	15.90	11.74	0.0	18.75	0.0	0.0	0.0	98.83	SP R 501	000701
0.0	0.0	58.35	10.75	10.83	0.0	20.24	0.0	0.0	0.0	100.17	SP R 501	000801
0.0	0.0	54.17	14.95	11.65	0.0	19.25	0.0	0.0	0.0	100.02	SP R 501	000901

SIO2	TIO2	AL2O3	CR2O3	FEO	MNO	MGO	CAO	NA2O	K2O	TOTAL	SAMPLE	ANAL.NO
0.0	0.0	51.72	16.27	12.38	0.17	19.44	0.0	0.0	0.0	99.98	SP R 501	010501
0.0	0.0	57.13	11.86	11.12	0.05	20.34	0.0	0.0	0.0	100.50	SP R 501	010601
0.0	0.0	53.41	14.93	12.02	0.12	19.45	0.0	0.0	0.0	99.93	SP R 501	010701
0.01	0.02	52.79	15.41	11.50	0.16	19.37	0.0	0.0	0.0	99.26	SP R 740	000101
0.02	0.09	46.75	21.41	13.18	0.26	18.39	0.0	0.0	0.0	100.10	SP R 740	000201
0.23	0.0	53.91	14.79	11.45	0.19	20.03	0.0	0.0	0.0	100.60	SP R 740	000202
0.04	0.06	48.95	20.16	12.24	0.24	18.75	0.0	0.0	0.0	100.44	SP R 740	000203
0.04	0.08	47.69	20.50	13.04	0.24	18.18	0.0	0.0	0.0	99.77	SP R 740	000204
0.02	0.06	46.23	21.79	12.81	0.28	18.36	0.0	0.0	0.0	99.55	SP R 740	000205
0.01	0.02	51.07	17.09	11.54	0.20	19.35	0.0	0.0	0.0	99.28	SP R 740	000301
0.0	0.0	63.57	6.35	9.16	0.11	22.26	0.0	0.0	0.0	101.45	SP R 740	000302
0.0	0.05	54.49	13.46	10.50	0.20	22.01	0.0	0.0	0.0	100.71	SP R 740	000303
0.0	0.05	53.18	15.69	11.42	0.0	20.50	0.0	0.0	0.0	100.84	SP R 740	000304
0.0	0.0	56.41	12.69	10.64	0.0	21.13	0.0	0.0	0.0	100.87	SP R 740	000305
0.0	0.12	46.71	22.35	12.70	0.0	18.93	0.0	0.0	0.0	100.81	SP R 740	000401
0.0	0.02	53.78	15.99	11.39	0.0	20.02	0.0	0.0	0.0	101.20	SP R 740	000402
0.0	0.08	47.60	20.93	12.16	0.0	18.79	0.0	0.0	0.0	99.56	SP R 740	000403
0.0	0.08	49.89	18.96	11.84	0.0	19.18	0.0	0.0	0.0	99.95	SP R 740	000404
0.09	0.0	50.43	18.00	11.48	0.20	18.55	0.0	0.0	0.0	98.75	SP R 740	000501

SIO2	TIO2	AL2O3	CR2O3	FEO	MNO	MGO	CAO	NA2O	K2O	TOTAL	SAMPLE	ANAL.NO
0.0	0.06	53.98	14.70	11.04	0.0	20.12	0.0	0.0	0.0	99.90	SP R 740	000601
0.0	0.11	49.06	18.92	11.89	0.0	18.77	0.0	0.0	0.0	98.75	SP R 740	000602
0.0	0.08	50.23	17.93	11.45	0.0	19.47	0.0	0.0	0.0	99.16	SP R 740	000603
0.0	0.08	52.32	16.40	11.32	0.0	19.78	0.0	0.0	0.0	99.90	SP R 740	000604
0.0	0.0	50.82	15.48	11.18	0.19	21.47	0.0	0.0	0.0	99.14	SP R 740	000701
0.0	0.03	54.25	12.09	10.66	0.20	22.26	0.0	0.0	0.0	99.49	SP R 740	000702
0.0	0.03	53.37	13.77	10.58	0.25	21.70	0.0	0.0	0.0	99.70	SP R 740	000703
0.0	0.05	49.41	19.37	11.73	0.0	19.24	0.0	0.0	0.0	99.80	SP R 740	000801
0.0	0.01	53.13	14.63	11.36	0.0	20.05	0.0	0.0	0.0	99.18	SP R 740	000802
0.0	0.0	51.68	16.85	11.57	0.0	19.00	0.0	0.0	0.0	99.10	SP R 740	000803
0.0	0.03	51.98	17.12	11.31	0.0	19.62	0.0	0.0	0.0	100.06	SP R 740	000901
0.0	0.0	56.79	11.55	10.52	0.0	20.64	0.0	0.0	0.0	99.50	SP R 740	000902
0.0	0.02	55.11	13.17	10.53	0.0	20.41	0.0	0.0	0.0	99.24	SP R 740	000903
0.0	0.03	51.40	18.13	11.54	0.0	19.25	0.0	0.0	0.0	100.35	SP R 740	001001
0.0	0.0	56.26	12.71	10.48	0.0	20.40	0.0	0.0	0.0	99.85	SP R 740	001002
0.0	0.0	54.85	13.71	11.32	0.0	20.43	0.0	0.0	0.0	100.31	SP R 740	001003
0.0	0.02	47.21	23.16	12.72	0.0	18.22	0.0	0.0	0.0	101.33	SP R 740	001401
0.0	0.0	53.99	16.32	11.28	0.0	19.72	0.0	0.0	0.0	101.31	SP R 740	001402
0.0	0.0	52.84	17.75	11.14	0.0	19.26	0.0	0.0	0.0	100.99	SP R 740	001403

SIO2	TIO2	AI2C3	CR2O3	FEO	MNO	MGO	CAO	NA2O	K2O	TOTAL	SAMPLE	ANAL.NO
0.0	0.03	51.65	18.07	11.92	0.0	19.50	0.0	0.0	0.0	101.17	SP R 740	001501
0.0	0.01	51.56	17.37	11.60	0.0	19.72	0.0	0.0	0.0	100.26	SP R 740	001601
0.0	0.0	53.95	14.50	11.13	0.0	19.91	0.0	0.0	0.0	99.49	SP R 740	001602
0.0	0.0	52.46	16.85	11.66	0.0	20.03	0.0	0.0	0.0	101.00	SP R 740	001603
0.0	0.03	48.90	19.79	11.96	0.0	19.50	0.0	0.0	0.0	100.18	SP R 740	001701
0.0	0.0	50.50	18.02	11.75	0.0	19.33	0.0	0.0	0.0	99.60	SP R 740	001702
0.0	0.07	54.42	14.41	12.00	0.26	19.28	0.0	0.0	0.0	100.44	SP R 696	000201
0.0	0.04	59.00	8.82	11.03	0.14	20.63	0.0	0.0	0.0	99.66	SP R 696	000202
0.0	0.03	54.75	12.18	12.03	0.27	19.90	0.0	0.0	0.0	99.16	SP R 696	000203
0.0	0.0	54.48	13.63	11.66	0.16	20.01	0.0	0.0	0.0	99.94	SP R 696	000301
0.0	0.0	58.13	10.20	10.95	0.13	20.78	0.0	0.0	0.0	100.19	SP R 696	000302
0.0	0.04	51.36	17.87	13.15	0.25	18.38	0.0	0.0	0.0	101.05	SP R 696	000401
0.0	0.0	55.54	12.75	11.65	0.30	19.59	0.0	0.0	0.0	99.83	SP R 696	000402
0.0	0.04	56.26	12.73	11.72	0.20	19.51	0.0	0.0	0.0	100.46	SP R 696	000501
0.0	0.0	60.61	7.65	10.19	0.14	20.77	0.0	0.0	0.0	99.36	SP R 696	000502
0.0	0.0	57.89	10.58	11.40	0.20	19.79	0.0	0.0	0.0	99.85	SP R 696	000503
0.0	0.0	57.34	10.95	11.06	0.18	20.23	0.0	0.0	0.0	99.76	SP R 696	000601
0.0	0.0	59.77	8.46	10.40	0.15	21.11	0.0	0.0	0.0	99.89	SP R 696	000602
0.0	0.02	53.01	15.13	12.35	0.27	18.82	0.0	0.0	0.0	99.60	SP R 696	000701

SIO2	TIO2	AI2C3	CR2O3	FEO	MNO	MGO	CAO	NA2O	K2O	TOTAL	SAMPLE	ANAL.NO
0.0	0.0	54.54	13.76	12.19	0.25	19.19	0.0	0.0	0.0	99.93	SP R 696	000801
0.0	0.0	59.32	9.33	10.91	0.22	20.48	0.0	0.0	0.0	100.26	SP R 696	000802
0.0	0.0	59.36	9.58	11.23	0.19	20.38	0.0	0.0	0.0	100.74	SP R 696	000901
0.0	0.0	60.55	7.09	10.98	0.16	20.53	0.0	0.0	0.0	99.31	SP R 696	001001
0.0	0.0	60.17	8.32	11.10	0.16	20.54	0.0	0.0	0.0	100.29	SP R 696	001101
0.0	0.0	62.85	5.78	10.52	0.11	20.73	0.0	0.0	0.0	99.99	SP R 696	001102
0.0	0.09	59.38	8.63	12.27	0.23	19.98	0.0	0.0	0.0	100.58	SP R 696	000100
0.18	0.0	57.11	11.11	12.77	0.15	18.58	0.0	0.0	0.0	99.90	SP R 123	010101
0.01	0.0	63.09	7.10	9.46	0.01	20.97	0.0	0.0	0.0	100.64	SP R 123	030100
0.0	0.04	58.11	9.48	12.16	0.20	19.59	0.0	0.0	0.0	99.58	SP R 123	100101
0.0	0.09	56.07	11.68	13.59	0.22	19.16	0.0	0.0	0.0	100.81	SP R 123	100201
0.0	0.05	57.76	9.74	12.61	0.16	19.59	0.0	0.0	0.0	99.91	SP R 123	100301
0.0	0.10	53.71	13.52	11.52	0.21	20.12	0.0	0.0	0.0	99.18	SP R 196	000101
0.0	0.08	52.31	14.60	12.05	0.23	19.86	0.0	0.0	0.0	99.13	SP R 196	000102
0.0	0.05	54.64	13.08	10.93	0.19	20.30	0.0	0.0	0.0	99.19	SP R 196	000201
0.0	0.05	57.20	10.77	10.36	0.18	21.56	0.0	0.0	0.0	100.12	SP R 196	000202
0.0	0.08	54.00	13.49	11.33	0.25	20.25	0.0	0.0	0.0	99.40	SP R 196	000301
0.0	0.09	53.04	14.39	11.12	0.25	20.22	0.0	0.0	0.0	99.11	SP R 196	000302
0.0	0.08	54.30	13.21	11.18	0.22	20.64	0.0	0.0	0.0	99.63	SP R 196	000401

SIO2	TIO2	AL2C3	CR2O3	FEO	MNO	MGO	CAO	NA2O	K2O	TOTAL	SAMPLE	ANAL.NO
0.0	0.04	54.39	13.14	11.18	0.21	20.80	0.0	0.0	0.0	99.76	SP R 196	000501
0.0	0.06	56.60	10.76	11.25	0.23	21.59	0.0	0.0	0.0	100.49	SP R 196	000502
0.0	0.05	56.12	11.81	10.80	0.20	21.37	0.0	0.0	0.0	100.35	SP R 196	000601
0.0	0.03	57.07	10.17	11.05	0.21	21.07	0.0	0.0	0.0	99.60	SP R 196	000701
0.0	0.01	58.08	9.27	10.55	0.15	21.23	0.0	0.0	0.0	99.29	SP R 196	000801
0.0	0.03	58.21	9.39	10.83	0.13	21.54	0.0	0.0	0.0	100.13	SP R 196	000901
0.0	0.01	56.84	10.69	10.97	0.19	20.97	0.0	0.0	0.0	99.67	SP R 196	001001
0.01	0.08	58.14	9.57	11.11	0.12	20.43	0.0	0.0	0.0	99.46	SP R 243	000101
0.25	0.12	52.49	14.69	12.05	0.21	19.13	0.06	0.0	0.0	99.00	SP R 243	000102
0.06	0.07	56.64	10.69	11.25	0.12	20.36	0.0	0.0	0.0	99.19	SP R 243	000103
0.04	0.0	58.50	9.45	11.27	0.08	20.22	0.0	0.0	0.0	99.56	SP R 243	000201
0.05	0.09	58.45	9.94	11.03	0.16	19.96	0.0	0.0	0.0	99.68	SP R 243	000401
0.19	0.06	53.78	14.70	11.77	0.18	18.84	0.07	0.0	0.0	99.59	SP R 243	000402
0.10	0.06	57.80	10.88	11.23	0.15	19.71	0.02	0.0	0.0	99.95	SP R 243	000403
0.05	0.06	58.16	10.39	11.35	0.18	19.84	0.0	0.0	0.0	100.03	SP R 243	000404
0.05	0.05	59.29	9.60	10.84	0.13	20.36	0.0	0.0	0.0	100.32	SP R 243	000501
0.18	0.03	56.56	11.26	11.36	0.16	19.49	0.08	0.0	0.0	99.12	SP R 243	000502
0.10	0.02	58.16	10.58	11.75	0.22	19.96	0.0	0.0	0.0	100.79	SP R 243	000503
0.06	0.14	59.13	9.76	10.85	0.16	20.44	0.0	0.0	0.0	100.54	SP R 243	000601

SIO2	TIO2	AL2O3	CR2O3	FEO	MNO	MGO	CAO	NA2O	K2O	TOTAL	SAMPLE	ANAL.NO
0.19	0.07	58.04	10.50	10.79	0.17	20.40	0.07	0.0	0.0	100.23	SP R 243	000603
0.07	0.13	42.20	26.20	13.30	0.37	18.28	0.0	0.0	0.0	100.55	SP 7319	000101
0.14	0.09	39.75	28.37	14.08	0.39	17.55	0.0	0.0	0.0	100.37	SP 7319	000102
0.09	0.13	41.03	27.41	13.55	0.36	18.26	0.02	0.0	0.0	100.85	SP 7319	000103
0.06	0.08	43.51	25.00	12.52	0.33	18.56	0.02	0.0	0.0	100.08	SP 7319	000201
0.08	0.11	43.80	25.47	13.28	0.34	17.64	0.01	0.0	0.0	100.73	SP 7319	000301
0.06	0.09	43.78	24.48	13.01	0.34	18.50	0.01	0.0	0.0	100.27	SP 7319	000401
0.03	0.03	42.13	25.36	13.22	0.36	18.25	0.0	0.0	0.0	99.38	SP 7319	000501
0.0	0.05	51.79	15.77	12.19	0.14	19.57	0.0	0.0	0.0	99.51	SP R 37	000201
0.0	0.06	49.80	18.17	11.70	0.27	20.34	0.0	0.0	0.0	100.34	SP R 37	000301
0.0	0.08	44.09	24.48	12.62	0.40	18.78	0.0	0.0	0.0	100.45	SP R 37	000302
0.0	0.05	55.01	13.44	10.86	0.14	21.10	0.0	0.0	0.0	100.60	SP R 37	000501
0.0	0.08	45.84	23.51	12.23	0.38	18.67	0.0	0.0	0.0	100.71	SP R 37	000502
0.07	0.0	60.12	8.73	9.70	0.17	20.86	0.02	0.0	0.0	99.67	SP R 37	010101
0.06	0.15	55.34	13.22	11.11	0.24	20.26	0.03	0.0	0.0	100.41	SP R 37	050101
0.18	0.22	42.64	26.72	13.46	0.45	16.88	0.13	0.0	0.0	100.68	SP R 37	050102
0.05	0.15	54.04	14.71	11.60	0.34	19.89	0.02	0.0	0.0	100.80	SP R 37	050104
0.36	0.14	52.07	16.85	11.35	0.32	19.30	0.32	0.0	0.0	100.71	SP R 37	050105
0.08	0.13	49.40	20.30	11.54	0.38	18.73	0.05	0.0	0.0	100.61	SP R 37	050106

SIO2	TIO2	AL2O3	CR2O3	FEO	MNO	MGO	CAO	NA2O	K2O	TOTAL	SAMPLE	ANAL.NO
0.27	0.21	42.55	26.88	13.66	0.45	16.84	0.22	0.0	0.0	101.08	SP R 37	050109
0.16	0.21	39.34	30.43	13.86	0.49	16.22	0.09	0.0	0.0	100.80	SP R 37	010200
0.12	0.19	41.17	27.50	13.67	0.49	16.63	0.09	0.0	0.0	99.86	SP R 37	050111
0.30	0.13	38.88	29.47	14.52	0.43	15.79	0.06	0.0	0.0	99.58	SP R 37	080100
0.13	0.15	39.63	27.59	14.95	0.42	16.54	0.0	0.0	0.0	99.41	SP R 37	090100
0.09	0.12	41.71	27.19	14.07	0.35	17.09	0.0	0.0	0.0	100.62	SP R 37	100100
0.0	0.24	48.14	17.42	13.25	0.25	20.66	0.0	0.0	0.0	99.96	SP R 131	000101
0.0	0.27	46.43	19.14	13.66	0.25	19.90	0.0	0.0	0.0	99.65	SP R 131	000102
0.0	0.43	41.49	23.11	14.89	0.35	19.22	0.0	0.0	0.0	99.49	SP R 131	000201
0.0	0.48	39.75	24.78	16.02	0.38	18.25	0.0	0.0	0.0	99.66	SP R 131	000202
0.0	0.34	42.43	22.71	14.26	0.30	19.46	0.0	0.0	0.0	99.50	SP R 131	000301
0.0	0.52	40.69	23.87	15.03	0.33	19.07	0.0	0.0	0.0	99.51	SP R 131	000302
0.0	0.44	40.60	24.07	14.92	0.40	19.12	0.0	0.0	0.0	99.55	SP R 131	000701
0.0	0.59	35.55	30.36	17.72	0.46	16.24	0.0	0.0	0.0	100.92	SP R 131	000401
0.0	0.61	34.81	30.26	18.80	0.47	15.53	0.0	0.0	0.0	100.48	SP R 131	000501
0.0	0.58	38.96	26.59	15.51	0.46	18.13	0.0	0.0	0.0	100.23	SP R 131	000601
0.0	0.25	33.56	32.88	17.26	0.58	16.14	0.0	0.0	0.0	100.67	SP R 25	000100
0.0	0.27	33.02	33.95	17.09	0.63	15.89	0.0	0.0	0.0	100.85	SP R 25	000201
0.0	0.25	33.19	32.84	17.54	0.63	16.07	0.0	0.0	0.0	100.52	SP R 25	000202

SIO2	TIO2	AL2O3	CR2O3	FEO	MNO	MGO	CAO	NA2O	K2O	TOTAL	SAMPLE	ANAL.NO
0.0	0.28	30.89	36.32	17.40	0.60	15.66	0.0	0.0	0.0	101.15	SP R 25	000302
0.0	0.27	31.04	36.33	16.37	0.64	16.15	0.0	0.0	0.0	100.80	SP R 25	000400
0.0	0.28	31.77	35.87	16.86	0.60	16.04	0.0	0.0	0.0	101.42	SP R 25	000500
0.0	0.26	30.92	35.76	17.76	0.64	15.25	0.0	0.0	0.0	100.59	SP R 25	000600
0.0	0.36	34.92	32.62	15.46	0.47	16.79	0.0	0.0	0.0	100.62	SP R 346	000100
0.0	0.38	34.41	32.49	15.77	0.50	16.59	0.0	0.0	0.0	100.14	SP R 346	000201
0.0	0.41	33.05	33.92	16.93	0.57	16.10	0.0	0.0	0.0	100.98	SP R 346	000301
0.0	0.39	32.07	34.75	17.41	0.55	15.50	0.0	0.0	0.0	100.67	SP R 346	000302
0.0	0.38	34.64	33.09	15.86	0.52	16.41	0.0	0.0	0.0	100.90	SP R 346	000401
0.0	0.38	33.04	34.12	16.68	0.55	15.81	0.0	0.0	0.0	100.58	SP R 346	000402
0.0	0.36	32.76	33.67	16.54	0.53	16.44	0.0	0.0	0.0	100.30	SP R 346	000501
0.0	0.23	35.59	30.84	16.18	0.53	15.96	0.0	0.0	0.0	99.33	SP R 927	000101
0.0	0.26	32.91	32.95	17.24	0.54	15.08	0.0	0.0	0.0	98.98	SP R 927	000102
0.0	0.37	31.07	36.24	17.58	0.66	14.59	0.0	0.0	0.0	100.51	SP R 927	000201
0.0	0.40	29.11	38.27	18.47	0.56	13.81	0.0	0.0	0.0	100.62	SP R 927	000202
0.0	0.32	30.27	36.79	17.32	0.60	14.53	0.0	0.0	0.0	99.83	SP R 927	000301
0.0	0.38	29.53	37.40	17.79	0.59	14.09	0.0	0.0	0.0	99.78	SP R 927	000401
0.0	0.0	32.61	34.42	17.66	0.45	15.25	0.0	0.0	0.0	100.39	SP R 927	000501
0.0	0.0	29.26	37.30	18.57	0.46	14.14	0.0	0.0	0.0	99.73	SP R 927	000601

APPENDIX 4

The Solubility of Al_2O_3 in Orthopyroxene in Spinel and Plagioclase Peridotites and Spinel Pyroxenite

MASAAKI OBATA

American Mineralogist, Volume 61, pages 804–816, 1976

The solubility of Al_2O_3 in orthopyroxenes in spinel and plagioclase peridotites and spinel pyroxenite

MASAAKI OBATA

Department of Earth and Planetary Sciences
Massachusetts Institute of Technology
Cambridge, Massachusetts 02139

Abstract

The solubility of Al_2O_3 in orthopyroxene coexisting with olivine and spinel in the system MgO–Al_2O_3–SiO_2 was calculated. The model used is based on the theoretical treatments by Wood and Banno (1973) and Wood (1974) for garnet–orthopyroxene equilibria and on the experimental data of MacGregor (1964) for the reaction orthopyroxene + spinel = forsterite + pyrope. The reaction curve was extrapolated outside the experimental range using a simple solution model for orthopyroxene proposed by Wood and Banno (1973). The solubility of Al_2O_3 in orthopyroxene is calculated to be much less sensitive to pressure than suggested by MacGregor (1974), and is essentially a function of temperature alone below 1000°C. Based on the results in the system MgO–Al_2O_3–SiO_2, the univariant curves for the reactions forsterite + anorthite = clinopyroxene + orthopyroxene + spinel and clinopyroxene + orthopyroxene + spinel = forsterite + garnet in the four-component system CaO–MgO–Al_2O_3–SiO_2, and the solubilities of Al_2O_3 in orthopyroxene in plagioclase peridotite and in spinel pyroxenite, were also calculated. Because of the compositional changes of pyroxenes which are involved in the reactions, the univariant lines curve significantly, and simple linear extrapolations of high-temperature experimental data to low temperatures are not valid. A method for applying the calculated results to natural rocks is proposed.

Introduction

Among chemical parameters of minerals, the solubility of Al_2O_3 in pyroxenes is one of the most sensitive indicaters of physical conditions, and is especially applicable to peridotites. Quantitative estimates of equilibriation pressure have become possible since the experimental work on the join $MgSiO_3$–$Mg_3Al_2Si_3O_{12}$ by Boyd and England (1964) and that in the system MgO–Al_2O_3–SiO_2 by MacGregor (1974). These experimental data have recently been applied to garnet peridotite xenoliths in kimberlites (Boyd, 1973; Boyd and Nixon, 1975) and to spinel peridotite xenoliths in basalts and peridotite intrusions (MacGregor, 1974; Mercier and Carter, 1975). Some apparent discrepancies in the experimental data for garnet peridotite between simple and complex systems were discussed through a theoretical treatment of orthopyroxene–garnet equilibria by Wood and Banno (1973) and Wood (1974). From more extensive experimental data by Akella and Boyd (1972, 1973, and 1974) and Akella (1976), we can now estimate equilibration pressure of garnet peridotites with some confidence, provided equilibration temperatures are known by independent methods. On the other hand, there are still some contradictions about the Al_2O_3 solubility in orthopyroxene in spinel peridotite among different authors: MacGregor's experiments (1974) suggest that the Al_2O_3 isopleths for orthopyroxene have definite positive slopes in the spinel peridotite field as well as in the garnet peridotite field, and that the Al_2O_3 content decreases with increasing pressure. This contradicts O'Hara's (1967) inference that the Al_2O_3 isopleths for clinopyroxene, and also by implication for orthopyroxene, have negative slopes, and that the solubility increases with increasing pressure. Moreover, there are notable discrepancies between MacGregor's experiments (1974) and the low-pressure experiments by Anastasiou and Seifert (1972) on the Al_2O_3 solubility in orthopyroxene, as noted by MacGregor (1974). Obviously more careful experiments and theoretical examination of this parameter are necessary before geologic applications can be made with

confidence. Theoretically the solubilities of Al_2O_3 for garnet peridotite and for spinel peridotite are not independent, and there is some way to examine internal consistencies of the experimental data.

The purpose of this paper is to demonstrate that the Al_2O_3 solubilities in orthopyroxene in spinel peridotite, plagioclase peridotite, and spinel pyroxenite may be uniquely derived by simple thermodynamic calculations from the published experimental data for garnet peridotite and from positions of boundaries between garnet–spinel and spinel–plagioclase peridotite facies.

Thermodynamic considerations

In order to calculate the Al_2O_3 solubility in orthopyroxene in various mineral assemblages, it is convenient to first write appropriate stoichiometric expressions of the aluminous pyroxene component, $MgAl_2SiO_6$,[1] in terms of sets of components in the phases present. For example, the equation

$$\underset{\text{garnet}}{Mg_3Al_2Si_3O_{12}} = \underset{\text{orthopyroxene solid solution}}{Mg_2Si_2O_6 + MgAl_2SiO_6} \quad (1)$$

has been used by Wood and Banno (1973) to analyze orthopyroxene–garnet equilibria. Similarly, the equation

$$\underset{\text{orthopyroxene}}{Mg_2Si_2O_6} + \underset{\text{spinel}}{MgAl_2O_4} = \underset{\text{olivine}}{Mg_2SiO_4} + \underset{\text{orthopyroxene}}{MgAl_2SiO_6} \quad (2)$$

may be used for an olivine–spinel–orthopyroxene assemblage,

$$\underset{\text{plagioclase}}{CaAl_2Si_2O_8} + \underset{\text{olivine}}{Mg_2SiO_4} = \underset{\text{clinopyroxene}}{CaMgSi_2O_6} + \underset{\text{orthopyroxene}}{MgAl_2SiO_6} \quad (3)$$

for a plagioclase–olivine–clinopyroxene–orthopyroxene assemblage,

$$\underset{\text{orthopyroxene}}{0.5Mg_2Si_2O_6} + \underset{\text{plagioclase}}{0.5CaAl_2Si_2O_8} + \underset{\text{spinel}}{0.5MgAl_2O_4} = \underset{\text{clinopyroxene}}{0.5CaMgSi_2O_6} + \underset{\text{orthopyroxene}}{MgAl_2SiO_6} \quad (4)$$

for a spinel–plagioclase–clinopyroxene–orthopyroxene assemblage, *etc.* Regarding these mathematical expressions as chemical reactions, the equilibrium condition for the reaction is:

$$-RT \ln K(i) = \Delta G^0(i) \quad (5)$$

where $K(i)$ and $\Delta G^0(i)$ are, respectively, equilibrium constant and free energy change of reaction *(i)* at the pressure and temperature of interest. The equilibrium constants for each reaction are:

$$K(1) = \frac{a^{opx}_{MgAl_2SiO_6} \cdot a^{opx}_{Mg_2Si_2O_6}}{a^{gar}_{Mg_3Al_2Si_3O_{12}}} \quad (6)$$

$$K(2) = \frac{a^{opx}_{MgAl_2SiO_6} \cdot a^{ol}_{Mg_2SiO_4}}{a^{opx}_{Mg_2Si_2O_6} \cdot a^{sp}_{MgAl_2O_4}} \quad (7)$$

$$K(3) = \frac{a^{opx}_{MgAl_2SiO_6} \cdot a^{cpx}_{CaMgSi_2O_6}}{a^{ol}_{Mg_2SiO_4} \cdot a^{pl}_{CaAl_2Si_2O_8}} \quad (8)$$

$$K(4) = \frac{a^{opx}_{MgAl_2SiO_6} \cdot (a^{cpx}_{CaMgSi_2O_6})^{1/2}}{(a^{opx}_{Mg_2Si_2O_6})^{1/2} \cdot (a^{pl}_{CaAl_2Si_2O_8})^{1/2}} \quad (9)$$

where a^{α}_{j} is the activity of component j in phase α.[2]

If the free energy change ΔG^0 and the activity–composition relationships are known, the Al_2O_3 solubility in orthopyroxene for each mineral assemblage can be calculated as a function of pressure and temperature. Wood and Banno (1973) proposed a simple mixing model for orthopyroxene solid solution, and calculated $\Delta G^0(1)$ using Boyd and England's (1964) experimental data on the Al_2O_3 solubility in orthopyroxene coexisting with pyrope. In spite of simplifying assumptions, the model satisfied available experimental data in simple and complex systems within the limits of experimental precision.

In this paper, the Wood-Banno model for the $Mg_2Si_2O_6$–$MgAl_2SiO_6$ orthopyroxene solid solution is adopted, that is:

(1) Octahedral Al atoms occupy only the smaller of the two octahedral positions, $M1$.

(2) Tetrahedral Al atoms are completely coupled to the octahedral Al atoms to maintain local charge balance.

(3) An ideal random mixing of Al and Mg atoms was assumed in $M1$ sites, so that considering assumption (2) entropy of mixing of the solution is calculated

[1] Although Ganguly and Ghose (1975) suggested that $Mg_3Al_2Si_3O_{12}$ is preferable to $MgAl_2SiO_6$ as an aluminous pyroxene component, the choice of a different component will not cause differences in the result.

[2] The names of phases are abbreviated as follows: cpx = clinopyroxene; opx = orthopyroxene; sp = spinel; ol = olivine; fo = forsterite; gar = garnet; py = pyrope; pl = plagioclase; an = anorthite.

from the proportion of Mg and Al atoms in the $M1$ site only.

(4) The solid solution is ideal at 1 bar and the non-ideality is introduced by the excess partial molar volume at high pressures.

The olivine–spinel–orthopyroxene equilibria in the system MgO–Al_2O_3–SiO_2 are first discussed; and based on the result, the assemblages plagioclase–olivine–clinopyroxene–orthopyroxene and spinel–plagioclase–clinopyroxene–orthopyroxene in the system CaO–MgO–Al_2O_3–SiO_2 will be treated. A method is then described whereby the results of calculations in simple systems can be used as indicators of equilibrium conditions in natural rocks.

Solubility of Al_2O_3 in orthopyroxene coexisting with forsterite and spinel in the system MgO–Al_2O_3–SiO_2

In the system MgO–Al_2O_3–SiO_2, $a^{ol}_{Mg_2SiO_4}$ and $a^{sp}_{MgAl_2O_4}$ in a spinel peridotite are unity, and

$$a^{opx}_{Mg_2Si_2O_6} = X^{M1}_{Mg} \cdot \gamma_{Mg_2Si_2O_6} \tag{10}$$

$$a^{opx}_{MgAl_2SiO_6} = X^{M1}_{Al} \cdot \gamma_{MgAl_2SiO_6} \tag{11}$$

$$X^{M1}_{Mg} + X^{M1}_{Al} = 1$$

where X^{M1}_{Mg} and X^{M1}_{Al} are the concentrations of Mg and Al atoms in the $M1$ site, and γ's are activity coefficients in orthopyroxenes. By introducing a parameter, $K'(2) \equiv X^{M1}_{Al}/X^{M1}_{mg}$, which is called the apparent equilbrium constant, we may write for reaction (2):

$$-RT \ln K'(2) = \Delta G^0(2) + \Delta G^{ex}(2) \tag{12}$$

where $G^{ex}(2)$ is an excess Gibbs free energy change of reaction (2) and

$$\Delta G^{ex}(2) = -RT \ln \left(\frac{\gamma_{MgAl_2SiO_6}}{\gamma_{Mg_2Si_2O_6}}\right) \tag{13}$$

$$\Delta G^{ex}(2) = \Delta H^{ex}(2) - T\Delta S^{ex}(2) \tag{14}$$

where the suffix "ex" denotes the excess term for reference to the ideal system (Thompson, 1967). $\Delta S^{ex}(2)$ equals zero for the ideal random mixing model of orthopyroxene used here, so relation (14) becomes:

$$\Delta G^{ex}(2) = \Delta H^{ex}(2) \tag{15}$$

Since

$$\left(\frac{\partial \Delta H}{\partial P}\right)_{S,T} = \Delta V \tag{16}$$

and

$$\left(\frac{\partial \Delta H^{ex}}{\partial P}\right)_{S,T} = \Delta V^{ex} \tag{17}$$

equation (12) becomes:

$$-RT \ln K'(2) = \Delta H^0_{1,T}(2) + (P-1)\Delta V^0(2) + (P-1)\Delta V^{ex}(2) - T\Delta S^0(2)$$

or

$$-RT \ln K'(2) = \Delta H^0_{1,T}(2) + (P-1)\Delta V(2) - T\Delta S^0(2) \tag{18}$$

where $\Delta H^0_{1,T}(2)$ and $\Delta S^0(2)$ are an enthalpy change at 1 bar, and entropy change of reaction (2), respectively. $\Delta V(2)$ is a molar volume change of reaction (2):

$$\Delta V(2) = V^0_{Mg_2SiO_4} + \bar{V}_{MgAl_2SiO_6} - \bar{V}_{Mg_2Si_2O_6} - V^0_{MgAl_2O_4} \tag{19}$$

where V^0_j and $\bar{V}_j$ are the molar volume of the pure phase and the partial molar volume of component j, respectively. The values of $\Delta H^0_{1,T}(2)$ and $\Delta S^0(2)$ are not known, but as described below, may be indirectly derived using values of $H^0_{1,T}(1)$ and $\Delta S^0(1)$ determined by Wood and Banno (1973) and Wood (1974), and the position of the univariant curve of the reaction orthopyroxene + spinel = forsterite + pyrope in the system MgO–Al_2O_3–SiO_2 (MacGregor, 1964).

An expression for the univariant reaction, opx + sp = fo + py may be written:

$$\underbrace{2[X^{M1}_{Mg}\,Mg_2Si_2O_6 \cdot X^{M1}_{Al}\,MgAl_2SiO_6]}_{\text{orthopyroxene solution}} + \underbrace{(X^{M1}_{Mg} - X^{M1}_{Al})MgAl_2O_4}_{\text{spinel}} = \underbrace{(X^{M1}_{Mg} - X^{M1}_{Al})Mg_2SiO_4}_{\text{forsterite}} + \underbrace{Mg_3Al_2Si_3O_{12}}_{\text{pyrope}} \tag{20}$$

which is simply a linear combination of equations (1) and (2):

$$(20) = (X^{M1}_{Mg} - X^{M1}_{Al}) \cdot (2) - (1) \tag{21}$$

Similar relations can therefore be written for molar enthalpy and molar entropy changes of reactions (1), (2), and (20):[3]

$$\Delta H(20) = (X^{M1}_{Mg} - X^{M1}_{Al}) \cdot \Delta H(2) - \Delta H(1) \tag{22}$$

$$\Delta S(20) = (X^{M1}_{Mg} - X^{M1}_{Al}) \cdot \Delta S(2) - \Delta S(1) \tag{23}$$

The composition of pyroxene may be calculated using equation (13) of Wood and Banno (1973). The Clapeyron equation

$$\frac{dP}{dT} = \frac{\Delta S(20)}{\Delta V(20)} \tag{24}$$

[3] It should be noted that these changes are on partial molar quantities of the components, and not on those of pure phases.

expresses $\Delta S(20)$ in terms of $\Delta V(20)$ and the slope of the univariant curve in P-T space. The slope can be read directly from MacGregor's (1964) phase diagram, and $\Delta V(20)$ can be calculated from published data[4] for spinel, forsterite, aluminous enstatite, and pyrope. A value for $\Delta S(20)$ is thus obtained. $\Delta H(20)$ is immediately known, because

$$\Delta H(20) = T\Delta S(20) \tag{25}$$

on the univariant curve. We also have relationships:

$$\Delta H(1) = \Delta H^0_{1,T}(1) + (P - 1)\,\Delta V(1) \tag{26}$$

$$\Delta S(1) = \Delta S^0(1) - R \ln (X^{M1}_{Al}) \cdot (X^{M1}_{Mg}) \tag{27}$$

[4] Sources of data for molar volumes and entropies of minerals used in this paper are given in Appendix 1.

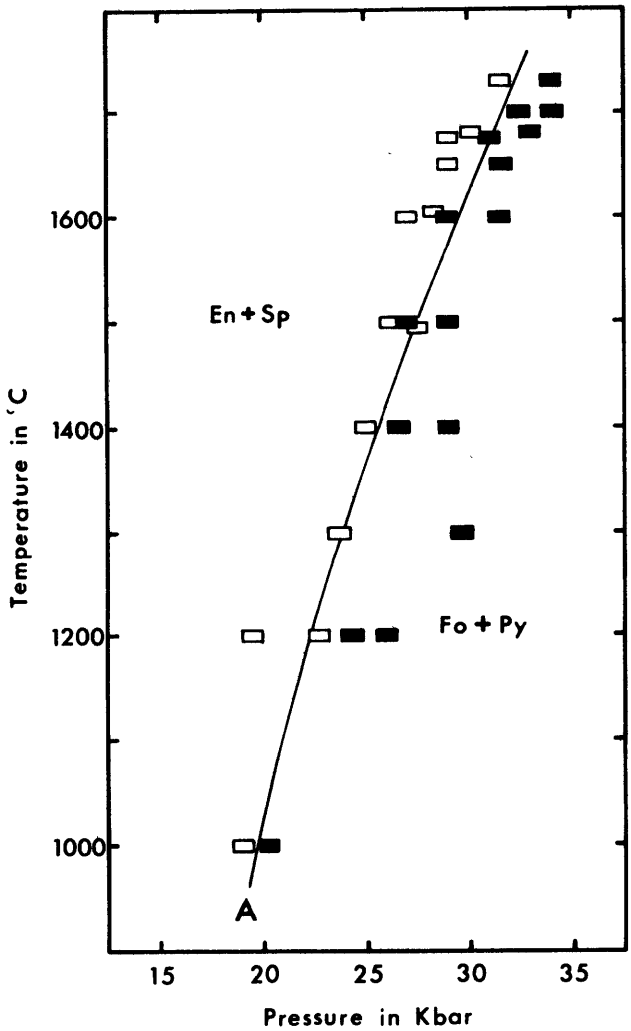

FIG. 1. Calculated univariant line (curve A) of the reaction opx+sp = fo+py in the system MgO–Al_2O_3–SiO_2 compared with the experimental data of MacGregor (1964): open rectangles = opx+sp; filled rectangles = fo+py.

and

$$\Delta H(2) = \Delta H^0_{1,T}(2) + (P - 1)\,\Delta V(2) \tag{28}$$

$$\Delta S(2) = \Delta S^0(2) - R \ln (X^{M1}_{Al}/X^{M1}_{Mg}) \tag{29}$$

Substituting the values of $\Delta H(20)$ and $\Delta S(20)$ which were obtained previously and ΔH and ΔS of equations (26), (27), (28), (29) into equations (22) and (23), we finally arrive at values of $\Delta H^0_{1,T}(2)$ and $\Delta S^0(2)$. ΔS^0 (2) is also, by definition,

$$\Delta S^0(2) = S^0_{Mg_2SiO_4} + S^0_{MgAl_2SiO_6} - S^0_{Mg_2Si_2O_6} - S^0_{MgAl_2O_4} \tag{30}$$

where S^0_j is an entropy of formation of component j in a pure phase at standard state (1 bar, 298°K). Temperature dependence of ΔS^0 was neglected, since heat capacity changes of the reactions are very small. Using published entropy data at standard state for forsterite, enstatite, and spinel, the entropy of $MgAl_2SiO_6$ pyroxene, as yet unknown, may be obtained. The entropy of pyrope may also be obtained using the relationship,

$$\Delta S^0(1) = S^0_{Mg_2Si_2O_6} + S^0_{MgAl_2SiO_6} - S^0_{Mg_3Al_2Si_3O_{12}} \tag{31}$$

Reading of the slope of the univariant curve has to be varied continuously with temperature to hold a value of ΔS^0 (2) constant. In the actual calculation, the best value of ΔS^0 (2) was sought such that the computed curve, which can be drawn by changing pressure and temperature in a stepwise manner starting from an arbitrary point of pressure and temperature using the Clapeyron equation (24), satisfies the experimental points. One of the calculated curves which best fits the experimental data of MacGregor (1964) is shown in Figure 1. The parameters of the curve are ΔS^0 (2) = 4.05 cal/deg/mol and $\Delta H^0_{1,T}(20)$ = 10.4 kcal/mole. Entropies of $MgAl_2SiO_6$ pyroxene and pyrope at standard state were calculated to be 33.0 cal/deg/mole and 61.6 cal/deg/mole, respectively.

A −10 percent friction correction was applied to all the pressure values of the runs as proposed by MacGregor (1974, p. 117). The values $\Delta H^0_{1,T}(1)$ and ΔS^0 (1) of 7012 cal/mole and 3.89 cal/deg/mole calculated by Wood (1974) were used instead of those calculated by Wood and Banno (1973) for reasons mentioned by Wood (1974, p. 3). Substituting the obtained values of $\Delta H^0_{1,T}(2)$ and $\Delta S^0(2)$ into equation (18), the MgO–Al_2O_3–SiO_2 phase diagram was constructed in pressure-temperature-composition space

(Fig. 2). This figure shows that, although the univariant curve of the reaction opx + sp = fo + py is nearly a straight line in the experimentally investigated area of pressure and temperature, the slope becomes steeper as temperature decreases and is almost vertical below 800°C. Slopes of Al_2O_3 isopleths for spinel peridotite are very shallow and almost horizontal below 1000°C. Anastasiou and Seifert (1972) determined the Al_2O_3 solubility in orthopyroxene on the reaction curve opx + sp = fo + cordierite, using a hydrothermal apparatus. Their data, 7.2 mole percent $MgAl_2SiO_6$ at 900°C–3 kbar, 13 mole percent $MgAl_2SiO_6$ at 1000°C–2.8 kbar, and 17.2 mole percent $MgAl_2SiO_6$ at 1100°C–2.6 kbar agree well with the calculated values of 8, 11, and 15 mole percent $MgAl_2SiO_6$ at the same conditions within the limits of experimental uncertainty. These, however, are in marked contrast to MacGregor's (1974) values of approximately 15, 21, and 24 mole percent $MgAl_2SiO_6$ respectively, at the same conditions. The reasons for large discrepancies between the values calculated here or those of Anastasiou and Seifert and MacGregor's data are not well understood.[5] MacGregor (1974) considered a possibility that the Al_2O_3 isopleths flatten as pressure decreases to match his experiments to those of Anastasiou and Seifert. The change of the slope may be caused through the changes of molar volume and/or molar entropy changes of reaction (2) with temperature and/or pressure at constant composition of pyroxenes. It is very difficult to expect the appearance of curvature of the isopleths only in the spinel peridotite field while the isopleths in the garnet peridotite field are well approximated by straight lines. The only possible way to have local rapid changes of the slopes of the isopleths is by having some kind of polymorphic transformation of aluminous enstatite. Examination of this possibility must await detailed X-ray crystallographic studies on aluminous enstatite at high pressure and temperature.

If the shallow slopes are correct, it is practically impossible to use the Al_2O_3 solubility in orthopyroxene in spinel peridotite as a geobarometer except at very high temperatures where the slopes are steeper. Nevertheless, this model for spinel peridotite enables us to calculate the solubilities of Al_2O_3 in orthopyroxene in plagioclase peridotite and in spinel pyroxenite as is shown in the following section.

Phase equilibria in the system of CaO–MgO–Al_2O_3–SiO_2 and the solubility of Al_2O_3 in orthopyroxene in plagioclase peridotite and in spinel pyroxenite

The apparent equilbrium constant of reaction (2) remains essentially constant even after the fourth component CaO is introduced into the system MgO–Al_2O_3–SiO_2, because the amounts of CaO entering orthopyroxene, spinel, and olivine are not great enough to cause significant changes of $\Delta V(2)$ in equation (18). Therefore, the calculated result for spinel peridotite in the system MgO–Al_2O_3–SiO_2 is a "bridge" between the MgO–Al_2O_3–SiO_2 and CaO–MgO–Al_2O_3–SiO_2 systems.

Kushiro and Yoder (1966) experimentally investigated the reactions an+fo=cpx+opx+sp, and cpx+opx+sp=gar+fo. It is possible to calculate these reactions using the model of the Al_2O_3 solubility

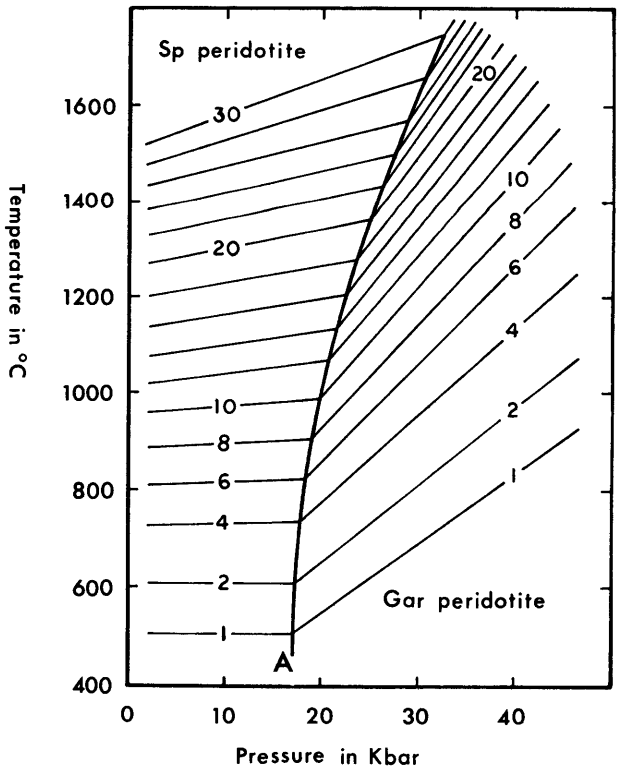

FIG. 2. Calculated phase diagram for the system MgO–Al_2O_3–SiO_2 in temperature–pressure–composition space. Curve *A* is the same as in Fig. 1. Isopleths refer to percentages of the *M*1 site in orthopyroxene occupied by aluminum atoms. The garnet peridotite portion is taken from Wood (1974).

[5] The thermodynamic treatment and the conclusions in the system MgO–Al_2O_3–SiO_2 are almost identical to those of Wood (1975), whose manuscript became available to the author after the 1975 International Conference of Geothermometry and Geobarometry at Pennsylvania State University. Wood discussed several possibilities for the discrepancies between the calculated and the experimental results and reached the conclusion that MacGregor's (1974) experiments are in error.

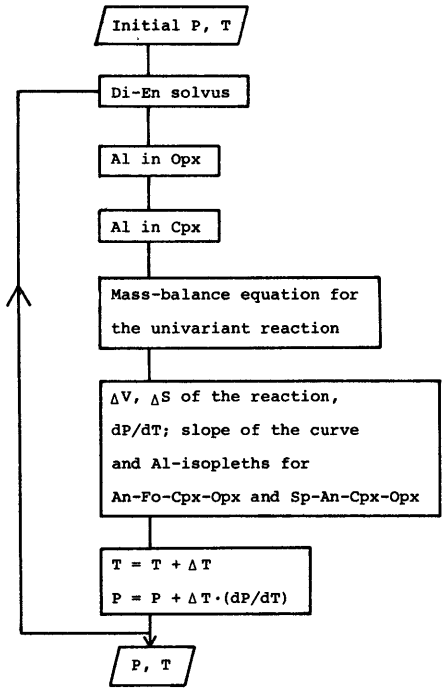

FIG. 3. Calculation scheme for the reaction an+fo = cpx+opx+ in the system $CaO–MgO–Al_2O_3–SiO_2$.

in orthopyroxene and experimental data on the diopside–enstatite solvus. Calculation for the reaction an+fo = cpx+opx+sp was performed as schematically illustrated in Figure 3. The data of Mori and Green (1975) were used to calculate the Ca/(Ca+Mg) ratio of coexisting ortho- and clinopyroxene. It was assumed that these numbers are independent of the Al_2O_3 content of the pyroxenes, judging from Boyd's (1970) data on the pyroxene solvus in the system $Al_2O_3–CaSiO_3–MgSiO_3$.[6] The procedure by which Al_2O_3 content in clinopyroxene was calculated from that in orthopyroxene is described in Appendix 2. If the compositions of pyroxenes are known, we may write a mass-balance equation for the reaction an+fo = cpx+opx+sp, and calculate the volume and entropy changes[7] of the reaction and finally the slope of the curve from the Clapeyron equation.

The calculation was started from 8.5 kbar, 1200°C, which is a well-bracketted experimental point. The agreement with the experimental runs is satisfactory as is seen in Figure 4. The ratio of the amount of Al_2O_3 in orthopyroxene to that in clinopyroxene changes regularly along the univariant curve from 1.2 at 1300°C to 0.9 at 500°C.

The same approach was taken to compute another univariant line for the reaction cpx+opx+sp = gar+fo. The method of each step of the calculation is the same as that for the reaction an+fo = cpx+opx+sp, except that the CaO content in garnet is also considered, as described in Appendix 2. The calculation was started from 18.5 kbar, 1300°C, with the ratio Ca/(Mg+Ca) of garnet varying from 0.13 at 1500°C to 0.16 at 500°C. The agreement with the

[6] Some experiments indicate that Al_2O_3 appreciably reduces enstatite solubility in clinopyroxene (O'Hara and Schairer, 1963; Herzberg and Chapman, 1976). The effect of the reduction was also examined in the calculation and was found to be no more than 1 kbar reduction of the position of the boundary around 1000°C, fixing the point at 8.5 kbar, 1200°C, yet the slope at lower temperatures (below 800°C) stays the same, and the general shape of the boundary remains unchanged regardless of the model used.

[7] The calculation procedure of entropies of complex pyroxenes is described in Appendix 3.

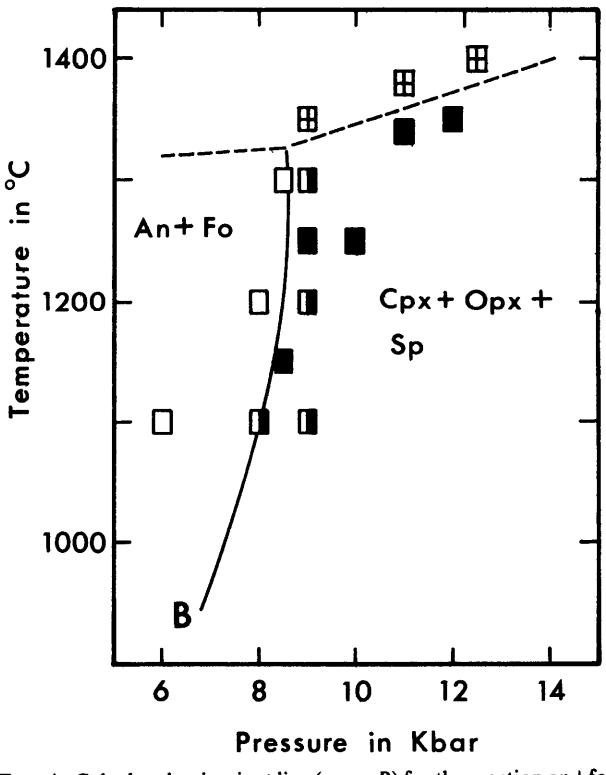

FIG. 4. Calculated univariant line (curve *B*) for the reaction an+fo = cpx+opx+sp in the system $CaO–MgO–Al_2O_3–SiO_2$, compared with the experimental data of Kushiro and Yoder (1966): open rectangles = an+fo; filled rectangles = cpx+opx+sp; half-filled rectangles = indeterminate; crossed rectangles = above solidus.

experimental data is excellent, as is shown in Figure 5.

Slopes of the Al_2O_3 isopleths for orthopyroxene coexisting with plagioclase + olivine + clinopyroxene and also with spinel + clinopyroxene + plagioclase were calculated along the univariant curve of the reaction an+fo = cpx+opx+sp using the Clapeyron equation for constant composition of orthopyroxene:

$$\left(\frac{\partial P}{\partial T}\right)_{X_{Al}^{M1}} = \frac{\Delta S}{\Delta V} \qquad (32)$$

where ΔS and ΔV are respectively molar entropy and molar volume changes of the reactions (3) or (4). Similarly, the slopes of the Al_2O_3 isopleths for garnet-clinopyroxene-orthopyroxene were calculated along the curve for the reaction cpx+opx+sp = gar+fo. In contrast to the three-component system $MgO-Al_2O_3-SiO_2$, the isopleths are not straight in the system $CaO-MgO-Al_2O_3-SiO_2$ since the Ca/(Ca+Mg) ratio of pyroxenes and the Al_2O_3 content in

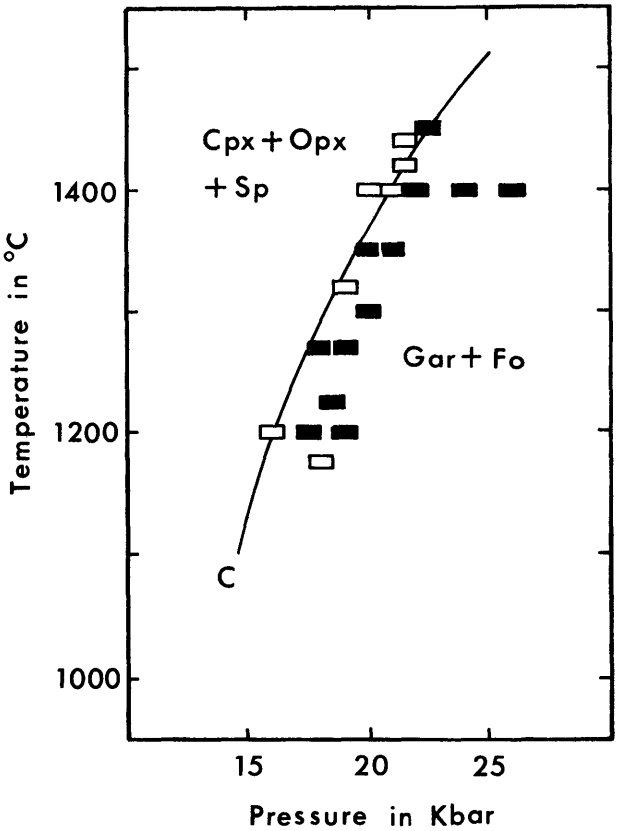

FIG. 5. Calculated univariant line (curve *C*) for the reaction cpx+opx+sp = gar+fo in the system $CaO-MgO-Al_2O_3-SiO_2$, compared with the experimental data of Kushiro and Yoder (1966): open rectangles = opx+cpx+sp; filled rectangles = gar+fo.

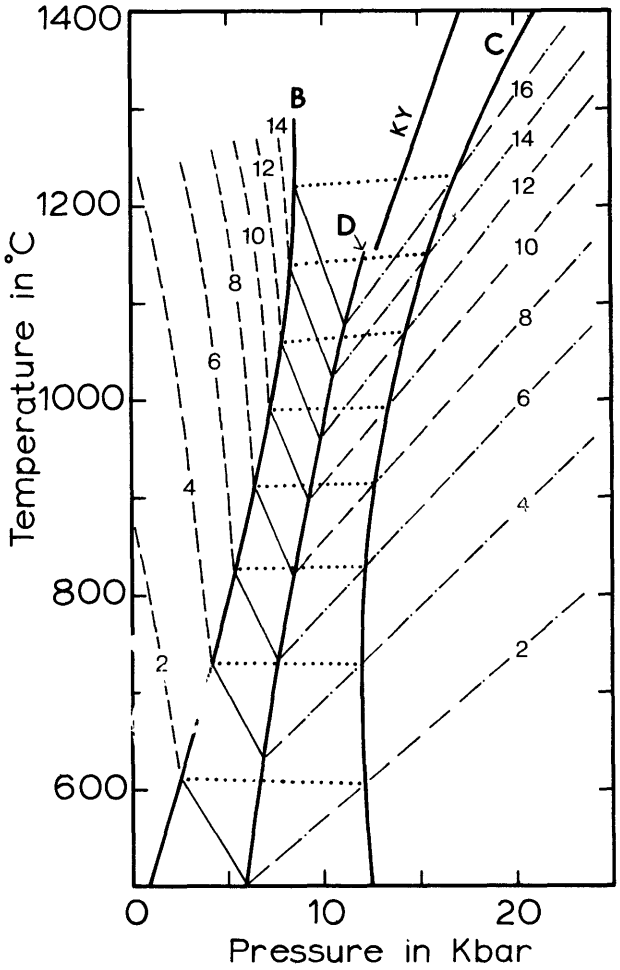

FIG. 6. Calculated Al isopleths for orthopyroxene in plagioclase periodotite (dashed lines), spinel peridotite (dotted lines), and garnet websterite or garnet peridotite (dash-dot lines) in the system $CaO-MgO-Al_2O_3-SiO_2$. Thick solid lines *B* and *C* are the same as in Fig. 4 and Fig. 5, respectively. Curve *D* is another univariant line for the reaction cpx+opx+sp+an = gar, which was graphically derived. KY is Kushiro and Yoder's (1966) experimentally-determined line for the same reaction in the four-component system.

clinopyroxene change with temperature, resulting in the gradual changes of molar entropy changes of the reactions. Isopleths for the plagioclase peridotite were drawn by calculating the slope from the Clapeyron equation (32) in a stepwise manner, starting from the points on the univariant line of the reaction an+fo = cpx+opx+sp, as was done in drawing the univariant lines, and the results are shown in Figure 6. They become less steep at high temperatures with constant values of X_{Al}^{M1}. Those for spinel peridotite and for spinel pyroxenite, on the other hand, may be safely approximated by straight lines, since extrapolations are not far enough to cause significant errors. Those for garnet peridotite will become steeper as

temperature increases with constant values of X_{Al}^{M1}, but here they are approximated by straight lines. Error by this simplification will be as much as one kilobar overestimate in pressure.

The curve *D*, which appeared by connecting intersection points of the isopleths for garnet–clinopyroxene–orthopyroxene with those for spinel–plagioclase–clinopyroxene–orthopyroxene, is another univariant line of a reaction cpx+opx+sp+an = gar. This reaction has been investigated by Kushiro and Yoder (1966), and the curve graphically drawn here is also consistent with their experimental curve (KY in Fig. 6).

Discussion

The calculated results in the four-component system $CaO–MgO–Al_2O_3–SiO_2$ are illustrated over a wide temperature range in Figure 6. The curve for the reaction cpx+opx+sp = gar+fo (curve *C*) retains the same character as that in the $MgO–Al_2O_3–SiO_2$ system (curve *A* in Fig. 2), *i.e.* it curves significantly and is nearly vertical below 800°C. The pressure is reduced by some 5-7 kbar from curve *A* by introducing CaO in the system, and the minimum value of the pressure of curve *C* is 12 kbar. The present theoretical calculation supports O'Hara *et al.*'s (1971) conclusion, based on their experiments, that simple linear extrapolation of the univariant line out of the experimentally investigated *P-T* range to uninvestigated lower temperatures is not valid, and that garnet peridotite is not stable in normal continental crust. The line for the reaction an+fo = cpx+opx+sp curves in the opposite direction, *i.e.*, the slope becomes less steep as temperature decreases, and this curve intersects the temperature axis above 400°C. This may imply high-temperature origins of plagioclase peridotites, either as direct crystallization products from magma or as recrystallized products of hot spinel or garnet peridotites of high-pressure origin. Curves *B* and *C* do not intersect each other, and there is no condition where plagioclase peridotite directly converts to garnet peridotite, in contrast to the prediction by Kushiro and Yoder (1966).

The Al_2O_3 solubility in orthopyroxene sensitively increases with pressure but is not so sensitive to temperature in plagioclase peridotite. In spinel pyroxenite it increases with both pressure and temperature. Since the solubility is insensitive to pressure in spinel peridotite, this parameter may be used as a geothermometer, and in fact is a better one than the frequently used Ca/(Ca+Mg) ratio in coexisting pyroxenes, which is insensitive to temperature below 1000°C.

Geothermometry and geobarometry

Although the bulk chemical composition of most mafic and ultramafic rocks are well expressed in the system $CaO–MgO–Al_2O_3–SiO_2$, the presence of other components, such as FeO, Na_2O, Cr_2O_3, Fe_2O_3, is not negligible in some cases. The effects of these minor components are removed by the use of the "apparent equilibrium constants" which are defined as

$$K'(1) = \frac{(X_{Mg}^{M2,opx} \cdot X_{Al}^{M1,opx})(X_{Mg}^{M2,opx} \cdot X_{Mg}^{M1,opx})}{a_{Mg_3Al_2Si_3O_{12}}^{gar}} \quad (33)$$

$$K'(2) = \frac{(X_{Mg}^{M2,opx} \cdot X_{Al}^{M1,opx})a_{Mg_2SiO_4}^{ol}}{(X_{Mg}^{M2,opx} \cdot X_{Mg}^{M1,opx})a_{MgAl_2O_4}^{sp}} \quad (34)$$

$$K'(3) = \frac{(X_{Mg}^{M2,opx} \cdot X_{Al}^{M1,opx})a_{CaMgSi_2O_6}^{cpx}}{(a_{Mg_2SiO_4}^{ol})(a_{CaAl_2Si_2O_8}^{pl})} \quad (35)$$

$$K'(4) = \frac{(X_{Mg}^{M2,opx} \cdot X_{Al}^{M1,opx})(a_{CaMgSi_2O_6}^{cpx})^{1/2}}{(X_{Mg}^{M2,opx} \cdot X_{Mg}^{M1,opx})^{1/2}(a_{CaAl_2Si_2O_8}^{pl})^{1/2}(a_{MgAl_2O_4}^{sp})^{1/2}} \quad (36)$$

corresponding to the equations (1), (2), (3), and (4), respectively. The simplest model, which is the ideal solution model, may be applied to crystallographic sites of the minerals as long as they are chemically close to the system $CaO–MgO–Al_2O_3–SiO_2$, and the activities are:

$$\begin{aligned} a_{Mg_3Al_2Si_3O_{12}}^{gar} &= (X_{Mg})^3(X_{Al})^2 \\ a_{Mg_2SiO_4}^{ol} &= (X_{Mg}^{M2})(X_{Mg}^{M1}) \\ a_{CaMgSi_2O_6}^{cpx} &= (X_{Ca}^{M2})(X_{Mg}^{M1}) \\ a_{CaAl_2Si_2O_8}^{pl} &= X_{CaAl_2Si_2O_8} \\ a_{MgAl_2O_4}^{sp} &= (X_{Mg}^{Tet})(X_{Al}^{Oct})^2 \end{aligned} \quad (37)$$

where X_{Mg}^{Tet} and X_{Al}^{Oct} are the concentrations of Mg and Al atoms in tetrahedral and octahedral sites in spinel, respectively. Rigorously, all of these sites in the solid solutions are expected to show positive non-ideal behavior (Saxena and Ghose, 1971), but since those excess terms will tend to cancel each other in calculation of K' in equations (33) to (36), it would be more consistent at the moment to adopt an ideal solution model for all the individual crystallographic sites of the participating phases, rather than applying more sophisticated models to some of the phases whose thermodynamic properties are better understood than others. This simplification may cause serious errors, if the chemical composition of the

phases are far from the system CaO–Al_2O_3–MgO–SiO_2 especially at low temperature, and in this case nonideality has to be taken into account.

As demonstrated for $K'(2)$ in equations (12) to (18), the equilibrium condition (5) may generally be rewritten as follows:

$$-RT \ln K'(i) = \Delta H^0_{1,T}(i) + (P-1)\Delta V(i) - T\Delta S^0(i) \quad (38)$$

$\Delta H^0_{1,T}(i)$ and $\Delta S^0(i)$ are independent of composition by definition, and $\Delta V(i)$ only depends on the amount of Al_2O_3 in orthopyroxene. If we neglect small changes of $\Delta V(i)$ which will be caused by a small shift of the amount of Al_2O_3 after the correction described below, it follows that the values of $K'(i)$ will not change by the introduction of components other than CaO, MgO, Al_2O_3, and SiO_2. The values of K' (2), K' (3), and K' (4), which are apparent equilibrium constants for, respectively, spinel periodotite, plagioclase periodtite, and spinel pyroxenite, have also been calculated along the univariant line of the reaction an+fo = cpx+opx+sp, and they are tabulated with the values of X^{M1}_{Al} in Table 1.

The method to find an Al_2O_3 isopleth for a given natural rock is as follows:

(1) Calculate activities of components $Mg_3Al_2Si_3O_{12}$, Mg_2SiO_4, $CaMgSi_2O_6$, $CaAl_2Si_2O_8$, $MgAl_2O_4$ in garnet, olivine, clinopyroxene, plagioclase, and spinel, respectively, by equations (37), and calculate $K'(i)$ by one of the equations (33) to (36), depending on the mineralogy of the rock. The method of Wood and Banno (1973, p. 118) may be followed to assign cations over $M1$ and $M2$ sites in ortho- and clinopyroxenes.

(2) Read a temperature which corresponds to the calculated value of K' for the mineral assemblage of the rock from Table 1.

(3) Using the diagram in Figure 6 and starting from the temperature point on the univariant line, draw a line parallel to the nearest isopleth for the particular mineral assemblage. The equilibrium condition for the rock lies somewhere on the line. Equilibration temperature and pressure may be uniquely obtained by combining another thermometer or barometer, such as the diopside–enstatite solvus or the partitioning of Fe and Mg between ferromagnesian minerals. For garnet periodtite and garnet pyroxenite, equation (2) in Wood (1974), which is a more direct reduction from the experimental data than the present model calculation, is to be used.

Evaluation of overall uncertainties in the calculated results is a difficult task, with direct experimental points being absent in plagioclase peridotite and spinal pyroxenite fields. Uncertainties in the calculated values of ΔS^0 (2) and ΔH^0 (2) are estimated to be ± 0.5 cal/deg/mole and ± 0.5 kcal/mole, respectively, without considering errors in the original experimental data. These result in the uncertainties in the positions of isopleths for spinel peridotite being approximately ± 20°C around 1000°C and ± 50°C around 800°C. The slope, however, will not be appreciably changed, since the values of volume change of the reaction (2) are very small compared with the large values of entropy change. The uncertainties in the spinel peridotite field are directly propagated into those in the position of the isopleths for plagioclase peridotite and for spinel pyroxenite; an uncertainty of ± 50°C in an isopleth for spinel periodotite at 800°C, for example, will cause uncertainties of approximately ± 1 kbar for plagioclase peridotite and of ± 2 kbar or ± 50°C for spinel peridotite. Other sources of uncertainties, especially the use of random mixing model of Al and Mg atoms in $M1$ site and the use of the ideal solution model for $MgSiO_3$–$MgAl_2SiO_6$ pyroxenes at one atmosphere, have not been considered, but they may become serious at low temperatures or for highly aluminous pyroxenes. The ordering of Al atoms in SiB site of orthopyroxene (Takeda, 1972; Ganguly and Ghose, 1975) may also cause some ordering of Al atoms in $M1$ site, but the effect has not been evaluated.

It is obvious now that more experimental work,[8] both to locate the positions of the facies boundaries and to determine the compositions of pyroxenes, is highly desirable to evaluate the thermodynamic model adopted here and to improve the accuracy of the diagram in Figure 6 for its practical use in geothermometry and geobarometry.

Conclusions

The solubility of Al_2O_3 in orthopyroxene is uniquely derived as a function of pressure and temperature in spinel and plagioclase peridotites and spinel pyroxenite, using published experimental data on pyroxene compositions in garnet periodotite and

[8] Recently three experimental studies relevant to the problem have appeared; Herzberg and Chapman (1976) on the Al_2O_3 solubility in clinopyroxene in spinel peridotite, and Presnall (1976) and Fujii and Takahashi (1976) on the Al_2O_3 solubility in orthopyroxene in spinel peridotite. All the results agree well with the present calculated results, confirming the minimal pressure dependence of the parameter in spinel peridotite, except that of Presnall, which suggests a negative slope for the 8.5 weight percent Al_2O_3 isopleth.

TABLE 1. Apparent equilibrium constants: K's and concentrations of Al atoms in the $M1$ site of orthopyroxene: X_{Al}^{M1} on the univariant line of the reaction: an + fo = cpx + opx + sp.

Temp.(C)	K'(2)×100	K'(3)×100	K'(4)×100	X_{Al}^{M1} ×100
1300	21.9	9.18	15.2	18.0
1250	20.2	9.43	14.6	16.8
1200	18.4	9.39	13.8	15.6
1150	16.7	9.14	12.9	14.3
1100	14.9	8.75	11.9	13.0
1050	13.2	8.22	10.8	11.7
1000	11.5	7.59	9.62	10.3
950	9.91	6.88	8.46	9.02
900	8.39	6.11	7.31	7.74
850	6.98	5.30	6.20	6.53
800	5.69	4.50	5.14	5.39
750	4.54	3.71	4.16	4.34
700	3.52	2.97	3.27	3.40
650	2.65	3.30	2.49	2.58
600	1.93	1.71	1.83	1.89
550	1.35	1.22	1.29	1.33
500	0.89	0.82	0.86	0.89

K'(2): for spinel peridotites (sp+ol+cpx+opx)
K'(3): for plagioclase peridotites (pl+ol+cpx+opx)
K'(4): for spinel pyroxenites (sp+pl+cpx+opx)

the locations of facies boundaries for garnet and spinel peridotites. The main conclusions are:

(1) The facies boundary between garnet and spinel peridotites and that between spinel and plagioclase peridotites curve significantly due to the compositional changes of pyroxenes with pressure and temperature. The former becomes vertical below 800°C and 12 kbar, and the latter curves in the opposite direction and becomes less steep as temperature decreases. This further constrains the geological occurrences of garnet and plagioclase peridotites in the earth's crust.

(2) The solubility of Al_2O_3 in orthopyroxene in spinel peridotite is insensitive to pressure, but may be used as a geothermometer. On the other hand, the parameter for plagioclase peridotite is very sensitive to pressure, and that for spinel pyroxenite is sensitive to both pressure and temperature. Practically, these parameters may be used as geothermometers and geobarometers, if the effects of components other than CaO, MgO, Al_2O_3, and SiO_2 are considered properly.

Appendix 1

Molar volumes and entropies at 1 bar and 298°K of forsterite, anorthite, spinel, diopside, and grossular and entropy of $CaAl_2SiO_6$ pyroxene are from Robie and Waldbaum (1968).

The entropy of clinoenstatite given by Robie and Waldbaum (1968) was used for orthoenstatite, since the difference between the two is very small (R. C. Newton, personal communication, 1975).

Molar volumes of pyrope and orthoenstatite are from Skinner (1956) and Turnock *et al.* (1973), respectively.

Partial molar volumes of $CaAl_2SiO_6$ and $Mg_2Si_2O_6$ in diopside solid solution are constant between diopside and diopside(50)–enstatite(50) and are 63.22 and 64.05 cm^3/gfw, respectively.

The partial molar volume of $CaMgSi_2O_6$ in orthopyroxene near $MgSiO_3$ was calculated to be 69.8 cm^3/gfw from the pressure dependence of the diopside–enstatite solvus (Mori and Green, 1975).

Partial molar volumes of $Mg_2Si_2O_6$ and $MgAl_2SiO_6$ components in orthopyroxene were calculated by equation (12) in Wood and Banno (1973), which is based on Skinner and Boyd (1964) and Chatterjee and Schreyer (1972).

Appendix 2

Method to calculate the amounts of Al_2O_3 in clinopyroxene and that of CaO in garnet from the composition of orthopyroxene

The aluminous pyroxene component $CaAl_2SiO_6$ in clinopyroxene may be related to the component $MgAl_2SiO_6$ by:

$$\underset{\text{opx}}{MgAl_2SiO_6} + \underset{\text{cpx}}{CaMgSi_2O_6} = \underset{\text{cpx}}{CaAl_2SiO_6} + \underset{\text{opx}}{Mg_2Si_2O_6} \quad (39)$$

The calcium garnet component $Ca_3Al_2Si_3O_{12}$ may be expressed as:

$$\underset{\text{cpx}}{CaMgSi_2O_6} + 1/3\ \underset{\text{gar}}{Mg_3Al_2Si_3O_{12}} = \underset{\text{opx}}{Mg_2Si_2O_6} + 1/3\ \underset{\text{gar}}{Ca_3Al_2Si_3O_{12}} \quad (40)$$

The equilibrium condition for these reactions may be written in the same form as equation (18):

$$-RT \ln K'(i) = \Delta H^0_{1,T}(i) + (P-1)\Delta V(i) - T\Delta S^0(i) \quad (41)$$

where $K'(i)$ are defined as:

$$K'(39) = \frac{(X_{Mg}^{M2,opx} \cdot X_{Mg}^{M1,opx})(X_{Ca}^{M2,cpx} \cdot X_{Al}^{M1,cpx})}{(X_{Ca}^{M2,cpx} \cdot X_{Mg}^{M1,cpx})(X_{Mg}^{M2,opx} \cdot X_{Al}^{M1,opx})} \quad (42)$$

$$K'(40) = \frac{(X_{Mg}^{M2,opx} \cdot X_{Mg}^{M1,opx}) X_{Ca}^{gar}}{(X_{Ca}^{M2,cpx} \cdot X_{Mg}^{M1,cpx}) X_{Mg}^{gar}} \quad (43)$$

The values of K' may be calculated using the above equations from Boyd's (1970) microprobe analyses of synthetic garnet, clino- and orthopyroxene which

were equilibrated at 1200°C and 30 kbar in the system Al_2O_3–$CaSiO_3$–$MgSiO_3$. The compositions of the phases are:

$$X_{Al}^{M1,opx} = 0.080,\ X_{Mg}^{M1,opx} = 0.920,\ X_{Mg}^{M2,opx} = 0.953,$$
$$X_{Al}^{M1,cpx} = 0.062,\ X_{Mg}^{M1,cpx} = 0.938,\ X_{Ca}^{M2,cpx} = 0.836,$$
$$\text{and}\quad X_{Ca}^{gar} = 0.15.$$

$\Delta H_{1,T}^0(39)$ and $\Delta H_{1,T}^0(40)$ were then calculated to be −168 cal/mole and 433 cal/mole, respectively, substituting the previously derived values of $S^0_{MgAl_2SiO_6}$ and $S^0_{Mg_3Al_2Si_3O_{12}}$, and volume data into equation (41). In the calculation of $\Delta V(i)$, clinopyroxene and garnet solid solutions were assumed to be ideal in terms of volume–composition relationships, based upon the unit cell data of clinopyroxenes on the joins $CaMgSi_2O_6$–$CaAl_2SiO_6$ and $CaMgSi_2O_6$–$Mg_2Si_2O_6$ (Clark *et al.*, 1962), and those of garnets on the join $Mg_3Al_2Si_3O_{12}$–$Ca_3Al_2Si_3O_{12}$ (Chinner *et al.*, 1960). K' (39) and K' (40) can now be calculated at any pressure and temperature by substituting the calculated values of $\Delta H_{1,T}^0$ (39) and $\Delta H_{1,T}^0$ (40) in equation (41). $X_{Al}^{M1,cpx}$ and X_{Ca}^{gar} may be calculated using equations (42) and (43), if the other quantities in these equations are known.

Appendix 3

Entropies of complex pyroxenes

Compositions of ortho- and clinopyroxenes in the three-component system Al_2O_3–$MgSiO_3$–$CaSiO_3$ may be generally expressed as

$$\underset{\text{orthopyroxene solution}}{(1-x-y)Mg_2Si_2O_6 \cdot x\ MgAl_2SiO_6 \cdot y\ CaMgSi_2O_6}$$

and

$$\underset{\text{clinopyroxene solution}}{(1-x'-y')CaMgSi_2O_6 \cdot x'\ CaAl_2SiO_6 \cdot y'\ Mg_2Si_2O_6}$$

Assigning Al and Ca atoms into $M1$ and $M2$ sites, respectively, atomic concentrations in the individual sites of orthopyroxene are:

$$X_{Mg}^{M1} = 1-x,\quad X_{Al}^{M1} = x,\quad X_{Mg}^{M2} = 1-y,$$
$$\text{and}\quad X_{Ca}^{M2} = y.$$

Similarly those of clinopyroxene are:

$$X_{Mg}^{M1} = 1-x',\quad X_{Al}^{M1} = x',\quad X_{Mg}^{M2} = y',$$
$$\text{and}\quad X_{Ca}^{M2} = 1-y'.$$

The Wood-Banno model for pyroxenes assumes random mixing of atoms in $M1$ and $M2$ sites and no interaction between the two sites. If we can neglect excess mixing entropy due to thermal vibration of atoms,[9] partial molar entropies of these pyroxene components are:

$$\begin{aligned}
\bar{S}_{Mg_2Si_2O_6} &= S^0_{Mg_2Si_2O_6} - R\ln(X_{Mg}^{M1}\cdot X_{Mg}^{M2})\\
\bar{S}_{MgAl_2SiO_6} &= S^0_{MgAl_2SiO_6} - R\ln(X_{Al}^{M1}\cdot X_{Mg}^{M2})\\
\bar{S}_{CaMgSi_2O_6} &= S^0_{CaMgSi_2O_6} - R\ln(X_{Mg}^{M1}\cdot X_{Ca}^{M2})\\
\bar{S}_{CaAl_2SiO_6} &= S^0_{CaAl_2SiO_6} - R\ln(X_{Al}^{M1}\cdot X_{Ca}^{M2})
\end{aligned} \tag{44}$$

The molar entropies of complex ortho- and clinopyroxenes: S^{opx} and S^{cpx} are by definition:

$$\begin{aligned}
S^{opx} &= (1-x-y)\bar{S}^{opx}_{Mg_2Si_2O_6} + x\bar{S}^{opx}_{MgAl_2SiO_6} + y\bar{S}^{opx}_{CaMgSi_2O_6}\\
S^{cpx} &= (1-x'-y')\bar{S}^{cpx}_{CaMgSi_2O_6} + x'\bar{S}^{cpx}_{CaAl_2SiO_6} + y'\bar{S}^{cpx}_{Mg_2Si_2O_6}
\end{aligned} \tag{45}$$

The entropy of pure $CaMgSi_2O_6$ pyroxene in the orthopyroxene phase and that of pure $Mg_2Si_2O_6$ pyroxene in the clinopyroxene phase are not known, but may be estimated empirically from experimental data for the enstatite–diopside solvus as described below.

The conditions of the two-pyroxene equilibrium may be written in the same form as equation (12):

$$-RT\ln K'(i) = \Delta G^0(i) + \Delta G^{ex}(i) \tag{46}$$

where $\Delta G^0(i)$ is the free energy change of reaction (i):

$$\underset{opx}{Mg_2Si_2O_6} = \underset{cpx}{Mg_2Si_2O_6} \tag{47}$$

and

$$\underset{opx}{CaMgSi_2O_6} = \underset{cpx}{CaMgSi_2O_6} \tag{48}$$

$K'(47)$ and $K'(48)$ are defined to be $X_{Mg}^{M2,cpx}/X_{Mg}^{M2,opx}$ and $X_{Ca}^{M2,cpx}/X_{Ca}^{M2,opx}$ respectively. The suffix "ex" denotes the excess term for reference to the ideal system. Differentiation of equation (46) with temperature gives:

$$\left(\frac{\partial[-RT\ln K'(i)]}{\partial T}\right)_P = -\Delta S^0(i) - \Delta S^{ex}(i) \tag{49}$$

For reaction (47),

$$\Delta S^0(47) + \Delta S^{ex}(47) = S^{0,cpx}_{Mg_2Si_2O_6} - S^{0,opx}_{Mg_2Si_2O_6} + S^{ex,cpx}_{Mg_2Si_2O_6} - S^{ex,opx}_{Mg_2Si_2O_6} \tag{47'}$$

[9] This approximation may be too crude for the $Mg_2Si_2O_6$–$CaMgSi_2O_6$ pyroxenes, but the treatment will be improved by considering the excess terms later.

and for reaction (48),

$$\Delta S^0(48) + \Delta S^{ex}(48) = S^{0,opx}_{CaMgSi_2O_6} - S^{0,opx}_{CaMgSi_2O_6} + S^{ex,opx}_{CaMgSi_2O_6} - S^{ex,opx}_{CaMgSi_2O_6} \quad (48')$$

where $S_j^{0,\alpha}$ and $S_j^{ex,\alpha}$ are the molar entropy of component j in pure phase α and the excess partial molar entropy of component j in phase α, respectively. For an orthopyroxene close to pure $Mg_2Si_2O_6$, the value of $S^{ex,opx}_{Mg_2Si_2O_6}$ will be very small and may be safely neglected, but $S^{ex,opx}_{Mg_2Si_2O_6}$ which may be a complex function of pressure, temperature, and composition, may not be negligible, since the composition of the coexisting clinopyroxene is far from pure $Mg_2Si_2O_6$. $S^{ex,opx}_{CaMgSi_2O_6}$ is negligible, but $S^{ex,opx}_{CaMgSi_2O_6}$ is not, by the same argument for equation (48′). The values of $S^{0,opx}_{Mg_2Si_2O_6} + S^{ex,opx}_{Mg_2Si_2O_6}$ and those of $S^{0,opx}_{CaMgSi_2O_6} + S^{ex,opx}_{CaMgSi_2O_6}$ may be calculated by obtaining the temperature dependences of $-RT \ln K'(i)$ determined from the experimental data of Mori and Green (1975), and by substituting Robie and Waldbaum's (1968) data for $S^{0,opx}_{Mg_2Si_2O_6}$ and $S^{0,opx}_{CaMgSi_2O_6}$ into equations (47′) and (48′). Substitution of the resulting values of $S^{0,opx}_{Mg_2Si_2O_6} + S^{ex,opx}_{Mg_2Si_2O_6}$ and $S^{0,opx}_{CaMgSi_2O_6} + S^{ex,opx}_{Mg_2Si_2O_6}$ for $S^{0,opx}_{Mg_2Si_2O_6}$ and $S^{0,opx}_{CaMgSi_2O_6}$, respectively, in equation (44) will reduce the error which may have been introduced by neglecting the excess term of mixing entropy for $Mg_2Si_2O_6$–$CaMgSi_2O_6$ pyroxenes.

Acknowledgments

The author thanks J. S. Dickey, Jr., A. J. Irving, and E. B. Watson for discussions and critical reading of the manuscript. Discussions with T. Mori, S. Banno, and A. B. Thompson at various stages of the work were very stimulating and are gratefully acknowledged. The paper has benefitted from the advice and criticisms of the reviewers; B. W. Evans, J. Ganguly, I. D. MacGregor, and B. J. Wood are thanked for their efforts. This work was supported by the Earth Science Section, National Science Foundation, NSF Grant DES 73-00264 to J. S. Dickey, Jr.

References

AKELLA, J. (1976) Garnet pyroxene equilibria in the system $CaSiO_3$–$MgSiO_3$–Al_2O_3 and in a natural mineral mixture. *Am. Mineral.* **61,** 589–598.

——— AND F. R. BOYD (1972) Partitioning of Ti and Al between pyroxenes, garnets, and oxides. *Carnegie Inst. Wash. Year Book,* **71,** 378–384.

——— AND ——— (1973) Effect of pressure on the composition of co-existing pyroxenes and garnet in the system $CaSiO_3$–$MgSiO_3$–$FeSiO_3$–$CaAlTi_2O_6$. *Carnegie Inst. Wash. Year Book,* **72,** 523–526.

——— AND ——— (1974) Petrogenetic grid for garnet peridotites. *Carnegie Inst. Wash. Year Book,* **73,** 269–273.

ANASTASIOU, P. AND F. SEIFERT (1972) Solid solubility of Al_2O_3 in enstatite at high temperatures and 1–5 kb water pressure. *Contrib. Mineral Petrol.* **34,** 272–287.

BOYD, F. R. (1970) Garnet peridotites and the system $CaSiO_3$–$MgSiO_3$–Al_2O_3. *Mineral. Soc. Am. Spec. Pap.* **3,** 63–75.

——— (1973) A pyroxene geotherm. *Geochim. Cosmochim. Acta,* **37,** 2533–2546.

——— AND J. L. ENGLAND (1964) The system enstatite–pyrope. *Carnegie Inst. Wash. Year Book,* **63,** 157–161.

——— AND P. H. NIXON (1975) Origins of the ultramafic nodules from some kimberlites of northern Lesotho and the Monastery Mine, South Africa. *Phys. Chem. Earth,* **9,** 431–454.

CHATTERJEE, N. D. AND W. SCHREYER (1972) The reaction enstatite$_{ss}$ + sillimanite = sapphirine$_{ss}$ + quartz. *Contrib. Mineral. Petrol.* **36,** 49–62.

CHINNER, G. A., F. R. BOYD AND J. L. ENGLAND (1960) Physical properties of garnet solid solutions. *Carnegie Inst. Wash. Year Book,* **59,** 76–78.

CLARK, S. P., J. F. SCHAIRER AND J. DE NEUFVILLE (1962) Phase relations in the system $CaMgSi_2O_6$–$CaAl_2SiO_6$–SiO_2 at low and high pressure. *Carnegie Inst. Wash. Year Book,* **61,** 59–68.

FUJII, T. AND E. TAKAHASHI (1976) On the solubility of alumina in orthopyroxene coexisting with olivine and spinel in the system MgO–Al_2O_3–SiO_2. *Mineral. J. (Japan),* **8,** No. 2, in press.

GANGULY, J. AND S. GHOSE (1975) Intracrystalline cation distributions in aluminous orthopyroxene, and its implications. *Extended Abstracts, International Conference on Geothermometry and Geobarometry,* Pennsylvania State University.

HERZBERG, C. T. AND N. A. CHAPMAN (1976) Clinopyroxene geothermometry of spinel-lherzolites. *Am. Mineral.* **61,** 626–637.

KUSHIRO, I. AND H. S. YODER, JR. (1966) Anorthite–forsterite and anorthite–enstatite reactions and their bearing on the basalt–eclogite transformation. *J. Petrol.* **7,** 337–362.

MACGREGOR, I. D. (1964) The reaction 4 enstatite + spinel = forsterite + pyrope. *Carnegie Inst. Wash. Year Book,* **63,** 157.

——— (1974) The system MgO–Al_2O_3–SiO_2: solubility of Al_2O_3 in enstatite for spinel and garnet peridotite compositions. *Am. Mineral.* **59,** 110–119.

MERCIER, J.-C. C. AND N. L. CARTER (1975) Pyroxene geotherms. *J. Geophys. Res.* **80,** 3349–3362.

MORI, T. AND D. H. GREEN (1975) Pyroxenes in the system $Mg_2Si_2O_6$–$CaMgSi_2O_6$ at high pressure. *Earth Planet. Sci. Lett.* **26,** 277–286.

O'HARA, M. J. (1967) Mineral paragenesis in ultrabasic rocks. In, P. J. Wyllie, Ed., *Ultramafic and Related Rocks.* John Wiley and Sons, Inc., New York, pp. 393–401.

——— AND J. F. SCHAIRER (1963) The join diopside–pyrope at atmospheric pressure. *Carnegie Inst. Wash. Year Book,* **62,** 107–115.

———, S. W. RICHARDSON AND G. WILSON (1971) Garnet peridotite stability and occurrence in crust and mantle. *Contrib. Mineral. Petrol.* **32,** 48–68.

PRESNALL, D. C. (1976) Alumina content of enstatite as a geobarometer for plagioclase and spinel lherzolites. *Am. Mineral.,* **61,** 582–588.

ROBIE, R. A. AND D. R. WALDBAUM (1968) Thermodynamic properties of minerals and related substances at 298.15°K (25.0°C) and one atmosphere (1.013 bars) pressure and at high temperatures. *U.S. Geol. Surv. Bull.* **1259.**

SAXENA, S. K. AND S. GHOSE (1971) Mg^{2+}–Fe^{2+} order–disorder and thermodynamics of the orthopyroxene crystalline solution. *Am. Mineral.* **56,** 532–559.

SKINNER, B. J. (1956) Physical properties of endmembers of the garnet group. *Am. Mineral.* **41.** 428–436.

——— AND F. R. BOYD (1964) Aluminous enstatites. *Carnegie Inst. Wash. Year Book,* **63,** 163–165.

TAKEDA, H. (1972) Crystallographic studies of coexisting aluminan orthopyroxene and augite of high pressure origin. *J. Geophys. Res.* **77,** 5798–5811.

THOMPSON, J. B., JR., (1967) Thermodynamic properties of simple solutions. In, P. H. Abelson, Ed., *Researches in Geochemistry.* Vol. 2, John Wiley and Sons, Inc. p. 341–375.

TURNOCK, A. C., D. H. LINDSLEY AND J. E. GROVER (1973) Synthesis and unit cell parameters of Ca–Mg–Fe pyroxenes. *Am. Mineral.* **58,** 50–59.

WOOD, J. B. (1974) The solubility of alumina in orthopyroxene coexisting with garnet. *Contrib. Mineral. Petrol.* **46,** 1–15.

——— (1975) The application of thermodynamics to some subsolidus equilibria involving solid solutions. *Fortschr. Mineral.* **52,** 21–45.

——— AND S. BANNO (1973) Garnet–orthopyroxene and orthopyroxene–clinopyroxene relationships in simple and complex systems. *Contrib. Mineral. Petrol.* **42,** 109–124.